2016

Advanced one dimensional plasmonic photocatalysts

Jinyan Xiong
University of Wollongong

UNIVERSITY OF WOLLONGONG

Institute for Superconducting and Electronic Materials (ISEM)

Faculty of Engineering and Information Sciences

Advanced One Dimensional Plasmonic Photocatalysts

Jinyan Xiong

This thesis is presented as part of the requirements for the award of the Degree

of

Doctor of Philosophy

of the

University of Wollongong

May 2016

DECLARATION

I, Jinyan Xiong, declare that this thesis, submitted in fulfilment of the requirements for the award of Doctor of Philosophy, in the Institute for Superconducting and Electronic Materials, Faculty of Engineering and Information Sciences, University of Wollongong, is wholly my own work unless otherwise referenced or acknowledged. This document has not been submitted for qualifications at any other academic institution.

Jinyan Xiong

May, 2016

DEDICATION

To my parents, sister, and Gang Cheng, who have always been there when I needed them.

ACKNOWLEDGEMENTS

First of all, I would like to show great thanks to my supervisors, Prof. Zhen Li and Prof. Shixue Dou, for their academic guidance, invaluable advice, financial support, understanding, and constant encouragement during my study. I specially thank Prof. Zhen Li for his supervision, patience, guidance, help, and advice on my studies and life. His profound knowledge, rigorous scientific style, and efficient ways of working were well worth learning.

I would like to express my special appreciation to the University of Wollongong (UOW) for providing me with the opportunity and financial support (Faculty Scholarship & International Postgraduate Tuition Award) to study at UOW to pursue the doctoral degree.

I want to thank the supporting from the Australian Research Council (ARC) through Discovery Projects DP 130102274 and DP130102699, by the Institute for Superconducting and Electronic Materials (ISEM) at UOW, and by the Jiangsu Provincial Key Laboratory of Radiation Medicine and Protection and the Priority Academic Program Development of Jiangsu Higher Education Institutions (PAPD) at the Soochow University.

I would like to acknowledge the use of the facilities in the UOW Electron Microscopy Centre, and Australian National Fabrication Facility (ANFF)-Materials node.

I would like to thank Dr. Tania Silver, who always critically read every manuscript during my PhD study, as well as this thesis.

I am grateful to my collaborators, including Prof. Jun Chen (University of Wollongong), Prof. Lianzhoou Wang (University of Queensland), Prof. Shanqing Zhang (Griffith University), Prof. Huagui Yang (East China University of Science and Technology), Dr. Shu Lei Chou (University of Wollongong), Ms. Weijie Li (University of Wollongong), Mr. Xulei Du (East China University of Science and Technology), and Ms. Qiao Sun (Soochow University), who provided important contributions to our joint publications during my PhD study. Special thanks to Prof. Jun Chen for his support, invaluable advice, and providing the photocatalytic test set-up for my experiments.

I would like to thank the staff for technical assistance at the ISEM, the Intelligent Polymer Research Institute (IPRI), the Electron Microscopy Centre (EMC) and the Australian Institute for Innovative Materials (AIIM) from UOW, especially including Dr. Germanas Peleckis (XRD), Dr. Dongqi Shi (XPS), Dr. Kosta Konstantinov (BET), Dr Patricia Hayes (UV-vis

and Raman), Dr. Tony Romeo (SEM), Dr David R. G. Mitchell (TEM), Dr. Gilberto Casillas (TEM), Candace Gabelish (Procurement and Chemical Inventory Officer), Joanne George (Laboratory and Safety Operations Officer), Narelle Badger (Adminstrative Assistant), Crystal Mahfouz (Administrative Assistant), and others for their kind assistance.

I also want to appreciate my dear colleagues and friends, and group members during my PhD study, who have contributed in different ways throughout my doctoral degree. Many thanks to Mr. Chao Han, Ms. Weijie Li, Mr. Zhiping Xiong, Ms. Xinqi Chen, Mr. Shaohua Zhang, Ms. Lijuan Zhang, Ms. Yujing Liu, Ms. Yuqing Liu, Ms. Kanlaya Pingmuang, Dr. George Tsekouras, Mr. Yang Zheng, Ms. Qiannan Liu, Mr. Zhe Hu, Mr. Mingzhe Chen, Mr. Weihong Lai, and others, for their generous help and friendship.

In the end, I would like to show my wholehearted appreciation and deep love to my great family, in particular my dear parents and my dear sister, for their great love, support, encouragement, and understanding. At the same time, I want to show great thanks to Dr. Gang Cheng, for his endless support whereever in abroad and domestic, encouragement, advice, help, and useful discussions through my life and my academic program.

TABLE OF CONTENTS

ABSTRACT

Semiconductors involved in photocatalysis have attracted considerable interest, owing to their great potential in the fields of environmental remediation, and renewable and clean energy exploitation. The limitations of ineffective sunlight utilization and low separation efficiency of electron-hole pairs of the commonly used semiconductor photocatalysts such as ZnO, Cu_2O, CdS, and Ag_2S, however, hinder their practical applications. To construct metal/semiconductor heterostructures through modification of such photocatalysts with novel plasmonic metals has been considered as a promising strategy for the improvement of the corresponding photocatalytic activity. Compared to other noble metals, one-dimensional (1D) Ag nanowires (Ag NWs) are more attractive because of their higher electrical and thermal conductivity, antibacterial characteristics, lower cost, nontoxicity, and wealth of optical and photoelectrochemical properties directly related to their geometry-dependent surface plasmon resonances, which makes them very popular for fabrication of advanced semiconductor/noble metal nanophotocatalysts.

In this doctoral work, semiconducting metal oxides and metal sulfides such as ZnO, Cu_2O, CdS and Ag_2S were chosen as examples for constructing semiconductor/noble metal photocatalysts. The compositon and structure of the resultant composites were characterized, and the optimum ratio of metal oxides/sulfides to Ag in the metal/semiconductor heterostructures showing excellent photocatalytic performance was investigated. The resultant 1D Ag@ZnO and Ag@Cu_2O core-shell nanowires prepared by a facile and general ambient strategy exhibited better photocatalytic performance and stability during organic contaminants photodegradation compared to zero-dimensional Ag@ZnO and Ag@Cu_2O core-shell nanoparticles and pure ZnO (/Cu_2O) nanocrystals under irradiation by solar light. The core-shell 1D hierarchical Ag@CdS nanowires also exhibited better photocatalytic performance than pure CdS. In addition, the 1D/two-dimensional (2D) hierarchical Ag-Ag_2S nanowire/nanosheet heterostructures showed excellent dye adsorption performance, although the catalytic activity was not significantly enhanced. Furthermore, they also exhibited great potential in lithium ion batteries and surface-enhanced Raman spectroscopy (SERS) detection of pollutants. This thesis will not only provide a facile and general approach to preparing 1D Ag@metal-oxide/sulfide hetero-nanostructured photocatalysts, but also explore the potential applications of such 1D heterostructures in energy-related fields. The main results of the thesis are summarized as follows:

1. Plasmonic Ag@ZnO core-shell hybrids, including hetero-nanowires and hetero-nanoparticles, have been synthesized at room temperature for application in photocatalysis. The morphology, particle size, crystal structure, and composition of the products were investigated by X-ray diffraction (XRD), scanning and transmission electron microscopy (SEM/TEM), X-ray photoelectron spectroscopy (XPS), and ultraviolet-visible (UV-VIS) spectroscopy. It is found that the concentration of $Zn(NO_3)_2 \cdot 6H_2O$ and the amount of water played crucial roles in the formation of Ag@ZnO core-shell hybrids. The resultant Ag@ZnO core-shell hybrids exhibited much higher photocatalytic activity and stability towards degradation of organic contaminants than pure ZnO nanocrystals under solar light irradiation. The 1D core-shell hetero-nanowires prepared under optimal conditions (i.e. 0.6 M $Zn(NO_3)_2 \cdot 6H_2O$ and 14.5 mL water) exhibited the best photocatalytic performance. The enhancement in their photocatalytic activity compared with the Ag@ZnO core-shell hybrids, especially by the 1D core-shell hetero-nanowires, could be attributed to the synergistic effects of the surface ZnO and the Ag nanowire cores with their surface plasmon resonance and electron sink effect, as well as the unique 1D core-shell nanostructure with its suitability for efficient mass transfer. The possible mechanism for degradation of Rhodamine B under solar light irradiation is discussed. This work provides a very convenient chemical route to the preparation of stable and highly efficient solar-light-driven plasmonic core-shell Ag@ZnO photocatalysts for cost-effective water purification.

2. A novel class of one-dimensional plasmonic $Ag@Cu_2O$ core-shell hetero-nanowires has been synthesized at room temperature for application in photocatalysis. The morphology, size, crystal structure, and composition of the products were investigated by XRD, SEM, TEM, XPS, and UV-VIS. The reaction time and the amount of Ag nanowires play crucial roles in the formation of well-defined 1D $Ag@Cu_2O$ core-shell hetero-nanowires. The resultant 1D $Ag@Cu_2O$ NWs exhibit much higher photocatalytic activity towards degradation of organic contaminants than $Ag@Cu_2O$ core-shell nanoparticles or pure Cu_2O nanospheres under solar light irradiation. The enhancement in photocatalytic activity could be attributed to the surface plasmon resonance and the electron sink effect of the Ag NW cores, as well as the unique 1D core-shell nanostructure.

3. One-dimensional Ag@CdS core-shell hetero-nanowires with hierarchical nanostructures have been successfully fabricated via a facile solvent thermal at low temperature. Based on the discussion of different reaction parameters, it can be concluded that the amounts of

thiourea and $Cd(NO_3)_2 \cdot 4H_2O$ not only have significant impact on, but also play important roles in the construction of hierarchical nanostructures assembled from nanosheets and nanoparticles. The optical properties of the as-fabricated 1D Ag@CdS hierarchical nanostructures were investigated by UV-VIS spectroscopy and the related photocatalytic properties have been evaluated by methyl orange degradation and water splitting. The photocatalysis experimental results indicate that the as-prepared 1D hierarchical Ag@CdS core-shell hetero-nanowires exhibit efficient photocatalytic capability towards degradation of methyl orange aqueous solutions and hydrogen generation from water splitting. It is hoped that these 1D Ag@CdS core-shell nanowires with hierarchical nanostructures could be a promising photocatalyst candidate.

4. Unique 1D/2D hierarchical Ag-Ag_2S heterostructures have been fabricated by an extremely simple solution route under ambient conditions. The morphology, size, crystal structure, and composition of the products were comprehensively investigated, and it was found the reaction time and the amount of S powder play crucial roles in the formation of well-defined 1D/2D hierarchical Ag-Ag_2S heterostructures. Diffusion and Ostwald ripening processes dominate the evolution of the heterostructures. The resultant 1D/2D Ag-Ag_2S hybrids exhibit great potential in Li/Na ion battery anodes, SERS detection, and the decoloration of organic dyes.

LIST OF FIGURES

(C) with different Ag core sizes and Fe_3O_4 shell thicknesses, and (D) with different morphologies and structures.

Figure 2.6 (A) UV-vis absorption spectra of different samples: ZnO NRA (black); Ag/ZnO NRA (red, with TEM image in inset) with an $AgNO_3$ concentration of 0.05 M;[13] (B) UV-vis absorption spectra: ZnO seed layer film; Ag/ZnO films with different $AgNO_3$ concentrations;[13] (C) UV-vis absorption spectra and corresponding images in inset: $AgVO_3$ and $Ag/AgVO_3$ nanoribbons.[14]

Figure 2.7 Schematic illustration of the basic process of semiconductor photocatalysis. [15]

Figure 2.8 Schematic illustration of photoinduced charge transfer to plasmonic metal/semiconductor heterostructured photocatalyst: (A) SPR effects (visible light irradiation); (B) Schottky junction (UV light irradiation).[16]

Figure 2.9 Scheme of plasmon-enhanced photocatalysis mechanisms in metal/semiconductor heteronanostructures: (A) SPR-mediated charge transfer;[2] (B) Plasmonic local electric field enhancement;[2] (C) Plasmonic scattering mechanism.[3]

Figure 2.10 TEM images of (A) Janus and (B) core-shell Au_{50nm}-TiO_2 nanostructures; (C) Possible visible-light-induced photocatalysis process for enhanced photocatalytic hydrogen evolution from Au-TiO_2 Janus nanostructures; (D) Generated hydrogen volume (under visible-light irradiation) over Au_{50nm}-TiO_2 (core-shell), TiO_2 (amorphous), and 50 nm Au nanoparticles; (E) Generated hydrogen volume (under visible-light irradiation) over Janus Au-TiO_2 comprising of different sized Au nanoparticles.[5]

Figure 2.11 SEM and TEM images: (A) Au@TiO_2, (B) Pd@TiO_2, (C) Pt@TiO_2; (D and E) Photocatalytic properties (under irradiation by visible light with $\lambda > 400$ nm) of core-shell M@TiO_2 nanospheres and P25 towards RhB photodegradation.[17]

Figure 2.12 (A) TEM and (B) HRTEM image (SAED pattern in the inset) of Ag/ZnO heterostructured nanocrystals with 5.0 at.% Ag;[18] (C) MO photodegradation on Ag/ZnO heterostructures;[18] (D) Acid orange II decomposition on ZnO and hollow Pt-ZnO microsphere photocatalysts under irradiation by UV light;[19] (E) Plot of RhB photodegradation over Au-ZnO nanocomposites;[20] (F) MO photodegration kinetics of ZnO and core-shell Au@ZnO nanostructures (TEM images in the insets) with different shell thicknesses under visible light

irradiation;[21] (G) Scheme of possible photocatalysis mechanism of core-shell Au@ZnO nanostructures under irradiation by visible light.[21]

Figure 2.13 TEM images of core-shell Cu@Cu_2O microspheres prepared at 12 (A), 24 (B), and 48 h (C);[22] (D) Curves of the reduction of NO concentration vs. visible-light irradiation time on various catalysts;[22] (E and F) TEM images of different core-shell Au-Cu_2O nanostructures: (E) nanocube and (F) octahedron;[23] (G) Plots of the amount of MO photodecomposed versus time using pristine Cu_2O and Au-Cu_2O core-shell photocatalysts;[23] (H and I) SEM images of the Ag/Cu_2O (h) and Ag/Cu_2O (i) heterogeneous nanocrystals;[24] (J) Pyronine B degradation rate over Cu_2O octahedral nanocrystals, Au/Cu_2O, and Ag/Cu_2O heterogeneous nanocrystals under UV light irradiation;[24] (K) SEM image of Cu_2O/Ag composite nanospheres with 0.05 mmol Ag;[25] (L) Time-dependence of MO (10 mg/L) degradation ratios (under visible light irradiation) over various photocatalysts.[25] (M) TEM image of core-shell Ag@Cu_2O nanoparticles;[11] (N) Degradation of MO by core-shell Ag@Cu_2O photocatalysts with different Cu_2O-shell thicknesses;[11] (O) TEM image of Au-Cu_2O hollow core-shell nanoparticles;[26] (P) MO photodegradation (under irradiation by visible light) versus irradiation time over photocatalysts.[26]

Figure 2.14 (A) Typical TEM image of core-shell Au@CdS nanoparticles, with the extinction vs. wavelength plot shown in the inset in comparison with pure CdS;[27] (B) Photocatalytic hydrogen generation over core-shell Au@CdS nanoparticles and CdS quantum dot supraparticles under light irradiation, with $\lambda \geq 420$ and $\lambda \geq 500$ nm, respectively;[27] (C) Hole-electron pair separation and transfer pathways on core-shell Au@CdS nanostructures towards photocatalytic H_2 evolution ($\lambda \geq 420$ nm);[27] (D) Hot electron transfer pathway on core-shell Au@CdS nanostructures towards photocatalytic H_2 evolution ($\lambda \geq 500$ nm);[27] (E) Photocatalytic degradation and (F) RhB photodegradation rate over spherical CdS NPs and CdS-spherical-NP−Au-NP composites with different Au NPs weight ratios;[28] (G) Scheme of charge separation on CdS-spherical-NP−Au-NP composite.[28]

Figure 2.15 (A) TEM image, with enlarged image in inset, of porous Ag_2S-Ag heterostructure nanotubes;[29] (B) MO photodegradation, and (C) Cr^{VI} photoreduction over various photocatalysts (H-1, H-2, and H-3, referring to Ag_2S-Ag nanotubes fabricated with 1.8, 3.5, and 5.4 mM of thioacetamide, respectively);[29] (D) TEM image of dumbbell-like Au-Bi_2S_3;[30] (E) Photodegradation of RhB over pure Bi_2S_3, normal and dumbbell-like Au-Bi_2S_3;[30] (F) Proposed photodegradation process for Au-Bi_2S_3 dumbbell-like nanostructure;[30] (G) TEM

image of Au-Bi_2S_3 heterostructures with Au nanoparticle positioned at the center of each Bi_2S_3 nanorod;[31] (H) The change in optical density of MB with time during reduction in presence of Au, Bi_2S_3, an Au and Bi_2S_3 mixture, and Au-Bi_2S_3 heterostructures;[31] (I) Rate of MB degradation with irradiation time under Xe lamp irradiation with a wavelength of 500 nm;[31] (J) TEM image of a single Au-CdSe pentapod-shaped heterostructure;[32] (K) Rhodamine 6G (R6G) dye photodegradation and (L) R6G dye photodegradation rate over Au/CdSe heterostructures and CdSe under illumination by UV light.[32]

Figure 2.16 (A) The preparation of Ag/TiO_2 nanowires by a photoreduction process in ethanol solvent;[33] (B) TEM image of a single Ag/TiO_2 nanowire;[33] (C) The kinetics of photodegradation of MB by different photocatalysts under visible-light irradiation (λ = 420 nm);[33] (D) TEM image of Ag/ZnO prepared with 0.05 M $AgNO_3$;[13] (E) Plots of ln(C_0/C) over time for MB photodegradation over different photocatalysts, with the inset showing the percentages degraded for the different samples.[13]

Figure 2.17 (A) Coupling between Cu_2O NWs and Au NPs;[34] (B) TEM image of Cu_2O-Au NW;[34] (C) MB photodegradation over Cu_2O NWs and Cu_2O NWs decorated with Au NPs coverage density is different);[34] (D) Proposed photocatalytic process over Cu_2O-Au NWs;[34] (E) Plots of ln(C_0/C) vs. irradiation time over CdS NWs-Au NPs and CdS NWs for 4-nitroaniline reduction (the weight addition ratio of Au NPs is different);[35] (F) Schematic illustration of proposed photocatalytic nitroaromatic reduction process (room temperature, N_2 purging, ammonium formate used as hole quencher, under visible light irradiation).[35]

Figure 2.18 (A) TEM image of an individual Ag@TiO_2 NW;[36] (B) Photocatalysis properties (under UV light irradiation) of different photocatalysts towards RhB decolorization at ambient temperature;[36] (C) Schematic diagram showing the transfer of electrons in Ag@TiO_2 NWs under UV irradiation;[36] (D) TEM image of core-shell Ag/ZnO nanowires (Ag content: 2.8 atom%);[37] (E) Plots of ln(C_0/C) versus irradiation time over different photocatalysts for RhB degradation;[37] (F) TEM image of Ag/CdS NWs;[38] (G) MB degradation efficiencies for different photocatalysts;[38] (H-J) TEM images of Ag NWs@CeO_2 with tailored shell thickness (H: 26.15 nm, I: 66.12 nm, J: 28.92 nm;[39] (K) Photocatalytic O_2 evolution (under visible light illumination) curves of pure CeO_2, core-shell Ag-NWs@CeO_2, and core-shell Ag-NPs@CeO_2 nanostructured catalysts prepared from 50 mM $AgNO_3$;[39] (L) MB degradation over Ag-NWs@CeO_2-2, Ag-NPs@CeO_2, and bare CeO_2 products;[39] (M) Schematic illustration of proposed process induced by the hot-electron effect.[39]

Figure 2.19 (A) SEM image of core-shell Ag/AgCl nanowires;[40] (B) Schematic illustration of formation of core-shell Ag/AgCl nanowires via in-situ oxidation;[40] (C) SEM image of hierarchical Ag/AgCl nanowire/nanoplate hetero-nanostructures;[40,41] (D) Photocatalysis properties (under visible light irradiation) of core-shell Ag/AgCl nanowires towards MO decomposition;[40] (E) Photocatalysis properties of hierarchical Ag/AgCl nanowire/nanoplate hetero-nanostructures and other photocatalysts towards RhB degradation under visible-light irradiation;[41] SEM images of (F) necklace-like Ag nanowire/Ag_3PO_4 cube heterostructures[42] and (G) core-shell Ag/Ag_3PO_4 coaxial hetero-nanowires[42,43] (H) Photocatalytic activities of Ag/Ag_3PO_4 heterostructures, pure Ag_3PO_4 cubes, and Ag nanowires towards RhB degradation under visible-light irradiation[42]: necklace-like Ag nanowire/Ag_3PO_4 cube heterostructures (purple line, Figure 2.19 F), core-shell Ag/Ag_3PO_4 coaxial hetero-nanowires (yellow green line, Figure 2.19 G), pure Ag_3PO_4 cubes (green line), Ag/Ag_3PO_4 heterostructure prepared in 0.1 M $[Ag(NH_3)_2]^+$ complex aqueous solution (blue line), Ag/Ag_3PO_4 heterostructure prepared in 0.05 M $[Ag(NH_3)_2]^+$ complex aqueous solution (red line), and pure Ag nanowire (black line). The images in the insets in (A), (C), and (F) are at higher magnification.

Figure 2.20 (A) SERS spectra of PATP (10^{-3} M) adsorbed on the surface of Ag-ZnO nanostructures (bottom spectrum: a few 1-20 nm Ag NPs, middle spectrum: aggregated 20-50 nm Ag NPs, top spectrum: much more large Ag particles);[44] (B) SERS spectra obtained from TiO_2 and Au/TiO_2 with various concentrations of R6G;[45] (C) SERS spectra of R6G on Ag/ZnO composites with different nanostructures (from bottom to top): (V) ZnO film on Si substrate; (IV) aggregated Ag NPs/ZnO film structure; (III) Ag/ZnO films on Si substrate; (II) Ag wavy film/ZnO HNS; (I) Ag NPs/ZnO hollow nanosphere (HNS);[46] (D) Raman spectra of R6G (10^{-4} and 10^{-8} M) on AOZ and AIZ arrays in comparision to that on pure ZnO HNS at concentration of 10^{-4} M (AOZ, AIZ, and HNS refer to Ag NPs on the top of ZnO hollow nanospheres, Ag NPs inside the ZnO hollow nanospheres, and the pure hollow nanospheres, respectively);[47] (E) SERS spectra of PATP adsorbed on an Au/ZnO assembly, an Au NP monolayer, and ZnO substrate.[48]

Figure 2.21 (A) SERS spectra of 10^{-6} M rhodamine B (RhB, structure shown in inset) on bare branched Cu_2O crystals and Ag/Cu_2O collected from galvanic replacement at different reaction stages;[49] (B) Raman spectra of 4-mercaptopyridine adsorbed on pure Ag films (the thicknee is 5 nm) and Ag/CuO;[50] (C) SERS spectra of thiophenol (10^{-5} M) adsorbed on

Figure 5.10 (A-C) XRD patterns, and (D-L) SEM images of as-prepared Ag@Cu_2O nanoparticles (A, and D-F), Ag nanoparticles (B, and G-I), and pure Cu_2O (C, and J-L).

Figure 5.11 (A-C) Variation in the light absorption of the MO solution in the presence of the as-prepared photocatalysts under solar light irradiation for different irradiation times: (A) Ag@Cu_2O NWs, (B) Ag@Cu_2O NPs, and (C) pure Cu_2O nanospheres; (D) photocatalytic activity of MO oxidation under solar light irradiation.

Figure 5.12 (A) XRD patterns of the sample before (a) and after (b) photocatalytic test; (B) XPS spectrum of Cu 2p, (C) SEM image and (D) TEM image of the sample after photocatalytic test.

Figure 5.13 Photocatalytic degradation of MO over the 1D Ag@Cu_2O core-shell hetero-nanowires in the presence of scavengers.

Figure 5.14 Schematic illustration of the transfer of photogenerated electron-hole pairs in the Ag@Cu_2O core-shell NWs under solar light irradiation.

Figure 6.1 (A) XRD pattern and (B) EDX spectrum of the as-prepared Ag@CdS heterostructures (A1), for which the added amount of $Cd(NO_3)_2 \cdot 4H_2O$/thiourea was 1.2 mmol/0.6 mmol, respectively.

Figure 6.2 (A and B) SEM images of the as-prepared Ag@CdS heterostructures (A1) with the added amount of $Cd(NO_3)_2 \cdot 4H_2O$/thiourea 1.2 mmol/0.6 mmol; (C) TEM image, (D) HRTEM image, (E) HAADF STEM image, and (F-H) the corresponding EDX elemental mapping analysis of an individual Ag@CdS heterostructure.

Figure 6.3 UV-Vis absorption spectra of Ag@CdS heterostructures (A1) with added amounts of $Cd(NO_3)_2 \cdot 4H_2O$/thiourea of 1.2 mmol/0.6 mmol.

Figure 6.4 (A) XRD pattern and (B) SEM image of the product (A2) prepared without ammonia with added amounts of $Cd(NO_3)_2 \cdot 4H_2O$/thiourea of 1.2 mmol/0.6 mmol.

Figure 6.5 SEM images of the products prepared in the presence of different amount of $Cd(NO_3)_2 \cdot 4H_2O$/thiourea: (A) 0.3 mmol/0.6 mmol, (B) 0.6 mol/0.6 mmol, (C) 1.8 mmol/0.6 mmol, (D) 2.4 mmol/0.6 mmol, (E) 1.2 mmol/1.2 mmol, (F) 1.2 mmol/2.4 mmol.

Figure 6.6 (A-C, G-L) SEM images and (D-F) TEM images of the product prepared in the presence of different amount of $Cd(NO_3)_2 \cdot 4H_2O$/thiourea: (A, D) 0.075 mmol/0.075 mmol, (B, E) 0.15 mmol/0.15 mmol, (C, F) 0.3 mmol/0.3 mmol, (G) 0.15 mmol/0.075 mmol, (H) 0.075 mmol/0.15 mmol, (I) 0.3 mmol/0.15 mmol, (J) 0.15 mmol/0.3 mmol, (K) 0.6 mmol/0.3 mmol, (L) 0.3 mmol/0.6 mmol.

Figure 6.7 (A) Photocatalytic activities of 1D Ag@CdS hierarchical nanowires and other as-prepared photocatalysts towards MO dye degradation under irradiation by solar light. (B) Photocatalytic hydrogen evolution curves of 1D Ag@CdS hierarchical nanowires and other as-prepared photocatalysts under irradiation by visible light with $\lambda > 420$ nm. (C) Degradation rates and hydrogen yield by various photocatalysts.

Figure 7.1 (A) XRD pattern and (B) EDX spectrum of the as-prepared Ag-Ag_2S heterostructures with the S/Ag ratio of 1:2.

Figure 7.2 (A, B) SEM image of the as-prepared Ag-Ag_2S heterostructures with the S/Ag ratio of 1:2; (C) TEM image, (D) HRTEM image, (E) SAED pattern, (F) HAADF image, and (G, H) corresponding EDX elemental mapping analysis of an individual Ag-Ag_2S heterostructure.

Figure 7.3 SEM images of the products obtained with the S/Ag ratio of 1:2 at different reaction times: (A) 0 min, (B) 30 min, (C) 1.5 h, (D) 2 h, (E) 4 h, (F) 6 h, (G) 8 h, (H) 12 h, and (I) 24 h.

Figure 7.4 TEM images (A, C, and E) and corresponding HRTEM images (B, D, and F) of the products obtained at different reaction times: (A, B) 30 min, (C, D) 4 h, and (E, F) 6 h.

Figure 7.5 (A) XRD patterns and (B) UV-Vis-NIR absorption spectra of the products obtained with the S/Ag ratio of 1:2 at different reaction times.

Figure 7.6 (A-D) SEM images of the products prepared with different molar ratios of sulfur powder to Ag nanowires: (A) 0.4:1, (B) 0.33:1, (C) 0.22:1, and (D) 0.2:1; (E) TEM image and (F) HRTEM image of the product prepared with an S to Ag ratio of 0.2:1; (G) XRD patterns of the products prepared with different molar ratios of sulfur powder to Ag nanowires.

Figure 7.7 (A-C) SEM images and (D) XRD pattern of the Ag-Ag_2S heterostructures obtained after 6 days.

LIST OF TABLES

LIST OF SCHEMES

Chapter 1 Introduction

1.1 General background

Semiconductor photocatalysis technology has been the object of great research efforts due to its great applications in renewable energy, and environmental protection and remediation.[52-56] In past decades, a variety of studies were devoted to the development of highly-efficient photocatalysis systems and the exploration of fundamental parameters that modify the photocatalytic performance. The most commonly investigated semiconductor photocatalysts, including metal oxides and metal chalcogenides such as TiO_2,[57-59] ZnO,[60,61] Cu_2O,[62,63] CdS[64-66] and Ag_2S,[29,67-69] have been proven to be excellent photocatalysts. The inherent limitations on the effective harvesting and broad spectrum absorption of natural sunlight, and the fast recombination rate of photogenerated electrons and holes, however, lead to inefficient utilization of green solar energy and reduced photocatalytic activity.[38,70-73] To date, different kinds of methods, including shape, size, and facet control, element doping, dye-sensitization, and heterostructure construction, have been developed to effectively enhance the photocatalytic performance through increasing the broad absorption of sunlight, prolonging the lifetime of photoinduced carriers, and enhancing the photocatalytic stability,[74] for example, via shape control,[75-79] doping with metal or non-metal elements,[80-84] dye-sensitization,[85-88] and construction of heterostructured photocatalyst systems by combining them with novel plasmonic metals (i.e. Ag, Au, Pd, Pt) and/or other semiconductors.[2,74,89-95] Among these, the construction of plasmonic metal/semiconductor heterojunctions is one of the most effective strategies because of the effects of surface plasmon resonance (SPR) and Schottky junctions,[16,91,96,97] which endow the heterojunction with good properties that are better than those of the individual components.

As a matter of fact, noble metals nanoparticles (NPs) can show SPR, which can be tailored by engineering the shape, size, and surroundings.[98] Therefore, noble metal NPs

can not only strongly absorb visible light, but also can serve as an electron sink and source of active reaction sites. Accordingly, under light irradiation, the photogenerated electron-hole pairs can be separated and the carriers transported efficiently at the interfaces of metal/semiconductor hybrids.[98]

During the past few years, one of the most commonly investigated types of plamonic metal/semiconductor heterostructured photocatalysts is semiconductor decorated with plasmonic metal nanoparticles. The metal nanoparticles on the outside are exposed to the reactants and the surrounding medium, however, which could lead to corrosion and detachment from the semiconductor photocatalyst.[11,36,70] An alternative option is to construct core-shell metal@semiconductor structures. As an important type of photocatalyst, one-dimensional (1D) semiconductor nanostructures and their hybrids with metal heterostructures have been intensively explored. The synthesis of 1D nanostructures and their potential applications in solar energy conversion have attracted much recent interest because of their unique 1D geometry with fast and long-distance electron transfer, good electron conductivity and mobility, large specific surface area, high light-harvesting efficiency, favourable length-to-diameter ratios, and high adsorption capacity.[96,99] More importantly, taking into account the shortcomings of single component nanomaterials, such as ineffective utilization of visible light, low quantum efficiency, and poor stability during the photocatalysis process, multi-component 1D-based nanohybrids are expected to overcome such drawbacks, and accordingly, are being studied for heterogeneous photocatalysis.[14,70,96,99,100]

1.2 Motivation

Semiconductor-involved photocatalysis has attracted considerable attention because it shows great potential in addressing the issues of environmental pollution and energy shortages. When the commonly used single-component semiconductors such as TiO_2, ZnO, Cu_2O, and CdS are used as photocatalysts, however, their limited broad spectrum absorption and utilization of green solar enegy and the low separation efficiency of their

photoinduced electron-hole pairs significantly reduce their photocatalytic activity and block their practical applications. Therefore, it is of significant importance to explore versatile methods to engineer the most commonly used oxides and sulfides to modify their optical properties, so that they can efficiently utilize natural solar energy, while, at the same time, offering other advantages, especially high separation efficiency of photogenerated carriers.

Heterostructured photocatalysts constructed by combining semiconductors with noble metals can combine the properties of the individual components and show synergistic interactions between their semiconducting and metallic components, which contribute to their high effectiveness in enhancing photocatalytic properties. In particular, the modification of such single-component photocatalysts with favourable plasmonic metals in the design of metal/semiconductor heterostructures has been developed as an effective strategy to boost their photocatalytic activities.

In comparision to other noble metals nanomaterials, Ag nanostructures have attracted increasing interest because of its higher electrical and thermal conductivity, antibacterial characteristics and nontoxicity, lower cost, and wealth of optical and photoelectrochemical properties directly related to their geometry-dependent surface plasmon resonances.[10,70,101] Furthermore, the unique geometrical of one-dimensional nanostructures on one hand makes it very popular for the fabrication of advanced semiconductor/noble metal nanophotocatalysts. On the other hand, combining with the electronic characteristics, one-dimensional Ag naonostructures also can provide direct pathways with a high slenderness ratio for charge transfer, decouple the direction of charge carrier collection, and induce low reflectance through light trapping and scattering, resulting in the enhancement of photocatalysis. Accordingly, Ag@semiconductor heterostructures comprising one-dimensional Ag nanostructures are being paid much more attention and have demonstrated promising applications in photocatalytic degradation of dyes and photocatalytic O_2 evolution.[36-43,102,103]

Studies of the structure/composition-property relationship of Ag@semiconductors have caused an urgent need for adjustable synthetic strategies, where the structure and composition can be simply tailored. Most of the synthesis approaches have suffered from drawbacks, however, such as requirements for high temperature, addition of surfactants, the involvement of other additives, and complicated processes. Hence, it is of considerable significance to develop an economical and facile route to the synthesis of one-dimensional Ag nanostructure-based hybrid photocatalysts with optimized structure, composition, and performance for constructing a highly-efficient heterostructured photocatalysis system.

Herein, the aim of this thesis is to design a facile and general strategy for the synthesis of 1D Ag-oxide/sulfide hetero-nanostructured photocatalysts. Several kinds of semiconductor oxides and sulfides such as ZnO, Cu_2O, and CdS have been used for the construction of such heterostructures. The photocatalytic performance optimization of the as-synthesized Ag@oxides and Ag@sulfides has been achieved through tailoring the mole ratio of oxides/sulfides to Ag and engineering the morphology of Ag nanostructures.

Chapter 1 briefly introduces the general background and motivation of this thesis.

Chapter 2 presents a comprehensive literature review on plasmonic photocatalysts.

Chapter 3 offers the details of the chemicals, synthesis methods, characterization techniques, photocatalytic tests, surface-enhanced Raman scattering (SERS) measurements, and battery performance measurements.

Chapter 4 focuses on ambient controlled synthesis of plasmonic Ag@ZnO core-shell hybrids, including hetero-nanowires and hetero-nanoparticles. The most effective factors, such as the concentration of $Zn(NO_3)_2 \cdot 6H_2O$ and the amount of water, for the formation of Ag@ZnO core-shell hybrids will be discussed. The possible mechanism

for the degradation of rhodamine B (RhB) over the Ag@ZnO core-shell hybrids, especially the 1D core-shell hetero-nanowires under solar light irradiation, will also be investigated.

Chapter 5 focuses on the room-temperature synthesis and characterization of one-dimensional plasmonic Ag@Cu_2O core-shell heteronanowires for photocatalysis application. The effective factors for the formation of well-defined 1D Ag@Cu_2O core-shell hetero-nanowires will be investigated. The reasons for the enhancement in photocatalytic activity of the resultant 1D Ag@Cu_2O NWs under solar light irradiation will also be discussed.

Chapter 6 focuses on synthesis and characterization of 1D Ag@CdS nanowires with hierarchical nanostructures. The impact of different reaction parameters on the formation of 1D hierarchical Ag@CdS nanostructures assembled from nanosheets and nanoparticles will be discussed. The photocatalytic performance towards photodegradation of methyl orange aqueous solutions and photocatalytic hydrogen generation over such 1D hierarchical Ag@CdS core-shell hetero-nanowires will be investigated.

Chapter 7 focuses on the ambient synthesis and characterization of unique 1D/2D Ag-Ag_2S hierarchical nanostructures. The formation mechanism of such interesting structures will be investigated. In addition to their applications in decoloration of organic dyes, their potential in SERS detection and Li/Na ion battery anodes will also be studied.

Chapter 8 summarizes the overall thesis work and gives some further suggestions for future work relevant to such 1D plasmonic photocatalysts.

Chapter 2 Literature Review

2.1 Surface plasmon resonance (SPR)

Plasmonics, which is inherently linked with nanotechnology and nanoscience, is mainly concerned with the manipulation and control of light on the nanometer scale, on the basis of plasmonic modes of localized surface plasmons or propagating surface plasmons.[1,104] In general, plasmons are oscillations of electron gas collected in the conduction band of a metal or semiconductor under the electromagnetic field of incident light.[105,106] Optical waves are able to couple to the free electron collective oscillations through localized excitations or propagating surface waves, which depend on the geometry.[1,104] Surface plasmons are oscillations spatially confined to the surfaces of conducting materials and strongly interact with incident light.[105] The surface plasmon resonance (SPR) of plasmonic nanostructures is the resonant photon-induced collective oscillation of conduction electrons, occurring while the incident light frequency satisfies the natural frequency of the surface electrons.[3,98,107]

For spherical metal or semiconductor nanostructures, when they are excited by incident light, a coulombic force will be established on the gas of negatively charged conduction electrons and induce them to oscillate collectively.[1] The oscillation can be in resonance with the incident light at a proper excitation frequency, leading to an intense oscillation of the surface electrons, called a localized surface plasmon resonance (LSPR) (Figure 2.1A).[1]

For non-spherically shaped metal or semiconductor nanostructures, the electron oscillation is localized at the edges and corners and/or along the principal axes of nanostructures in a non-isotropic manner, resulting in an additional structure-dependent depolarization and splitting of the SPR into several different modes, including transverse and longitudinal modes.[104] For a nanowire (Figure 2.1B), a propagating surface plasmon travelling along the surface of the nanowire structure (length axis) can be created due to the excitation of the free electrons when incident light is coupled to

the nanowire structure.[1] The incident light is not uniform across the nanowire structure, and surface plasmons propagate back and forth along it.[1] Reflection from the ends of the nanowire structure can change the phase and resonant length, and the propagation lengths can be in the tens of micrometers, so the propagating surface plasmon wavelength can be manipulated by the geometry of the structure.[1,108]

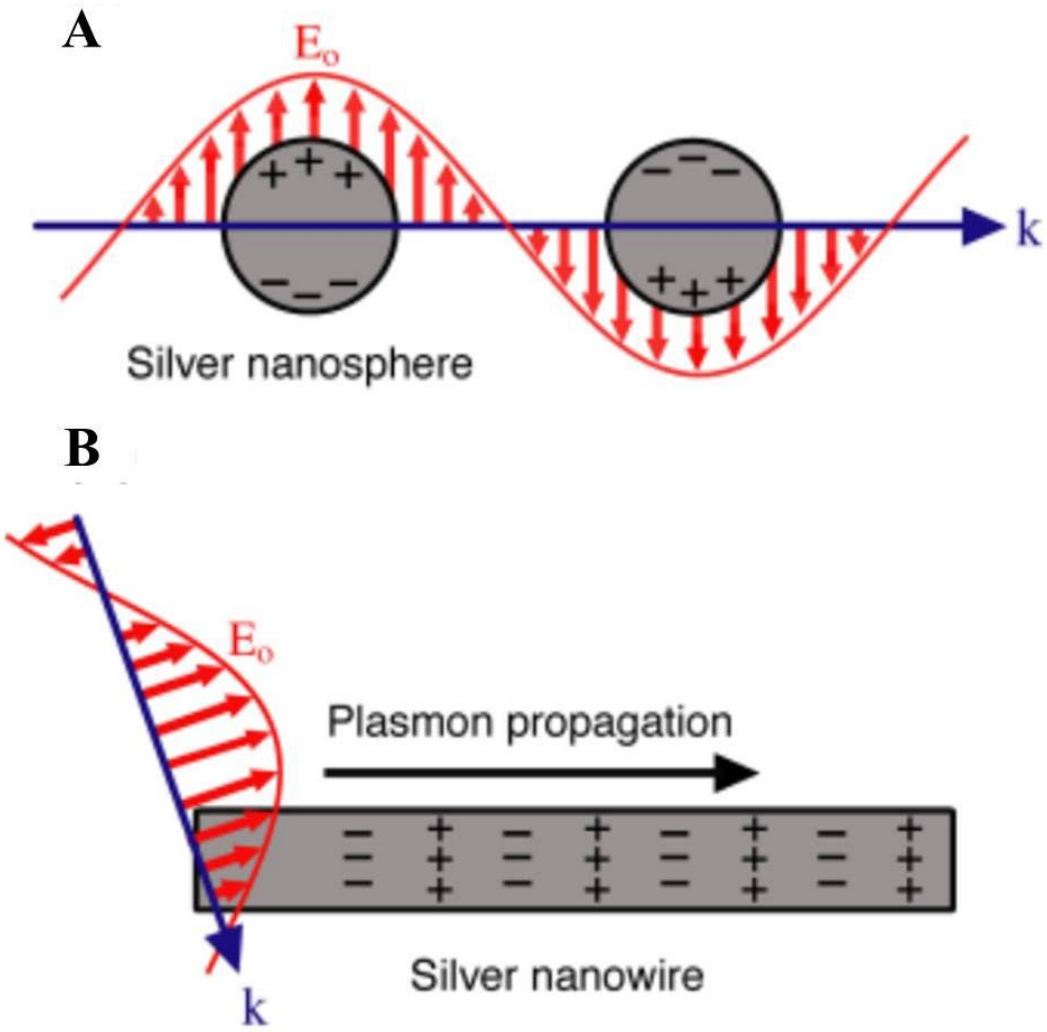

Figure 2.1 Scheme of the electric field (E_o) of the incident light (wavevector **k**) induced SPR in a spherical nanostructure (A) and a nanowire structure (B).[1]

In both cases, the light can be concentrated into the nanoscale upon resonant excitation, and the intense light localization causes the electromagnetic field arround the plasmonic

nanostructures to be highly enhanced, which can be described by evanescent waves in the direction perpendicular to the interface.[109] The field can be further enhanced by enlarging the surface curvature of the plasmonic nanostructures (making it sharper).[2,109,110] For example, Figure 2.2A displayed the electric field intensity improvement towards Au nanostructures with different shapes from finite-difference time-domain (FDTD) simulations.[2] For an Au nanorod or nanoplate, it was observed that the field improvment at the tips was stronger than that at a gold nanosphere under identical conditions.[2] Furthermore, different kinds of nanomaterials showed different resonant photon wavelengths. As shown in Figure 2.2B, spherical copper (Cu) silver (Ag), and gold (Au) nanoparticles showed different resonant behaviour when excited with solar radiation.[3] In addition to the nature of nanostructured materials, their size and shape have important impact on the SPR intensity and resonant wavelength.[1,3,105,111-114] For example, the resonant wavelength of Ag nanostructures could be varied for shapes such as nanowires (diameter of 90 ± 12 nm and > 30 aspect ratio), nanocubes (edge length of 79 ± 12 nm), and nanospheres (diameter of 38 ± 12 nm) (Figure 2.2C).[3] The resonant frequency also can be engineered via controlling the sizes of plasmonic nanoparticles. Figure 2.2D showed the spectra of Ag nanocubes having various edge lengths (36, 58, 99, and 172 nm). When increasing the edge length from 36 to 172 nm, it can be seen that the centroid of the resonance wavelength shows a big change and displays an obvious red shift.[4] Taking Au nanorods as another example (shown in Figure 2.2E), their longitudinal plasmon resonance wavelength can be tailored from the visible to the near-infrared region through manipulating the slenderness ratio.[2] It is possible to design and synthesize plasmonic nanostructures that can cover the whole solar spectrum and beyond.[1,3,113]

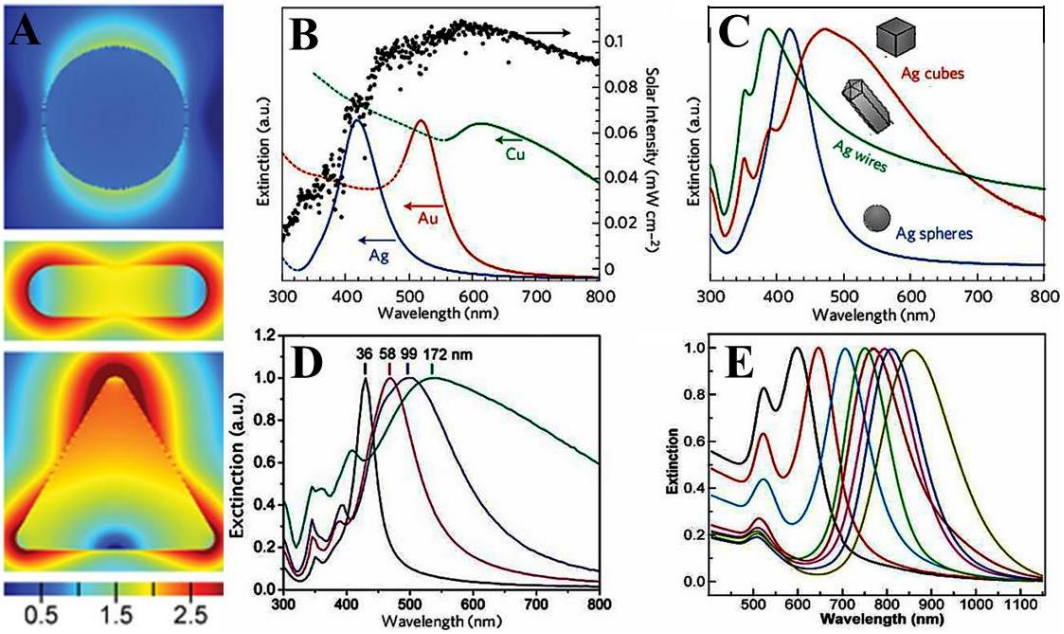

Figure 2.2 (A) Electric field intensity enhancement contours on the logarithmic scale of Au nanocrystals (different shapes, the same volume), obtained from FDTD calculations. (Top: nanosphere with diameter of 50 nm; Middle: nanorod with diameter and length of 30 and 102 nm, respectively; Bottom: nanoplate with thickness and edge length of 10 and 87 nm, respectively);[2] (B) Normalized extinction spectra of Cu (diameter: 133 ± 23 nm), Au (diameter: 25 ± 5 nm), and Ag (diameter: 38 ± 12 nm) spherical nanoparticles. The black curve is the intensity of solar radiation. The metal extinction curves showing dashed portions reveal interband transitions (in these regions, no SPR);[3] (C) Normalized extinction spectra for Ag nanowires (diameter: 90 ± 12 nm, aspect ratio: > 30), Ag nanocubes (79 ± 12 nm, edge length), and Ag nanospheres (diameter: 38 ± 12 nm);[3] (D) Normalized extinction spectra for Ag nanocubes having different edge lengths: 36 nm, 58 nm, 99 nm, and 172 nm;[4] (E) Extinction spectra for Au nanorods having different slenderness ratios.[2]

2.2 Techniques for the synthesis of metal/semiconductor nanostructures

Controlled synthesis of plasmonic metal/semiconductor heterostructures has been the object of tremendous efforts, owing to their significant potentials in photocatalysis

(photodegradation of organic pollutants, photocatalytic hydrogen evolution towards water splitting, and photocatalytic CO_2 reduction), surface-enhanced Raman scattering, and biotechnological applications. Generally, in the synthesis of such heterostructures, the growth of the outer shell material is more complicated than the preparation of the core material. Hence, this part will focus on techniques for the fabrication of outer shell materials. So far, various synthesis techniques, with the most frequently used approaches including wet-chemical deposition, photoreduction, solvothermal/hydrothermal method, self-assembly, ion exchange, etc., have been developed to fabricate high-quality plasmonic metal/semiconductor heterostructures.

2.2.1 Wet-chemical deposition

Wet-chemical deposition is an extremely simple and low-cost method, and it is the most frequently adopted strategy for preparing plasmonic metal/semiconductor photocatalysts.[95,107] In this typical synthesis process, the precursors and reagents react in the dispersed solution containing support materials to form hybrid nanostructures with metal cores − semiconductor shells or plasmonic metal coatings on semiconductors.[95,96,107] Generally, the reaction temperature and time, pH of reaction system, and precursors and reagents concentrations and amounts could have significant impact on the formation of such plasmonic metal/semiconductor photocatalysts.[95,107]

2.2.2 Photoreduction method

The photoreduction method is also called photodeposition and is often used to fabricate plasmonic photocatalysts with relatively high deposition ratios of plasmonic noble metal anchored on the surfaces of semiconductors under light irradiation.[96,107] In a typical process, when the semiconductor dispersion under vigorous stirring is illuminated under a suitable light having a certain wavelength, the photogenerated electrons in the conduction band (CB) can combine with a specific metal source (metal salt or complex) containing metal ions at the interface to produce metal nanoparticles on

the semiconductor support, and the holes left in the valence band (VB) are captured by a sacrificial scavenger.[96,107,115] Scheme 2.1 illustrates a possible photoreduction process for the fabrication of metal nanoparticles (NPs) deposited on the semiconductor support.

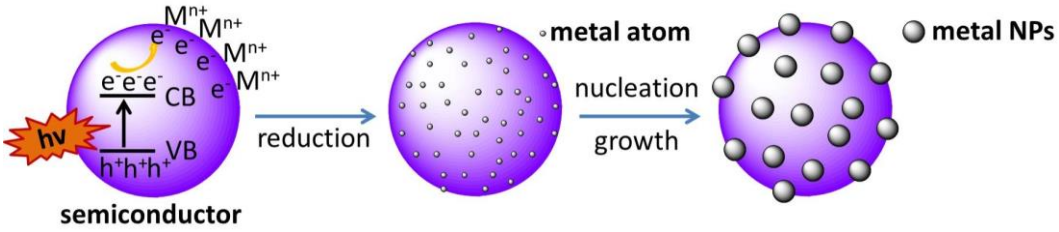

Scheme 2.1 Schematic illustration of the photoreduction process for metal nanoparticles (NPs) deposited on a semiconductor support.

2.2.3 Solvothermal/hydrothermal methods

Solvothermal/hydrothermal methods, where the reaction takes place in a solvent, are conveniently and widely employed to synthesize plasmonic metal/semiconductor heterostructures.[91,95] In a typical process, the reagents and precursors with an appropriate ratio are mixed in an appropriate solvent and then put into a Teflon-lined autoclave, where they are then kept at a predetermined temperature once it is enclosed in a stainless steel vessel. The relatively high temperature and pressure, along with the special reaction environment, not only enhance the solubility of precursors, but also accelerate the processing of reaction between the reagents and precursors.[91,95,96]

2.2.4 Self-assembly method

For this method, both metal and semiconductor nanostructures are pre-prepared. In a typical preparation process, certain amounts of pre-made semiconductor nanostructures and metal nanoparticles are mixed in a proper solvent by sonication to form a uniform dispersion, followed by vigorous stirring for a period. The metal nanoparticles are

assembled on the semiconductor nanostructures by introducing a small molecular linker.[2,27,28,35,116-119] The advantage of this method is that the morphology and structure of hybrids can be precisely controlled.

2.2.5 Ion exchange

The ion exchange method is a new technique to prepare heterostructure-based photocatalysts by exchange reaction which occurs at the interface of the heterostructure. The preliminary requirement is that the solubility of the products produced from exchange reaction is lower than for the reactants.[91,95,107] During the ion exchange reaction, external anions or cations are transferred into the parent nanostructure, and the original ions simultaneously diffuse out of the nanostructure at the same time.[91,95] This method shows big advantages, especially in the selective fabrication of a complex hybrid nanostructure with an epitaxial heterointerface, while keeping the original morphology and structure of the semiconductor, as well as precisely controlling the composition.[2] Such a method is often used to fabricate Ag/AgX (X = Cl, Br)-based hybrid photocatalysts, and it is often combined with an *in-situ* photoreduction process, with the aim of producing metallic species.[107]

It should be noted that the above-mentioned methods are often combined with each other or other fabrication methods, such as ion exchange coupled with photoreduction, or assembly/hydrothermal/wet-chemical deposition combined with calcination treatment. In addition, microwave-assisted method,[29] ultrasonic method,[120] electron beam evaporation,[121] and radio-frequency magnetron sputtering also have been used for fabrication of metal/semiconductor photocatalysts.[122]

2.3 Properties of plasmonic metal/semiconductor nanostructures

Metal/semiconductor hybrid plasmonic nanostructures exhibit synergistic properties by combining surface plasmon resonance with semiconducting properties. On the one hand,

after the metal component is combined with semiconductors, its plasmonic property will be altered, because the dielectric property of the surrounding medium has a significant influence on the surface plasmon resonance. On the other hand, the semiconductor component will retain its main properties (such as the energy band structures) except for the semiconductor-metal interface, although some other properties, such as ultraviolet-visible-near-infrared absorption, photocatalysis, and Raman scattering, will be tuned and/or enhanced thanks to the cooperative action with the SPR effect of metal.[2,6,7,9-12,14,34] In general, the surface plasmon resonance peaks of metals commonly exhibit a red-shift to longer wavelengths after being combined with semiconductors, because the high refractive index of the semiconductors can promote the dielectric effect.[5-7,9-11,123] The ultraviolet-visible (UV-vis) light absorption of semiconductors will also be broadened after they are combined with plasmonic metals, which might result from the SPR effect of metal nanoparticles.[6,13,14,34]

For the core@shell metal@semiconductor hybrids, the SPR wavelengths can be systematically altered by their dimensions and morphology, such as their geometrical arrangement and interfacial structures, core structure and composition, shell structure and composition, and shell thickness and shell packing density.[5-12,124] For instance, morphology tailoring can tune the surface plasmon resonance properties of the hybrid nanostructures. Figure 2.3A displays experimental extinction spectra of Au-TiO_2 core-shell and Janus nanostructures, and Au nanoparticles in isopropyl alcohol.[5] It can be seen that the gold nanoparticles with sizes of 50 nm exhibit an LSPR peak in the visible region, while Au-TiO_2 core-shell and Janus nanostructures show red-shifts for the LSPR peak. It is proposed that with the combination of Au NPs with TiO_2, the refractive index of the dielectric environment surrounding Au NPs shows an overall increase. Compared with Au-TiO_2 Janus nanostructures, the Au-TiO_2 core-shell nanostructures exhibit a larger red-shift in LSPR, because the Au-TiO_2 Janus nanostructures have one side of the Au NPs exposed to the solvent and showing a lower refractive index (1.4) than that of TiO_2 (2.5), which is fully coated on all sides of the Au cores for core-shell Au-TiO_2

nanostructures. The experimentally measured red-shifts are in good accordance with discrete dipole approximation (DDA) simulations (Figure 2.3B). In addition, the widths of the LSPR experimental spectra are greater than those of the simulated ones because of fluctuations in the actual size and shape of such measured nanostructures.

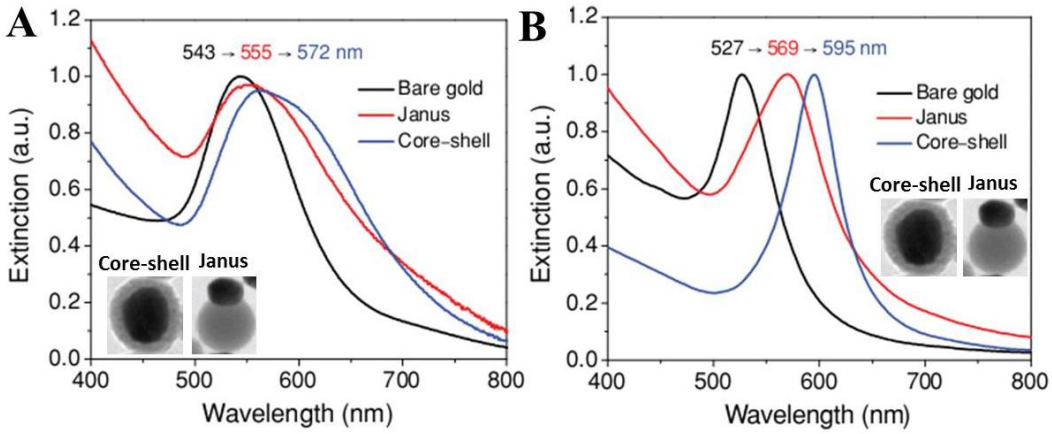

Figure 2.3 Optical-extinction spectra of Au nanoparticles with diameters of 50 nm and of core-shell Au_{50nm}-TiO_2 Janus nanostructures from experimental tests (in isopropyl alcohol) (A) and discrete-dipole approximation simulations (B).[5]

Similar phenomena are also observed in Au@TiO_2[6] and Au@Cu_2O[7-9] core-shell nanostructures. As displayed in Figure 2.4A, the core-shell Au@TiO_2 NPs have a sharp absorption peak at ~330 nm (329.7 nm) which could be the characteristic absorption peak of TiO_2. The SPR response of Au cores apparently shifts from 529.4 nm to ~600 nm with a weak absorption peak. The weak SPR response results from the thick TiO_2 shells for single Au@TiO_2 core-shell NPs. The SPR peaks of Au nanoparticles that are red-shifted from 520 nm to 598 nm with weak absorption are also observed in Au@Cu_2O core-shell nanostructures (Figure 2.4B). For larger core-shell particle sizes, the SPR absorption bands of the metal nanocrystals could disappear.[125] Furthermore, the SPR wavelengths could be tuned by the shell thickness and shell packing density, as well as geometrical interfacial structures. Figure 2.4C and 2.4D show the experimental and simulated extinction spectra of core-shell Au@Cu_2O nanoparticles (from bottom to

top: shell thickness of 6, 15, 27, 39, 53, 62, and 75 nm) and Au nanoparticles (black line at bottom, the diameter is 49 nm). The SPR peaks of Au nanoparticles gradually red-shift from 578 nm (Au cores) to near-infrared wavelengths with increasing shell thickness, and the peaks that appear progressively on the blue side of 600 nm for core-shell nanostructures are due to the optical characteristics of the Cu_2O shell.[8]

Unlike the core-shell structure with dense Cu_2O shells, the extinction spectra of the hybrid nanoparticles with partial Cu_2O domains loosely surrounding the Au core in Figure 2.4E show that the extinction spectra are affected by both shell thickness and packing density. Decreasing the packing density and thickness of the Cu_2O shells results in a decrease in effective local permittivity of Cu_2O shells, leading to an SPR blue-shift to shorter wavelengths.[8] In addition, the optical properties can be altered by geometrical interfacial structures.[9] For example, Figure 2.4F shows the experimental extinction spectra of yolk-shell Au-Cu_2O nanostructures obtained at different reaction time. The extinction features from 300 to 600 nm could represent the characteristic absorption peak of Cu_2O nanoshells,[126] while the SPR peaks of the Au core in the near-infrared show blue-shifts to shorter wavelengths with increasing gaps between the Cu_2O shell and the Au core. The Au-Cu_2O nanostructures with collapsed Cu_2O shells obtained at 90 min exhibit similar plasmonic features to the bare Au nanoparticles.

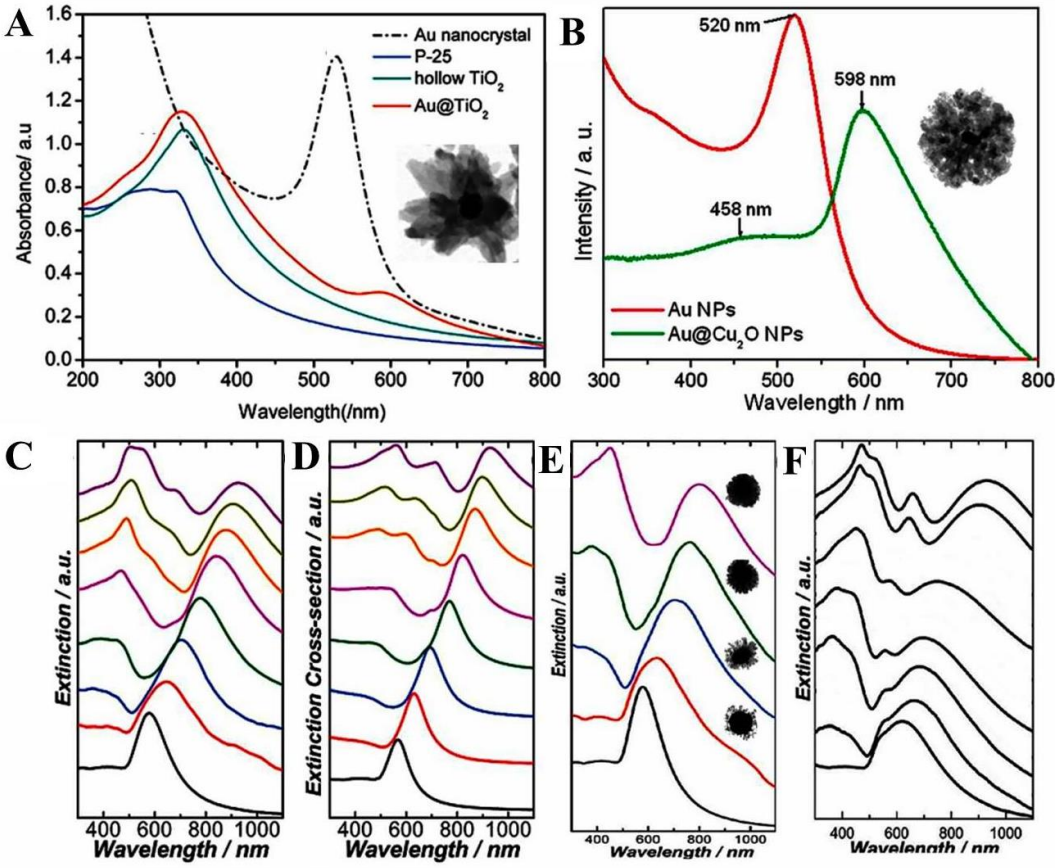

Figure 2.4 UV-vis adsorption spectra: (A) core-shell Au@TiO_2 nanoparticles, Au and TiO_2 nanoparticles, hollow TiO_2 particles,[6] and (B) Au and Au@Cu_2O core-shell nanoparticles;[7] (C) Experimentally measured and (D) Spectra (calculated extinction) for Au nanoparticles with diameter of 49 nm and Au@Cu_2O core-shell NPs with different shell thickness (from bottom to top: 6, 15, 27, 39, 53, 62, and 75 nm);[8] (E) Spectra (experimental extinction) of Au nanoparticles and Au@Cu_2O nanoparticles with decreasing packing density and shell thickness (from top to bottom);[8] (F) Spectra (experimental extinction) of Au nanoparticles (bottom, 63 nm) and yolk-shell Au@Cu_2O nanostructures (from top to bottom) fabricated at 2, 5, 20, 40, 60, and 90 min.[9]

Beside Au serving as cores, Ag nanostructures can also be used as cores for semiconductor coatings, such as from TiO_2, Cu_2O, and Fe_3O_4, and similar phenomena are observed for Au-core@semiconductor-shell hybrid nanostructures.[10-12] Figure 2.5A shows that the SPR mode of Ag NWs is gradually red-shifted and the intensity decreases with a thicker coating of TiO_2 nanoshells. When coating with a TiO_2 shell with thickness of 10 nm, the longitudinal mode almost disappears, and the transverse plasmon resonance of the Ag NWs is red-shifted to 32 nm. It an be found the red-shift in the plasmon becomes more obvious with increasing TiO_2 shell thickness, and the resonance wavelength could be 476 nm when the shell thickness of TiO_2 is 65 nm.[10] The LSPR absorption peaks for various Ag@Cu_2O nanoparticles gradually red-shift from 415 nm for bare Ag nanoparticles to ~675 nm for Ag@Cu_2O nanoparticles with Cu_2O shell thickness of 40 nm (Figure 2.5 B).[11]

Ag@Fe_3O_4 core-shell nanostructures show similar optical properties to Au@Cu_2O core-shell nanostructures. As shown in Figure 2.5C, both of dipole plasmon and quadrupole resonance in the SPR peaks are red-shifted from the ultraviolet to the near-infrared region as both of Ag core size and Fe_3O_4 shell thickness increase. For flower-like Ag@Fe_3O_4 nanostructures with partial Fe_3O_4 shells loosely packed on the Ag core, the quadrupole resonance almost disappears, which appears at 427 nm in the core-shell Ag@Fe_3O_4 nanostructures with dense uniform Fe_3O_4 nanoshells coating the Ag cores, and the dipole plasmon peak is blue-shifted to shorter wavelengths in the flower-like Ag@Fe_3O_4 nanostructures (Figure 2.5D), which could be due to the decrease in both the thickness of Fe_3O_4 shell and the size of Ag core, as well as the partial loosely packed Fe_3O_4 shell around the Ag core.[12]

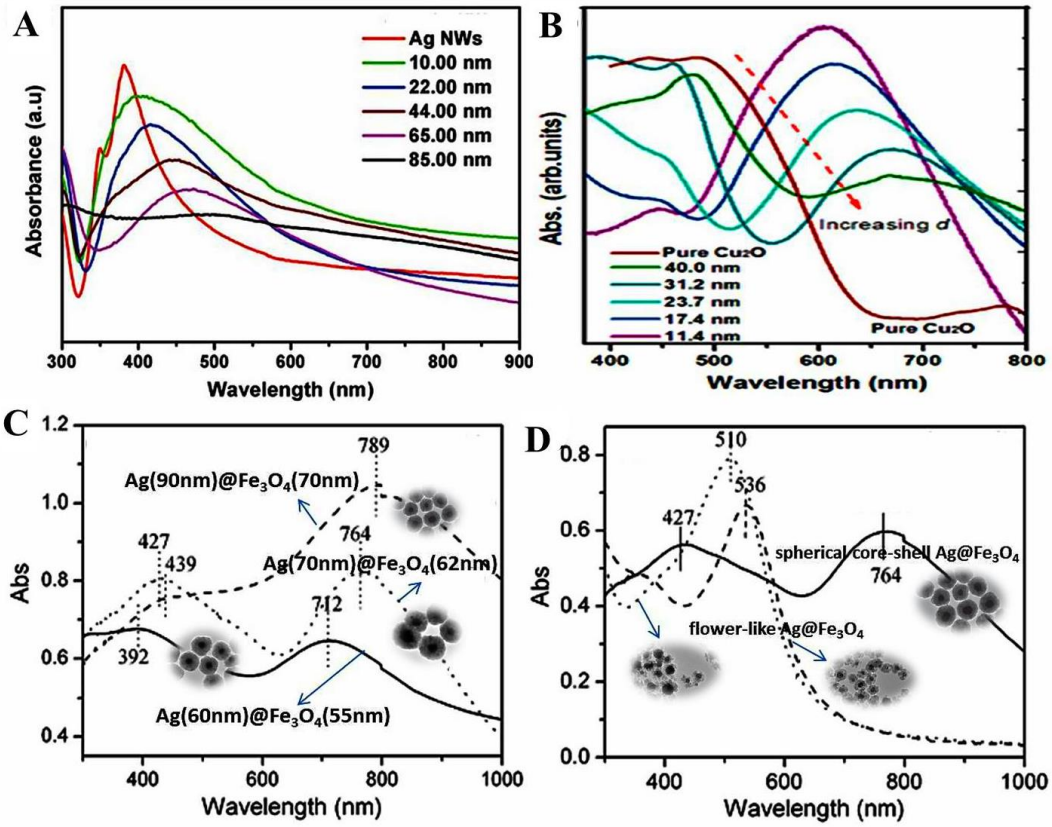

Figure 2.5 UV-vis absorption spectra of different samples: (A) core-shell Ag@TiO_2 nanowires (TiO_2 has different shell thickness);[10] (B) core-shell Ag@Cu_2O nanoparticles with various shell thickness;[11] UV-vis-near-infrared (NIR) spectra of Ag@Fe_3O_4 nanostructures:[12] (C) with different Ag core sizes and Fe_3O_4 shell thicknesses, and (D) with different morphologies and structures.

When depositing a plasmonic metal on the surface of a semiconductor support to form a hybrid nanostructure, the optical properties such as the UV-vis absorption spectrum of the semiconductor can be systematically tuned by varying the loading amount of the metal.[13,14] For example, the absorption spectrum of Ag/ZnO nanorod arrays (NRA) with Ag nanoparticles deposited on ZnO nanorods shows no significant difference in the band gap compared with pure ZnO, and it exhibits a broad and intense absorption property towards visible light (400-700 nm) because of the SPR effect of the Ag NPs (Figure 2.6A).[13] Besides, the absorption intensity of Ag/ZnO NRA having different Ag

contents becomes stronger when the concentration of $AgNO_3$ is increased, and the SPR peaks are red-shifted from ~425 to ~463 nm (Figure 2.6B).[13]

A similar phenomenon can be observed in UV-vis absorption spectra of the $Ag/AgVO_3$ nanoribbons, where $Ag/AgVO_3$ samples with different Ag contents on the surfaces of $AgVO_3$ nanoribbons exhibit broader and stronger absorption of visible light in comparision to pure $AgVO_3$ (Figure 2.6C). Among the $Ag/AgVO_3$ samples, the 0.05-$Ag/AgVO_3$ sample exhibits the highest absorption, and further increased Ag content in 0.10-$Ag/AgVO_3$ could not enhance the absorption, because the extra Ag content is coated on the surfaces of the $AgVO_3$, and thus retards the light absorption.[14]

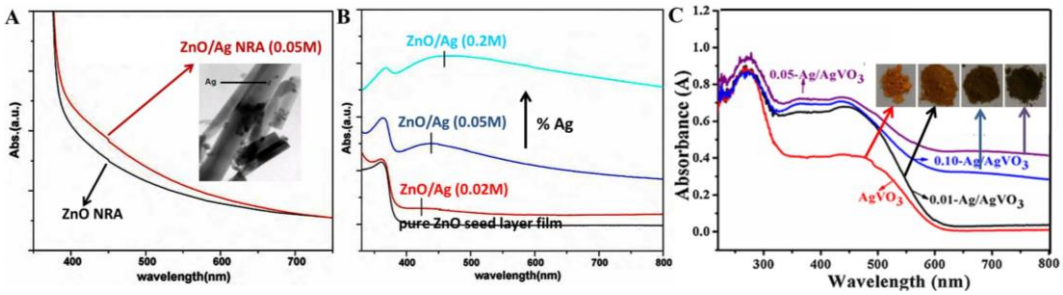

Figure 2.6 (A) UV-vis absorption spectra of different samples: ZnO NRA (black); Ag/ZnO NRA (red, with TEM image in inset) with an $AgNO_3$ concentration of 0.05 M;[13] (B) UV-vis absorption spectra: ZnO seed layer film; Ag/ZnO films with different $AgNO_3$ concentrations;[13] (C) UV-vis absorption spectra and corresponding images in inset: $AgVO_3$ and $Ag/AgVO_3$ nanoribbons.[14]

2.4 Applications of plasmonic metal/semiconductor nanostructures

2.4.1 Plasmon-enhanced photocatalysis

2.4.1.1 The basic principle of semiconductor photocatalysis

The basic function of photocatalysis is to start or speed up redox reaction with the involvement of semiconductor catalysts under certain types of light illumination.[15,91]

The mechanism of the photocatalytic process is shown in Figure 2.7.[15] Firstly, once a semiconductor is irradiated by photons having energy that is greater than or equal to its band-gap energy (E_g), an electron (e_{cb}^-) in the valence band (VB) is excited into the conduction band (CB), leaving a hole (h_{vb}^+) behind in the VB (stage I).[15,91,95] Secondly, the excited electrons (e_{cb}^-) and holes (h_{vb}^+) move to the active sites on the surface of the semiconductor catalyst (stage II).[15,91,95] Thirdly, the generated electrons (e_{cb}^-) in the CB exhibit a strong reduction capacity, and the holes (h_{vb}^+) in the VB exhibit a strong oxidative potential, so that they can serve as the reducing agent (stage III) and oxidizing agent (stage IV) to drive reduction and oxidation on the semiconductor surface.[15,91,95] In addition, they can be captured in a metastable state (stages VI and VII).[15] More specifically, at stages III, IV, and V, for photocatalytic degradation of pollutants or water splitting, photoinduced electrons (e_{cb}^-) can reduce adsorbed oxygen (O_2) to produce superoxide ($HO_2\cdot$) radicals or reduce water to generate H_2, and holes (h_{vb}^+) can directly oxidize the organic pollutants or react with surface adsorbed H_2O to form hydroxyl radicals ($OH\cdot$), which can subsequently oxidize almost all organic pollutants, resulting in mineralization and complete degradation, or oxidize H_2O to generate O_2.[95] It should be noted that, at stage II, the photoexcited electrons and holes can rapidly recombine, which is a competitive process with the transportation process (stage II).[15,95]

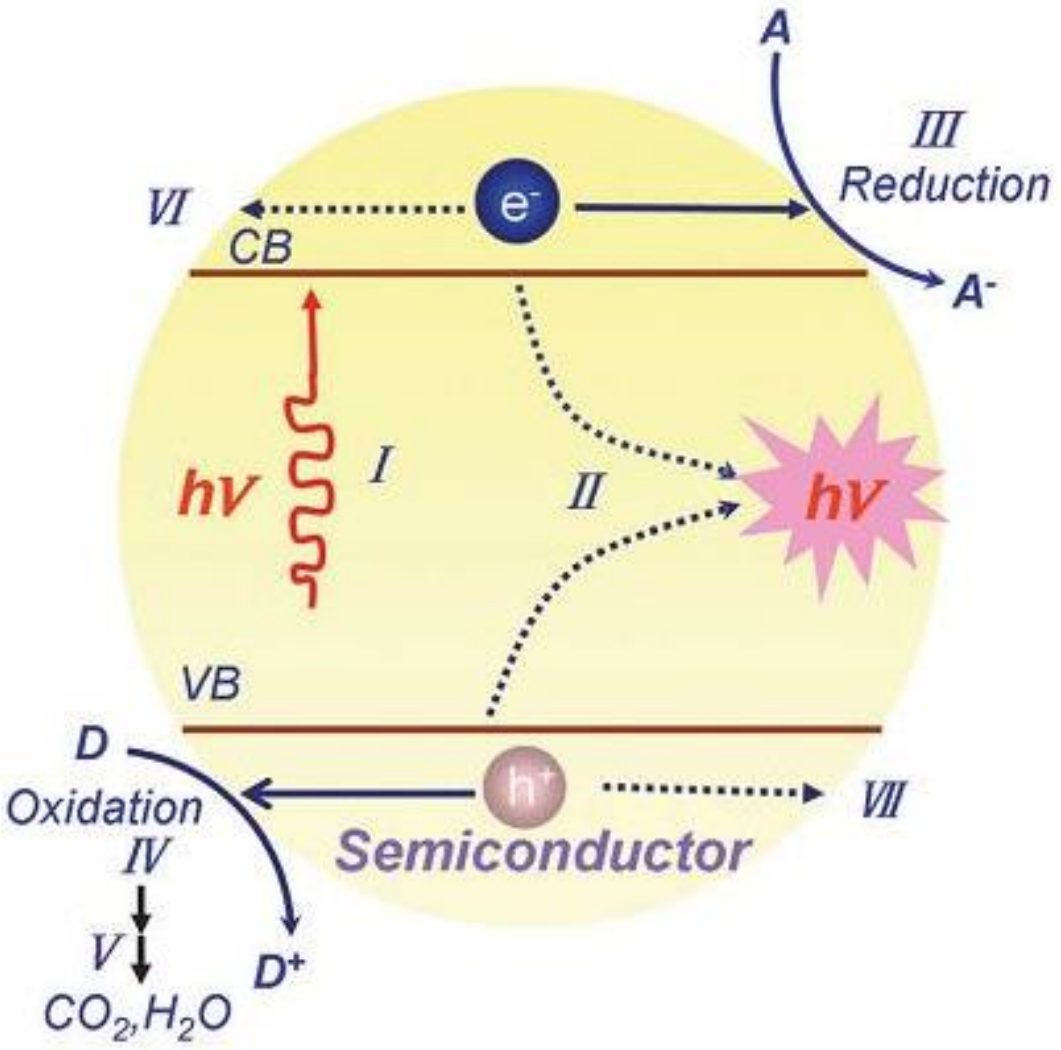

Figure 2.7 Schematic illustration of the basic process of semiconductor photocatalysis.[15]

According to the above-mentioned fundamental principles of semiconductor photocatalysis, it can be concluded that the electron-hole recombination could decrease photocatalytic efficiency of semiconductor catalyst. In order to reach higher photocatalytic activity, the photoinduced electron-hole pairs should be efficiently separated and quickly transferred to the surface/interface to suppress the recombination. Hence, different kinds of approaches, including tuning the morphology and structure, doping with non-metal or metal elements,[127] and constructing heterostructures by combining the semiconductor with plasmonic metals and/or other semiconductors, have

been explored to enhance the photocatalytic activity of a single semiconductor catalyst. Among these approaches, the formation of a semiconductor/plasmonic metal heterostructured hybrid is one of the most promising ways to improve the separation and transportation efficiency of photoinduced electron-hole pairs.[2]

2.4.1.2 Plasmonic metal/semiconductor photocatalysis

The SPR effects of noble metal nanostructures can enhance the local electromagnetic field and light absorption. In a general, noble metal nanostructures have wide applications when involving a certain type of light, such as in photocatalysis and surface-enhanced Raman spectroscopy (SERS), because the SPR can be adjusted from visible to near-infrared, or within the entire solar spectrum and beyond.[3,98,111] When used for photocatalysis, noble metal nanostructures play important roles in improving the photocatalytic performance of plasmonic metal/semiconductor hybrid photocatalysts because of SPR effects and charge separation effects (forming Schottky junctions by Fermi level equilibration at the metal-semiconductor interfaces).[16,91,96] However, the SPR and charge-separation effects take place in different excitation situations.[2] When the SPR of metal component is excited, the SPR effect occurs, while the charge separation effect occurs only when the semiconductor ingredient is excited.[2]

First, the SPR of a noble metal can not only enhance the light scattering at the heterostructure interface, but also enhance the light absorption from UV to the near-infrared region.[6,13,14,34,96] Moreover, the SPR of a noble metal can transfer energy to a nearby semiconductor, leading to a rapid electron transfer to the nearby semiconductor from the excited noble metal.[98] Figure 2.8A displays a schematic illustration of photoinduced charge transfer on a plasmonic metal/semiconductor hybrid under irradiation by visible light thanks to the occurrence of SPR effects. [16 3,96]

Second, if the Fermi level (E_F) of a semiconductor and a metal is comparable, when the metal and the semiconductor interact with each other, a Schottky junction will be

formed at the interface.[96] Because of the formation of Schottky barrier, a built-in electric field close to the interface is formed, resulting from the equilibrium alignment of the Fermi level for the metal and semiconductor, and it can prohibit the recombination of photogenerated electron-hole pairs. As a matter of fact, the Fermi level of metal typically is located between the VB maximum and the CB minimum of a common semiconductor photocatalyst (Figure 2.8B), which also contributes to the formation of Schottky barrier.[2,16,96,98,128-130]

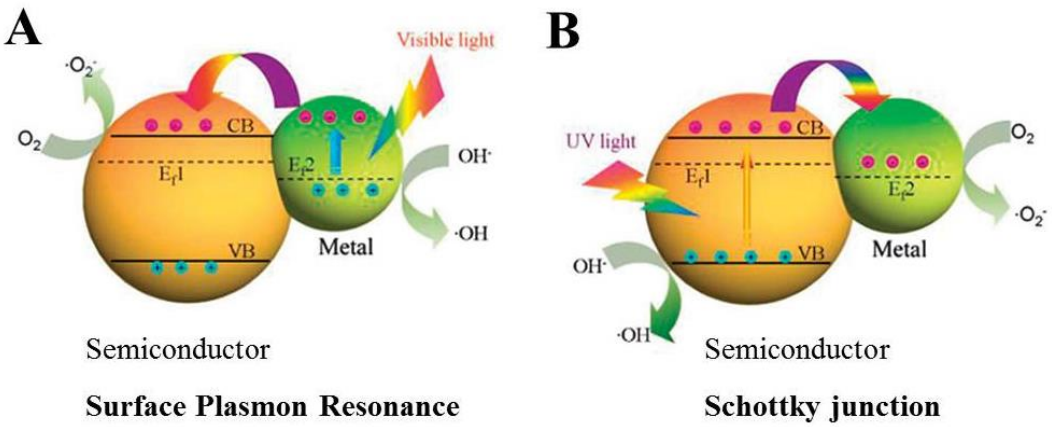

Figure 2.8 Schematic illustration of photoinduced charge transfer to plasmonic metal/semiconductor heterostructured photocatalyst: (A) SPR effects (visible light irradiation); (B) Schottky junction (UV light irradiation).[16]

2.4.1.3 Mechanisms for SPR-enhanced photocatalysis

There are two major possible mechanisms for SPR-enhanced photocatalysis.[131]

(1) SPR-mediated charge transfer (plasmonic sensitization)

The charge injection mechanism has been found to induce a fast charge carrier transfer in plasmonic metal/semiconductor photocatalysts, where charge carriers are directly injected into the nearby semiconductor surface from excited plasmonic metal nanostructures.[3,132-145] The mechanism is similar to the one for dye sensitization, where

dye molecules adsorbed on a semiconductor can absorb light with certain wavelength and transfer charges to the semiconductor.[2,105,146,147] In a plasmonic metal/semiconductor photocatalytic system, the plasmonic metal seems to act as a dye sensitizer, which can absorb resonant photons as well as transferring the energetic electrons to the nearby semiconductor from the metal through resonant excitation of the SPR (Figure 2.9 A).[2,3]

(2) Near-field electromagnetic and scattering mechanisms

As mentioned in the beginning of this chapter, irradiated metal NPs near their plasmon resonance frequency can produce significantly intense and spatially non-homogeneous local electromagnetic fields in the near-field region near the NP surfaces.[2] The near-field electromagnetic mechanism is based on the interaction between the semiconductor and the strong SPR-induced electric field, which is localized close to the metal nanostructure.[3] The overlapping of the light absorption of semiconductors with the SPR of metal nanostructures can be enhanced due to the strongly enhanced electromagnetic field.

When the hybrid metal/semiconductor nanostructure with overlapping SPR and interband-transition energies is irradiated with incident light at a suitable wavelength, the semiconductor and plasmonic metal components will be simultaneously excited to generate electrons and holes in the semiconductor. Therefore, the semiconductor component localized near the photoexcited plasmonic metal in the hybrid is subjected to a strong electric field, with intensity several orders of magnitude higher than that of the far-field incident light (Figure 2.9B).[2] Since the production rate of electron-hole pairs in a semiconductor is proportional to the local excitation light intensity, it is therefore greatly increased, with highest rate at the semiconductor-liquid interface[3] or near the surface (Figure 2.9B).[2] The charge carriers selectively produced at the semiconductor/liquid interface are easily separated from each other, and they have a

shorter migration distance to take part in the photoreaction, so that they can thereafter enhance the photocatalytic performance. Several works have attributed photocatalytic improvement to this enhancement of plasmonic local electric field.[148-156] In the meanwhile, it is believed that metal nanoparticles in the metal/semiconductor hybrid can act as electron sinks, where photoexicited electrons in the semiconductor are transferred to metal NPs from CB, which prevent fast recombination of photoinduced electron-hole pairs, thereby improving its photocatalytic property.[24,34,144,157-159]

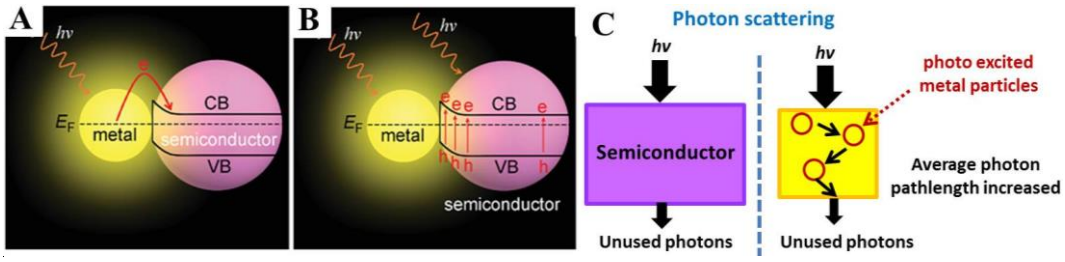

Figure 2.9 Scheme of plasmon-enhanced photocatalysis mechanisms in metal/semiconductor heteronanostructures: (A) SPR-mediated charge transfer;[2] (B) Plasmonic local electric field enhancement;[2] (C) Plasmonic scattering mechanism.[3]

When the diameter of one plasmonic nanostructure is larger than ~50 nm, besides the local electric fields, the SPR is accompanied by an efficient scattering of resonant photons.[3,114,160] Furthermore, such a scattering of photons arising from the plasmonic metal prolongs their average path length in the metal/semiconductor hybrid, and therefore increases the generation rate of electrons and holes in the semiconductor (Figure 2.9C).[3] To some extent, the plasmonic nanostructure in this condition substantially acts as a nanomirror. In other words, some resonant photons could be scattered and effectively given many passes through the hybrid material if they are not absorbed by the semiconductor on the first pass.[3]

2.4.1.4 Plasmonic metal/oxide semiconductor photocatalysts

Up to now, among the reported plamonic metal/semiconductor photocatalysts, the most investigated semiconductors have been metal oxides, such as TiO_2,[5,6,17,33,118,132,144,149,157,158,161] ZnO,[13,18,19,116,162] Cu_2O,[11,22-24,34,133,163-165] CeO_2,[143,166-170] and WO_3.[122] Up to now, different kinds of metal/oxide plasmonic hybrid photocatalysts, such as M/TiO_2 (M = Pt, Pd, Au, Ag), Pt/ZnO, Ag/ZnO, Au/ZnO, Au/Cu_2O, Ag/Cu_2O, Cu/Cu_2O, M/CeO_2 (M = Pt, Au, Ag, Pd), Ag/WO_3, Au/ZrO_2, and Au/WO_3 have been constructed and fabricated by various methods. The synthesis methods and photocatalysis reactions of the above mentioned plasmonic metal/oxide semiconductor photocatalysts are summarized in Table 2.1.

Table 2.1 Plasmonic metal/oxide semiconductor photocatalysts with their synthesis methods and photocatalytic reactions.

Photocatalyst	Preparation method	Photocatalytic reaction	Light source	Reference
core-shell Au@TiO_2 hollow spheres	hydrothermal combined with calcination	hydrogen generation	300 W Xe lamp with UV light	157
Au NPs/TiO_2 film	electron beam evaporation	photoreduction of CO_2	365 nm UV light	121
cuplike TiO_2 decorated with Au	wet-chemical deposition	MB degradation	visible light (780 nm $\geq \lambda \geq$ 400 nm)	90
Au deposited mesoporous S,N-TiO_2	wet-chemical deposition combined with calcination	hydrogen generation	visible light	144
Au/TiO_2 NPs	photoreduction	water splitting	254 nm UV lamp	158

Au/TiO_2 NPs	assembly, reflux and chemical deposition	activation of horseradish peroxidase enzyme	366 nm UV lamp or 470 nm LED	118
Au NPs loaded on anatase TiO_2 NPs	deposition-precipitation	degradation of nonylphenol	visible light	171
Au-loaded TiO_2 NPs	deposition-precipitation or photodeposition	H_2O reduction	visible light	172
Au NPs loaded on rutile TiO_2	deposition-precipitation	aerobic oxidation of amines	300 W Xe lamp with a cut-off filter	132
$Au@TiO_2$ yolk-shell hollow spheres	wet-chemical deposition combined with calcination	reduction of CO_2	UV-vis light	148
Janus and core-shell Au-TiO_2	chemical deposition	hydrogen production	visible light ($\lambda > 400$ nm)	5
core-shell $M@TiO_2$ nanospheres (M=Au, Pd, Pt)	hydrothermal	RhB degradation	300 W xenon lamp ($\lambda > 400$ nm)	17
wedge-like core-shell $Au@TiO_2$ NPs	hydrothermal	degradation of gaseous acetaldehyde	UV or visible light	6
$M@TiO_2$ microspheres (M=Au, Pt, Ag)	wet-chemical deposition	oxidation of benzene	visible light ($\lambda > 400$ nm) from 300 W Xe	173

TiO_2 NWs/Ag NPs	photoreduction	MB degradation	arc lamp visible light from 500 W xenon lamp	33
Au NP/ZnO NR	assembly by dithiol linking	RhB degradation	365 nm UV LED array lamp	116
Au NPs-loaded ZnO nanorods	wet-chemical deposition	RhB degradation	300 W high-pressure mercury lamp with λ = 365 nm	162
Pt-ZnO hollow microspheres	solvothermal	orange II degradation	7 W 365 nm UV lamp	19
petal-like Au-ZnO	hydrothermal	RhB, MB, CRM and RB degradation	sunlight	20
Au@ZnO core-shell NPs	wet-chemical deposition	MO degradation	visible light	21
Ag/ZnO nanorod arrays	photoreduction	MB degradation	ultraviolet light	13
M/Cu_2O (M=Ag,Au) nanocrystals	photoreduction	Pyronine B degradation	300 W low pressure mercury lamp	24
Cu_2O NW-Au NP assemblies	assembly	MB degradation	300 W xenon lamp equipped with UV filter	34
Ag@Cu_2O core-shell NPs	wet-chemical deposition	MO degradation	8 W visible light lamps (400 < λ <	11

			700 nm)	
Ag NPs deposited on Cu_2O nanospheres	wet-chemical deposition	MO degradation	visible-light from 500 W xenon lamp	25
core-shell Au-Cu_2O cubes and octahedra	wet-chemical deposition	MO degradation	500 W Xe lamp	23
$Cu@Cu_2O$ core-shell microspheres	interfacial hydrothermal	removal of NO	visible light ($\lambda > 420$ nm) from 300 W tungsten halogen lamp	22
$Au@Cu_2O$ core-shell NPs	wet-chemical deposition	MO degradation	8 W visible light lamps ($400 < \lambda < 700$ nm)	133
Au nanograins on Cu_2O octahedra	wet-chemical deposition	MO degradation	visible light ($\lambda > 400$ nm) from 500 W xenon lamp	165
$Au@Cu_2O$ octahedra	wet-chemical deposition	MO decolorization	$\lambda > 400$ nm from 500W xenon lamp	174
hollow Au-Cu_2O core-shell NPs	wet-chemical deposition	MO degradation	($\lambda > 400$ nm) 300 W Xe lamp	26
Au/CeO_2 NPs	photodeposition	oxidation of benzyl alcohol	visible light from a green	175

			LED	
core-shell and yolk-shell $Pt@CeO_2$ nanospheres	hydrothermal	oxidation of benzyl alcohol	visible light	169
Au supported on CeO_2 NPs	deposition-precipitation combined with calcination	oxygen generation	visible light (λ>400 nm)	143
$Au@CeO_2$ core-shell nanospheres and nanorods	wet-chemical deposition	oxidation of benzyl alcohol	λ>420 nm Xe lamp	176.
$Ag@CeO_2$ core-shell NWs and NPs	wet-chemical deposition	O_2 evolution MB degradation	λ > 400 nm 300 W Xe lamp	39
Au NP loaded CeO_2 nanorods	photodeposition	aerobic oxidation of propylene	λ > 420 nm Xe lamp (500 mW cm^{-2})	166
silk mat-like Pd/CeO_2 NPs	assembly combined with calcination	aerobic alcohols oxidation and anaerobic reduction of nitro-compounds	λ > 420 nm 300 W Xe lamp	167
core-shell Pd@ hollow CeO_2	hydrothermal combined with calcination	substituted aromatic nitro compounds reduction	visible light (λ > 420 nm)	168
Au-porous	photoreduction	decomposition	Xe lamp	170

CeO_2 spherical NPs		of gaseous IPA	(λ>420 nm)	
Au-buffered WO_3 thin films	radio-frequency magnetron sputtering	MB decomposition	20W fluorescent lamps	[122]
Ag loaded mesoporous WO_3	ultrasound assisted insertion method	acetaldehyde degradation	visible light (λ > 420 nm)	[120]
Au/ZrO_2 NPs	wet-chemical deposition	reduction of nitrobenzene	λ > 400 nm	[153]

Hybrid Au-TiO_2 nanostructures with two different morphologies, Janus and core-shell structures, have been fabricated through a chemical deposition process based on controlling the hydrolysis of TiO_2 precursor, titanium diisopropoxide bis(acetylacetonate), in an isopropanol and ammonia solution containing 50 nm Au nanoparticles at room temperature.[5] Specifically, Janus Au-TiO_2 nanostructures can be obtained by the addition of titanium diisopropoxide bis(acetylacetonate) in one portion (Figure 2.10A), and core-shell Au-TiO_2 nanostructures can be prepared by the addition of the same volume of titanium diisopropoxide bis(acetylacetonate) in three portions (Figure 2.10B).

The photocatalytic performances of core-shell and Janus Au-TiO_2 nanostructures were investigated by hydrogen generation from a 1:2 v/v isopropyl alcohol/aqueous solution under irradiation by visible light with λ > 400 nm (Figure 2.10C-E). As displayed in Figure 2.10D, both of core-shell and Janus Au_{50nm}-TiO_2 photocatalysts exhibited improved photocatalytic activities towards H_2 evolution compared to the pure Au nanoparticles (50 nm, diameter) and the amorphous TiO_2 NPs, with Janus Au_{50nm}-TiO_2 showing the highest activity. The initial rate of H_2 production over Janus structure was 1.5 mL min^{-1}, and the volume of H_2 was 138 mL after 3 h, which is about 1.7 times higher than for the core-shell structure (0.9 mL min^{-1}, 80 mL H_2 after 3 h), while both

the pure Au NPs and the amorphous TiO_2 NPs exhibit very poor photocatalytic activities, with less than 5 mL H_2 generation for that irradiation time.

The enhancement for the Janus structure result from enhanced light absorption aroused by the stronger localization of the plasmonic electric field near the Janus interface, thus generating electron-hole pairs near TiO_2 surface. Hence, the photoexcited electrons migrate along a very short pathway to the surface of TiO_2 for photocatalytic H_2 evolution, achieving the suppression of charge-carrier recombination (Figure 2.10C). Moreover, the larger sizes of the Au nanoparticles in the Janus Au-TiO_2 hybrid nanostructures lead to higher photocatalytic activity in H_2 production due to their stronger plasmon-enhanced electric field, as shown in Figure 2.10E.

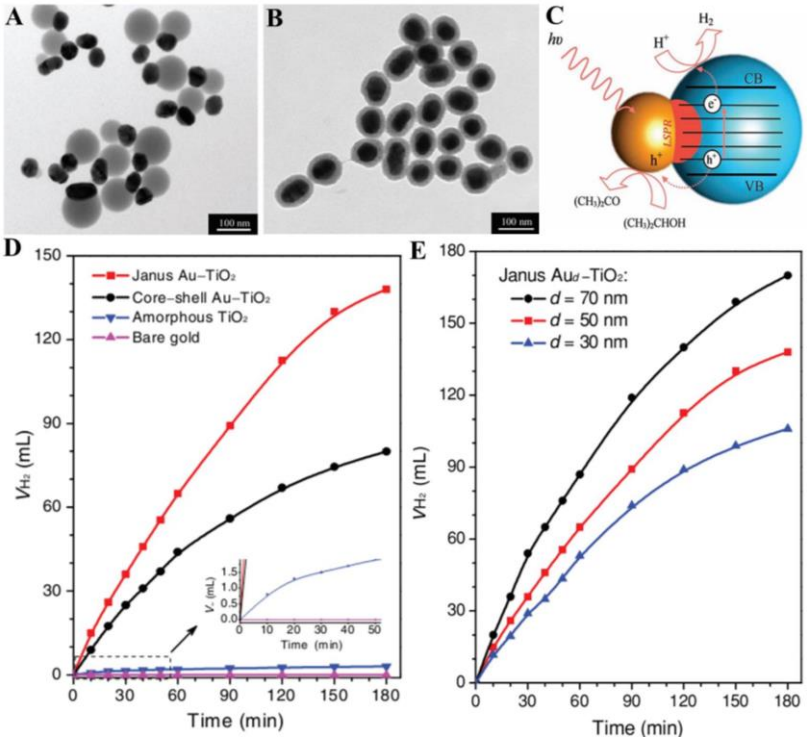

Figure 2.10 TEM images of (A) Janus and (B) core-shell Au_{50nm}-TiO_2 nanostructures; (C) Possible visible-light-induced photocatalysis process for enhanced photocatalytic hydrogen evolution from Au-TiO_2 Janus nanostructures; (D) Generated hydrogen volume (under visible-light irradiation) over Au_{50nm}-TiO_2 (core-shell), TiO_2

(amorphous), and 50 nm Au nanoparticles; (E) Generated hydrogen volume (under visible-light irradiation) over Janus Au-TiO_2 comprising of different sized Au nanoparticles.[5]

A series of M@TiO_2 (M = Pt, Pd, Au) core-shell nanospheres have been synthesized by a general hydrothermal treatment of TiF_4 and colloidal noble metal nanoparticles, where the metal nanoparticles are first grown via the reduction of a metal salt such as $HAuCl_4$, H_2PdCl_4, or H_2PtCl_6 with sodium citrate, and coating of TiO_2 on the pre-grown metal nanoparticles is then achieved through TiF_4 hydrolysis under hydrothermal treatment.[17] Figure 2.11A-C shows typical SEM and inset TEM images of Au@TiO_2, Pd@TiO_2, and Pt@TiO_2, which comprise metal cores and TiO_2 rugged shells to form a flowerlike structure.[17] The photocatalytic degradation of Rhodamine B (RhB) over these core-shell Au@TiO_2 nanospheres has been evaluated, and it was found that Au@TiO_2 core-shell hybrid nanospheres exhibited greater photocatalytic activity than the commercial P25 nanoparticles under irradiation by visible light with $\lambda > 400$ nm.[17]

As observed in Figure 2.11D, RhB is degraded under illumination for 2 h over the core-shell Pd@TiO_2 nanospheres, while the commercial TiO_2 nanoparticles exhibited poor catalytic activity, with only ~70% of the RhB degraded over the same illumination time. As for Pt@TiO_2 and Au@TiO_2 core-shell nanospheres, the degradation rate of RhB is similar to that over P25 at the initial stage, and then they show higher photocatalytic activity than P25 after irradiation for 20 min. Figure 2.11E displays photocatalytic activity curves for RhB degradation and the calculated reaction rate constant *k*. It is observed that all M@TiO_2 (M = Pt, Pd, Au) core-shell nanoparticles display better photocatalytic performance than commercial P25 nanoparticles, and the Pd@TiO_2 hybrid nanostructures have the largest kinetic rate constant (2.29 h^{-1}) among all the photocatalysts, while the kinetic rate constants are 0.96 h^{-1}, 0.83 h^{-1}, and 0.72 h^{-1} for Pt@TiO_2, Au@TiO_2, and P25, respectively. Due to the fact that metal cores can improve the visible light absorption intensity of TiO_2 and trap electrons, rapid recombination of

electrons and holes is strongly prohibited, hence resulting in enhancement of their visible light photocatalytic performance.[17]

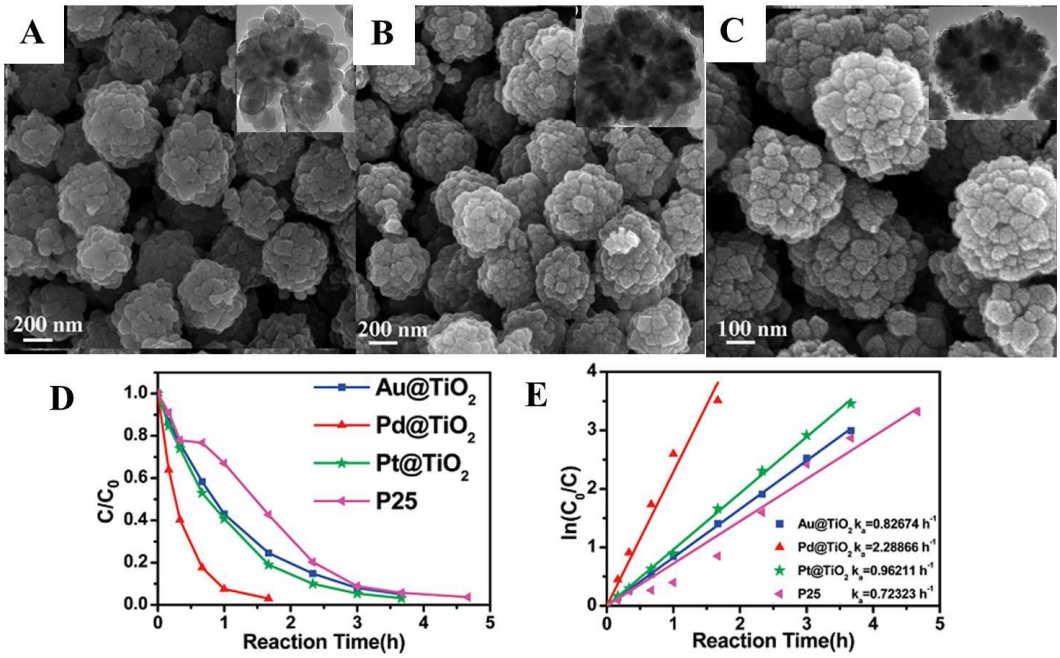

Figure 2.11 SEM and TEM images: (A) Au@TiO_2, (B) Pd@TiO_2, (C) Pt@TiO_2; (D and E) Photocatalytic properties (under irradiation by visible light with $\lambda > 400$ nm) of core-shell M@TiO_2 nanospheres and P25 towards RhB photodegradation.[17]

Ag nanoparticles (NPs) located on the surfaces of ZnO nanorod hybrids with different Ag contents have been prepared in one step via an ethanol-involved solvothermal approach without any surfactants, where intermolecular dehydrolysis and the reduction of Ag^+ species are utilized. Figure 2.12A displays a TEM image of the obtained sample with 5.0 at.% Ag, which consisted of ZnO nanorods and Ag NPs (highlighted by white circles). The high-resolution TEM (HRTEM) image (Figure 2.12B) reveals a distinct interface between the Ag NP and the ZnO nanorod, indicating the successful formation of chemical bonds in this heterodimer.[18] Figure 2.12C shows methyl orange (MO) photodegradation over different photocatalysts under irradiation by UV light. It is observed that degradation of MO over bare Ag NPs can be ignored, while the Ag/ZnO hybrid exhibits better photocatalytic activity than bare ZnO and P-25. Furthermore, the

Ag/ZnO heterostructures with 5.0 at.% Ag display the highest photodegradation efficiency. This indicates that the involvement of the Ag nanoparticles and oxygen vacancies within the ZnO nanorods prevent the recombination of photoinduced electron-hole pairs and thereby improve their photodegradation performance.[18]

Yu et al. also have fabricated hierarchical hollow Pt-ZnO nanocomposite microspheres by the solvothermal method, and all the nanocomposite microspheres with different Pt contents exhibit enhanced photocatalytic activity toward acid orange II decomposition in comparision to pure ZnO (Figure 2.12D).[19] Among the Pt-ZnO nanocomposites, Pt(2%)-ZnO shows the highest degradation rate with 86% degradation after irradiation for 5 h, while it is 52 % for Pt(0.5%)-ZnO, 59 % for Pt(1%)-ZnO, 55% for Pt(4%)-ZnO, and only 41% for pure ZnO under the same conditions.[19] The enhanced photodegradation activity of Pt-ZnO microspheres was ascribed to their special structure and efficient charge separation by Pt NPs within ZnO nanostructures.[19]

In addition, petal-like Au-ZnO nanocomposites also show improved photocatalytic performance towards RhB phoyodegradation under sunlight illumination (Figure 2.12E).[20] As displayed in the insets of Figure 2.12F, core-shell Au@ZnO nanostructures have been synthesized through a chemical deposition process, where Au and $Zn(CH_3COO)_2$ solutions are mixed together with vigorous stirring, followed by the addition of sodium hydroxide solution at 90°C under continuous stirring.[21] Figure 2.12F shows the kinetics of MO photodegradation on ZnO and core-shell Au@ZnO nanostructures having different shell thicknesses: 60%-75% of the MO can be degraded over core-shell Au@ZnO photocatalyst after visible light illumination for 200 min, while only 9% of the MO is degraded over pure ZnO after the same period. Such enhanced photocatalytic activity over core-shell Au@ZnO NPs results from SPR in the Au core, which can generate electrons under visible illumination. The photoinduced electrons are transferred to the conduction band of ZnO, and then they are captured by

adsorbed O_2 on its surface to produce $\cdot O^{2-}$ that can decompose organic pollutants (Figure 2.12G).[21]

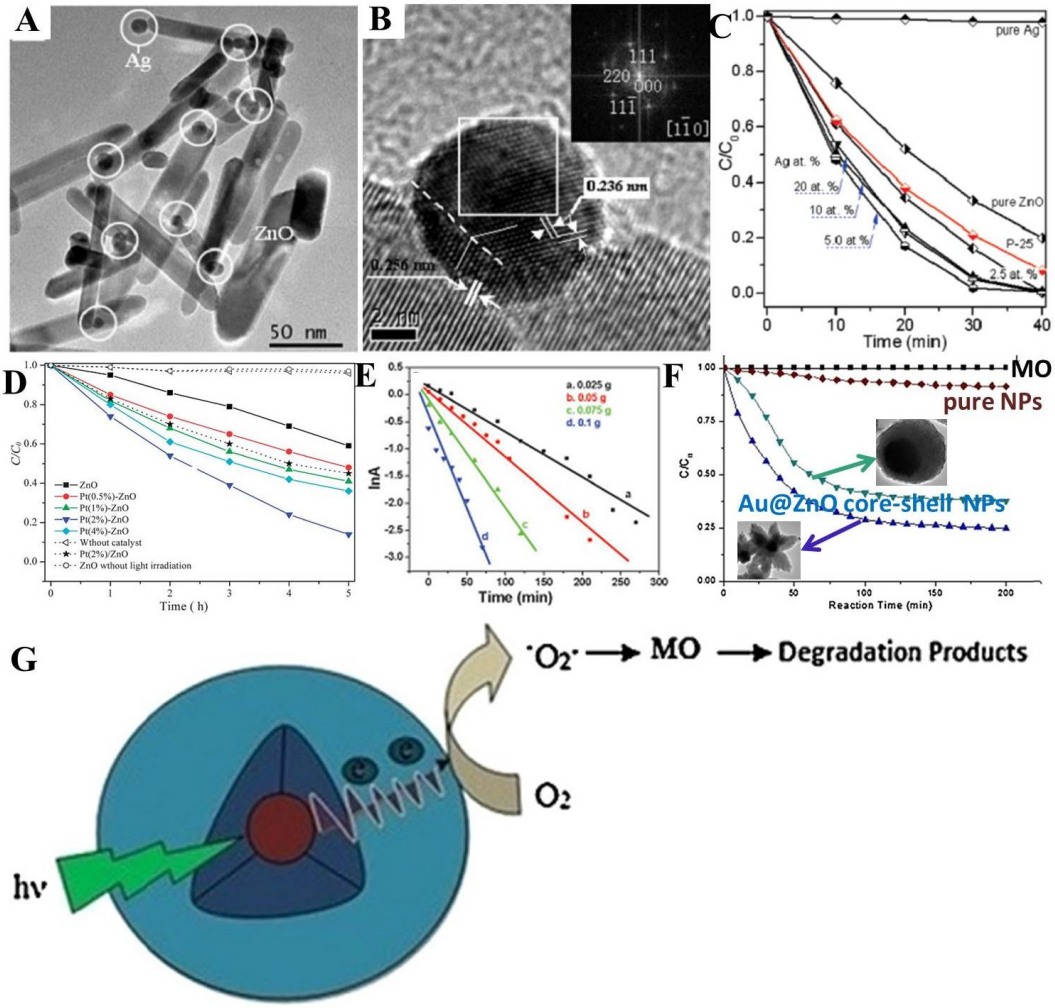

Figure 2.12 (A) TEM and (B) HRTEM image (SAED pattern in the inset) of Ag/ZnO heterostructured nanocrystals with 5.0 at.% Ag;[18] (C) MO photodegradation on Ag/ZnO heterostructures;[18] (D) Acid orange II decomposition on ZnO and hollow Pt-ZnO microsphere photocatalysts under irradiation by UV light;[19] (E) Plot of RhB photodegradation over Au-ZnO nanocomposites;[20] (F) MO photodegration kinetics of ZnO and core-shell Au@ZnO nanostructures (TEM images in the insets) with different shell thicknesses under visible light irradiation;[21] (G) Scheme of possible photocatalysis mechanism of core-shell Au@ZnO nanostructures under irradiation by visible light.[21]

In addition to the above-described extensively investigated oxide semiconductors such as TiO_2 and ZnO, other oxides such as Cu_2O and CeO_2 also have been widely employed to construct plasmonic metal/oxide semiconductor photocatalysts. For example, Ai et al. have synthesized core-shell Cu@Cu_2O microspheres by an interfacial hydrothermal method, and the content of Cu_2O shell in the hybrid microspheres can be tailored through changing the reaction time.[22] Figure 2.13A-C shows TEM images of core-shell Cu@Cu_2O microspheres obtained at 12, 24, and 48 h, respectively, and the Cu_2O shell content in the hybrid increased with increasing reaction time. Their visible-light-induced photocatalytic activities towards degradation of gaseous NO were investigated. As shown in Figure 2.13D, the Cu@Cu_2O photocatalysts obtained at 12 and 24 h show almost no photocatalytic property, which might have resulted from the low content of photoactive Cu_2O and the extremely high content of inactive Cu in the Cu@Cu_2O hybrid. The Cu@Cu_2O microspheres obtained after 48 h, however, exhibit better photocatalytic performance than the bare Cu_2O nanospheres, which can oxidize 24.7% of NO after irradiation for 10 min, whereas 19.6% of NO can be photocatalytically oxidized on Cu_2O nanospheres under the same conditions. Such an enhancement could result from the Cu NPs core in the Cu@Cu_2O microspheres, which can act as good electron acceptors thanks to Schottky barriers at the interfaces between Cu and Cu_2O, and further facilitate more efficient transportation of photogenerated electrons from the Cu_2O shells, while preventing charge recombination on the Cu_2O shells.[22]

Besides the degradation of gaseous NO over plasmonic metal/Cu_2O photocatalysts, they also show excellent photocatalytic activities towards degradation of organic dyes. For example, Kuo and co-workers have prepared core-shell Au-Cu_2O heterostructures via a facile chemical bath deposition method, where octahedral Au nanocrystals synthesized in advance through the hydrothermal approach are simply mixed with $CuCl_2$ solution, sodium dodecyl sulfate (SDS), NaOH solution, and $NH_2OH \cdot HCl$, and aged for 2 h. The

different shapes, including nanocubes and octahedra, are achieved by adding different amounts of $NH_2OH \cdot HCl$ reductant (Figure 2.13E and F).[23] As shown in Figure 2.13G, Au-Cu_2O core-shell nanocubes and octahedra both exhibit better photocatalytic properties than pure Cu_2O nanocubes and octahedra, and 44.4% and 49.0% μmol/cm^2 of MO can be decomposed over the core-shell cubes and octahedra, while only 18.8% and 37.6% mmol/cm^2 of MO are decomposed for pure Cu_2O cubes and octahedra, respectively. The results also indicate that low photoinduced charge recombination significantly enhances the photocatalytic activity of Au-Cu_2O core-shell nanocubes and octahedra.[23]

M/Cu_2O (M = Ag, Au) heterogeneous nanocrystals, with noble metal NPs on the surfaces of Cu_2O octahedral nanocrystals (Figure 2.13H and 2.13I), have been fabricated via a simple photoreduction process, and they exhibit enhanced photocatalytic degradation of Pyronine B compared with pure Cu_2O irradiated under UV light.[24] As can be seen in Figure 2.13J, 36%, 74%, and 75% of Pyronine B can be degraded after 150 min of UV irradiation over Cu_2O, Ag/Cu_2O, and Au/Cu_2O, respectively.[24] Cu_2O/Ag composite nanospheres with Ag NPs deposited on the surfaces of Cu_2O nanospheres have been prepared by a simple chemical reduction process, where $AgNO_3$ solution is added dropwise into the Cu_2O-containing mother solution under stirring for 30 min (Figure 2.13K).[25] The contents of Ag NPs in the hybrid can be controlled by the different concentrations of $AgNO_3$ solution. All the Cu_2O/Ag composite nanospheres with different Ag contents show enhanced activity towards MO photodegradation under visible light illumination in comparision to pure Cu_2O. As shown in Figure 2.13L, 86.56%, 96.11%, and 76.10% of MO was degraded over Cu_2O/Ag with 0.025 mmol Ag, 0.05 mmol Ag, and 0.1 mmol Ag after visible-light irradiation for 110 min, respectively, while 72.13% of MO could be decomposed over pure Cu_2O. The enhanced photocatalytic performance of the Cu_2O/Ag composite nanospheres could result from the SPR effect and electron sink effect of the Ag NPs. The decreased photodegradation property of Cu_2O/Ag with 0.1 mmol Ag compared to

Cu_2O/Ag with 0.05 mmol Ag might be due to the excessive aggregation of Ag NPs, which can decrease the number of active sites capturing the photoexcited electrons and block the visible-light absorption by Cu_2O, degrading the efficiency of the photon utilization.[25] The photocatalytic activity of metal core/Cu_2O shell hybrid nanostructures can be varied by modulation of the shell thickness and core geometry.[11,26]

Li et al. have prepared Ag@Cu_2O core-shell NPs with various shell thicknesses (Figure 2.13M) through the same chemical deposition process as reported by Kuo et al.,[23] which exhibited enhanced photocatalytic activity compared to pristine Cu_2O NPs, because of the presence of the LSPR in the Ag core. As displayed in Figure 2.13N, the photocatalytic performance of the Ag@Cu_2O NPs was strongly influenced by the shell thickness, because increasing the Cu_2O shell thickness lead to red-shifts of the LSPR. Specifically, the photodegradation performance of the Ag@Cu_2O NPs was boosted on increasing shell thickness from 11.4 to 31.2 nm, and the photocatalytic activity was diminished with further increasing shell thickness to 40 nm.[11] The transient absorption measurements and photocatalysis action spectra showed that the coexistence of both plasmon-induced resonant energy transfer and direct electron transfer mechanisms was responsible for the plasmonic energy transfer to Cu_2O from Ag, resulting in electron-hole pair separation in the Cu_2O.[11] Furthermore, hollow Au-Cu_2O core-shell NPs (Figure 2.13O and 2.13P)[26] synthesized via the wet chemical deposition method also exhibited better capability towards visible-light-driven MO degradation in comparision to solid core-shell Au-Cu_2O NPs, hollow Au NPs, and pure Cu_2O, because of the low recombination of photoinduced electron-hole pairs, which could mainly be attributed to the Schottky barriers and the dominant plasmon-induced resonant energy transfer mechanism, as well as the stronger plasmon resonance and near-field enhancement.[26]

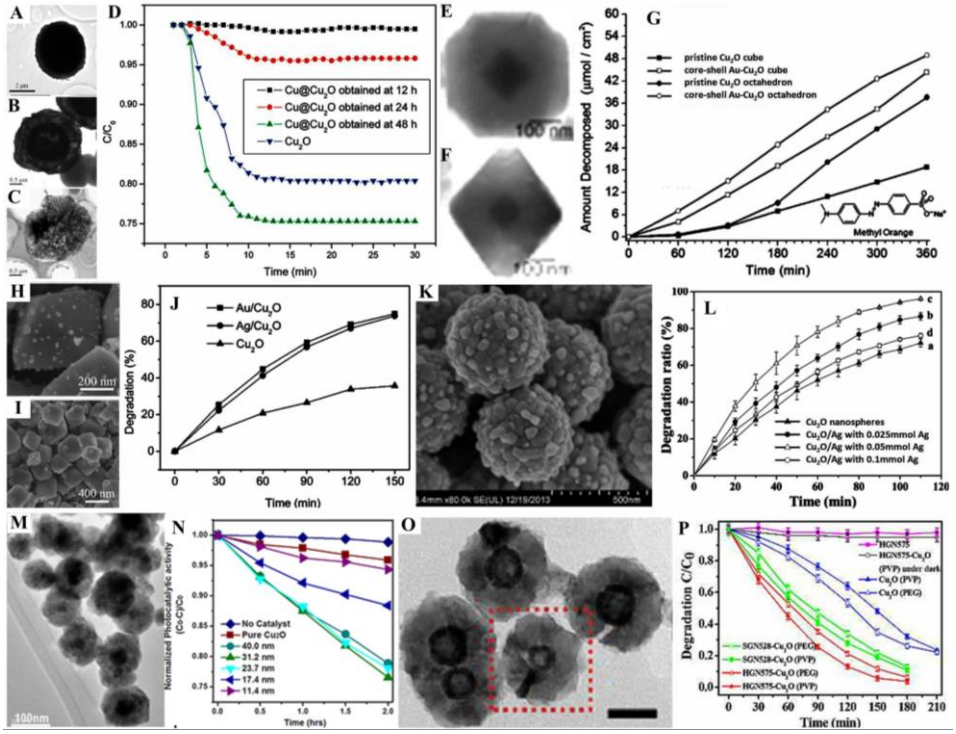

Figure 2.13 TEM images of core-shell Cu@Cu_2O microspheres prepared at 12 (A), 24 (B), and 48 h (C);[22] (D) Curves of the reduction of NO concentration vs. visible-light irradiation time on various catalysts;[22] (E and F) TEM images of different core-shell Au-Cu_2O nanostructures: (E) nanocube and (F) octahedron;[23] (G) Plots of the amount of MO photodecomposed versus time using pristine Cu_2O and Au-Cu_2O core-shell photocatalysts;[23] (H and I) SEM images of the Ag/Cu_2O (h) and Ag/Cu_2O (i) heterogeneous nanocrystals;[24] (J) Pyronine B degradation rate over Cu_2O octahedral nanocrystals, Au/Cu_2O, and Ag/Cu_2O heterogeneous nanocrystals under UV light irradiation;[24] (K) SEM image of Cu_2O/Ag composite nanospheres with 0.05 mmol Ag;[25] (L) Time-dependence of MO (10 mg/L) degradation ratios (under visible light irradiation) over various photocatalysts.[25] (M) TEM image of core-shell Ag@Cu_2O nanoparticles;[11] (N) Degradation of MO by core-shell Ag@Cu_2O photocatalysts with different Cu_2O-shell thicknesses;[11] (O) TEM image of Au-Cu_2O hollow core-shell nanoparticles;[26] (P) MO photodegradation (under irradiation by visible light) versus irradiation time over photocatalysts.[26]

Zhang et al. has prepared silk-mat-like Pd/CeO_2 hybrid NPs with tiny Pd nanoparticles attached on nanosized CeO_2 through assembly in conjunction with rotary vacuum evaporation and a calcination process, which exhibited enhanced photocatalytic activity towards aerobic oxidation of alcohols or anaerobic reduction of nitro-compounds compared to Pd/commercial CeO_2, bare CeO_2-NPs, and commercial CeO_2. According to the yield ratio of aldehydes or aromatic amines, the photocatalytic activity of silk-mat-like Pd/CeO_2-NPs was about 7-13 or 1.5-2 times higher, respectively, than that of Pd/commercial CeO_2. Such enhanced photoactivities was attributed to several synthetic factors, including the unique silk-mat-like structure and morphological composition, the longer lifetime of photoinduced charge carriers, the more efficient charge transfer, as well as higher surface area.[167] Similarly, core-shell Pt@CeO_2 nanospheres,[169] Au@CeO_2 core-shell nanospheres and nanorods,[176] Au NP loaded CeO_2 nanorods,[166] and Au/CeO_2 NPs[175] prepared by different methods exhibited excellent visible-light-induced photocatalytic oxidation of benzyl alcohol. In addition, Ag@CeO_2 core-shell NWs and NPs, as well as Au supported on CeO_2 NPs, showed excellent capability towards O_2 evolution or degradation of methylene blue (MB).[39,143]

2.4.1.5 Plasmonic metal/chalcogenide semiconductor photocatalysts

As one of the most important classes of semiconductors, chalcogenides have been attracting great interest due to their appealing properties and related applications. Similar to the above-introduced plasmonic metal/oxide semiconductor heterostructures, plasmonic metal/chalcogenide semiconductor heterostructures with different morphologies and structures have been fabricated through various methods for photocatalysis application. Among the chalcogenide photocatalysts, the most commonly studied ones are CdS,[27,28,35,38,102,117,177-185] CdSe,[32,186,187] Bi_2S_3,[30,31] ZnS,[188-190] Ag_2S,[29] Cu_2S,[191] PdS,[192] etc.. The preparation methods and photocatalytic reactions of the above-mentioned plasmonic metal/chalcogenide semiconductor photocatalysts are summarized in Table 2.2.

Table 2.2 Plasmonic metal/chalcogenide semiconductor photocatalysts with their synthesis methods and photocatalytic reactions.

Photocatalyst	Preparation method	Photocatalytic reaction	Light source	Reference
dumbbell-like Au-Bi_2S_3 core-shell NRs	wet-chemical deposition	RhB degradation	300 W Xe lamp	[30]
Au NP positioned at the center of Bi_2S_3 nanorod	wet-chemical deposition	MB degradation	λ=500 nm 150 W Xe lamp (100 mW/cm^2)	[31]
starfish-like Au-CdS	self-assembly	RhB degradation	visible light	[117]
porous Ag_2S-Ag nanotubes	microwave-assisted method	MO degradation and Cr^{VI} reduction	visible light	[29]
Au/CdS hexagonal NPs	chemical reduction	hydrogen production	visible light (λ>420nm and a flux of 35 mW/cm^2)	[178]
CdS NWs-Au NPs	electrostatic self-assembly	reduction of nitroaromatic compounds	300 W Xe arc lamp (λ>420 nm)	[35]
Au-nanorod-CdS-nanorod	impregnation method	oxidation of salicylic acid and reduction of p-nitrophenol	UV light	[179]
Au@CdS	self-assembly	hydrogen	300 W	[27]

core-shell nanospheres		generation	Xenon lamp (λ>420 nm)	
Pt/CdS	photoreduction	hydrogen generation	Xe lamp (λ>420 nm)	180
Au-loaded ZnS flowers	deposition-precipitation	hydrogen generation	350 W xenon arc lamp	189
core-satellite ZnS nanospheres-Au NPs	hydrothermal	thionine (TH) degradation	500 W xenon lamp (175 mW/cm^2) with UV illumination	190
core-shell Au-CdS nanocrystals	hydrothermal	RhB degradation	500 W xenon lamp (175 mW/cm^2) with visible light illumination	177
CdSe-Au nanodumbbells	photoreduction	MB degradation	532 nm 27 mW CW laser	186
Au-CdS NPs	continuous spray pyrolysis	MB degradation	200 W halogen lamp with UV filter (visible light)	182
CdS spherical NPs-Au NPs	self-assembly	RhB degradation	350 W Xe light (λ>420 nm or λ>500 nm)	28
Au-Cu_2S core-shell disk-like	solvothermal	MB and RhB degradation	visible light from 100 W	191

nanocrystals			halogen lamp	
PbS-Ag nanotubes	microwave-assisted cation exchange	Congo red degradation and Cr^{VI} reduction	visible light	192
Au/ZnS core/shell nanocrystals	hydrothermal	oxidation of methanol	500 W xenon lamp (100 mW/cm^2)	188
CdS-coated Ag NWs	hydrothermal	RhB decomposition	500 W 100 mW/cm^2 Xe lamp	102
Ag/CdS core-shell NWs	hydrothermal	MB degradation	500 W halogen lamp	38
Ag/CdS NPs	ultrasonic-assisted sol-gel synthesis	Direct Red degradation	UV lamps or visible light	185
pentapod Au-CdSe	wet-chemical deposition	R6G decolorization	UV light	32
Pt-tipped CdSe nanorods	wet-chemical deposition	hydrogen generation	visible light ($\lambda \geq 420$ nm)	187
CdS-Au-TiO_2 sandwich nanorod array	chemical bath deposition	hydrogen generation	300 W Xe lamp	181

Hybrid Au@CdS core-shell NPs with self-assembly of CdS quantum dots on the surface of the pre-grown Au nanoparticles (shown in Figure 2.14A) have been obtained in-situ, which exhibited enhanced photocatalytic activity towards hydrogen generation from aqueous solutions consisting of Na_2S (0.1 M) and Na_2SO_3 (0.1 M) sacrificial reagents, compared to pure CdS under irradiation by visible light with $\lambda \geq 420$ nm and $\lambda \geq 500$ nm.[27] As displayed in Figure 2.14B, the Au@CdS core-shell NPs showed better photodegradatiom performance under irradiation by visible light with $\lambda \geq 420$ nm, which increased in a stable manner during the entire reaction time, while the

photocatalytic activity increased slowly for pure CdS supraparticles with increasing reaction time. The Au@CdS core-shell NPs generated about 1100 μL of H_2 after 16 h. It was about 1.9 times larger than pure CdS supraparticles with 600 μL H_2 generation over this irradiation time. The corresponding efficiency of pure CdS supraparticles and Au@CdS core-shell NPs were 201.9 and 383.6 μmol $h^{-1}g^{-1}$, respectively.[27]

Under illumination with $\lambda \geq 500$ nm, however, the amount of H_2 generation is significantly decreased.[27] The reason could be that CdS could not be excited under irradiation with $\lambda \geq 500$ nm. In this case, the photocatalytic hydrogen generation should only result from the SPR effect of Au NPs, while the injection efficiency of photoexcited hot electrons into CdS shells from Au cores was very low. The proposed mechanistic pathways of core-shell Au@CdS NPs were different under irradiation by visible light with $\lambda \geq 420$ nm and $\lambda \geq 500$ nm. When irradiated with $\lambda \geq 420$ nm light (Figure 2.14C),[27] the significantly improved photocatalytic performance of Au@CdS core-shell NPs compared to pure CdS supraparticles should be ascribed to: ① photogenerated electrons in CdS shells reduce aqueous H^+ to form H_2 at the surface of CdS, part of the photogenerated holes are quenched by Na_2SO_3 and Na_2S, and the remaining photoexcited holes in CdS shells are quickly captured by Au NP cores to form Au-S bonds; ② improved separation of electrons and holes because of the strong electromagnetic field resulting from the SPR effect of Au NP cores; ③ a small amount of hot electron injection into CdS shells from Au cores. When illuminated with $\lambda \geq 500$ nm light (Figure 2.14D), only photogenerated hot electrons injected into CdS shells from Au cores with low efficiency could contribute to hydrogen generation.[27]

Han et al. prepared spherical CdS nanoparticle − Au NP hybrids with different Au NP weight ratios by a facile self-assembly approach through Au-SH bonding, and the hybrids exhibited obviously enhanced photocatalytic activity towards RhB degradation in comparision to CdS spherical NPs under irradiation by Xe lamp light.[28] As shown in Figure 2.14E, spherical CdS nanoparticle − Au NP hybrids showed better photocatalytic

activity in comparision to pure CdS spherical nanoparticles, and the CdS spherical nanoparticle − 0.5 wt% Au NP hybrid showed the best photocatalytic performance, as it could degrade 78.9% of the RhB within 10 min. The photocatalytic activity was diminished, however, when the Au content was further increased to 1 wt% or 3 wt%, because the excess Au NPs may act as recombination centers to degrade the photocatalytic performance.[28,35] The RhB photodegradation rate constant (*k*) was calculated from a pseudo-first-order approximation, and the results are displayed in Figure 2.14F. In comparision to pure CdS spherical nanoparticles (rate constant k = 0.0710 min^{-1}), spherical CdS nanoparticles − Au NPs hybrids having different Au NP contents showed remarkably enhanced photocatalytic activity, and their rate constant *k* values were 0.1423, 0.1054, and 0.1090 min^{-1} for Au NPs content of 0.5, 1, and 3 wt%, respectively. The highest photocatalytic activity for CdS spherical nanoparticles − Au NPs (0.5 wt%) was double that of bare CdS.[28] It is proposed the improvement of the CdS spherical nanoparticles − Au NPs hybrids could have resulted from tight interfacial contact between Au NPs and spherical CdS NPs, which could effectively transfer photogenerated electrons to Au NPs from CB of CdS spherical NPs, leading to improved charge separation and lifetime longer lifetime (Figure 2.14G).[28]

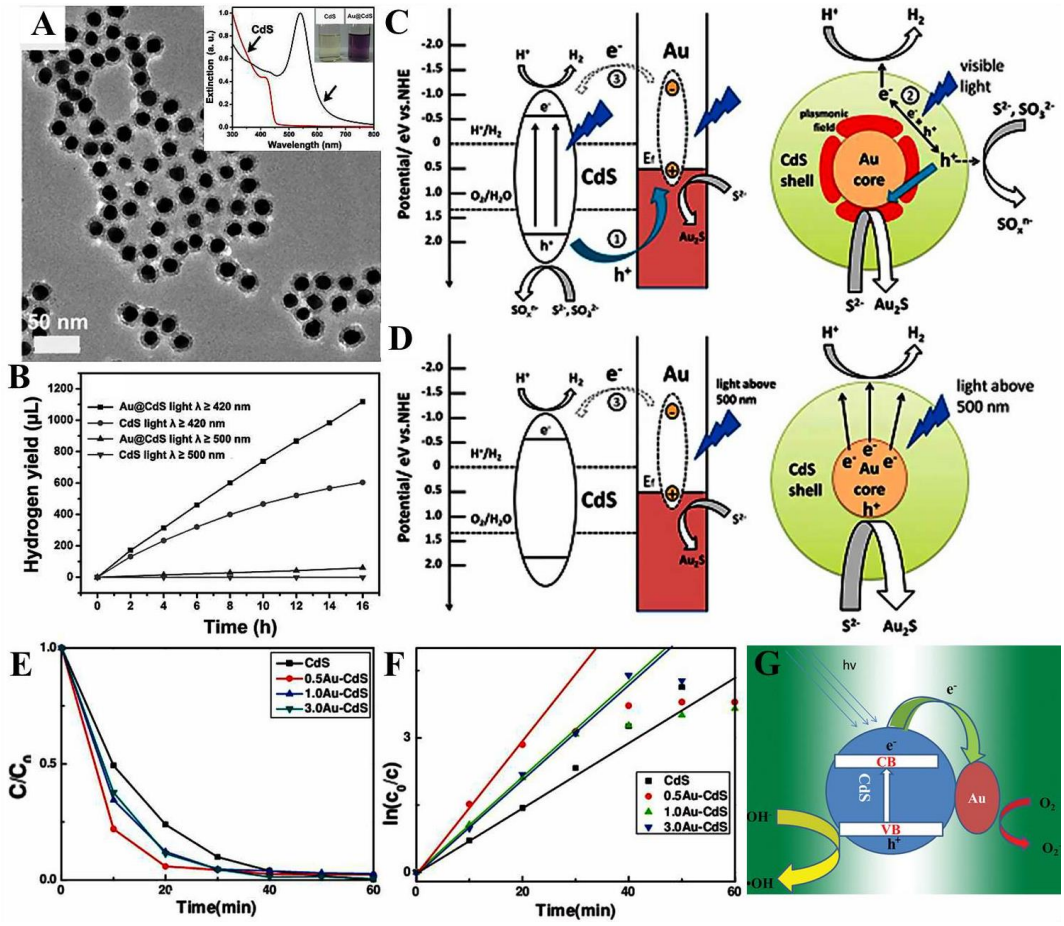

Figure 2.14 (A) Typical TEM image of core-shell Au@CdS nanoparticles, with the extinction vs. wavelength plot shown in the inset in comparison with pure CdS;[27] (B) Photocatalytic hydrogen generation over core-shell Au@CdS nanoparticles and CdS quantum dot supraparticles under light irradiation, with $\lambda \geq 420$ and $\lambda \geq 500$ nm, respectively;[27] (C) Hole-electron pair separation and transfer pathways on core-shell Au@CdS nanostructures towards photocatalytic H_2 evolution ($\lambda \geq 420$ nm);[27] (D) Hot electron transfer pathway on core-shell Au@CdS nanostructures towards photocatalytic H_2 evolution ($\lambda \geq 500$ nm);[27] (E) Photocatalytic degradation and (F) RhB photodegradation rate over spherical CdS NPs and CdS-spherical-NP−Au-NP composites with different Au NPs weight ratios;[28] (G) Scheme of charge separation on CdS-spherical-NP−Au-NP composite.[28]

In addition to the most extensively studied CdS, other chalcogenide semiconductor photocatalysts such as Ag_2S, Bi_2S_3, ZnS, CdSe, and Cu_2S have been also attracted much attention in recent years. For instance, porous Ag_2S-Ag heterostructured nanotubes (Figure 2.15A) have been prepared via a microwave-assisted strategy through reacting Ag_2CO_3 nanorods with thioacetamide in ethanol, and they exhibited good photocatalytic properties towards MO degradation and Cr^{VI} reduction.[29] As shown in Figure 2.15B, all the porous Ag_2S-Ag heterostructured nanotubes prepared with different concentrations of thioacetamide showed better photocatalytic performance towards MO degradation compared with pure Ag_2S and P25, with the highest performance for sample H-2. Over sample H-2, about 92.1 % of MO was removed after irradiation for 30 min, while the degradation rates over pure Ag_2S, P25, sample H-1, and sample H-3 were about 7.8 %, 25.4 %, 13.9 %, and 82.5 %, respectively, displaying relatively low photodegradation properties. Figure 2.15C showed the photocatalytic activity of Cr^{VI} reduction over the same photocatalysts under irradiation by visible light, and sample H-2 exhibited the best photoreduction property, which was similar to the results for MO degradation. The enhanced photocatalytic capability of the porous Ag_2S-Ag heterostructured nanotubes may result from the efficient transfer of photoinduced electrons to Ag from the CB of Ag_2S in the hybrid nanostructure. Furthermore, the Ag content has a great influence on its photocatalytic performance, with such hybrid having a moderate Ag_2S/Ag molar ratio showing the best photocatalytic activity, while excess Ag content could decrease photocatalytic efficiency because of less availability of Ag_2S surface toward pollutant adsorption and light absorption.[29]

Ma et al. fabricated dumbbell-like Au-Bi_2S_3 core-shell nanorods (NRs) (shown in Figure 2.15D) via the chemical deposition method by keeping a mixed solution of Au nanorods (NRs), L-ascorbic acid, hexamethylenetetramine, and bismuth acetate at 80 ℃ for 8 h.[30] The resulting dumbbell-like Au-Bi_2S_3 core-shell NRs exhibited highly enhanced photocatalytic property towards RhB degradation compared with normal Au-Bi_2S_3 NRs and pure Bi_2S_3 under 300 W xenon lamp irradiation.[30] As shown in Figure

2.15E, 62% of the RhB could be degraded after light irradiation for 60 min, whereas only 30% and 38.8% of RhB could be degraded with pure Bi_2S_3 and normal Au-Bi_2S_3, respectively, for the same period of irradiation time. The dumbbell-like Au-Bi_2S_3 displayed better photocatalytic activity than that of general Au-Bi_2S_3, which could be attributed to the strong local electric field and significantly improved absorption of visible-light.[30] The proposed mechanisms for the improvement of photocatalytic performance in the dumbbell-like core-shell Au-Bi_2S_3 NRs may be: (i) enhanced light absorption for Bi_2S_3 arised from plasmon scattering and a large local field, meanwhile, the recombination of near-surface photoexcited electron-hole pairs is prevented because of the short diffusion length; (ii) Au-facilitated light harvesting and the interfacial charge migration process also contributed, as well as interfacial resonant energy transfer, such as hot electron injection to Bi_2S_3 from Au metal, and electron-hole pair excitation in Bi_2S_3 (Figure 2.15F).[30] Another unique Au-Bi_2S_3 hybrid nanostructure with Au nanoparticles positioned at the center of Bi_2S_3 nanorods exhibited much improved photocatalytic performance towards methylene blue degradation under Xe lamp irradiation with a wavelength of 500 nm compared to a mixture of Au and Bi_2S_3, Bi_2S_3, and Au. The degradation rate constants of Au-Bi_2S_3 hybrid nanostructures, a mixture of Au and Bi_2S_3, Bi_2S_3, and Au were 0.037, 0.007, 0.004, and 0.002 min^{-1}, respectively (Figure 2.15G-I).[31]

Hybrid colloidal Au-CdSe pentapod heterostructures (Figure 2.15J) have been developed by a chemical deposition route, and they showed better photocatalytic performance for Rhodamine 6G (R6G) dye photodegradation compared to CdSe under UV illumination with λ = 365 nm.[32] As shown in Figure 2.15K, 87.2% of R6G dye is degraded by such hybrid after 150 min of light illumination, whereas only 27.3% degradation is observed for pure CdSe nanocrystals. The kinetic rate constants were calculated to be 0.002 and 0.013 min^{-1} for pure CdSe and Au-CdSe pentapod heterostructures, respectively (Figure 2.15L). It is proposed that the potential energy differences between Au and CdSe can reduce the recombination of photogenerated

electrons and holes, which would contribute to enhanced photogradation performance of Au-CdSe heterostructures.[32]

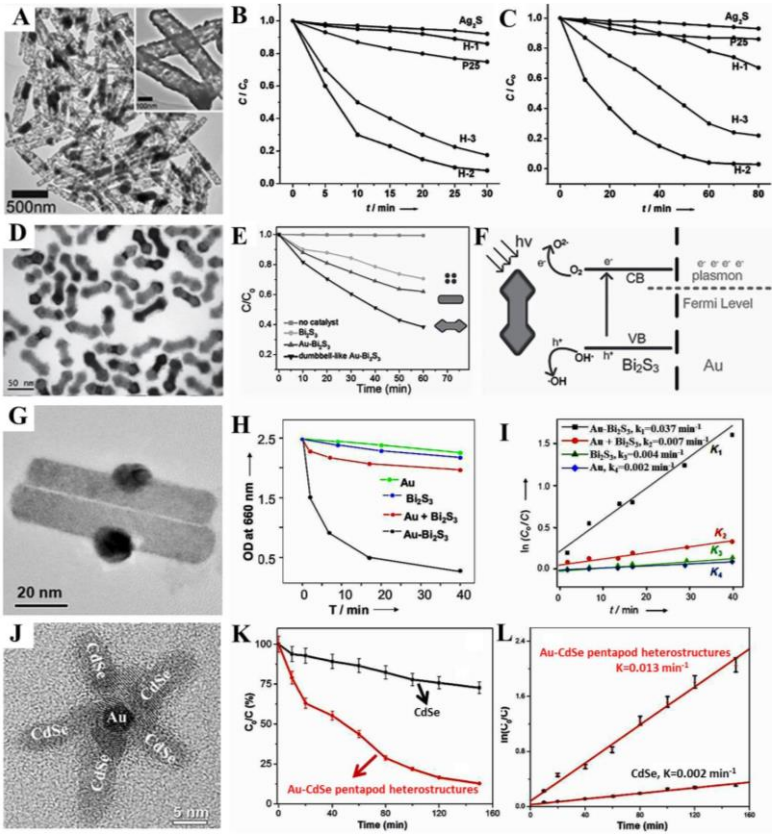

Figure 2.15 (A) TEM image, with enlarged image in inset, of porous Ag_2S-Ag heterostructure nanotubes;[29] (B) MO photodegradation, and (C) Cr^{VI} photoreduction over various photocatalysts (H-1, H-2, and H-3, referring to Ag_2S-Ag nanotubes fabricated with 1.8, 3.5, and 5.4 mM of thioacetamide, respectively);[29] (D) TEM image of dumbbell-like Au-Bi_2S_3;[30] (E) Photodegradation of RhB over pure Bi_2S_3, normal and dumbbell-like Au-Bi_2S_3;[30] (F) Proposed photodegradation process for Au-Bi_2S_3 dumbbell-like nanostructure;[30] (G) TEM image of Au-Bi_2S_3 heterostructures with Au nanoparticle positioned at the center of each Bi_2S_3 nanorod;[31] (H) The change in optical density of MB with time during reduction in presence of Au, Bi_2S_3, an Au and Bi_2S_3 mixture, and Au-Bi_2S_3 heterostructures;[31] (I) Rate of MB degradation with irradiation time under Xe lamp irradiation with a wavelength of 500 nm;[31] (J) TEM image of a single Au-CdSe pentapod-shaped heterostructure;[32] (K) Rhodamine 6G (R6G) dye

photodegradation and (L) R6G dye photodegradation rate over Au/CdSe heterostructures and CdSe under illumination by UV light.[32]

2.4.1.6 Construction and performance of 1D plasmonic metal/semiconductor photocatalysts

Compared with the commonly used nanoparticles or bulk materials, one-dimensional nanostructures have had a profound impact on the application of photocatalysis, because they can effectively avoid agglomeration, possess direct electrical pathways for rapid and long-distance photoelectron transport, and have higher length-to-diameter ratios and larger specific surface areas, leading to significant improvement of the light absorption and scattering.[95,96,99,193] Accordingly, it is of significant interest to design and synthesize 1D plasmonic metal/semiconductor hybrids and composite photocatalysts with unique properties, and investigate their versatile photocatalytic applications. Table 2.3 summarizes some 1D plasmonic metal/semiconductor photocatalysts and their preparation methods, as well as their photocatalytic reactions.

Table 2.3 1D plasmonic metal/semiconductor photocatalysts with their preparation methods and photocatalytic reactions.

Photocatalyst	Preparation method	Photocatalytic reaction	Light source	Reference
Au/TiO_2 nanotube	photoreduction	water splitting	visible light ($\lambda \geq 420$ nm)	194
M/TiO_2 nanotube arrays (M=Au,Ag,Pt,Cu)	photoreduction and chemical deposition	CR degradation	253 nm UV light 575 nm visible light	195
M-TiO_2 nanotube arrays (M=Au, Ag, Pt)	layer-by-layer self-assembly	MO degradation	UV light from 300 W Xe arc lamp	196

Ag/TiO_2 core-shell nanowire arrays	electrodeposition	MB degradation	UV light, visible light	197
$Ag@TiO_2$ core-shell NWs	hydrolysis combined with hydrothermal	RhB degradation	$\lambda \geq 420$ nm 300 W Xe lamp	198
Ag/TiO_2 nanowires	photoreduction	MB degradation	visible-light (λ=420 nm)	33
Au NPs/$KNbO_3$ NWs	deposition-precipitation	RhB degradation	UV light (λ=365 nm) visible light (λ>420 nm)	199
Au NPs/ZnO nanorods	chemical deposition	RhB degradation	λ=365 nm from 300 W high-pressure mercury lamp	162
Au NPs-CdS NWs	self-assembly	Reduction of nitroaromatic compound	$\lambda \geq 420$ nm 300 W Xe lamp	35
PbS-Ag nanotubes	microwave-assisted cation-exchange	CR degradation and Cr^{VI} reduction	visible light	192
$Ag@CeO_2$ core-shell NWs	chemical deposition	O_2 evolution and MB degradation	visible light (λ>400 nm)	39
worm-like Ag/ZnO core-shell NWs	ultrasonic assisted	RhB degradation	UV light from 500 W	37

	chemical deposition		fluorescent Hg lamp	
Ag@TiO_2 core-shell NWs	solvothermal	RhB degradation	300 W xenon lamp	36
Au NPs-Cu_2O NWs	assembly	MB degradation	300 W xenon lamp with UV filter	34
CdS-coated Ag NWs	hydrothermal	RhB decomposition	500 W 100 mW/cm^2 Xe lamp	102
Ag/CdS core-shell NWs	hydrothermal	MB degradation	500 W halogen lamp	38
Ag/TiO_2 nanofiber	solvothermal	RhB degradation	visible light	103
Ag NPs/ZnO nanorods array	photoreduction	MB degradation	ultraviolet light	13
Ag NPs/$AgVO_3$ nanoribbons	chemical reduction	basic fuchsin degradation	visible light	14
Ag/AgCl core-shell NWs	in situ oxidation reaction	MO decomposition	visible light	40
hierarchical Ag/AgCl nanowire/nanoplate	in situ oxidation reaction	RhB degradation	visible light	41
necklace-like Ag NW/Ag_3PO_4 cubes	in situ oxidation reaction	RhB degradation	visible light	42
core-shell coaxial Ag/Ag_3PO_4 NWs	in situ oxidation reaction	RhB degradation	visible light	43

As displayed in Table 2.3, most TiO_2 nanotubes or nanowires decorated with various metal nanoparticles prepared by different methods show excellent photocatalytic performance. For instance, Ag/TiO_2 nanowires with Ag NPs deposited on TiO_2 nanowires have been prepared by a simple photoreduction strategy (Figure 2.16A),[33] where an ethanol dispersion of $AgNO_3$ and TiO_2 nanowires, which was pre-prepared by the solvothermal method, is illuminated by a 50 W mercury lamp (λ = 254 nm) for 30 min under stirring. Figure 2.16B illustrateed the preparation of Ag/TiO_2 by a photoreduction process in ethanol as the solvent. The photocatalytic activity of such Ag/TiO_2 nanowires towards MB dye degradation under irradiation by visible light has been evaluated.[33] As shown in Figure 2.16C, the degradation of MB was negligible without a photocatalyst. The Ag/TiO_2 nanowires exhibited better photocatalytic performance than pure TiO_2, which can degrade about 29 % of MB after irradiation for 90 min, while pure TiO_2 nanowires show rather poor photocatalytic activity, with only about 6 % of MB decomposed under the same conditions. The enhanced photocatalytic performance of Ag/TiO_2 nanowires is associated with enhanced light absorption and low electron-hole pair recomnination because of the SPR effect of Ag NPs.[33]

Highly ordered ZnO nanorod arrays (ZnO NRA) decorated with Ag nanoparticles (Figure 2.16D) have been obtained by using a facile photodeposition method, where ZnO NRA on the glass substrate were fabricated via dip coating method and chemical solution deposition, and then Ag nanoparticles were deposited on ZnO NRA via irradiating ZnO NRA in $AgNO_3$ solution with UV light.[13] The amount of Ag deposited can be tailored through varying $AgNO_3$ concentrations. Samples of ZnO NRA decorated with different Ag contents were tested for their photocatalytic activity towards methylene blue photodegradation under ultraviolet light irradiation.[13] Figure 2.16E displayed the photodcatalytic activity and calculated rate constant (k) values from linear fitting towards MB degradation, while the inset shows the calculated photodegradation ratios after irradiation for 1 h under UV light illumination. All ZnO/Ag samples with various contents of deposited Ag show improved photogradation

performance in comparision to bare ZnO NRA. Furthemore, the photodegradation efficiency changed from 39.6% to 49.3% for different ZnO/Ag hybrid photocatalysts with ZnO/Ag (0.05 M) exhibiting the highest photodegradation activity, while only 36.2% of MB was degraded for pure ZnO NRA. Such improved photocatalytic activity could result from the efficient separation of photoinduced charge in Ag/ZnO, which reduces the rapid recombination of photoinduced electron-hole pairs owing to the SPR effect of the deposited Ag.[13]

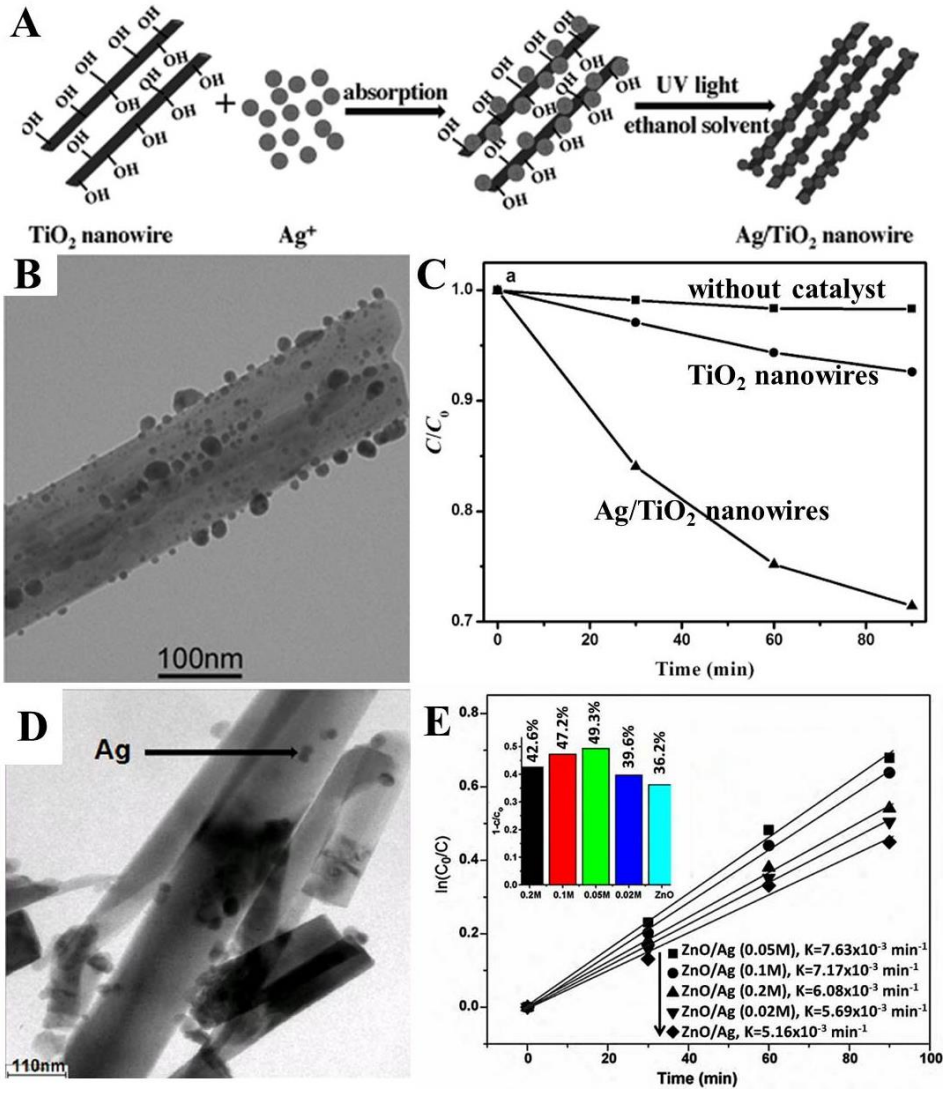

Figure 2.16 (A) The preparation of Ag/TiO_2 nanowires by a photoreduction process in ethanol solvent;[33] (B) TEM image of a single Ag/TiO_2 nanowire;[33] (C) The kinetics of

photodegradation of MB by different photocatalysts under visible-light irradiation (λ = 420 nm);[33] (D) TEM image of Ag/ZnO prepared with 0.05 M $AgNO_3$;[13] (E) Plots of ln(C_0/C) over time for MB photodegradation over different photocatalysts, with the inset showing the percentages degraded for the different samples.[13]

In addition to the most investigated 1D photocatalysts, such as TiO_2 and ZnO decorated with plasmonic metal nanoparticles, other 1D photocatalysts have also been investigated, such as Cu_2O and CdS decorated with noble metals. For instance, Pan et al. prepared Cu_2O-Au nanowires with tunable coverage of Au through an assembly method by mixing oleylamine-capped Au NPs with poly(*o*-anisidine)-capped Cu_2O NWs in various ratios (Figure 2.17A).[34] It can be seen from the typical TEM image that the hybrid consisted of many Au spherical NPs with diameters of 3-5 nm attached on Cu_2O NWs (Figure 2.17B). Their photocatalytic performance was studied by MB degradation under irradiation by visible light.[34] As displayed in Figure 2.17C, Cu_2O-Au nanowires with different coverage of Au exhibited better photocatalytic performance than pure Cu_2O, with the Cu_2O-Au (2) sample showing the best photocatalytic property.

The improvement of Cu_2O-Au NWs could be due to the SPR effect and electron sink effect of Au NPs. On the one hand, Au NPs can act as electron sinks because of the Schottky barrier at the interface, where the photogenerated electrons in CB of Cu_2O NWs can be transferred quickly for enhancing charge transfer and prevent their recombination, resulting in enhanced photocatalytic performance (Figure 2.17D). On the other hand, the light is enhanced due to the local field enhancement effect, resulting in improved photocatalytic activity (Figure 2.17D).

Furthermore, CdS nanowire-Au nanocomposites with different ratios of Au NPs have been prepared via a similar electrostatic self-assembly method, and they also exhibited enhanced photocatalytic activity toward reduction of 4-nitroaniline in comparison to CdS nanowires under irradiation by visible light.[35] As displayed in Figure 2.17E, it can

be observed that all CdS NW-Au NPs exhibited much better activity than pure CdS NWs, and the CdS NW-Au NP 1 wt% sample shows the highest photocatalytic activity (rate constant k = 0.418 min^{-1}). Also, excess Au NPs reduce the photocatalytic performance of such hybrid. The proposed possible reaction mechanism (Figure 2.17F) for the photocatalytic performance was that the enhancement upon nitroaromatic reduction could result from electron sink effect of Au NPs, owing to the Schottky barrier at the interface rather than the SPR effect.[35]

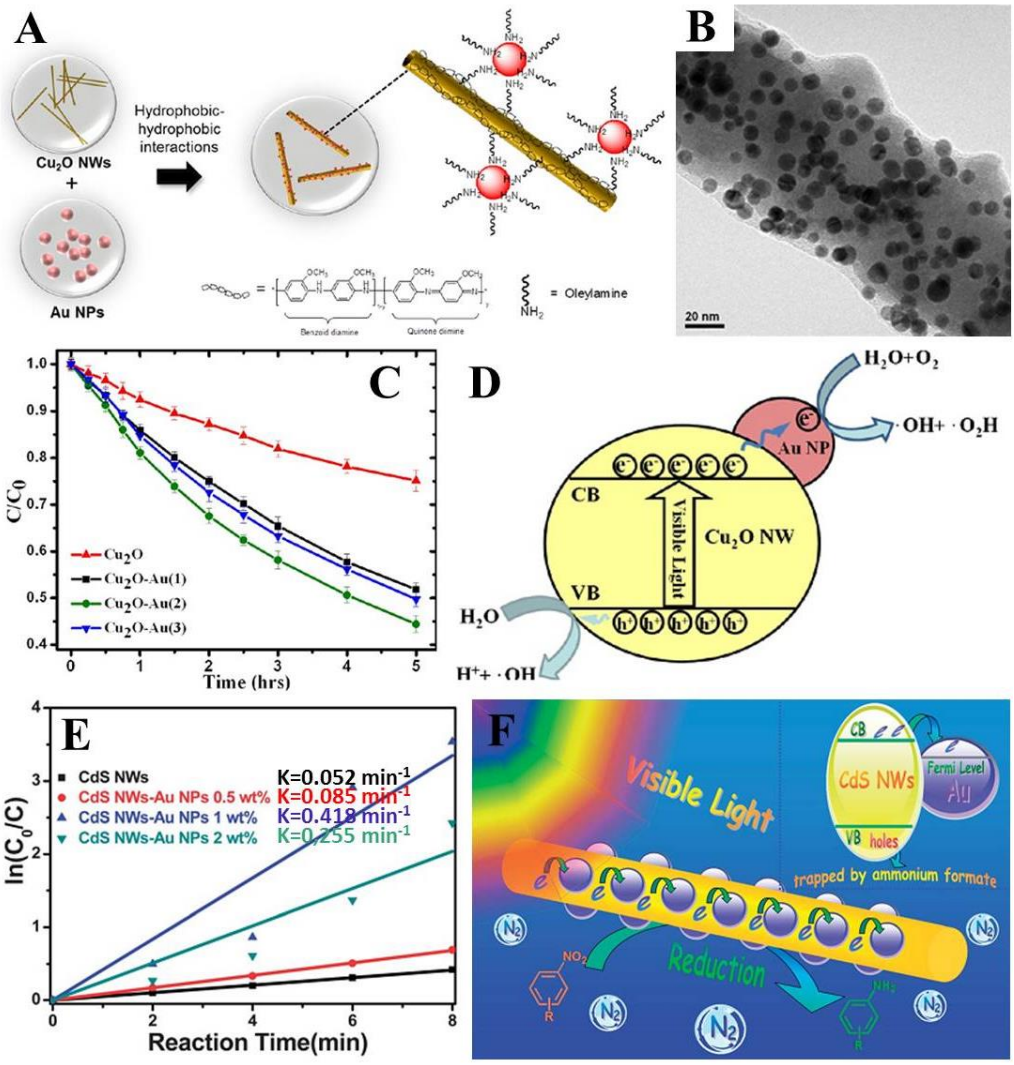

Figure 2.17 (A) Coupling between Cu_2O NWs and Au NPs;[34] (B) TEM image of Cu_2O-Au NW;[34] (C) MB photodegradation over Cu_2O NWs and Cu_2O NWs decorated with Au NPs coverage density is different);[34] (D) Proposed photocatalytic process over

Cu_2O-Au NWs;[34] (E) Plots of ln(C_0/C) vs. irradiation time over CdS NWs-Au NPs and CdS NWs for 4-nitroaniline reduction (the weight addition ratio of Au NPs is different);[35] (F) Schematic illustration of proposed photocatalytic nitroaromatic reduction process (room temperature, N_2 purging, ammonium formate used as hole quencher, under visible light irradiation).[35]

In addition to the most investigated 1D hybrid photocatalysts consisting of 1D semiconductors decorated with plasmonic metal NPs, 1D plasmonic metals covered with semiconductor hybrid photocatalysts are also attracting tremendous attention, especially with Ag NWs selected as cores to be coated with different semiconductor photocatalysts.

For example, Ag@TiO_2 core-shell NWs have been fabricated via a solvothermal method, and the TEM image (Figure 2.18A) showed that a layer of TiO_2 NPs about 30 nm in thickness was covering the surface of an Ag NW with a diameter of around 50 nm. Their photocatalytic performance was evaluated by RhB decolorization under UV light illumination, as shown in Figure 2.18B, and the Ag@TiO_2 core-shell NWs exhibited the highest photocatalytic activity compared with pure TiO_2, P25, and pure Ag NWs. The enhanced photodegradation performance of the Ag@TiO_2 core-shell NWs could result from several synergistic effects, including the fast efficient transfer of photoinduced electrons to Ag NWs from the CB of TiO_2 where they recombine with holes (Figure 2.18C), the unique web-like porous superstructure, and the good dispersion of TiO_2 NPs.[36]

Similarly, worm-like Ag/ZnO core-shell NWs (Figure 2.18D) and Ag/CdS core-shell NWs (Figure 2.18F) have been prepared via an ultrasonical chemical deposition method and the hydrothermal method, respectively, and they exhibited excellent photocatalytic activity towards degradation of organic dyes.[37,38] Figure 2.18E shows the curves of RhB photodegradation over core-shell Ag/ZnO NWs with various Ag contents compared to

pure Ag NWs and ZnO, and the calculated reaction rate constant (k) values based on linear fitting for the above photocatalysts. It can be seen that the RhB degradation over Ag NWs was negligible ($k = 6.68\times10^{-5}\text{min}^{-1}$), and all the Ag/ZnO core-shell NWs showed better photocatalytic activities than pure ZnO particles (k = 0.0034 min^{-1}). Among them, Ag/ZnO core-shell NWs containing 2.8 at % Ag exhibited the best activity (k = 0.0793 min^{-1}), approximately twofold that of Ag/ZnO hybrids containing 4.9 at % Ag (0.041 min^{-1}) and 0.8 at % Ag (0.032 min^{-1}).[37] Figure 2.18g displayed MB degradation over Ag/CdS NWs, CdS particles, and Ag NWs (Figure 2.18F).[38] As displayed in Figure 2.18G, the photocatalytic activity of Ag/CdS NWs was significantly enhanced compared with CdS particles. 95.35% of MB was degraded over the Ag/CdS NWs after 240 min of visible light irradiation, while only about 50% of MB was degraded over pure CdS within the same irradiation time.[38] The enhanced photocatalytic performance of both of Ag/ZnO NWs and Ag/CdS NWs could result from interfacial charge transfer in the hybrids, where the photogenerated electrons are rapidly transferred to the Ag NWs from the VB of ZnO or CdS, leading to the efficient separation of photogenerated electron-hole pairs and prolonging their lifetime.[37,38]

Another successful example is the preparation of Ag@CeO_2 NWs by a simple chemical deposition route, where the Ag NW solution is first incubated in 4-mercaptobenzoic acid in ethanol at 60^{o}C, and then the mixture is immersed in an aqueous bath containing polyvinyl pyrrolidone (PVP), hexamethylenetetramine, and $Ce(NO_3)_3$ to coat the NWs with CeO_2 shells at 95^{o}C.[39] The thicknesses of CeO_2 shell can be controlled through altering the amounts of $Ce(NO_3)_3$. Figure 2.18H-J show typical TEM images of Ag@CeO_2 NWs with different shell thicknesses. The interfaces between CeO_2 NPs and Ag NWs can be clearly observed, and the CeO_2 shell thickness of the AgNWs@CeO_2-1, 2, 3 samples is 26.15, 66.12, and 28.92 nm, respectively. The photocatalytic activity of core-shell Ag NWs@CeO_2 nanostructures was investigated by O_2 evolution through water oxidation in aqueous solutions using silver nitrate (50 mM) as the sacrificial agent, as well as MB degradation under irradiation with λ > 400 nm.[39] As displayed in Figure

2.18K, all the Ag NWs@CeO_2 samples with different shell thicknesses exhibit much higher photocatalytic O_2 evolution than pure CeO_2. Furthermore, Ag NWs@CeO_2-2 and Ag NWs@CeO_2-3 samples show higher activity than that of Ag NPs@CeO_2, and the Ag NWs@CeO_2-2 hybrid displays the highest activity. In addition, the average O_2 evolution rates for Ag NWs@CeO_2-2, Ag NWs@CeO_2-3, Ag NPs@CeO_2, Ag NWs@CeO_2-1, and pure CeO_2 are 61.8 μmol $g^{-1}h^{-1}$, 53.5 μmol $g^{-1}h^{-1}$, 44.3 μmol $g^{-1}h^{-1}$, 42.5 μmol $g^{-1}h^{-1}$, and 35.8 μmol $g^{-1}h^{-1}$, respectively. In addition, the photocatalytic activity towards degradation of MB shows a similar tendency. As can be observed from Figure 2.18L, the Ag NWs@CeO_2-2 sample has the first order kinetic photodegradation constant of 0.640 h^{-1}, while the kinetic constant of Ag NPs@CeO_2 and pure CeO_2 is 0.460 h^{-1} and 0.366 h^{-1}, respectively.[39]

It is proposed that the enhanced photocatalytic activity of Ag NWs@CeO_2 could result from its ability to trap electrons and the SPR effect (higher local electric field enhancement than that of Ag NPs because of the improved longitudinal plasmon light absorption for visible light compared to Ag NPs).[39] Figure 2.18M illustrateed the charge injection mechanism with plasmon-induced charge transfer. The CeO_2 shell was porous and loose packed in such unique structure, which allowed the reactants and active species to pass through. Once there is irradiation under visible light, both the CeO_2 shell and the Ag NW core could absorb photons and produce photoinduced electrons and holes. The SPR-induced excited electrons that have enough energy can be directly injected into the CB of CeO_2. Simultaneously, in order to achieve energy equilibrium, the holes within the VB of CeO_2 also can be transferred to Ag NW core, preventing a fast charge recombination, and thereby improving the photocatalytic performance.[39]

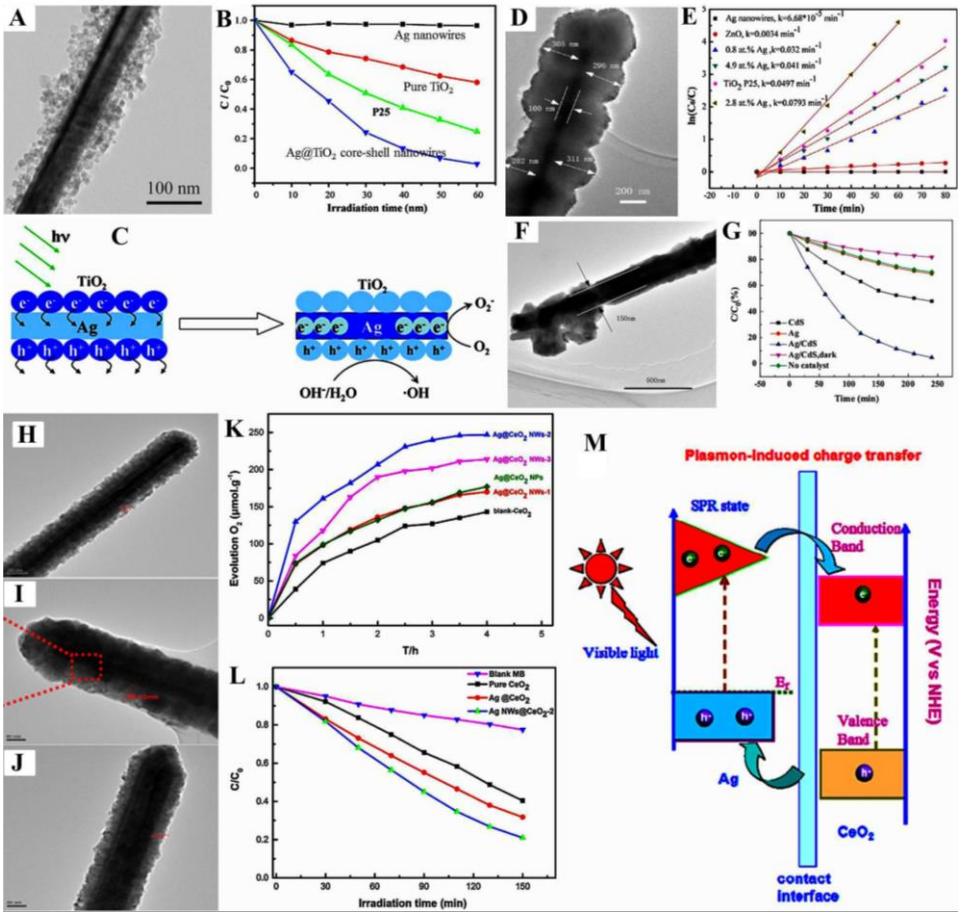

Figure 2.18 (A) TEM image of an individual Ag@TiO_2 NW;[36] (B) Photocatalysis properties (under UV light irradiation) of different photocatalysts towards RhB decolorization at ambient temperature;[36] (C) Schematic diagram showing the transfer of electrons in Ag@TiO_2 NWs under UV irradiation;[36] (D) TEM image of core-shell Ag/ZnO nanowires (Ag content: 2.8 atom%);[37] (E) Plots of ln(C_0/C) versus irradiation time over different photocatalysts for RhB degradation;[37] (F) TEM image of Ag/CdS NWs;[38] (G) MB degradation efficiencies for different photocatalysts;[38] (H-J) TEM images of Ag NWs@CeO_2 with tailored shell thickness (H: 26.15 nm, I: 66.12 nm, J: 28.92 nm;[39] (K) Photocatalytic O_2 evolution (under visible light illumination) curves of pure CeO_2, core-shell Ag-NWs@CeO_2, and core-shell Ag-NPs@CeO_2 nanostructured catalysts prepared from 50 mM $AgNO_3$;[39] (L) MB degradation over Ag-NWs@CeO_2-2, Ag-NPs@CeO_2, and bare CeO_2 products;[39] (M) Schematic illustration of proposed process induced by the hot-electron effect.[39]

Uniform one-dimensional core-shell Ag/AgCl nanowires with diameters of 110-120 nm and AgCl shell thicknesses of 40-50 nm have been fabricated via a facile room temperature in-situ oxidation reaction from Ag NWs and $FeCl_3$ (Figure 2.19A).[40] According to the redox potentials of $E^0_{AgCl/Ag}$ = +0.223 V and $E^0_{Fe3+/Fe2+}$ = +0.771 V, the Ag atoms on the surfaces of Ag NWs could be oxidized into AgCl nanocrystals by Fe^{3+} in situ, as illustrated in Figure 2.19B.[40] In addition, metallic cations have an important influence on the morphology and structure of Ag/AgCl nanoproducts through variation of the oxidation rate between metal ions and Ag. For example, when $FeCl_3$ solution is replaced by $CuCl_2$ solution, hierarchical Ag/AgCl nanowire/nanoplate hetero-nanostructures are obtained (Figure 2.19C).[40,41]

From the photocatalytic performance towards visible-light-induced MO dye decomposition, as displayed in Figure 2.19D,[40] it can be clearly seen that all 1D Ag/AgCl core-shell structures showed excellent photocatalytic properties, and the photocatalytic activities of the hybrid can be engineered by altering the constitutions of core and shell. The Ag/AgCl core–shell nanowires with an 8:92 ratio of Ag to AgCl showed better performance than other samples with different ratios and single AgCl nanostructures. [40] Furthermore, their photocatalytic performance was different from what would be expected from the morphology and structure. As shown in Figure 2.19E, the hierarchical Ag/AgCl nanowire/nanoplate hetero-nanostructures exhibited better photocatalytic activity than that of AgCl nanoparticles, Ag/AgCl nanowires, and N-doped TiO_2 towards visible-light-driven RhB photodegradation.[41]

As the redox potential of $E^0_{O2/OH-}$ = +0.401 V, which is a little larger than that of $E^0_{[Ag(NH3)]+/Ag}$ = +0.373 V, silver can also be oxidized by O_2 from the atmosphere in the $[Ag(NH_3)_2]^+$ complex by a similar strategy,.[43] Therefore, when Na_2HPO_4 aqueous solution is added into the $[Ag(NH_3)_2]^+$ complex aqueous solution (0.15 M) containing Na_2HPO_4, a necklace-like Ag nanowire/Ag_3PO_4 cube heterostructure with growth of submicron Ag_3PO_4 cubes on Ag nanowire has been synthesized at room temperature

(Figure 2.19F).[42] The compositions and structures of the Ag/Ag_3PO_4 heterostructures can be tailored through tuning the concentration of $[Ag(NH_3)_2]^+$, which then has an influence on the photocatalytic performance. As shown in Figure 2.19G, core-shell coaxial Ag/Ag_3PO_4 hetero-nanowires, with Ag nanowires entirely capped by Ag_3PO_4 nanocrystals, could be obtained with increasing $[Ag(NH_3)_2]^+$ concentration up to 0.2 M.[42,43] Their photocatalytic properties were evaluated through visible-light-induced RhB photodegradation.[42,43]

As displayed in Figure 2.19H, all Ag/Ag_3PO_4 heterostructured and pure Ag_3PO_4 photocatalysts showed excellent photocatalytic activities towards RhB degradation, while bare Ag nanowires have almost no activity. It is notable that the photocatalytic activities of these Ag/Ag_3PO_4 heterostructures vary with different morphologies and compositions. Among them, the necklace-like Ag nanowire/Ag_3PO_4 cube heterostructure (shown in Figure 2.19F) showed the best photocatalytic performance. It could achieve complete degradation of RhB in only 2 min, while Ag/Ag_3PO_4 core-shell coaxial hetero-nanowires (Figure 2.19G) and pure Ag_3PO_4 cubes took about 6 and 8 min, respectively. The Ag nanowire/Ag_3PO_4 cube photocatalysts prepared with lower concentrations of $[Ag(NH_3)_2]^+$ complex exhibited much poorer photocatalytic activities than the pristine Ag_3PO_4 cubes, which could be a result of the high content of Ag metal and low content of Ag_3PO_4 in the hybrid nanostructures.[42] The enhanced photocatalytic performance of Ag/Ag_3PO_4 hybrid nanostructures with a proper morphology and composition ratio may be primarily attributed to the fast electron transfer through the Ag NWs and low combination of photogenerated electron-hole pairs at the interfaces between Ag metal and Ag_3PO_4, resulting from the equilibration of the Fermi level.[15,43]

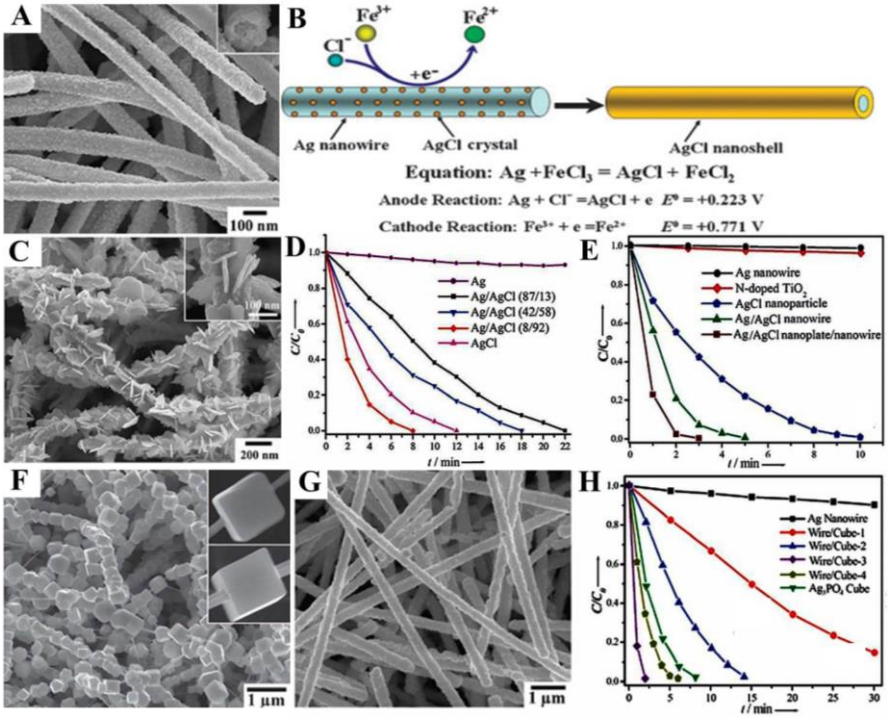

Figure 2.19 (A) SEM image of core-shell Ag/AgCl nanowires;[40] (B) Schematic illustration of formation of core-shell Ag/AgCl nanowires via in-situ oxidation;[40] (C) SEM image of hierarchical Ag/AgCl nanowire/nanoplate hetero-nanostructures;[40,41] (D) Photocatalysis properties (under visible light irradiation) of core-shell Ag/AgCl nanowires towards MO decomposition;[40] (E) Photocatalysis properties of hierarchical Ag/AgCl nanowire/nanoplate hetero-nanostructures and other photocatalysts towards RhB degradation under visible-light irradiation;[41] SEM images of (F) necklace-like Ag nanowire/Ag_3PO_4 cube heterostructures[42] and (G) core-shell Ag/Ag_3PO_4 coaxial hetero-nanowires[42,43] (H) Photocatalytic activities of Ag/Ag_3PO_4 heterostructures, pure Ag_3PO_4 cubes, and Ag nanowires towards RhB degradation under visible-light irradiation[42]: necklace-like Ag nanowire/Ag_3PO_4 cube heterostructures (purple line, Figure 2.19 F), core-shell Ag/Ag_3PO_4 coaxial hetero-nanowires (yellow green line, Figure 2.19 G), pure Ag_3PO_4 cubes (green line), Ag/Ag_3PO_4 heterostructure prepared in 0.1 M $[Ag(NH_3)_2]^+$ complex aqueous solution (blue line), Ag/Ag_3PO_4 heterostructure prepared in 0.05 M $[Ag(NH_3)_2]^+$ complex aqueous solution (red line), and pure Ag nanowire (black line). The images in the insets in (A), (C), and (F) are at higher magnification.

2.4.2 Surface-Enhanced Raman Scattering (SERS)

Surface-enhanced Raman scattering (SERS) is a phenomenon that the weak Raman signals of molecules are significantly enhanced when they are adsorbed on the surfaces of nanostructures of plasmonic metals, such as Ag, Au, and Cu.[2,200-203] Up to the present, the SERS mechanism has been generally described in terms of two mechanisms, electromagnetic field enhancement and chemical enhancement.[2,203] The strong local electric field of plasmonic metal nanostructure makes metal/semiconductor hybrids, such as Au/ZnO,[48] Ag/ZnO,[44,46,47,204] Au/TiO_2,[45] Ag/TiO_2,[205,206] Ag/Fe_2O_3,[51] Ag/Cu_2O,[49] and Ag/CuO,[50] become promising SERS substrate candidates. For instance, ZnO nanorod arrays decorated with Ag NPs and TiO_2 nanorod arrays decorated with Au NPs have been employed as SERS substrates.[44,45]

Figure 2.20A showed the SERS results for 4-aminothiophenol (PATP) with concentration of 10^{-3} M adsorbed on Ag-ZnO heterogeneous nanorod arrays (HNRs) with different densities of Ag NPs attached on ZnO nanorod arrays over zinc foil. It was found that the Raman intensity of PATP adsorbed on the Ag-ZnO HNRs with a few 1-20 nm Ag NPs is very weak. The SERS spectra of PATP are clearly observed when the ZnO nanorods are covered with the 20-50 nm aggregated Ag NPs, which could be due to the greatly increased electric field resulting from the SPR effect of surface Ag NPs. The SERS intensity of PATP became significantly weaker, however, when much larger Ag particles were deposited on ZnO nanorods.[44] The results showed that the enhancement factor of PATP adsorbed on Ag-ZnO HNRs was about 10^6.[44] Figure 2.20B showed the SERS spectra of Rhodamine 6G (R6G) adsorbed on TiO_2 and Au/TiO_2 nanorod array substrates. Compared with the TiO_2 nanorod array, the characteristic Raman peaks of R6G with various concentrations on Au/TiO_2 nanorod array substrate were clearly observed, indicating that the electromagnetic effect from SPR of the Au NPs contributes to the amplified Raman signals.[45]

Besides the above mentioned semiconductor nanorod arrays decorated with plasmonic metal nanostructures, other different nanostructured hybrids have been fabricated for SERS detection. Ag/ZnO nanohybrids constructed with Ag NPs inside or deposited on the top of hollow ZnO nanospheres, and Au NPs/ZnO assemblies have been prepared as SERS substrates.[46-48] Figure 2.20C displayed the Raman spectra of R6G on various ZnO/Ag structures. Among all the structures, the hollow ZnO nanospheres decorated with Ag NPs exhibited the highest SERS intensity, while the ZnO film showed the lowest Raman scattering intensity. [46] This enhancement may result from SPR effect of an individual Ag NP and the strong plasmon coupling effect within two touching Ag NPs on the ZnO hollow nanospheres, which further enhanced the SPR effect.[46]

Furthermore, the intensity of SERS spectrum on the Ag NPs inside ZnO hollow nanospheres is comparable to that on Ag NPs capping tops of the ZnO hollow nanospheres, although the existence of a ZnO isolated layer outside with 20 nm (Figure 2.20D).[47] Distinguishable Raman signals could still be detected when the R6G concentration was reduced down to 10^{-8} M. No Raman signal can be observed, however, on pure hollow ZnO nanospheres, even if the concentration of R6G is increased to 10^{-4} M.[47] Figure 2.20E also shows the SERS spectra of PATP adsorbed on an Au/ZnO assembly, an Au NP monolayer, and ZnO substrate.[48] Although the Raman signal of PATP is not detected on the pure ZnO, the SERS spectrum intensity of PATP adsorbed on the Au/ZnO is significantly stronger than that on pure Au NP monolayer. Such great Raman enhancement must have arisen from the presence of ZnO, which transmits the electrons and augments the charge transfer to PATP molecules from Au NPs.[48]

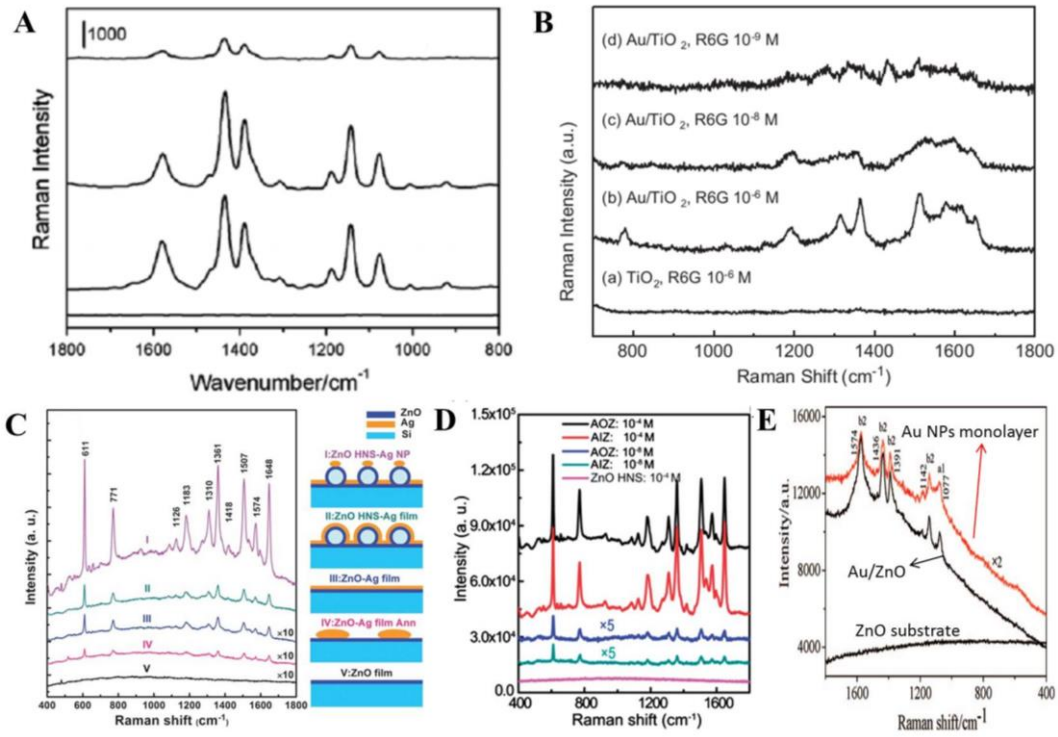

Figure 2.20 (A) SERS spectra of PATP (10^{-3} M) adsorbed on the surface of Ag-ZnO nanostructures (bottom spectrum: a few 1-20 nm Ag NPs, middle spectrum: aggregated 20-50 nm Ag NPs, top spectrum: much more large Ag particles);[44] (B) SERS spectra obtained from TiO_2 and Au/TiO_2 with various concentrations of R6G;[45] (C) SERS spectra of R6G on Ag/ZnO composites with different nanostructures (from bottom to top): (V) ZnO film on Si substrate; (IV) aggregated Ag NPs/ZnO film structure; (III) Ag/ZnO films on Si substrate; (II) Ag wavy film/ZnO HNS; (I) Ag NPs/ZnO hollow nanosphere (HNS);[46] (D) Raman spectra of R6G (10^{-4} and 10^{-8} M) on AOZ and AIZ arrays in comparision to that on pure ZnO HNS at concentration of 10^{-4} M (AOZ, AIZ, and HNS refer to Ag NPs on the top of ZnO hollow nanospheres, Ag NPs inside the ZnO hollow nanospheres, and the pure hollow nanospheres, respectively);[47] (E) SERS spectra of PATP adsorbed on an Au/ZnO assembly, an Au NP monolayer, and ZnO substrate.[48]

In addition to the commonly investigated metal oxides such as TiO_2 and ZnO, hybrids composed of plasmonic metal nanostructures and other metal oxides such as Cu_2O/Ag, CuO/Ag, and Fe_2O_3@Ag also have been fabricated for SERS application.[49-51] Figure 2.21A presents the SERS spectra of 10^{-6} mol L^{-1} RhB on bare branched Cu_2O crystals and Ag/Cu_2O collected at different reaction stages. All the Ag/Cu_2O structures obtained at different times show high Raman signals, with the sample obtained at 30 s showing the highest intensity, while the bare branched Cu_2O crystals showed very limited SERS activity. The enhancement could have resulted from the proper sizes of Ag nanoparticles and the close packed structure, providing more SERS hot spots at the interstitial sites.[49] As shown in Figure 2.21B, the Raman spectra of 4-mercaptopyridine (4-Mpy) on 5 nm Ag/CuO is enhanced than that on the pure 5 nm Ag film, due to the SPR of Ag and the charge transfer between Ag and CuO NPs.[50] The SERS signal is also highly influenced by the LSPR and excitation laser wavelength. The SERS spectra of thiophenol on Fe_2O_3@Ag nanostructures with uniform Ag nanoparticles aggregated on the Fe_2O_3 surface have been investigated under three excitation wavelengths, as shown in Figure 2.21C.[51] It can be observed that the largest enhancement will be obtained when the excitation wavelength is very close to the plasmon resonance of the substrate. The average SERS enhancement factors of such Fe_2O_3@Ag nanostructures are estimated to be approximately 10^6-10^7 with the three different laser excitations.[51]

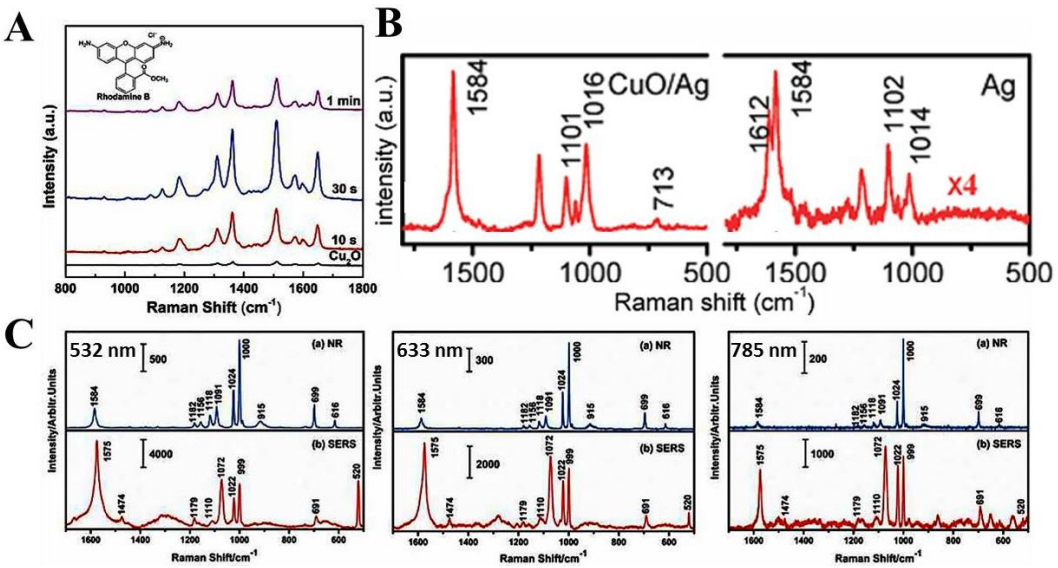

Figure 2.21 (A) SERS spectra of 10^{-6} M rhodamine B (RhB, structure shown in inset) on bare branched Cu_2O crystals and Ag/Cu_2O collected from galvanic replacement at different reaction stages;[49] (B) Raman spectra of 4-mercaptopyridine adsorbed on pure Ag films (the thicknee is 5 nm) and Ag/CuO;[50] (C) SERS spectra of thiophenol (10^{-5} M) adsorbed on Fe_2O_3@Ag and normal Raman spectra of neat thiophenol under different laser excitations (532, 633, and 785 nm).[51]

Chapter 3 Experimental Methods

The syntheses, X-ray diffraction (XRD), ultraviolet-visible (UV-vis) absorption spectroscopy, energy-dispersive X-ray (EDX) spectroscopy, scanning electron microscopy (SEM), and EDX elemental mapping conducted on SEM, Brunauer–Emmett–Teller (BET) specific surface area measurements, Raman spectroscopy, and photocatalytic testing in this thesis were performed by the author herself. The (high resolution) transmission electron microscopy (TEM, HRTEM), selected area electron diffraction patterns (SAED), high-angle annular dark-field (HAADF) scanning TEM, EDX spectroscopy, and EDX elemental mapping conducted on TEM were carried out by Dr. David R. G. Mitchell and Dr. Gilberto Casillas-Garcia at the UOW Electron Microscopy Centre (EMC), and Mr. Chao Han. X-ray photoelectron spectroscopy (XPS) was performed by Dr. Dongqi Shi. Battery performance measurements were carried out by Ms. Weijie Li. Hydrogen production testing was carried out by Mr. Xulei Du.

3.1 Chemicals and equipments for synthesis

3.1.1 Chemicals

Silver nitrate ($AgNO_3$), hydrazine solution (35 wt % in H_2O), sodium chloride (NaCl), polyvinylpyrrolidone (PVP40), zinc nitrate hexahydrate ($Zn(NO_3)_2 \cdot 6H_2O$), sulphur powder, Methylene blue (MB), Methyl orange (MO), Rhodamine B (RhB), triethanolamine (TEOA), p-benzoquinone (PBQ), cadmium nitrate tetrahydrate ($Cd(NO_3)_2 \cdot 4H_2O$), ammonium hydroxide solution (28%-30% NH_3 basis), and thiourea were purchased from Sigma-Aldrich. Copper(II) nitrate 3-hydrate ($Cu(NO_3)_2 \cdot 3H_2O$) was purchased from BDH laboratory supplies. Ethylene glycol (EG), 1,2-propanediol, and sodium hydroxide (NaOH) were purchased from Alfa Aesar. Carbon tetrachloride (CCl_4) was purchased from Mallinckrodt Pharmaceuticals. Ethanol and isopropanol (IPA) were purchased from Ajax Finechem. All of the chemicals were analytical grade and used directly without further purification. Deionized water was used in all experiments.

3.1.2 Equipments

Figure 3.1 displays the main synthesis set-up and equipment for the synthesis of 1D Ag nanowires (NWs) and Ag NW-based nanohybrids. As shown in Figure 3.1A, the oil bath set-up is composed of a magnetic stirring hot plate with a thermal detector, an oil and water bath, and a flask containing the reagents and solvent. The sonicator in Figure 3.1B was used to obtain homogeneous reaction systems. When the reaction was finished and cooled down to room temperature, the products were collected using a centrifuge (shown in Figure 3.1C). Figure 3.1D shows an oven which was used to dry the samples.

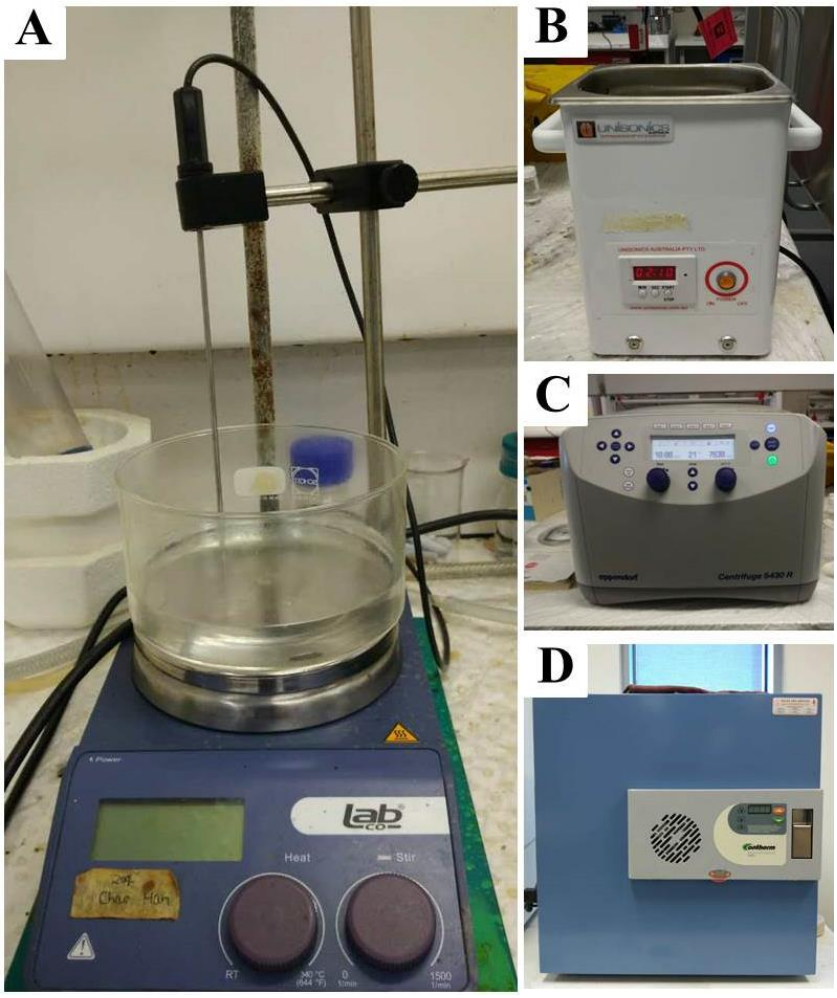

Figure 3.1 Synthesis equipment for Ag nanowires and Ag-based nanohybrids: (A) oil/water bath set-up, (B) sonicator, (C) centrifuge, and (D) oven.

3.2 Sample synthesis

In this doctoral work, all the materials were prepared in the liquid phase. All the experimental details are provided in the following chapters.

3.2.1 Synthesis of Ag NWs

In this thesis, Ag NWs were prepared by a polyol reduction process from a silver precursor, a reducing agent, a stabilizer, and a trace amount of oxidative etchant under appropriate reaction conditions.[1] In this thesis, $AgNO_3$ was chose as precursor, ethylene glycol (EG) or 1,2-propanediol as both a solvent and a reductant, the surfactant PVP as a stabilizer, and NaCl to supply Cl^- as coordination ligand. Upon the injection of $AgNO_3$ into a pre-heated polyol in the presence of PVP and a trace amount of NaCl, the solvent polyol could reduce the Ag^+ ions at an elevated temperature, leading to the nucleation and growth of 1D Ag nanowires. [1,70,71,113,207]

3.2.2 Synthesis of Ag@ZnO, Ag@Cu_2O, Ag@CdS, and 1D/2D Ag-Ag_2S NWs

In this thesis, Ag@ZnO, Ag@Cu_2O, Ag@CdS, and 1D/2D Ag-Ag_2S NWs were prepared by an extremely simple and low-cost wet-chemical deposition route, which was introduced in Chapter 2. [95,107] In this doctoral work, pre-made Ag NW solutions were mixed with Zn, Cu, Cd, or S precursors and other reagents in different concentrations and amounts under constant magnetic stirring for different times at room temperature or proper temperatures to produce Ag NW-based hybrid nanostructures with different morphologies.[70,71,207]

3.3 Characterization techniques

3.3.1 X-ray diffraction (XRD)

Powder X-ray diffraction is an effective technique most commonly used for the identification of unknown crystalline inorganic materials. It can identify the

composition, purity, and crystal phase, as well as yielding information on the average particle size, when the XRD patterns are compared to standard reference patterns of such compounds. The XRD measurements in this doctoral work were performed on a GBC MMA X-ray diffractometer using Cu Kα1 radiation (40 kV). The powder product was well-pressed, placed on the sample holder, and the XRD patterns were recorded from 20 ° to 80 ° with a scanning rate of 4 °/min or 2 °/min, and voltage and current settings of 40 kV and 25 mA, respectively.

3.3.2 Scanning electron microscopy (SEM) and energy-dispersive X-ray spectroscopy (EDS/EDX)

The scanning electron microscope (SEM) is a type of electron microscope which can be used for scanning over samples. By scanning a sample with a focused beam of electrons, the electrons interact with atoms in the sample, and then generate various signals. These can be detected and also contain very useful information about the surface topography and the composition of the sample. In general, data are collected over a selected area of the surface of the sample and thus produce a two-dimensional image.

In addition, energy-dispersive X-ray spectra (EDS/EDX) and EDX mappings can also be collected on SEM, which could further provide qualitative and quantitative information, as well as information on the spatial distribution of elements and the chemical composition. In this doctoral work, the samples were simply dispersed on conductive carbon tape, which was pasted on the sample holder used to collect SEM images, and SEM images were collected using a field-emission scanning electron microscope (JSM-7500FA, JEOL) operated at an accelerating voltage and current of 5 kV and 10 μA, respectively. The corresponding EDX spectra and EDX mappings were collected on an SEM operating at an acceleration voltage and current of 15 kV and 20 μA, respectively.

3.3.3 Transmission electron microscopy (TEM)

Transmission electron microscopy (TEM) is a microscopy technique with significantly high resolution that utilizes energetic electrons to provide information on the morphology of the sample. High-resolution transmission electron microscopy (HRTEM) and its corresponding selected area electron diffraction (SAED), energy dispersive X-ray (EDX) spectroscopy, and EDX mapping can provide further crystallographic and compositional information on samples. During operation, a beam of electrons is transmitted through an ultra-thin specimen made by depositing a dilute sample solution on a copper gird, so that the electron beam interacts with the specimen as it passes through. In this thesis, TEM images, HRTEM images, high-angle annular dark-field (HAADF) images, SAED patterns, and EDX spectra and EDX mapping on TEM were collected on two field-emission transmission electron microscopes (JEM-2011, JEOL and ARM-200F, JEOL) at an accelerating voltage of 200 kV.

3.3.4 Ultraviolet/visible (UV/vis) absorption spectroscopy

Ultraviolet-visible (UV-vis) spectroscopy is commonly used for analyzing the optical properties of different materials. UV-vis spectroscopy performed in liquid is an absorption spectroscopy technique in the ultraviolet-visible-near-infrared spectral region, with the signal coming from excited electrons in molecules absorbing different wavelengths of light. In this thesis, ultraviolet/visible (UV/vis) absorption spectra were collected at room temperature on a UV-3600 (Shimadzu) spectrometer.

3.3.5 X-ray photoelectron spectroscopy (XPS)

X-ray photoelectron spectroscopy (XPS) is a surface chemical analysis and surface-sensitive quantitative spectroscopic technique that quantifies the chemical and electronic states of the elements within the first few atomic layers of a surface. In this doctoral work, X-ray photoelectron spectroscopy (XPS) was performed on a VG

Scientific ESCALAB 2201XL photoelectron spectrometer with Al Kα X-rays as the excitation source to analyze the samples' elemental composition.

3.3.6 Brunauer–Emmett–Teller (BET) analysis

BET analysis can be used to measure specific surface areas, pore volumes, and pore size distributions by employing the physical adsorption of gas molecules on a solid surface. In this doctoral work, the BET specific surface areas of the samples were analyzed by a Quantachrome NOVA 1000. All the samples were degassed at 150 ℃ before nitrogen adsorption measurements.

3.4 Photocatalytic measurements

3.4.1 Photodegradation of organic dyes [70,71,207]

Figure 3.2A shows the set-up used for organic dye photodegradation in this thesis. The photodegradation of organic dyes was evaluated under a LSC-100 Solar Simulator with an air mass (AM) 1.5G filter (Newport) at room temperature. In a typical experiment, prior to irradiation, a photocatalyst was added into an organic dye solution at room temperature under stirring in the dark to ensure the establishment of an adsorption-desorption equilibrium between the photocatalyst and the organic dye. Then, the solution was exposed to solar light irradiation under magnetic stirring, and the suspension was collected and then centrifuged to remove the photocatalyst after each irradiation time interval. The concentrations of organic dyes were analysed by a Shimadzu UV-3600 spectrophotometer, and their characteristic absorptions were used to evaluate their photocatalytic degradation.

3.4.2 Hydrogen evolution

Figure 3.2B shows the setup used for the hydrogen evolution in this thesis. The hydrogen evolution reaction over the as-synthesized photocatalyst was performed in a

glass gas-closed-circulation system with a top irradiation-type reaction vessel (LabSolar H_2). A 300-W Xenon lamp (Perfect, China) with a 420 nm cut-off filter ($\lambda \geq 420$ nm) was used as the visible-light source. The temperature of the reactant solution was maintained at 20℃ by a flow of cooling water during the test. In a typical experiment, 30 mg of photocatalyst was added into 50 mL of aqueous solution containing 0.25 M Na_2SO_3 and 0.35 M Na_2S as sacrificial reagents. Prior to the hydrogen evolution reaction, the system was evacuated by a pump, and the solution was stirred for 30 min to remove the dissolved air in the water. The amount of hydrogen gas was automatically analyzed by an on-line gas chromatograph (GC-2014C) with a thermal conductivity detector (TCD) and 5A molecular sieve capillary column.

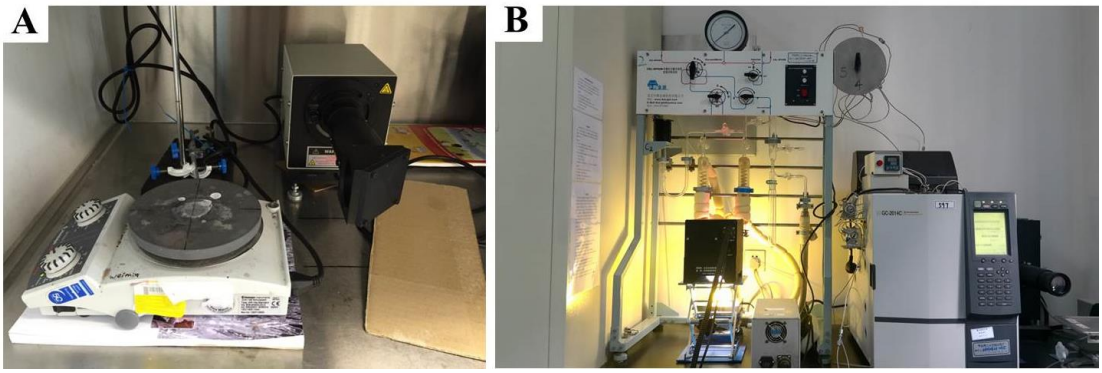

Figure 3.2 Set-ups for (A) photodegradation of organic dyes and (B) hydrogen evolution.

3.5 Battery performance measurements [207]

The electrode slurry for lithium/sodium ion batteries was prepared by mixing the active powder material, carbon black, and a binder. The slurry was pasted on copper foil, followed by drying in a vacuum oven overnight at 80 ℃ and pressing at a pressure of 30 MPa to enhance the contact between the mixture and the copper foil. For the lithium ion battery testing, lithium foil was employed as both reference and counter electrode. The electrolyte was 1 M $LiPF_6$ in an ethylene carbonate (EC)/ diethyl carbonate (DEC) solution (1:1 v/v). For the sodium ion battery testing, sodium foil was employed as both

reference and counter electrode. The electrolyte was 1 M $NaClO_4$ in an EC/DEC solution (1:1 v/v). The cells were assembled in an argon-filled glove box, and their electrochemical performance was tested with a Land Test System.

3.6 SERS measurement [207]

A mixture of test material and organic dye solution was ultrasonically dispersed and shaken in the dark at room temperature. Then, the dispersion was dropped onto a glass slide for the SERS measurement. In this thesis, all SERS spectra were collected on a JY HR 800 Raman spectrometer under excitation of 632 nm with a power of 13.5 mW.

Chapter 4 Ambient controlled synthesis of advanced core-shell plasmonic Ag@ZnO photocatalysts

The contents of this chapter were published in CrystEngComm, 2016, 18, 1713-1722.[71]

4.1 Introduction

Semiconductor-based heterogeneous photocatalysis, which allows direct conversion of solar energy into chemical energy via a renewable route, could be one of the most viable long-term solutions, with the potential to address the issues of energy shortages and environmental pollution.[15,208,209] During the past several decades, construction of heterostructures by combining semiconductors with noble metals has attracted increasing interest due to its very high effectiveness in improving the photocatalytic activity, arising from the combined properties and synergistic interactions of the metallic and semiconducting components.[97,210] As one of the most extensively studied semiconductor photocatalysts, zinc oxide (ZnO) has certain advantages, such as high photocatalytic activity, abundant natural resources, non-toxicity, and low cost, as well as physical and chemical stability.[19,21,211-214] The inherent limitations of the high rate of electron-hole recombination and very low response in the visible range, however, lead to reduced photocatalytic efficiency and inefficient utilization of sunlight.[21,92,93,210,215]

To enhance the photocatalytic performance with improved light harvesting efficiency and to prolong the life of photogenerated carriers, modifications in ZnO have been explored through its composition with novel plasmonic metals.[216-222] In particular, considerable attention has been paid to the controlled fabrication of heterostructured photocatalysts composed of ZnO and noble metals, such as composites of ZnO hierarchical nanostructures decorated with various noble metals,[223-229] mesoporous Ag-ZnO nanocomposites,[93] nanoparticulate Ag-ZnO hybrids,[230] rod-like Ag-ZnO nanocomposite,[18,216] core-shell Au-ZnO nanoparticles,[21,231] and hollow Pt-ZnO core-shell nanocomposite.[19]

Compared with other noble metals, Ag is more attractive because of its high electrical and thermal conductivity, antibacterial characteristics, low cost, and nontoxicity. Ag nanostructures exhibit a wealth of optical and photoelectrochemical properties directly related to their geometry-dependent surface plasmon resonances, which makes it very popular for fabrication of advanced semiconductor/noble metal nanophotocatalysts.[70,207,232] For most ZnO/Ag nanophotocatalysts, Ag nanoparticles were decorated on the ZnO surface, and reports on a core-shell structure with an Ag core were rather scarce, although the configuration of Ag@ZnO can eliminate possible disadvantages by the shielding effect on Ag nanoparticles (e.g. decrease in photocatalytic active surfaces and obstruction of the exciting light).[231] Moreover, these Ag core@ZnO shell structures have a controllable chemical composition and chemical stability, and are able to electrically insulate the metal nanoparticles from the reactants and the surrounding medium.[19,21]

Among the reported syntheses, Ag@ZnO core-shell nanoparticles prepared in N,N-dimethylformamide showed higher activity towards degradation of 9-phenyl-2,3,7-trihidroxy-6-fluorone (PF) as compared to pure ZnO under ultraviolet (UV) excitation.[233] Subsequently, hierarchical hetero-assemblies made of interwoven Ag core nanowires covered by ZnO branched nanorods were fabricated via a solution bottom-up strategy, and they also exhibited enhanced photocatalytic properties under UV light irradiation.[234] Liu and co-workers synthesized worm-like Ag-ZnO core−shell heterostructured composites with the assistance of ultrasonic irradiation, and the heterostructures also showed improved photocatalytic activity towards degradation of Rhodamine B (RhB) compared to pure ZnO particles.[37] Nevertheless, the synthesis of these Ag-ZnO core-shell heterostructures involved the use of heating, ultrasonication, toxic solvents, or complicated processes. In addition, the resultant Ag-ZnO heterostructure only showed enhanced photocatalytic activity under irradiation with UV light, which accounts for only 4% of the incoming solar light on the earth, while the largest proportion of solar light (i.e. visible light) was not efficiently utilized. It remains

a great challenge to develop facile and rational strategies for ambient and controllable fabrication of Ag-ZnO core-shell hybrid nanostructures, which have optimal composition and structure, and exhibit excellent photocatalytic activity under excitation with solar light.

In this chapter, a rapid and simple ambient strategy is reported for controllable synthesis of Ag-ZnO core-shell heterostructures with excellent photocatalytic performance under solar excitation. By fine-tuning the amount of water in the reaction mixture, ZnO shells with different sizes and morphologies coating the Ag cores are easily tailored. The impact of the ZnO morphology, the Ag/ZnO molar ratio, and the Ag core on the photocatalytic property of Ag@ZnO heterostructures has been optimized and discussed. The unique one-dimensional (1D) Ag@ZnO hetero-nanowires prepared from 0.6 M $Zn(NO_3)_2$ $6H_2O$ and 14.5 mL H_2O exhibited the highest photocatalytic activity towards degradation of Rhodamine B under solar light irradiation compared to pure ZnO and Ag@ZnO nanoparticles. The enhanced photocatalytic performance of Ag@ZnO hetero-nanowires is attributed to their unique morphology for efficient separation of electron-hole pairs.

4.2 Experimental section

4.2.1 Experimental Methods

Ag nanowires (Ag NWs) were fabricated by a modified polyol process.[70,207] In a typical synthesis, 10 mL 1,2-propanediol containing PVP40 was loaded into a 25-mL vial and heated with magnetic stirring in an oil bath at 135 ℃ for 1 h. NaCl was then quickly added, and the stirring was continued for another 5 min, followed by addition of 7 mL of 0.1 M $AgNO_3$ solution. The mixed solution was then heated at 135 ℃ with magnetic stirring for 1 h, yielding the grey Ag NWs.

Ag nanoparticles (Ag NPs) were prepared by a similar procedure without NaCl.

Core-shell Ag@ZnO hetero-nanowires were synthesized by a simple solution process. Typically, 1 mL of 0.6 M $Zn(NO_3)_2 \cdot 6H_2O$ solution and 14.5 mL Milli-Q water were added into 8 mL freshly prepared Ag NW solution under constant magnetic stirring for 30 min. Then, 0.5 mL of 4.8 M NaOH solution was added into the reaction mixture. The reaction mixture was stirred for 1 h, and then the resultant Ag@ZnO core-shell nanowires were separated by centrifugation, washed with Milli-Q water and absolute ethanol to remove impurities, and then dried at 60 ℃ (**A1**). Other samples (**A2**−**A14**) were also prepared under the identical conditions by varying the volume of water and concentration of $Zn(NO_3)_2 \cdot 6H_2O$. The detailed experimental parameters are listed in Table 4.1.

Core-shell Ag@ZnO hetero-nanoparticles were prepared using a similar approach to that for Ag@ZnO core-shell hetero-nanowires, except that 8 mL of Ag NP solution was added rather than Ag NW solution.

Pure ZnO nanostructures were prepared using a similar procedure to that for Ag@ZnO core-shell hetero-nanowires, except that 1,2-propanediol was added rather than the Ag NW solution.

Table 4.1 Experimental conditions for the synthesis of Ag@ZnO samples.

Sample	Ag[a]	$Zn(NO_3)_2$ $6H_2O$[b]	NaOH[c]	H_2O
A1	NWs	0.6 M	0.5 mL	14.5 mL
A2	NWs	0.6 M	0.5 mL	1.167 mL
A3	NWs	0.6 M	0.5 mL	2.5 mL
A4	NWs	0.6 M	0.5 mL	6.5 mL
A5	NWs	0.6 M	0.5 mL	22.5 mL
A6	NWs	0.3 M	0.25 mL	14.75 mL
A7	NWs	1.2 M	1 mL	14 mL
A8	NPs	0.6 M	0.5 mL	1.167 mL
A9	NPs	0.6 M	0.5 mL	2.5 mL
A10	NPs	0.6 M	0.5 mL	6.5 mL
A11	NPs	0.6 M	0.5 mL	14.5 mL
A12	NPs	0.6 M	0.5 mL	22.5 mL
A13	NPs	0.3 M	0.25 mL	14.75 mL
A14	NPs	1.2 M	1 mL	14 mL

Note: [a] The volume of silver nanowires or nanoparticles was 8 mL, [b] The volume of $Zn(NO_3)_2 \cdot 6H_2O$ solution was 1 mL, [c] The concentration of NaOH was 4.8 M.

4.2.2 Characterization

The X-ray diffraction (XRD) measurements were performed on a GBC MMA X-ray diffractometer using Cu $K\alpha_1$ radiation (40 kV). The XRD patterns were recorded from 20 ° to 80 ° with a scanning rate of 4 °/min. Scanning electron microscope (SEM) images were collected using a field-emission scanning electron microscope (JSM-7500FA,

JEOL) operated at an accelerating voltage of 5 kV. Transmission electron microscope (TEM) images were recorded on a field-emission transmission electron microscope (JEM-2011, JEOL), using an accelerating voltage of 200 kV. Ultraviolet/visible (UV/vis) absorption spectra were collected at room temperature on a UV-3600 (Shimadzu) spectrometer. X-ray photoelectron spectroscopy (XPS) was performed on a VG Scientific ESCALAB 2201XL photoelectron spectrometer with Al Kα X-rays as the excitation source to analyse the samples' elemental composition. Analysis of the XPS data was carried out using the commercial CasaXPS 2.3.15 software package.

4.2.3 Photocatalytic test

Photocatalytic activity of the as-synthesized Ag@ZnO core-shell hybrids was evaluated by the degradation of RhB under irradiation with a LSC-100 Solar Simulator with an AM1.5G filter (Newport). In an experiment, 20 mg photocatalyst was added into 50 mL of 10^{-5} M RhB solution at room temperature. Prior to irradiation, the suspension was stirred in the dark to ensure the establishment of an adsorption-desorption equilibrium between the photocatalyst and the RhB. Then, the solution was exposed to solar light irradiation under magnetic stirring. At each irradiation time interval, 2 mL of the suspension was collected and then centrifuged to remove the photocatalyst. The concentration of RhB was analysed by a Shimadzu UV-3600 spectrophotometer, and the characteristic absorption of RhB at 554 nm was used to evaluate its photocatalytic degradation. All of the measurements were carried out at room temperature.

4.3 Results and discussion

The X-ray diffraction (XRD) pattern and typical scanning electron microscopy (SEM) images of pure Ag NWs for A1 are given in Figure 4.1. Figure 4.1A shows the XRD pattern of the as-synthesized Ag NWs applied for the subsequent heterogrowth of ZnO nanoshells to form Ag@ZnO core-shell nanowires. All diffraction peaks match well with that of standard Ag pattern (JCPDS No. 4-783), indicating the high purity of Ag

NWs. Figure 4.1B and 4.1C show typical SEM images of the as-prepared Ag NWs. It can be clearly seen that as-synthesized Ag NWs possess relatively smooth surface, and have an average diameter of about 100 nm and a length of several micrometers.

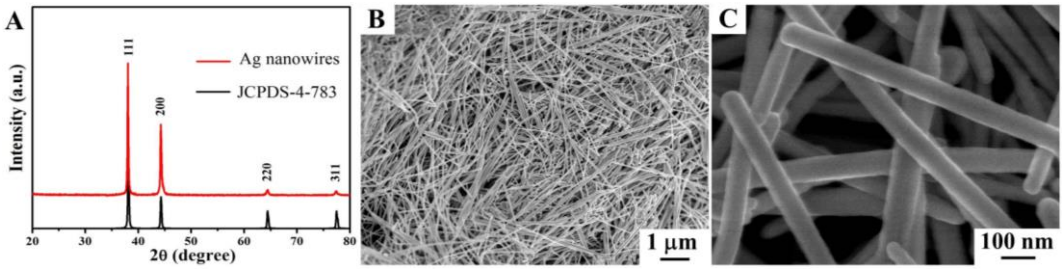

Figure 4.1 (A) XRD pattern and (B and C) SEM images of as-synthesized Ag NWs.

Figure 4.2(A) shows a typical scanning electron microscope (SEM) image of the Ag@ZnO core-shell hetero-nanowires (**A1**), clearly demonstrating that the surface of the Ag@ZnO core-shell hetero-nanowires is not as smooth as that of the Ag NWs, due to the coating of densely packed ZnO nanoparticles. The enlarged SEM image [Figure 4.2(B)] reveals that many ZnO nanoparticles have densely grown on the surfaces of the Ag nanowires. TEM and high resolution TEM (HRTEM) were used to further characterize the Ag@ZnO core-shell hetero-nanowires [Figure 4.2(C and D)]. Figure 4.2(C) clearly shows an individual Ag@ZnO hetero-nanowire with a rough surface, which consists of an 83-nm Ag core and a ZnO shell. The interface between the Ag nanowire and ZnO nanoparticles is also clearly observed. The HRTEM image in Figure 4.2(D) shows lattice fringes of 0.282 nm, which corresponds to ZnO (100).

Furthermore, the distribution of elements in the Ag@ZnO core-shell hetero-nanowires was studied with energy-dispersive X-ray (EDX) elemental mapping [Figure 4.2(E)]. The left image in Figure 4.2(E) is the area where the elemental mapping was performed. The green, blue, and red colors represent the distributions of silver, zinc, and oxygen, respectively. The presence of the three elements in the nanowires is in agreement with the proposed Ag@ZnO composition. The spatial distribution of the colors verifies the

core-shell structure, where the element Ag is located in the core and the elements Zn and O of ZnO are homogenously distributed throughout the whole NW, showing that the Ag NW core is surrounded with a uniform ZnO shell.

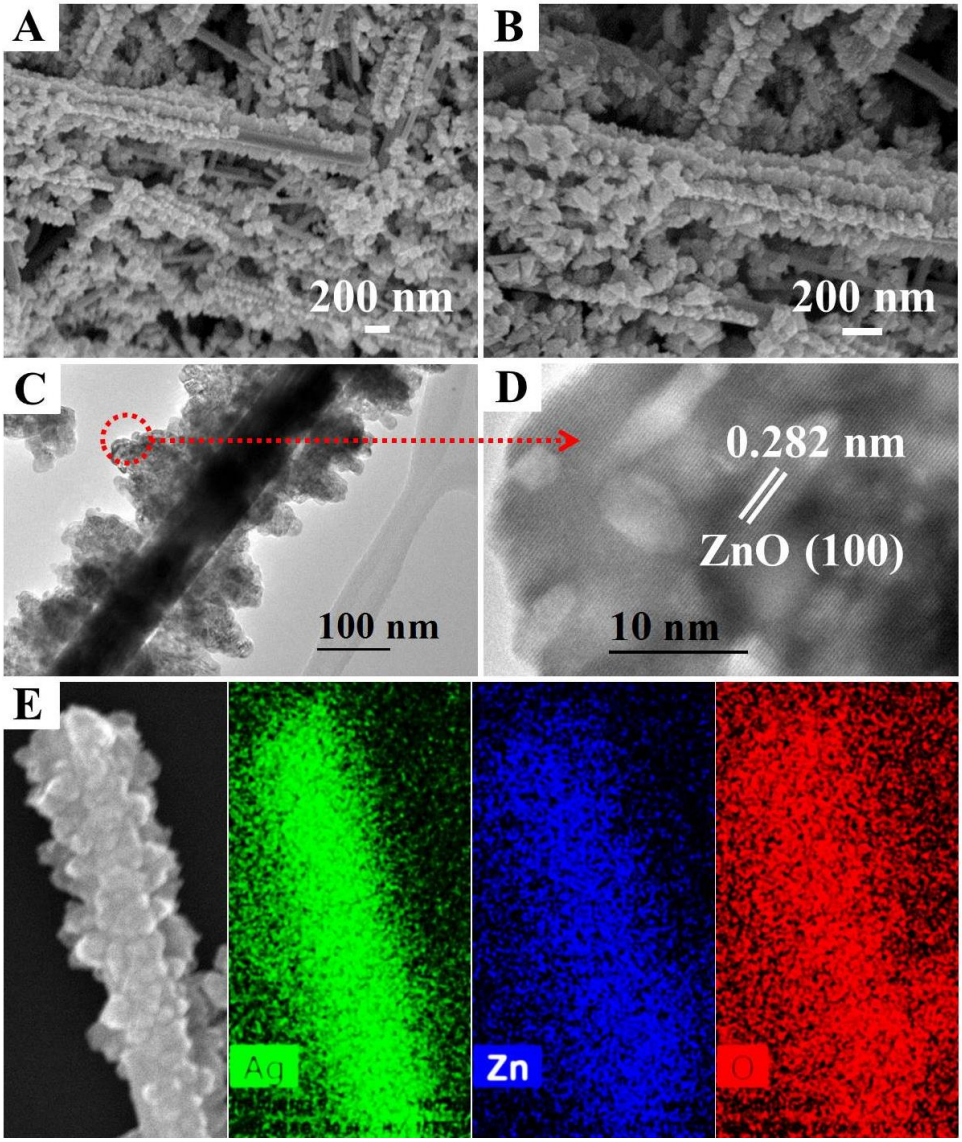

Figure 4.2 (A and B) SEM images of the as-prepared Ag@ZnO core-shell hetero-nanowires (**A1**). (C) TEM image and (D) HRTEM image of an individual Ag@ZnO core-shell hetero-nanowire. (E) EDX elemental mapping analysis of the Ag@ZnO core-shell hetero-nanowires.

The crystalline structure and optical properties of the as-prepared Ag@ZnO core-shell hetero-nanowires (**A1**) are shown in Figure 4.3. The X-ray diffraction (XRD) pattern is compared with standard patterns of Ag (JCPDS 4-783) and ZnO (JCPDS 5-667) in Figure 4.3(A), where every peak can be indexed to Ag or ZnO, supporting the formation of Ag@ZnO core-shell hetero-nanowires. The absence of other impurity peaks indicates the high purity of the core-shell Ag@ZnO hetero-nanowires fabricated by this simple solution process. In addition, the peaks of ZnO are characteristic of a hexagonal structure with a lattice constant a = 3.25 Å. Its relatively weak peaks indicate the low crystallinity of the ZnO shell compared to the Ag core.

Ag NWs show intense surface plasmon resonance (SPR) absorption in the visible region, which is highly sensitive to their diameter and length-to-diameter ratio, as well as the optical and electronic properties of their surroundings.[11,235-237] The ultraviolet-visible (UV-vis) absorption spectra of pure ZnO nanoflowers, pure Ag NWs, and Ag@ZnO core-shell hetero-nanowires (**A1**) in ethanol are presented in Figure 4.3(B). ZnO nanoflowers exhibit a UV absorption band at ~380 nm. The pure Ag NWs exhibit two absorbance peaks at 350 and 385 nm. The peak at 350 nm could be attributed to the longitudinal mode of the nanowires, similar to that of bulk Ag[238-240] or the out-of-plane quadrupole resonance of Ag NWs.[241-243] The peak at 385 nm is assigned to the transverse plasmon resonance of Ag NWs.[238-240] Upon the formation of the ZnO shell, the surface plasmon band of the Ag@ZnO core−shell nanowires is distinctly broadened and shows a red-shift compared to that of pure Ag NWs, probably due to a strong interfacial electronic coupling between neighboring ZnO particles and Ag NWs.[37,244,245] The electron transfer from Ag to ZnO in the Ag@ZnO core−shell nanowires is due to the higher Fermi energy level of Ag than ZnO. This transfer results in deficiency of electrons on the surface of the Ag nanowires, leading to the red-shift in the surface plasmon absorption.[37,246] Similar results for ZnO−Au composites[247] and worm-like Ag/ZnO core−shell heterostructural composites[37] have been reported elsewhere. Their broad absorbance in the UV to visible window clearly demonstrates that our Ag@ZnO

nanowires become photoactive in both the UV and the visible light region, which is crucial for full use of sunlight.

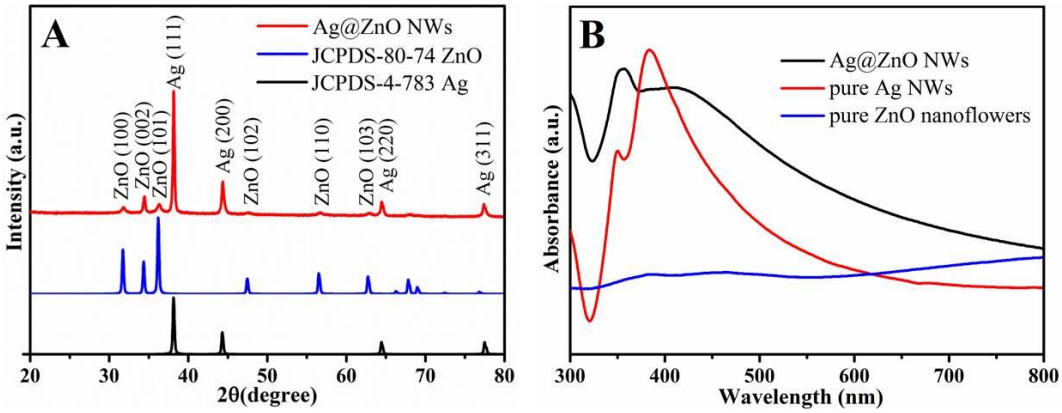

Figure 4.3 (A) XRD patterns and (B) UV-vis absorption spectra of as-prepared 1D Ag@ZnO core-shell hetero-nanowires (**A1**), pure Ag NWs, and pure ZnO nanoflowers in ethanol.

X-ray photoelectron spectroscopy (XPS) measurements were carried out to investigate the surface elemental composition and electronic states of Ag@ZnO core-shell hetero-nanowires (**A1**), as shown in Figure 4.4. The survey spectrum in Figure 4.4(A) shows the absence of other elements apart from C, Zn, O, and Ag, indicating the high purity of the product, which is consistent with the above XRD and EDX results. High-resolution spectra of Ag, Zn, and O species are shown in Figure 4.4(B-D), respectively. The two peaks centred at 367.2 and 373.2 eV are attributed to Ag $3d_{5/2}$ and Ag $3d_{3/2}$, respectively, which are shifted remarkably to lower binding energies compared with those of bulk Ag (Ag $3d_{5/2}$, 368.2 eV; Ag $3d_{3/2}$, 374.2 eV).[129,211] This result is similar to those obtained from worm-like Ag/ZnO core–shell heterostructured composites,[37] dendrite-like ZnO@Ag heterostructures,[129] Ag–ZnO heterostructured nanofibers,[211] and ZnO nanorod/Ag nanoparticle heterostructures.[18,248] The shift of Ag binding energy is mainly attributed to electron transfer from metallic Ag to ZnO crystals (i.e., formation of monovalent Ag). The Fermi levels of the two components equilibrate when the metal nanostructure comes into contact with the semiconductor. When Ag NWs (work

function of 4.26 eV) and ZnO nanoparticles (work function of 5.3 eV) become attached together, some electrons are transferred from Ag to ZnO at the interfaces of the ZnO/Ag core–shell heterostructures, resulting in monovalent Ag (i.e. Ag^{1+}).[37,129,248] The binding energy of Ag^{1+} is much lower than that of zero-valent Ag (Ag^0). Therefore, the shift of Ag $3d_{5/2}$ and Ag $3d_{3/2}$ to lower binding energies further verifies formation of the ZnO/Ag heterostructure.[37] The Zn 2p peaks shown in Figure 4.4(C) have values of about 1021.0 eV ($2p_{3/2}$) and 1043.9 eV ($2p_{1/2}$), confirming the main presence of Zn^{2+} in the sample.[249,250] The O 1s peak is centred at 530.6 eV [Figure 4.4(D)], which is similar to the reported value for ZnO.[249] All the XPS results further confirm that the core-shell nanowire heterostructure is composed of ZnO and Ag.

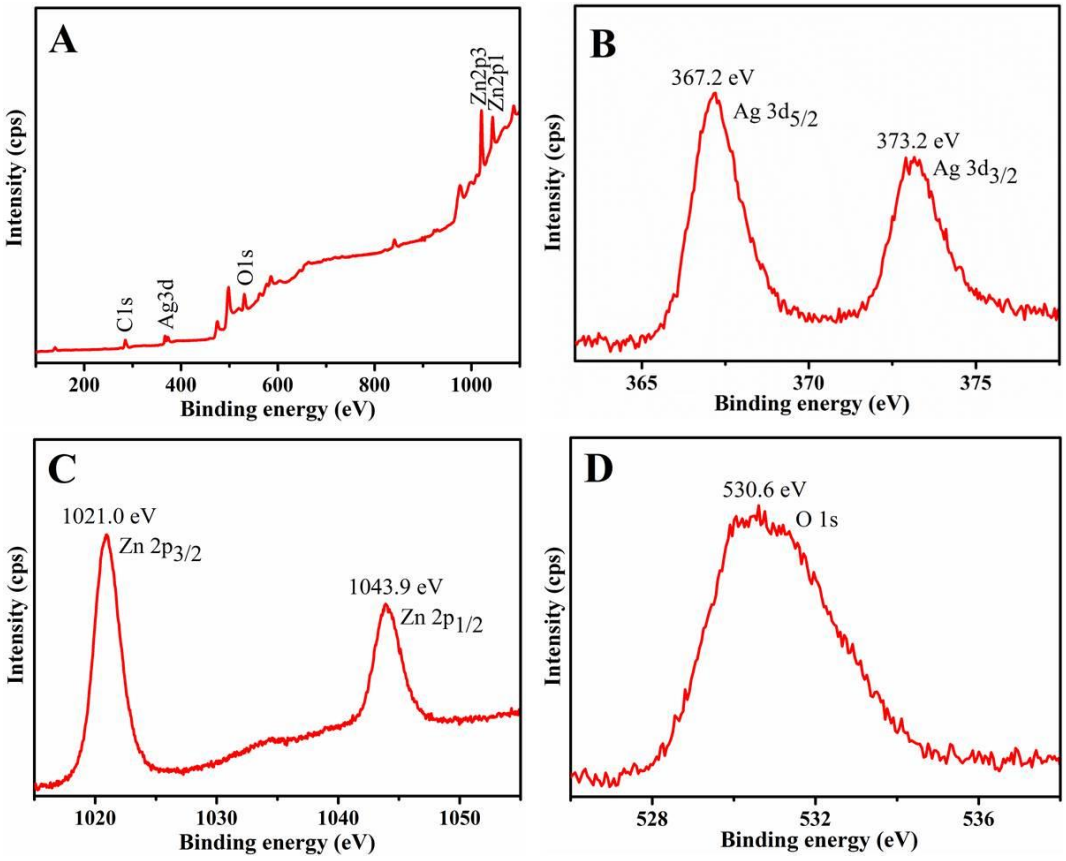

Figure 4.4 XPS spectra of the 1D Ag@ZnO core-shell hetero-nanowires (**A1**): (A) survey-scan spectrum, (B) Ag 3d, (C) Zn 2p, and (D) O 1s.

All the above results confirm our success in obtaining Ag@ZnO core-shell hetero-nanowires through this simple solution approach. It should be noted that the volume of water and the concentration of $Zn(NO_3)_2$ $6H_2O$ play important roles in the formation of Ag@ZnO core-shell hetero-nanowires. As shown in Figure 4.5(A-D), when 1.167 mL or 2.5 mL of water is used, the Ag NWs are coated with many very small ZnO nanoparticles (**A2** and **A3**). Increasing the water to 6.5 mL leads to dense ZnO nanoparticles with larger sizes that are deposited on the surfaces of Ag NWs [**A4**, Figure 4.5(E and F)]. Flower petals consisting of nanoparticles are partly coated on the surfaces of the Ag NWs, however, when the volume of water is further increased to 22.5 mL [**A5**, Figure 4.5(G and H)]. Changing the concentration of $Zn(NO_3)_2$ $6H_2O$ could also result in different structured Ag@ZnO nanowires. When the concentration of $Zn(NO_3)_2$ $6H_2O$ is decreased to 0.3 M, flower petals of ZnO assembled from small nanoparticles are partly coated on the surfaces of the Ag NWs (**A6**), as displayed in Figure 4.6(A and B). When the concentration of $Zn(NO_3)_2$ $6H_2O$ is increased to 1.2 M, the ZnO nanoparticles are randomly distributed on the surfaces of Ag NWs [**A7**, Figure 4.6(C and D)]. The above results demonstrate that Ag@ZnO core-shell hetero-nanowires with different morphologies can be achieved by tuning the amount of water or the concentration of $Zn(NO_3)_2$ $6H_2O$. On the basis of the above results, the synthesis of Ag@ZnO NWs is schematically shown in Scheme 4.1.

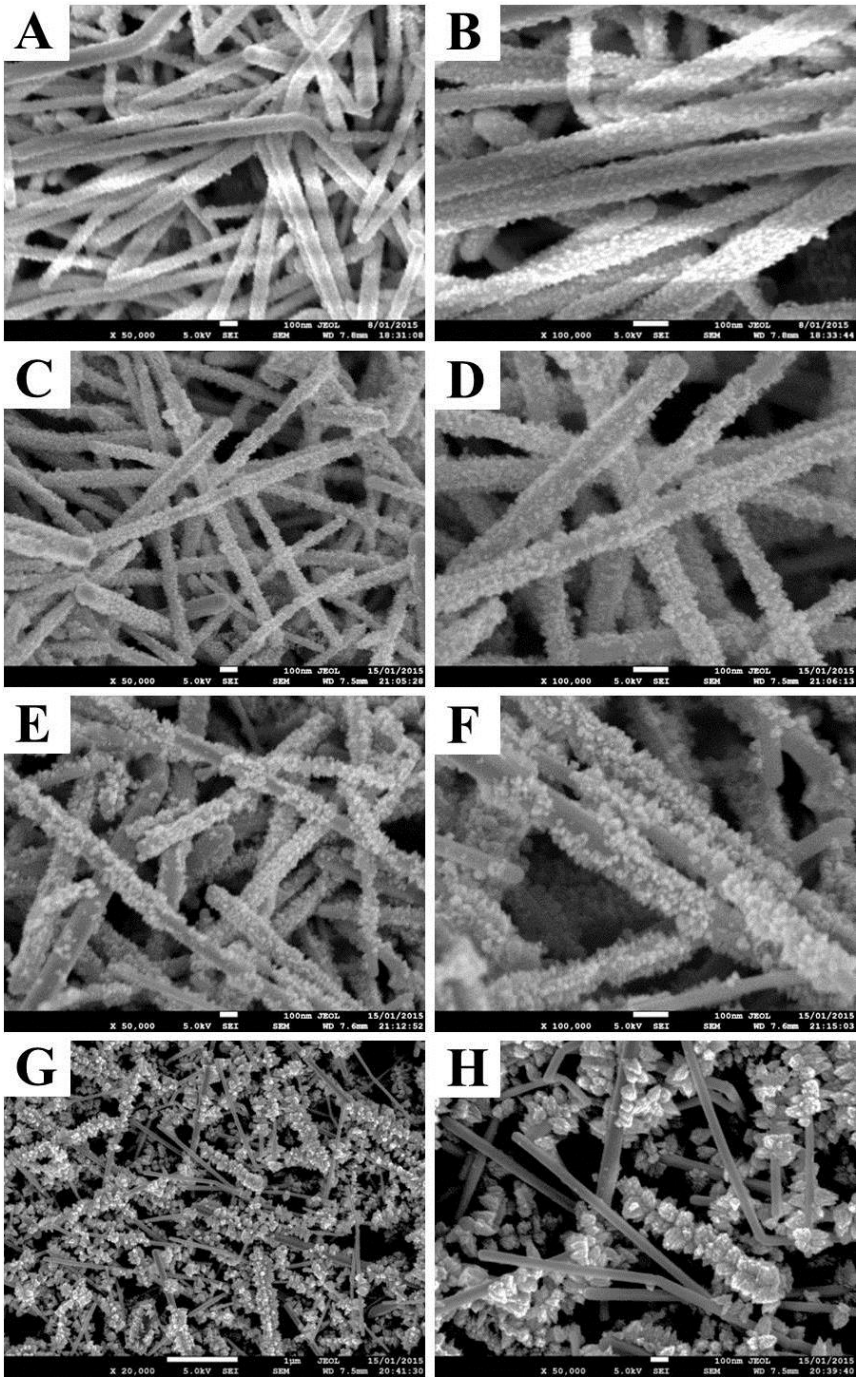

Figure 4.5 SEM images of the products (**A2**−**A5**) prepared with different volumes of water: (A and B) 1.167 mL, (C and D) 2.5 mL, (E and F) 6.5 mL, and (G and H) 22.5 mL.

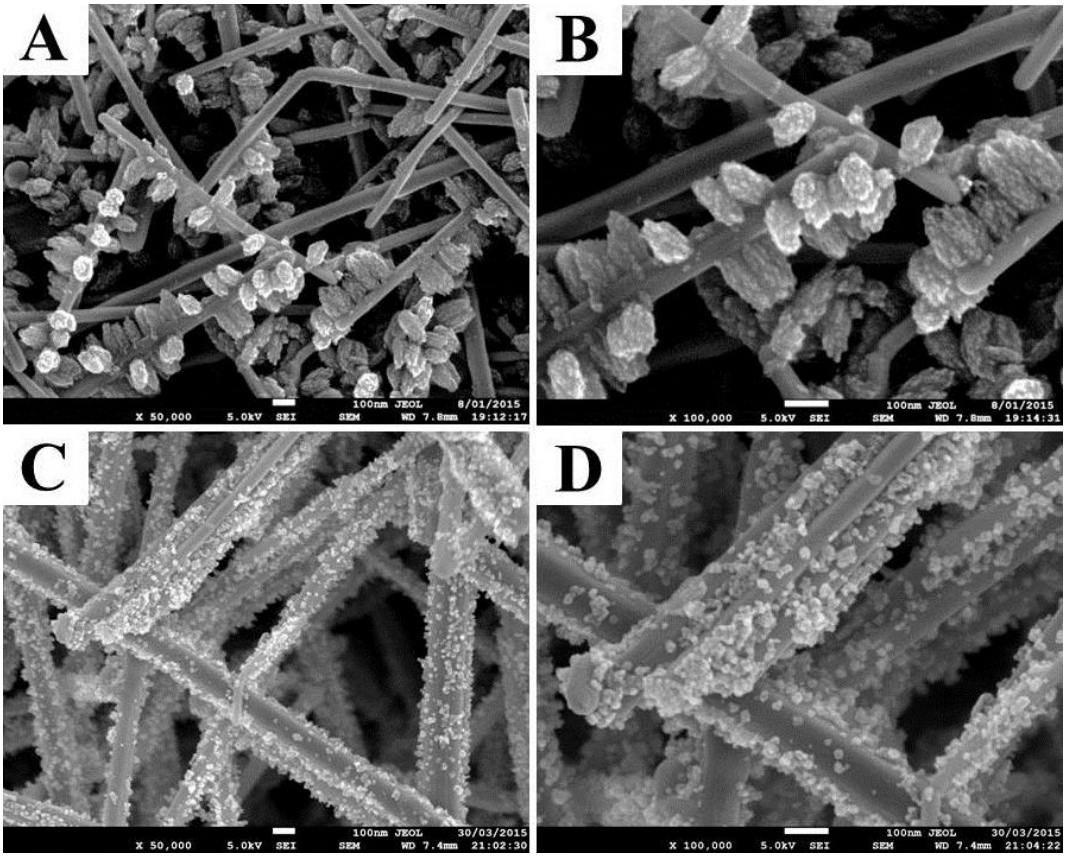

Figure 4.6 SEM images of the products (**A6** and **A7**) prepared with different concentrations of $Zn(NO_3)_2$ $6H_2O$: (A and B) 0.3 M, and (C and D) 1.2 M.

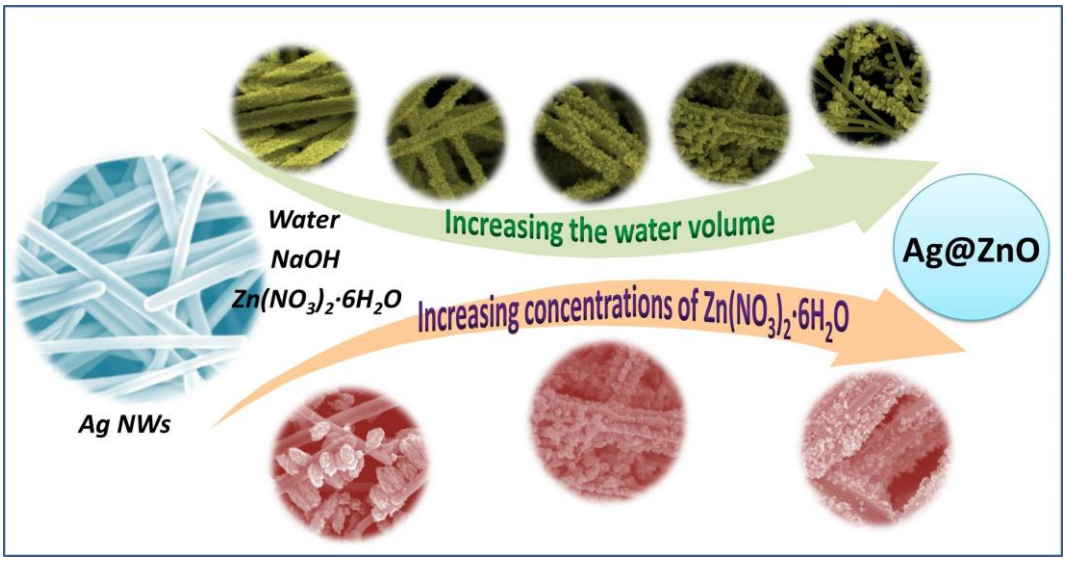

Scheme 4.1 Schematic representation of the synthesis of Ag@ZnO NWs

In order to demonstrate the applicability of our simple method, core-shell Ag@ZnO nanoparticles (NPs) were prepared under similar conditions by using Ag NPs as seeds. The resultant Ag@ZnO NPs (**A8**−**A12**) were examined by XRD and SEM, respectively. The XRD results [Figure 4.7(A-E)] clearly reveal that all the diffraction peaks can be indexed to Ag (JCPDS 4-783) and ZnO (JCPDS 5-667), and no other impurity diffraction peaks were observed. The SEM images [Figure 4.7(F-O)] show that large quantities of Ag@ZnO NPs with different morphologies were successfully fabricated in the presence of different volumes of water. The particle size and morphology of the ZnO shell can be tailored by changing the volume of water in the system. When the volume of water is 1.167 mL-6.5mL, the Ag core nanoparticles are packed with small ZnO nanoparticles [**A8**−**A10**, Figure 4.7(F-K)]. On increasing the volume of water to 14.5 mL, the ZnO nanoparticles aggregate to construct a flower-like structure [**A11**, Figure 4.7(L and M)], and the density of flower petals decreases with further increases in the volume of water [**A12**, Figure 4.7(N and O)].

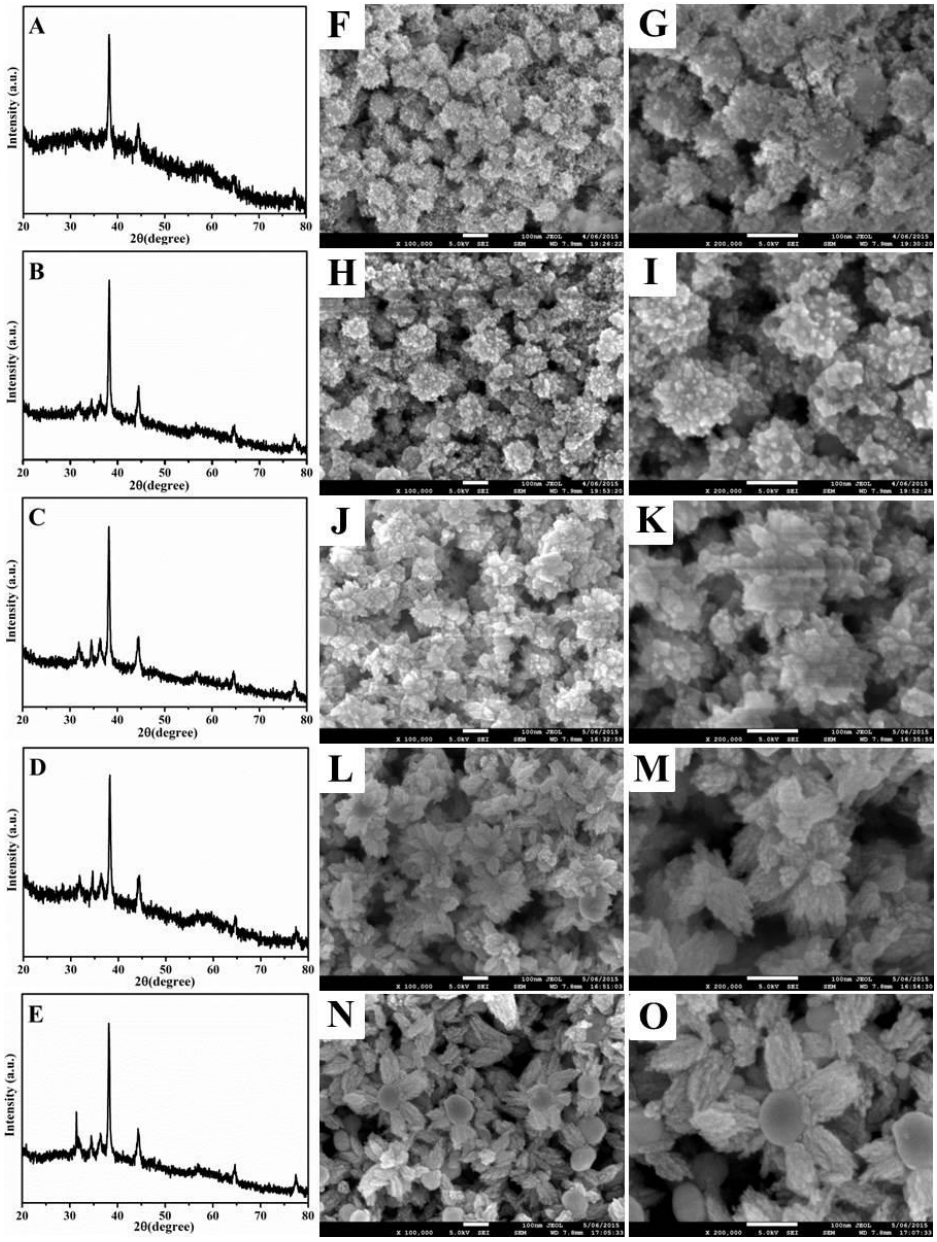

Figure 4.7 (A-E) XRD patterns and SEM images of the products (**A8**−**A12**) prepared in the presence of different volumes of water: (F and G) 1.167 mL, (H and I) 2.5 mL, (J and K) 6.5 mL, (L and M) 14.5 mL, and (N and O) 22.5 mL.

In addition, the effect of the concentration of $Zn(NO_3)_2 \cdot 6H_2O$ solution was also investigated. When the concentration of $Zn(NO_3)_2 \cdot 6H_2O$ solution is decreased to 0.3 M,

the ZnO crystals form a partial coating on the surfaces of Ag NPs, as can be seen from the SEM images [**A13**, Figure 4.8(C and D)]. When the concentration of $Zn(NO_3)_2$ $6H_2O$ solution is increased to 1.2 M, the ZnO nanocrystals cover the surfaces of the Ag NPs to form a flower-like heterostructure [**A14**, Figure 4.8(E and F)]. These results demonstrate that the final morphology of the Ag@ZnO nanostructures greatly depends on the morphology of the Ag seeds, the volume of water in the system, and the concentration of $Zn(NO_3)_2$ $6H_2O$ solution.

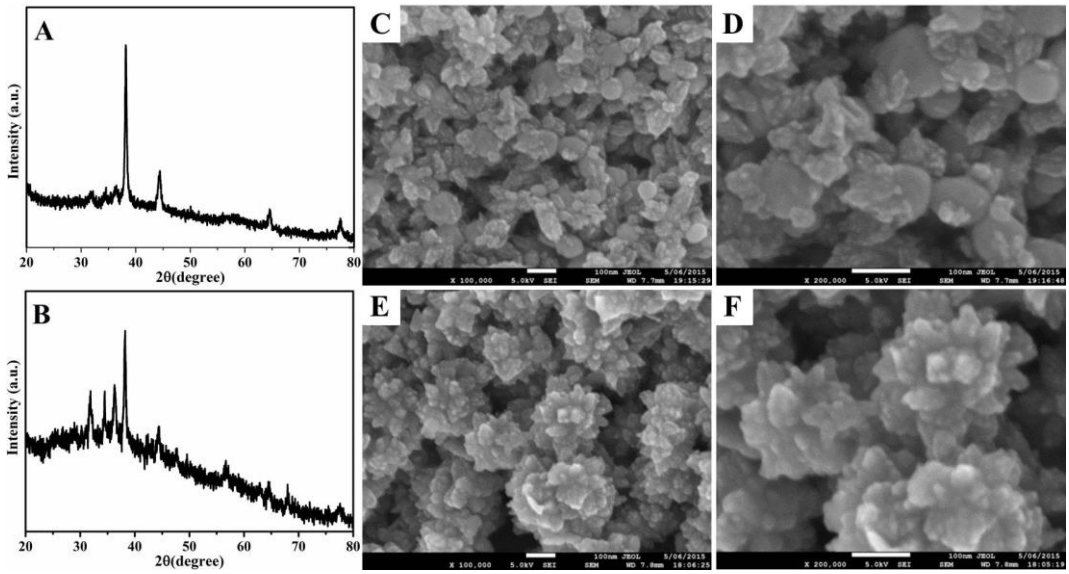

Figure 4.8 (A and B) XRD patterns and (C-F) SEM images of the products (**A13** and **A14**) prepared in the presence of different concentrations of $Zn(NO_3)_2$ $6H_2O$ solution: (C and D) 0.3 M, and (E and F) 1.2 M.

Pure ZnO NPs were also prepared by using 1,2-propanediol instead of Ag NW solution for comparison. The resultant ZnO NPs were examined by XRD and SEM, respectively. The XRD results [Figure 4.9(A-E)] clearly reveal that all the diffraction peaks can be indexed to ZnO (JCPDS 5-667), and no impurity diffraction peaks were observed. The SEM images [Figure 4.9(F-O)] show that large quantities of ZnO nanocrystals with different morphologies were successfully fabricated in the presence of different volumes of water in the system. The size and morphology of ZnO particles is very sensitive to

the volume of water, and it can be clearly seen that the ZnO sample comprises very small nanoparticles with a diameter of 8−20 nm when the volume of added water is 1.167 mL [Figure 4.9(F and G)]. When the volume of water is increased to 2.5 mL, the product becomes irregular crystals with diameters of 100−200 nm, assembled from tiny nanoparticles [Figure 4.9(H and I)]. On increasing the volume of water to 6.5 mL, the ZnO nanoparticles aggregate to form flower-like structures with diameters of 600−800 nm [Figure 4.9(J and K)], and the diameter of the flower-like structures increased to ~1 μm on further increasing the volume of water [Figure 4.9(L-O)].

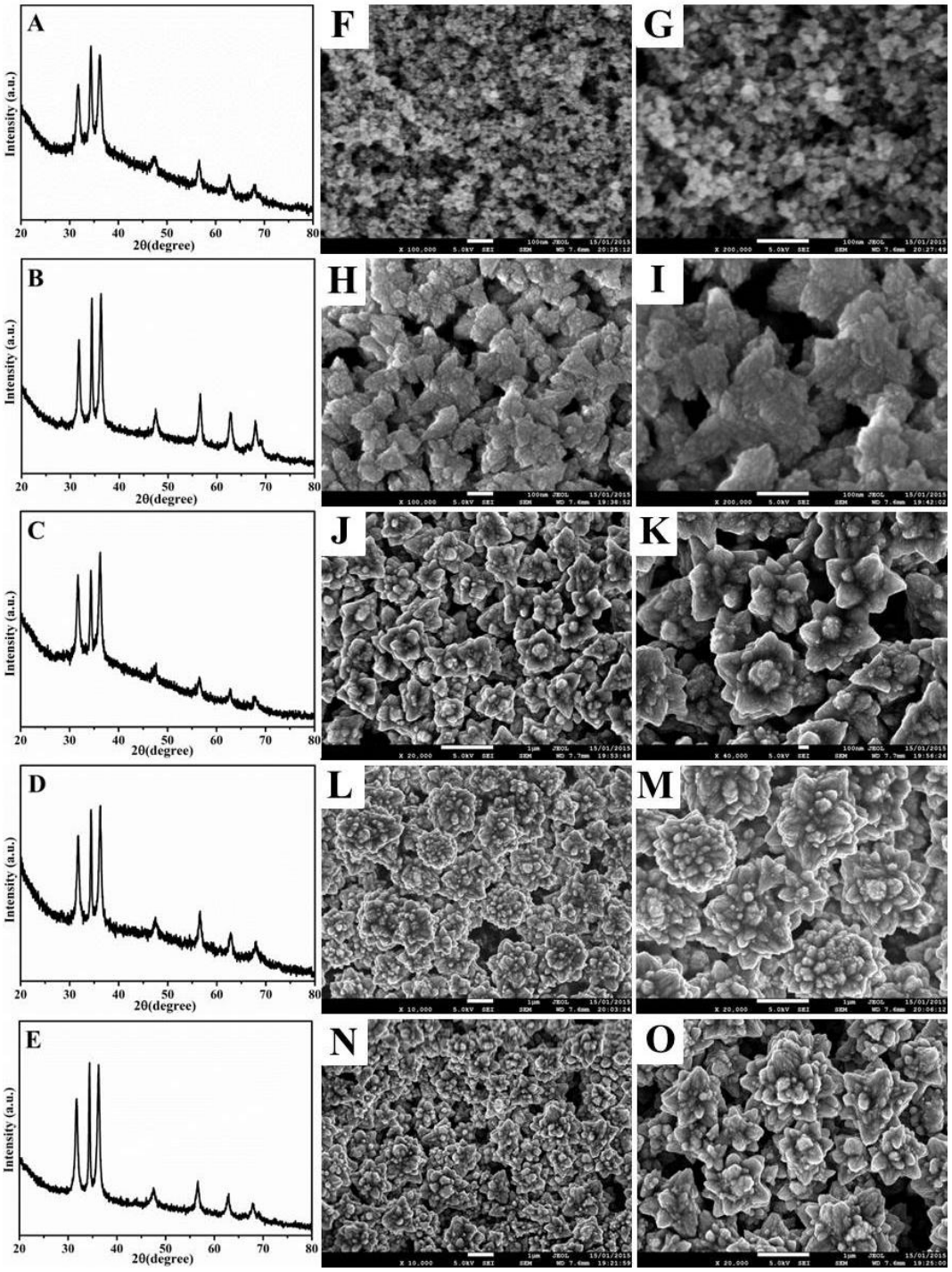

Figure 4.9 (A-E) XRD patterns, and SEM images of the products prepared in the presence of different volumes of water: (F and G) 1.167 mL, (H and I) 2.5 mL, (J and K) 6.5 mL, (L and M) 14.5 mL, and (N and O) 22.5 mL.

Photoluminescence (PL) spectra were widely used to investigate recombination rate of photogenerated electrons and holes in the photocatalysts during their photocatalysis reaction.[251,252] Figure 4.10 shows the PL spectra of the tested photocatalysts (i.e. A1, A11, A2, and pure ZnO) with an excitation wavelength of 325 nm. An UV emission peak centered at around 380 nm and a visible emission in the range of 550 nm – 590 nm with high intensity are observed in all photocatalysts. The UV emission corresponds to the near band edge emission of ZnO, and represents the recombination of free excitons through an exciton−exciton collision process.[37,253] The visible emission is attributed to the presence of oxygen related defects and interstitials.[232] Moreover, The A1 and A11 photocatalysts show a diminished PL intensity in comparison with pure ZnO and A2, indicating that introduction of Ag nanowires and Ag nanoparticles inhibited the recombination of electrons and holes generated in ZnO, which improved the separation of electron-hole pairs and contributed to the enhancement of photocatalytic activity of Ag@ZnO core-shell photocatalysts. Based on the above consideration, all Ag@ZnO core-shell photocatalysts have better photocatalytic activity than pure ZnO, and A1 sample is the best photocatalyst among the Ag@ZnO heterostructures as it has the lowest PL emission.

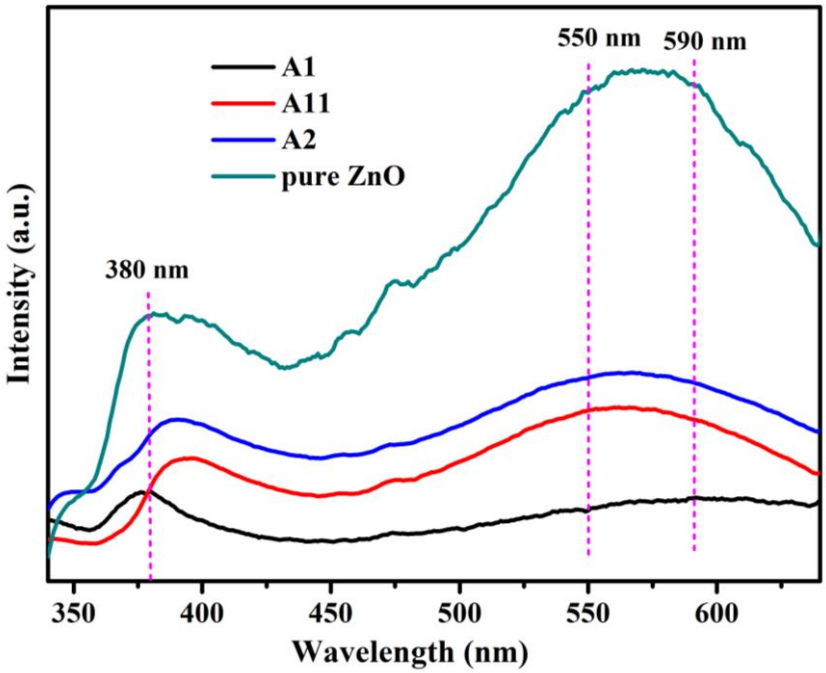

Figure 4.10 The PL spectra of A1, A11, A2, and pure ZnO with an excitation wavelength of 325 nm.

The resultant Ag@ZnO core-shell nanowires and nanoparticles are expected to show higher photocatalytic activity than pure ZnO NPs, due to the plasmonic enhancement of the Ag cores. The performance of the Ag@ZnO NWs (**A1**−**A7**) was evaluated by the photodegradation of RhB under solar light irradiation. For comparison, the Ag NWs, Ag@ZnO NPs (**A8**), and pure ZnO nanoflowers were also tested under identical experimental conditions. If the photodegradation of RhB is considered as a pseudo-first-order reaction;[37,211,254] its photocatalytic reaction kinetics can be expressed as follows: $C = C_0e^{-kt}$, where k is the degradation rate constant, and C_0 and C are the initial concentration of RhB and the concentration of the pollution at a reaction time of t, which corresponds well to the absorbance of RhB at 554 nm, respectively. Figure 4.11(A) shows the photodegradation curves of RhB in the form of $\ln(C_0/C)$ as a function of time, and the k values determined from linear fitting for the as-prepared photocatalysts are listed in Table 4.2. It can be clearly observed that the degradation of RhB over only Ag NWs under solar light irradiation is negligible.

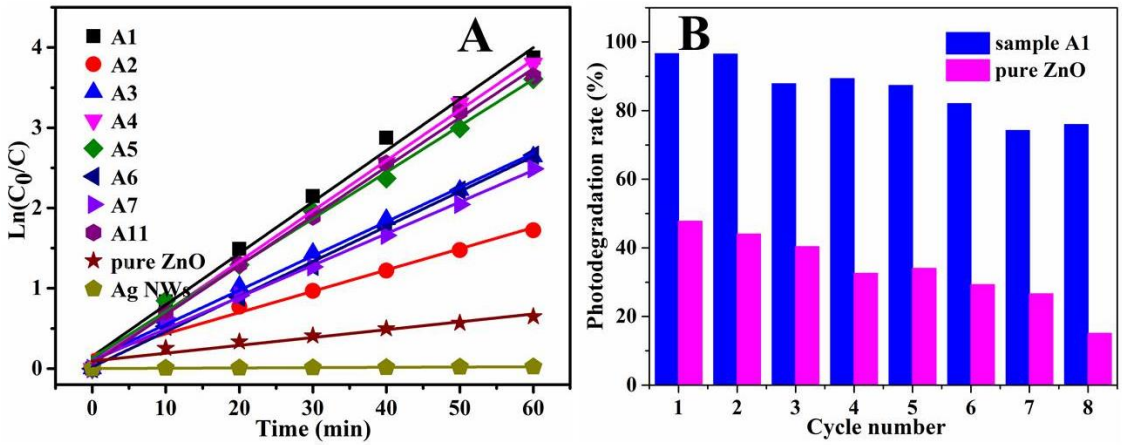

Figure 4.11 (A) Rhodamine B degradation curves of ln(C_0/C) versus time for Ag@ZnO heterostructured composite, Ag nanowires, and pure ZnO used as catalyst. (B) Cycling runs in the photocatalytic degradation of RhB in the presence of sample A1 and pure ZnO under solar light irradiation.

Table 4.2 Reaction rate constant (k) for photocatalytic degradation of RhB under solar light irradiation.

Sample	A1	A2	A3	A4	A5
k/min^{-1}	0.0641	0.0265	0.0427	0.0629	0.0578
Sample	A6	A7	A11	Pure ZnO	Ag NWs
k/min^{-1}	0.0437	0.0395	0.0613	0.0098	0.0004

In contrast, the as-prepared Ag@ZnO core−shell composites and pure ZnO nanoflowers all exhibit excellent photocatalytic performance. In particular, Ag@ZnO core−shell NWs with various morphologies and proportions, and Ag@ZnO core-shell NPs show higher photocatalytic activities than that of the pure ZnO nanoflowers, while the Ag@ZnO core-shell NWs (**A1**) prepared with 0.6 M $Zn(NO_3)_2$ $6H_2O$ and 14.5 mL water exhibit the highest catalytic activity, which can decolor 99% of RhB within 60 min, with a rate constant (k) of 0.0641 min^{-1}. It should be noted that sample A1 with 1D structured Ag NWs and fusiform ZnO with a high carrier transport property serve as

spatially extended active centers to provide direct and fast electron/hole transfer to their acceptors (H_2O, O_2, RhB), which increases the chance for RhB dye to be degraded, compared with other 1D structured Ag@ZnO NWs with the same nominal ratio of Ag:ZnO (1:2), including samples A2-A5. A similar kinetics and rate constant value (0.0613 min^{-1}) is also observed with Ag@ZnO core-shell NPs, which is about 6.3 times larger compared to that of the pure ZnO nanoflowers (0.0098 min^{-1}). Furthermore, increasing or decreasing the nominal ratio of Ag:ZnO of Ag@ZnO core−shell NWs could also have impact on the activity. For example, samples A6 and A7 with the Ag:ZnO ratio of 1:1 and 1:4 showed better activities compared to that of sample A2 with Ag:ZnO ratio of 1:2. However, they showed poorer activities than those of samples A1, A3, A4 and A5. The results clearly demonstrate that the hetero-growth of ZnO nanoshells on Ag NWs and NPs to build core-shell heterostructures has been proven to be a useful and successful strategy for improving the photocatalytic properties of ZnO crystals, and the photocatalytic performance of the Ag@ZnO core−shell heterostructures can be optimized by tailoring their morphology and proportions.

One main disadvantage of ZnO is its poor stability in degradation of organic pollutants in aqueous solution due to photo-corrosion. To investigate the stability and repeatability of photocatalytic performance in the solar light region, sample **A1** and pure ZnO were compared for their ability to degrade RhB in eight repeated cycles, and the results are shown in Figure 4.11(B). It was noteworthy that sample **A1** exhibited much higher stability than pure ZnO under solar light irradiation. The RhB degradation rate decreased from 48% for the first cycle to 15% for the eighth cycle over pure ZnO photocatalyst, showing poor stability. However, the photocatalytic efficiency was reduced by about 10% and 25% after five cycles and eight cycles, respectively. The above results indicated that the presence of the Ag NWs could partly suppress the loss in activity. Two possible reasons for the favorable photostability as follows. Firstly, the unique micro/nano 1D Ag@ZnO structure with high activity and stability. Secondly, the interaction between Ag and ZnO could reduce the defect sites of ZnO, and effectively

inhibit the photocorrosion of ZnO, resulting in the improvement of photostability in photocatalyst.[216,255-257]

It was reported that in the photodegradation of organic pollutants, reactive species such as $\cdot O_2^-$, h^+, e^+, and $\cdot OH$ play the bridge role in photocatalysts under light irradiation,[70,258-261] and they could vary with the different photocatalysts.[259,262] To investigate the photocatalytic mechanism and to understand the better performance of 1D Ag@ZnO core-shell photocatalyst (**A1**), the effect of scavengers on the degradation of RhB was examined to clarify the contribution of different reactive species during the photocatalysis study. P-benzoquinone (PBQ) is used as O_2^- scavenger,[258,260,261] triethanolamine (TEOA) as h^+ scavenger,[259,261] CCl_4 as electron scavenger,[261] and isopropanol (IPA) as $\cdot OH$ scavenger.[260] These scavengers were added into the RhB solution together with the 1D Ag@ZnO core-shell hetero-nanowires before irradiation. As illustrated in Figure 4.12, the almost complete inhibition of RhB degradation in the presence of PBQ suggests that $\cdot O_2^-$ is the major reactive species for the photocatalytic degradation of RhB. The dramatic decrease in degradation of RhB in the presence of TEOA demonstrate that h^+ also plays an important role in the photodegradation of RhB over such 1D Ag@ZnO heteronanowires, which was further confirmed by slight RhB degradation enhancement after adding CCl_4 to capture photogenerated electrons. Meanwhile, the decrease in degradation of RhB arising from the removal of oxygen with bubbling N_2 revealed that molecular oxygen also plays an important role over such 1D Ag@ZnO heteronanowires. This is attributed to the electron trapping role of molecular oxygen, which could produce $\bullet O_2^-$ to inhibit the recombination of electron−hole pairs and leave an excess of holes to oxidize RhB. The elimination of molecular oxygen would diminish the amount of holes and prevent the oxidation of RhB due to the fast recombination of electron−hole pairs. The addition of IPA also indicates that $\cdot OH$ contributes greatly to the degradation of RhB.

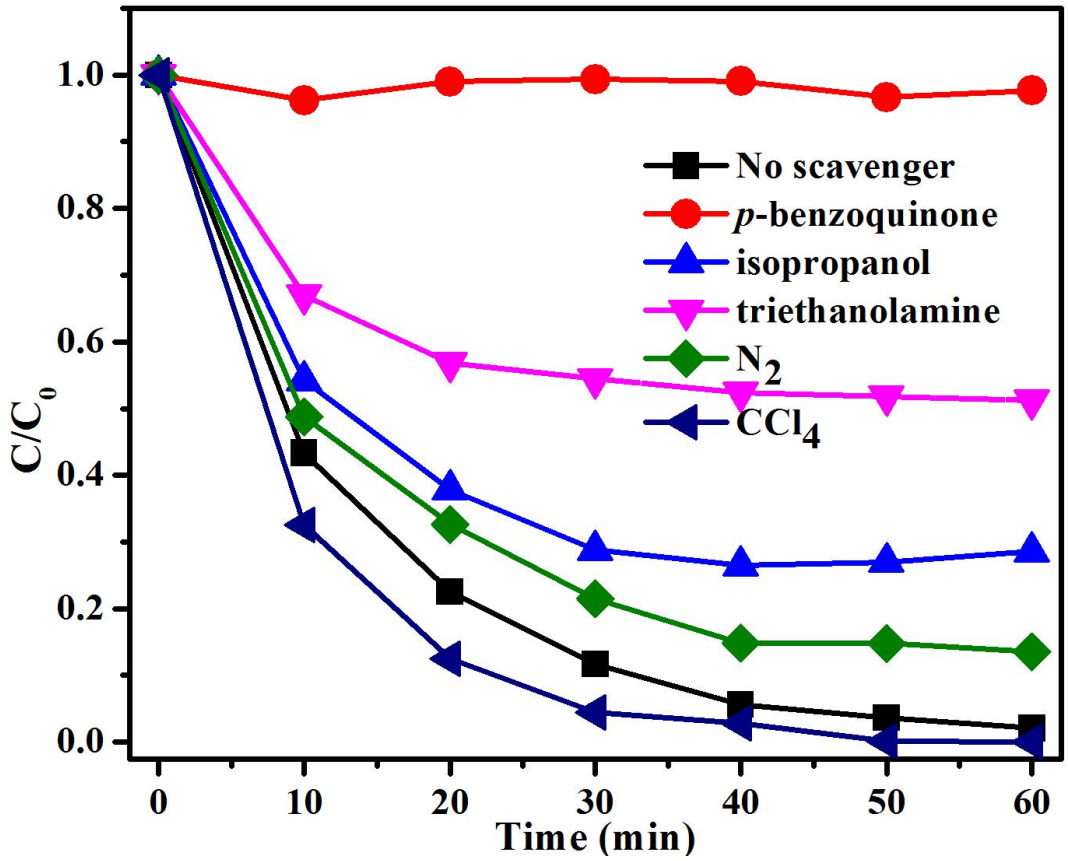

Figure 4.12 Photocatalytic degradation of RhB over the 1D Ag@ZnO core-shell hetero-nanowires (**A1**) in the presence of scavengers.

As the real photocatalytic mechanism of Ag@ZnO hybrids is very complicated, it is necessary to discuss the band structure of Ag@ZnO heterostructures in detail. The work function of ZnO (5.2 eV) is larger than that of Ag (4.26 eV), which leads to the migration of electrons from Ag to the conduction band (CB) of ZnO to achieve Fermi energy level (E_{fm}) equilibration when coupling of Ag NWs/NPs with ZnO. The transfer of electrons can lead to trapping of charges and increased carrier life. A schematic illustration of the photocatalytic reaction of RhB on Ag@ZnO heterostructures is presented in Scheme 4.2. For photocatalysis under solar light irradiation, the enhancement in both the UV region and the visible light region should be considered, which may be ascribed to the synergistic effects of Ag NWs/NPs and surface ZnO. As evidenced by the SEM and TEM images, there are clear interfaces between Ag NWs

and ZnO nanoparticles, which can effectively suppress the recombination rate of electron-hole pairs.

The enhanced photocatalytic performance in the UV region was attributed to the formation of Schottky barriers at the metal-semiconductor interface between the Ag NW/NP core and the ZnO nanoparticle shell, which facilitates the capture and quick transfer of photoexcited electrons from the ZnO nanoshells to the Ag NWs/NPs under solar light irradiation.[216] When the Ag@ZnO core-shell heterojunctions are irradiated by UV light, electrons (e^-) in the valence band (VB) can be excited to the CB with simultaneous generation of the same amount of holes (h^+) in the VB. As presented in Scheme 4.2, the bottom energy level of the CB of ZnO is higher than the E_F of the Ag/ZnO heterostructures, so that photoexcited electrons can transfer rapidly from ZnO particles to Ag nanowires, driven by the potential energy. Ag NWs/NPs, acting as electron sinks, not only reduce the recombination of photoinduced electrons and holes but also prolong the lifetime of photogenerated pairs. Subsequently, the electrons accumulated in the Ag NWs/NPs or the conduction band of ZnO are transferred to O_2 molecules to produce superoxide radical anions ($\bullet O_2^-$) through multiple-electron reduction reactions to decompose organic pollutant.[211,263] Accumulation of the photoinduced holes in the valence band of the ZnO nanoshells leads to the production of the hydroxyl radical (•OH) at the surface, which is responsible for the oxidation decomposition of the RhB molecules.[211] Both the sensitizing property of the dye and the electron scavenging ability of silver together contribute to the interfacial charge transfer process to utilize the photoexcited electrons, as well as the VB holes, to form these active oxygen species.[248] In addition, the defects at the Ag@ZnO interface have also been demonstrated to suppress the charge recombination by transferring the photogenerated electrons to the dye in solution.[18]

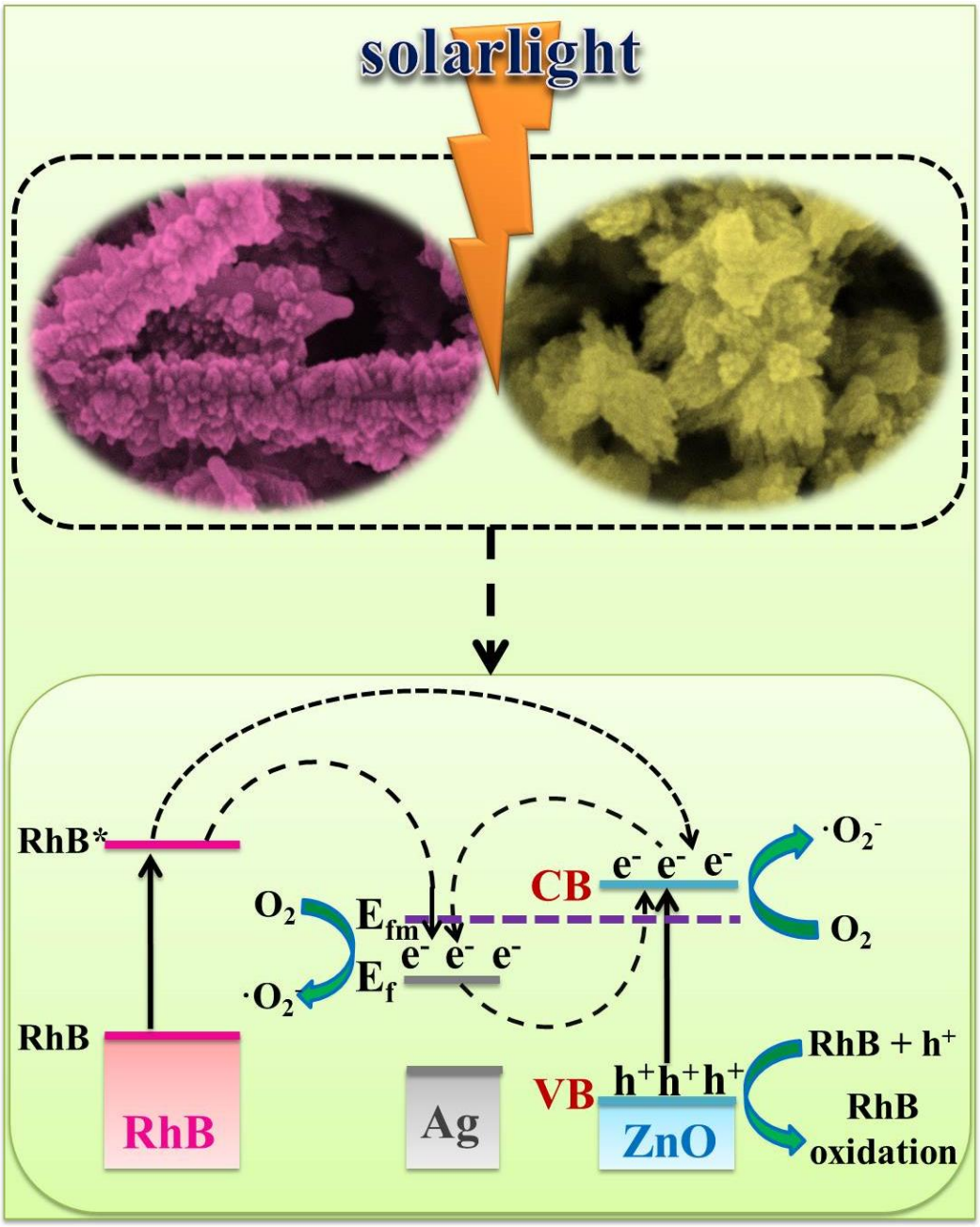

Scheme 4.2 Schematic illustration of the transfer of photogenerated electron-hole pairs in the Ag@ZnO core-shell NWs/NPs under solar light irradiation.

For the enhancement in the visible light region, the adsorbed RhB would also be photoactivated by the visible light, so that electrons can transfer from the singlet excited RhB (RhB*) to the conduction band (CB) of ZnO, Ag NWs/NPs, and the shallow trap levels in the band gap of ZnO.[216,248,264] The electrons on the ZnO surface are

subsequently trapped by the Ag NWs/NPs, which separates the $RhB^{\bullet+}$ and the electrons, preventing the recombination process.[265] Moreover, the surface plasmon resonance of Ag NWs/NPs excited by the solar light improves the excitation of surface electrons and the transfer of interfacial electrons.[216] Upon irradiation with visible light, the electrons in E_{fm} were injected quickly into the conduction band (CB) of ZnO via a surface phonon resonance (SPR) mechanism, leaving behind holes on the metal surface. Separated electrons might then be consumed by the dissolved oxygen to produce various reactive oxidative species, thus promoting photocatalysis under visible light irradiation.[216,266]

The unique 1D Ag@ZnO core-shell NWs are expected to have excellent electron conductivity and mobility. The metal nanowires with a high carrier transport property serve as spatially extended catalyzing centres, which can facilitate fast and long-distance electron transport, and the fast transfer of photoinduced electrons and holes over the Ag NWs and ZnO nanoshells suppresses the recombination of electron-hole pairs, which is favorable for increasing the chances for RhB to be degraded, compared with Ag@ZnO core-shell nanoparticles. Furthermore, the high length-to-diameter ratio of the 1D metal-core@semiconductor-shell hetero-nanostructures may remarkably enhance the light absorption, trapping, and scattering through a local field enhancement effect of plasmonic Ag NWs, and thus increase the quantity of photogenerated electrons and holes available to participate in the photocatalytic reactions, leading to an enhanced photocatalytic property of the ZnO. It should be noted, however, that the photocatalytic mechanism over such Ag@ZnO core-shell NWs/NPs is still not completely understood, and a more detailed study is still underway.

4.4 Conclusion

In summary, plasmonic Ag@ZnO core-shell hybrids, including hetero-nanowires and hetero-nanoparticles, have been fabricated by a facile solution process at room temperature. The resulting unique heterostructures exhibit greater plasmonic enhancement of photocatalytic activity in RhB oxidizing than pure ZnO under solar

light irradiation. The photocatalytic activity and cycling stability of the 1D core-shell hetero-nanowires prepared under optimal conditions is better than that of pure ZnO, which can be attributed to the efficient separation of electron−hole pairs in such 1D Ag@ZnO hetero-nanowires. Such rational design and fabrication of metal-core@semiconductor-shell architectures with hetero-nanowires and hetero-nanoparticles may hold great potential in solar energy utilization.

Chapter 5 Facile synthesis of highly efficient one-dimensional plasmonic photocatalysts through Ag@Cu_2O core-shell hetero-nanowires

The contents of this chapter were published in ACS Applied Materials & Interfaces, 2014, 6, 15716-15725.[70]

5.1 Introduction

The synthesis of one-dimensional (1D) nanostructures and their potential applications in solar energy conversion have attracted much recent interest due to their unique 1D geometry with fast and long-distance electron transfer, good electron conductivity and mobility, larger specific surface area, light-harvesting efficiency, and length-to-diameter ratio, and high adsorption capacity.[99,267-281] An important application of 1D nanostructures is in photocatalytic degradation of organic pollutants, and recent decades have witnessed an exponential growth in the design and fabrication of highly efficient and active photocatalysts due to the growing awareness of environmental pollution issues and safety considerations. Various semiconducting nano-photocatalysts, especially metal oxide semiconductors such as TiO_2 and ZnO, are being extensively investigated.[60,272,273,282,283] The wide band gap of some metal oxides limits their light absorption in UV region, however, leading to less use of sunlight.[72]

In order to effectively utilize sunlight, noble plasmonic nanostructured metals, such as Au, Ag, and Pt, are deposited on the surface of semiconductors. The metals act as electron traps that introduce efficient interfacial charge separation in the composites, leading to an improvement in photocatalytic activity over an extended wavelength range.[98,105,133,196] Metal nanoparticles are most commonly used, and they can also be attached to the surface of semiconductors to form core-satellite or core-shell semiconductor@metal nanostructures. The external metal nanoparticles are exposed to reactants and the surrounding medium, however, which could cause corrosion and

detachment from the photocatalysts.[11,284,285] An alternative option is to construct core-shell metal@semiconductor structures.

In addition to the use of plasmonic metal nanostructures, the selection of narrow-band-gap semiconductor photocatalysts can also effectively improve absorption of light harvesting. Cuprous oxide (Cu_2O) is one such attractive and environmentally friendly *p*-type direct semiconductor, with a small band gap (2.17 eV) and unique optical and electrical properties, which make it an appealing candidate for photocatalytic applications.[78,286-290] In order to overcome the aforementioned disadvantages of semiconductor-core@metal-shell plasmonic heterostructured photocatalysts, and to further enhance the photocatalytic performance of pure Cu_2O, metal-core@Cu_2O-shell hetero-nanostructures, such as Cu@Cu_2O core-shell microspheres,[291] Ag@Cu_2O core-shell nanoparticles,[11] and Au@Cu_2O core-shell cubes and octahedra,[292] have been widely chosen as photocatalysts in recent years. Compared with other noble metals, Ag is more attractive due to its high electrical and thermal conductivity, antibacterial characteristics, low cost, and nontoxicity. Ag nanostructures exhibit a wealth of optical and photoelectrochemical properties directly related to their geometry-dependent surface plasmon resonances, which makes 1D Ag nanostructures great potential candidates in the field of photocatalysis.[42,43,238,284,293-295] However, there is still no report on highly efficient plasmonic heterostructured photocatalysts based on 1D Ag-core@Cu_2O-shell architectures to our knowledge, which might be able to fully take advantage of the potential of 1D nanostructures.

In this chapter, a general procedure for rapid fabricating 1D Ag@Cu_2O core-shell hetero-nanowires for photodegradation of organic dyes is reported. The core-shell hetero-nanowires are made by overgrowth of Cu_2O nanocrystals on the surface of as-prepared Ag nanowires (NWs) via a simple solution process (Scheme 5.1). The resultant 1D core-shell Ag@Cu_2O nanowires show better photocatalytic degradation of methyl orange (MO) to core-shell Ag@Cu_2O nanoparticles and pure Cu_2O nanospheres.

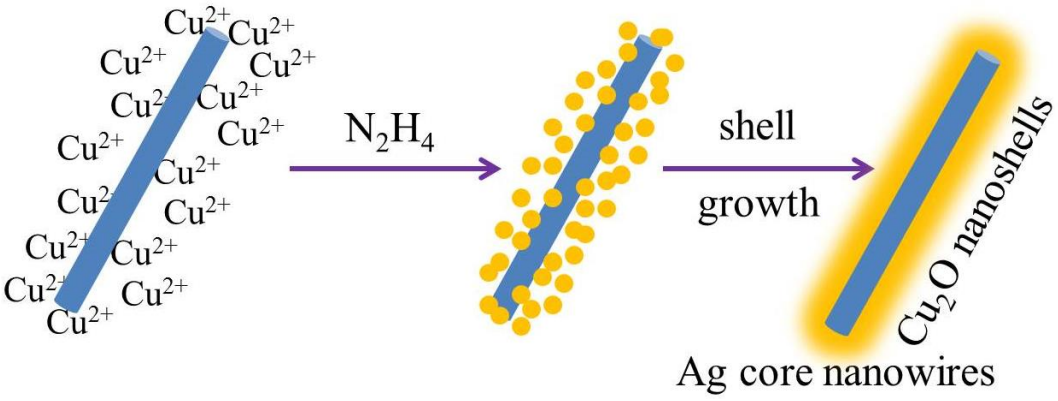

Scheme 5.1 Schematic illustration of the plausible formation process of the 1D Ag@Cu_2O core-shell hetero-nanowires.

5.2 Experimental section

5.2.1 Sample preparations

Ag nanowires (Ag NWs) were fabricated by a modified polyol process.[296] In a typical synthesis, 10 mL EG containing PVP40 was loaded into a 25-mL vial, and heated with magnetic stirring in an oil bath at 120 ℃ for 1 h. 1 mL of NaCl in EG solution (1 mM) was then quickly added, and stirring for another 5 min. Finally, $AgNO_3$ (0.1 M solution in EG) was added to the mixture. The mixture solution was then heated at 120 ℃ with magnetic stirring for 1 h, yielding the grey Ag NWs.

Ag nanoparticles (Ag NPs) were prepared by the similar procedure without NaCl.

Core-shell Ag@Cu_2O hetero-nanowires were synthesized by a simple solution process used for the synthesis of Au@Cu_2O nanoparticles with some modifications.[297] Typically, 8 mL freshly prepared Ag NW solution was added into 50 mL of 0.05 M $Cu(NO_3)_2$ $3H_2O$ aqueous solution under constant magnetic stirring for 30 min. Then, 100 L of N_2H_4 H_2O solution was added into the reaction mixture. The reaction mixture was stirred for 30 min, and then the resultant Ag@Cu_2O core-shell nanowires

were separated by centrifugation, and washed with de-ionized water and absolute ethanol to remove impurities, and then dried at 60 ℃.

Core-shell Ag@Cu_2O hetero-nanoparticles were prepared using the similar approach to Ag@Cu_2O core-shell hetero-nanowires, except 8 mL of Ag NPs solution was added rather than Ag NWs solution.

Pure Cu_2O nanospheres were prepared using the above similar procedure without Ag solution.

5.2.2 Characterization

The X-ray diffraction (XRD) measurements were performed on a GBC MMA X-ray diffractometer using Cu Kα_1 radiation (40 kv). The XRD patterns were recorded from 20 ° to 80 ° with a scanning rate of 2 °/min. SEM images were taken using a field-emission scanning electron microscope (JSM-7500FA, JEOL) operated at an accelerating voltage of 5 kV. TEM images were recorded on a field-emission transmission electron microscope (JEM-2011, JEOL), using an accelerating voltage of 200 kV. UV/vis absorption spectra were taken at room temperature on a UV-3600 (Shimadzu) spectrometer. X-ray photoelectron spectroscopy (XPS) was performed by a VG Scientific ESCALAB 2201XL photoelectron spectrometer with Al Ka X-ray as the excitation source to analyze samples' elemental composition. Analysis of the XPS data was carried out using the commercial CasaXPS 2.3.15 software package.

5.2.3 Photocatalytic test

Photocatalytic activity of the as-synthesized Ag@Cu_2O core-shell nanowires was evaluated by the degradation of MO under the irradiation of a LSC-100 Solar Simulator (Newport). In an experiment, 5 mg photocatalyst was added into 50 mL of MO solution at room temperature. Prior to irradiation, the suspension was stirred in the dark to

ensure the establishment of an adsorption-desorption equilibrium between the photocatalysts and MO. Then the solution was exposed to solar light irradiation under magnetic stirring. At each irradiation time interval, 2 mL of the suspension was collected and then centrifuged to remove the photocatalysts. The concentration of MO was analyzed by a Shimadzu UV-3600 spectrophotometer, and the characteristic absorption of MO at 464 nm was used to evaluate its photocatalytic degradation. All of the measurements were carried out at room temperature.

5.3 Results and discussion

Figure 5.1 shows a typical XRD pattern and typical scanning electron microscope (SEM) images of the as-prepared the Ag nanowires prepared by a modified polyol reduction process,[296] which serve as templates for the subsequent hetero-growth of Cu_2O nanoshells to form $Ag@Cu_2O$ core-shell nanowires. These Ag nanowires are well crystallized (Figure 5.1A) and possess relatively smooth surfaces, and have an average diameter of about 100 nm and a length of about 10 μm (Figure 5.1B-D).

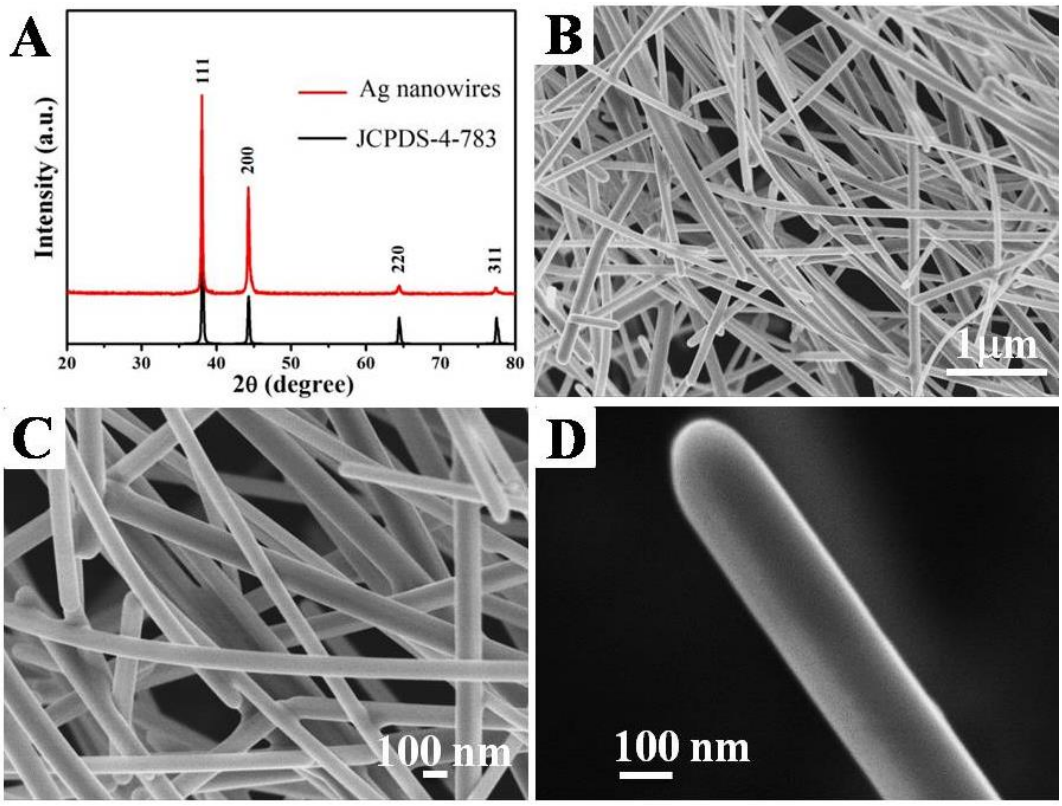

Figure 5.1 (A) XRD pattern and (B-D) SEM images of the Ag nanowires (Ag NWs).

The crystalline structure and morphology of the as-prepared Ag@Cu_2O core-shell hetero-nanowires is shown in Figure 5.2. The X-ray diffraction (XRD) pattern is compared with standard patterns of Ag (JCPDS 4-783) and Cu_2O (JCPDS 5-667) in Figure 5.2(A), where every peak can be indexed to Ag or Cu_2O, supporting the formation of Ag@Cu_2O core-shell hetero-nanowires. The absence of other impurity peaks indicates the high purity of the core-shell Ag@Cu_2O hetero-nanowires fabricated by this simple solution process. In addition, the peaks of Cu_2O are characteristic of a cubic structure with a lattice constant of a = 4.27 Å. Its relatively weak peaks indicate the low crystallinity of Cu_2O shell than that of Ag core. SEM images of the Ag@Cu_2O core-shell hetero-nanowires are displayed in Figure 5.2(B-D), which clearly show that the surface of the Ag@Cu_2O core-shell hetero-nanowires is not as smooth as that of the Ag NWs, due to the coating by a layer of dense Cu_2O nanoparticles. The enlarged SEM

image [Figure 5.2(D)] reveals that many tiny Cu_2O nanoparticles have densely grown on the entire surface of the Ag nanowires, including both ends, to form a rough surface.

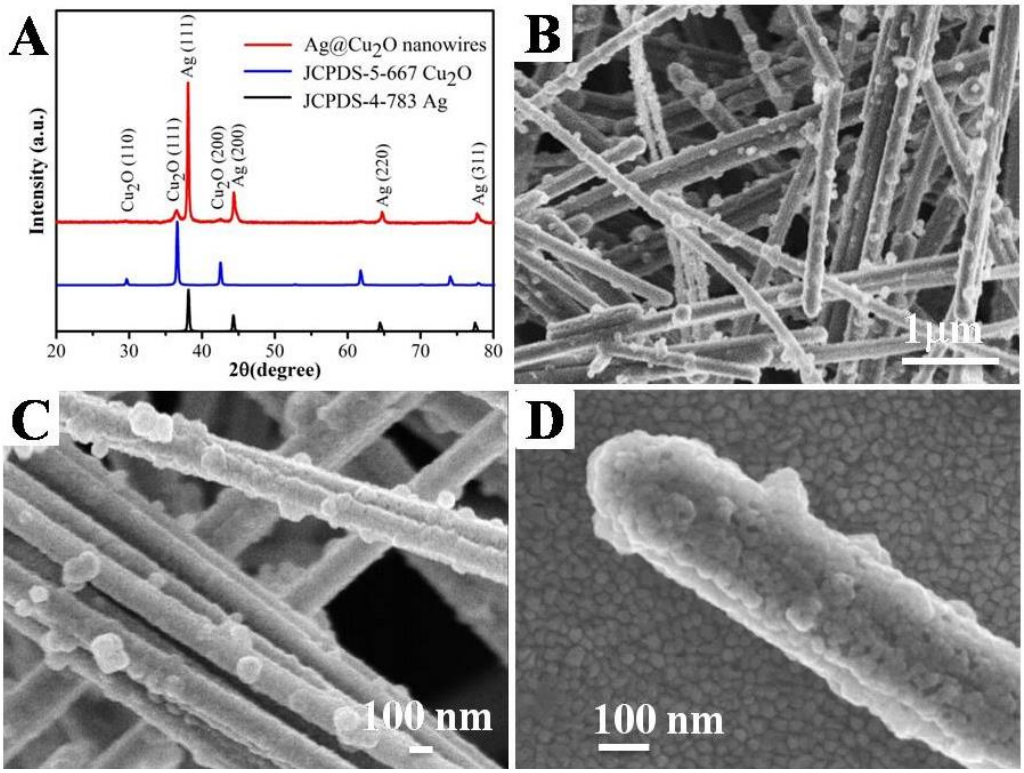

Figure 5.2 (A) XRD pattern and (B-D) SEM images of the as-prepared Ag@Cu_2O core-shell heteronanowires.

Transmission electron microscopy (TEM) was used to further characterize Ag@Cu_2O core-shell hetero-nanowires [Figure 5.3 (A, B)]. Figure 5.3(A) clearly shows individual Ag@Cu_2O hetero-nanowire with a rough surface and a diameter of 170 nm, which consists of 90-nm Ag core and 40-nm Cu_2O shell. The interface between Ag nanowire and Cu_2O nanoparticles is also clearly observed. The HRTEM image in Figure 5.3(B) shows the lattice fringes of 0.25 and 0.24 nm, which correspond to Cu_2O (111) and Ag (111), respectively. The similar lattice fringes observed are attributed to the same cubic crystal structures of Ag and Cu_2O and their small lattice mismatch (i.e. a_{Ag} = 4.08 Å and a_{Cu2O} = 4.27 Å). The distribution of elements in the Ag@Cu_2O core-shell hetero-nanowires is shown in Figure 5.3(C). The upper-left image in Figure 5.3(C) is the area

where the elemental mapping was performed. The green, blue, and red colors represent the distribution of the elements silver, copper, and oxygen, respectively. The presence of the three elements in the nanowires is in agreement with the proposed Ag@Cu_2O composition. The spatial distribution of the colours verifies the core-shell structure, with an Ag core inside and Cu_2O shell outside. The composition of the core-shell hetero-nanowires was further confirmed by the energy dispersive X-ray (EDX) spectrum [(Figure 5.3 (D)]. The EDX results also demonstrate that the as-prepared product is mainly composed of Ag, Cu, and O.

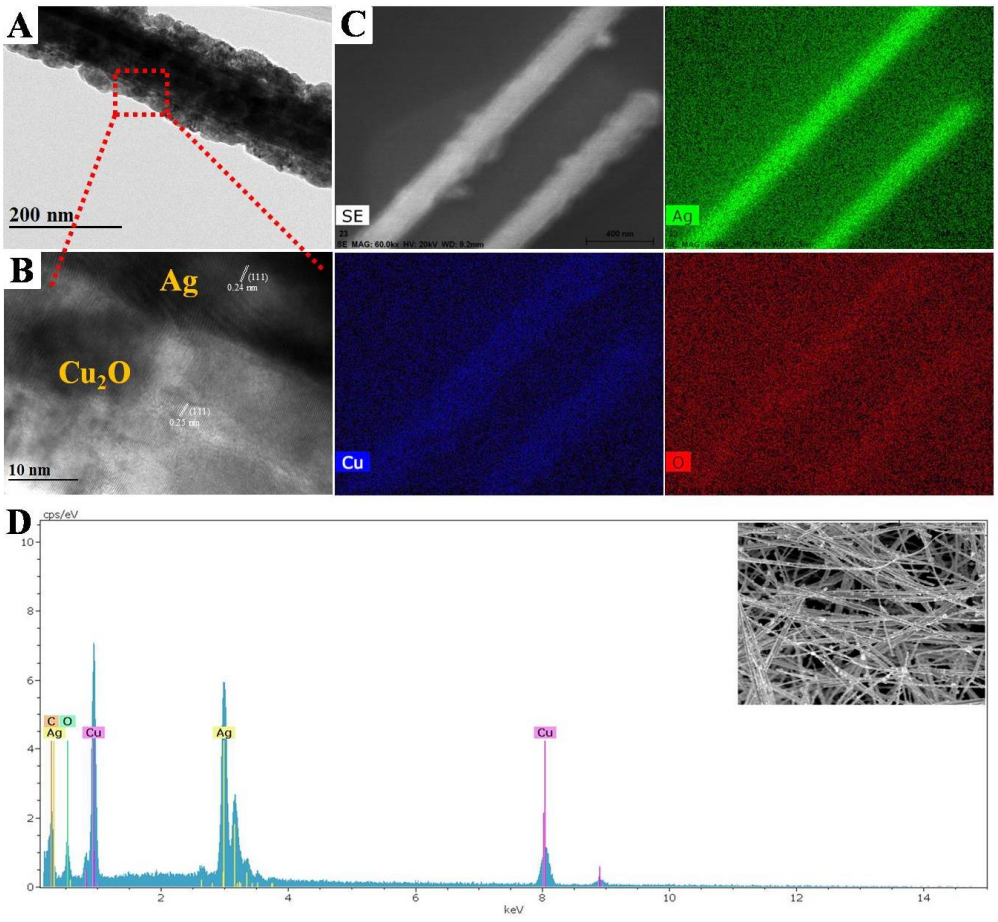

Figure 5.3 (A) TEM image and (B) HRTEM of an individual Ag@Cu_2O core-shell hetero-nanowire; (C) EDX elemental mapping analysis of the Ag@Cu_2O core-shell heteronanowires; (D) EDS pattern of as-synthesized 1D Ag@Cu_2O core-shell hetero-nanowires.

X-ray photoelectron spectroscopy (XPS) measurement has been performed to investigate the surface elemental composition and electronic state of Ag@Cu_2O core-shell hetero-nanowires, as shown in Figure 5.4. The survey spectrum in Figure 5.4(A) shows that except for C, Cu, O and Ag, no other elements are observed in the spectrum, indicating the high purity of the product. The peak at 284.5 eV can be readily assigned to the binding energies of C1s. High-resolution spectra of Ag, Cu and O species are shown in Figure 5.4(B-D), respectively. Two strong peaks at 374.2 eV and 368.1 eV [Figure 5.4(B)] are respectively assigned to Ag2d 3/2 and Ag2d 5/2, which correspond to pure metallic Ag according to the reported results.[298,299] From the high resolution scanning spectra of Cu 2p [Figure 5.4(C)], two main peaks at binding energies of 932.1 and 952.2 eV, together with two shakeup satellites at 942.9 and 962.3eV, were observed in the sample. The peaks at 932.1 and 952.2 eV can be attributed to the binding energies of Cu 2p3/2 and Cu 2p1/2 from Cu^+.[288,291,300] The satellite peaks at 942.9 and 962.3 eV located at higher binding energies are typically associated with Cu^{2+} in CuO or probably $Cu(OH)_2$ species,[291,300,301] implying the presence of Cu^{2+} on the sample surface. These results demonstrate that copper species in Ag@Cu_2O are mainly present as Cu^+, and only a small amount of Cu^{2+} is presented in the sample. This is reasonable as Cu_2O is easy to be oxidized in the process of experiment.[302] Surface Cu_2O could be oxidized into CuO and/or $Cu(OH)_2$ species when they were exposed in air with humidity. The peak at 530.8 eV in Figure 5.4(D) corresponds to O 1s, which is originated from the lattice oxygen of Cu_2O.[291,303] The X-ray photoelectron spectroscopy (XPS) results further confirm the successful synthesis of Ag@Cu_2O core-shell hetero-nanowires.

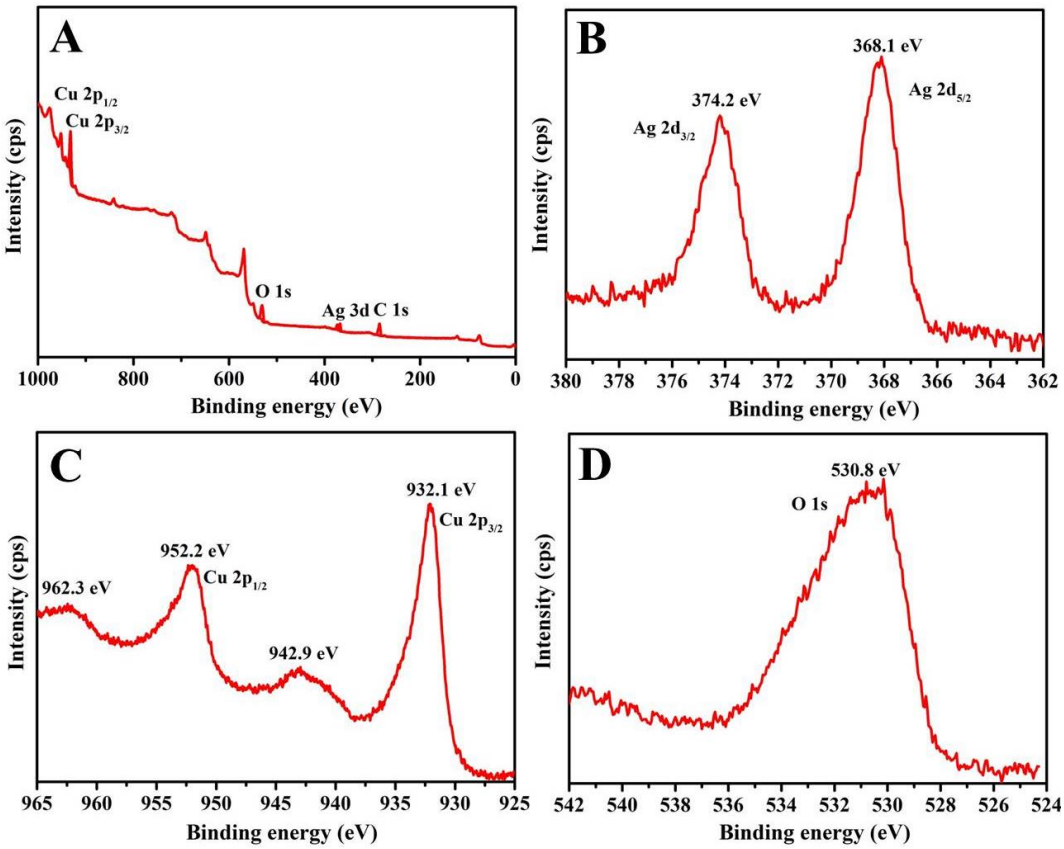

Figure 5.4 XPS spectra of the 1D Ag@Cu_2O core-shell hetero-nanowires: (A) survey-scan spectrum, (B) Ag 2d, (C) Cu 2p, and (D) O 1s.

Ag NWs show intense surface plasmon resonance (SPR) absorption in the visible region, which is highly sensitive to their diameter, length-to-diameter ratio, as well as the optical and electronic properties of their surroundings.[11,235-238] The ultraviolet-visible (UV-vis) absorption spectra of Ag@Cu_2O core-shell hetero-nanowires and pure Ag NWs in ethanol are presented in Figure 5.5. The pure Ag NWs exhibit two absorbance peaks at 350 and 385 nm. The peak at 350 nm could be attributed to the longitudinal mode of nanowires similar to that of bulk Ag[238-240] or the out-of-plane quadrupole resonance of Ag NWs.[241-243] The peak at 385 nm is assigned to the transverse plasmon resonance of Ag NWs.[238-240] Upon the formation of Cu_2O shell, the Ag core plasmon is red-shifted and also appears to be suppressed. On one hand, the transverse plasmon resonance of the Ag core is significantly red-shifted from 385 nm to 515 nm, due to the

higher refractive index of Cu_2O (~2.7 at wavelengths above 600 nm)[7,297,304] than ethanol (~1.359)[238,285] and its high dielectric constant (e=7.2).[297,304,305] On the other hand, surface plasmon resonance (SPR) absorption bands of the Ag NWs appears to be suppressed, due to the thick Cu_2O shells and large particle size.[10,125] Their broad absorbance from visible to UV window is crucial for full use of sunlight.

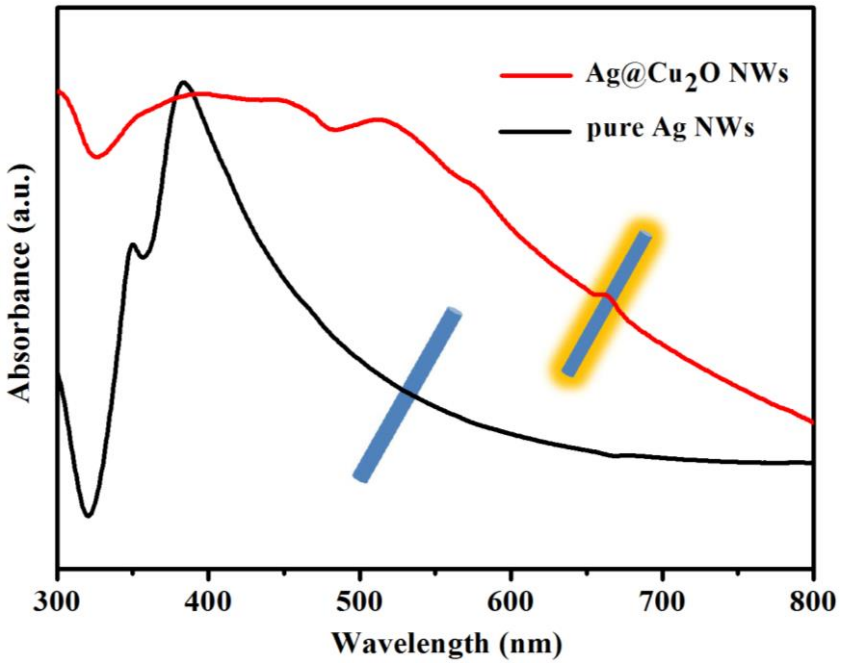

Figure 5.5 UV-vis absorption spectra of as-prepared 1D Ag@Cu_2O core-shell heteronanowires and pure Ag NWs in ethanol.

All the above results confirm our success in obtaining Ag@Cu_2O core-shell hetero-nanowires through this simple solution approach. Figure 5.6 presents SEM images of the core-shell hetero-nanowires collected at different reaction times. As shown in Figure 5.1(B-D), before the growth of Cu_2O, the Ag NWs possess very smooth surfaces. After the Ag NWs were dispersed in $Cu(NO_3)_2$ solution, the hetero-growth of Cu_2O on the surface of the Ag NWs occurred immediately upon the addition of the reducing agent N_2H_4, accompanied by the rapid change of the reaction solution from grey to yellow. As shown in Figure 5.6(A), a well-defined core-shell heterostructure with a rough surface was formed within 2 min, indicating that the formation of Cu_2O is very fast. As the

growth reaction progresses, the obtained core-shell hetero-nanowires show no significant changes, and the surfaces of the Ag NWs are totally covered by the Cu_2O nanoparticles [Figure 5.6(B-D)]. If the reaction was carried out for 12 h, however, some Cu_2O nanoparticles disappeared, and the smooth surface of the Ag NWs was observed [Figure 5.6(E)]. Further prolonging the reaction time to 24 h led to disappearance of most Cu_2O nanoparticles [Figure 5.6(F)]. These results indicate the reversibility of the Cu_2O reactions in our system. The reason for the gradual disappearance of the Cu_2O nanoparticles could be due to the gradual oxidation/dissolving of the Cu_2O by NO_3^- ions in the acidic environment (Figure 5.7). The pH of reaction mixture is maintained between 3.72 and 3.03 within the initial 60 min, however, it is increased to 4.32 after reaction for 24 h. Therefore, the pH of the solution significantly influences the formation of the Cu_2O nanoparticles on the surface of the Ag NWs.

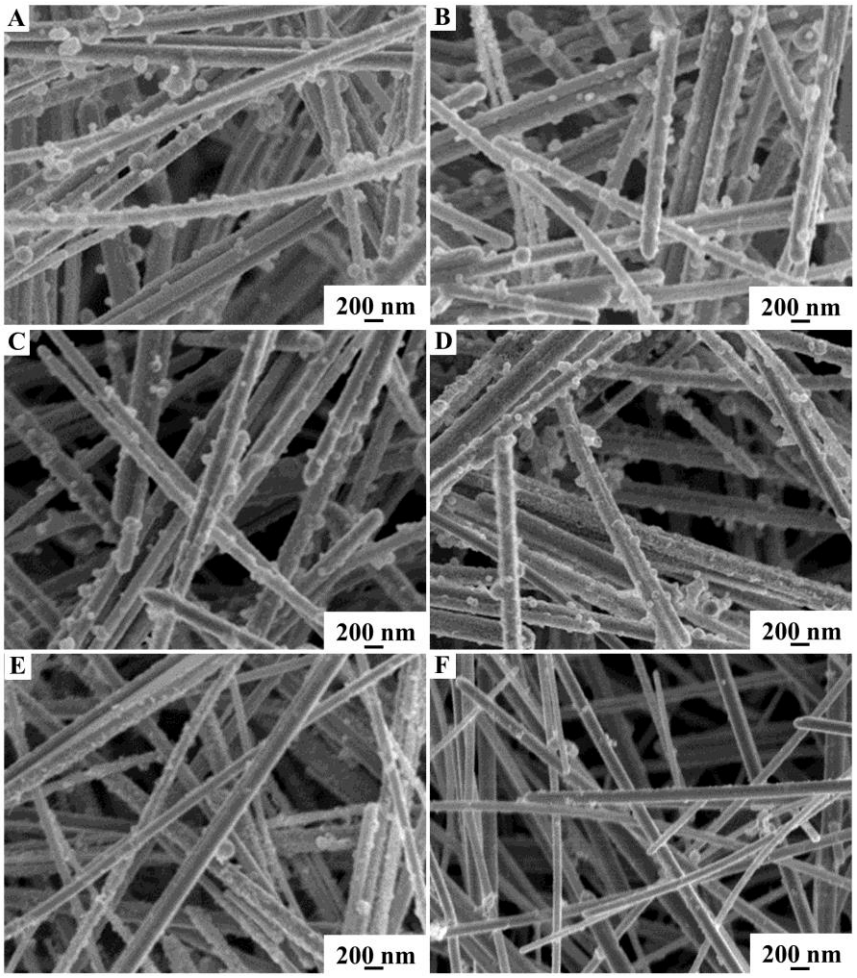

Figure 5.6 SEM images of the products obtained at different reaction times: (A) 2 min, (B) 20 min, (C) 40 min, (D) 60 min, (E) 12 h and (F) 24 h.

Figure 5.7 Photographs of reaction systems composited of Ag NWs, Cu $(NO_3)_2$ solution and N_2H_4 before and after reaction at different stages.

Figure 5.8 presents UV-vis absorption of the core-shell hetero-nanowires collected at different reaction times. As shown in Figure 5.8, the Ag@Cu_2O NWs obtained at 2 min, 20 min, 40 min, and 60 min exhibit similar absorption profiles, in which the SPR peak of Ag cores remained at 515 nm, and didn't shift with the increase of reaction time. This means that Ag NWs were extensively covered by sufficient Cu_2O shell [Figure 5.6(A-D)], and their optical properties were not influenced by external surroundings.[304] The SPR peak of Ag cores in the product obtained at 12 h, however, shifted to shorter wavelength at 395 nm, principally due to the change in the refractive index of surroundings caused by the dearease of Cu_2O thickness. As shown in Figure 5.6(E), Ag cores are not completely covered and some parts are exposured to solvent, which leads to the change in the effective refractive index of surroundings. The decrease in the refractive index causes the shift of SPR band to shorter wavelength.[304] The SPR peak in the product collected at 24 h shifted to 386 nm due to the disappearance of most Cu_2O shells [Figure 5.6(F)], resulting in a similar spectrum to that of pure Ag NWs.

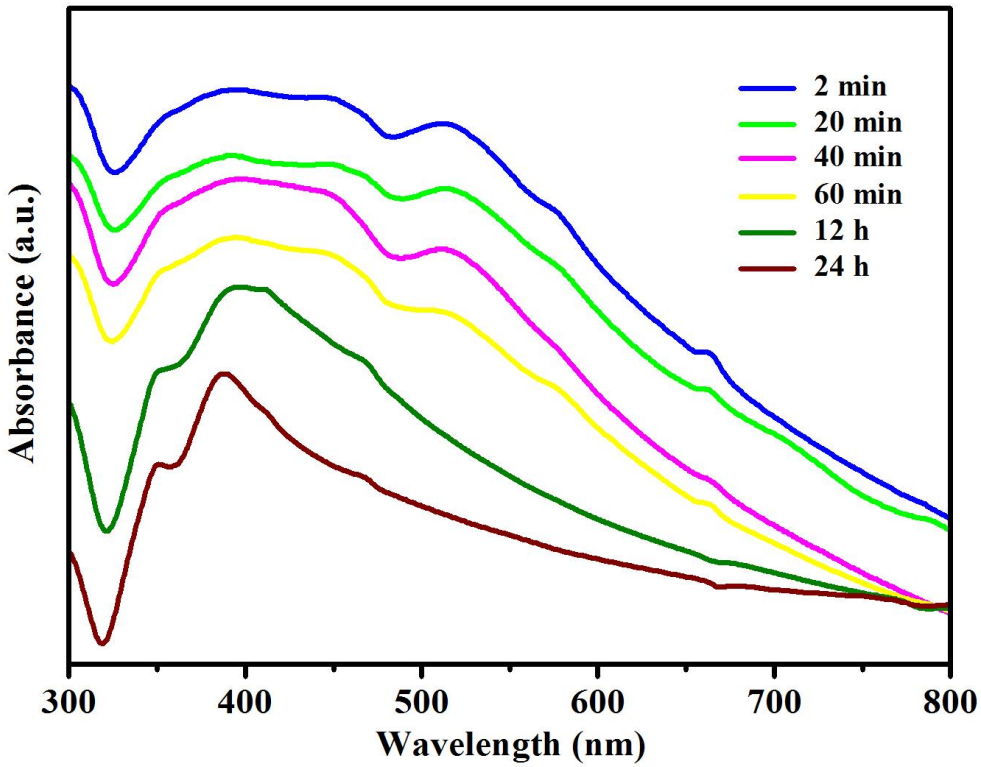

Figure 5.8 UV-vis absorption spectra of the products obtained at different reaction times.

It should be noted that the amount of Ag NWs and $Cu(NO_3)_2$ solution also play important roles in the formation of $Ag@Cu_2O$ core-shell hetero-nanowires. As shown in Figure 5.9(A), when 1 mL of Ag NW solution (~0.038 mmol) is used, the Ag NWs are coated with many nanoparticles, while many free Cu_2O nanospheres with a diameter of about 200 nm are formed at the same time. The reason could be the fast formation of Cu_2O via the reduction of $Cu(NO_3)_2$ and insufficient amount of Ag NWs as anchoring sites, leading to the self-aggregation of the excessive produced Cu_2O nanocrystallites. Increasing the Ag NW solution to 4 mL (~0.15 mmol) leads to an increase in the formation of $Ag@Cu_2O$ core-shell NWs and a decrease in the fraction of free Cu_2O nanospheres [Figure 5.9(B)]. Further increasing the volume of the Ag NW solution to 8 mL (~0.3 mmol) resulted in well-defined $Ag@Cu_2O$ core-shell hetero-nanowires. The Ag NWs are fully covered by Cu_2O nanoparticles, and there are almost no free standing

Cu_2O nanospheres to be found [Figure 5.9(C)]. A thin layer of very small nanoparticles are partly coated on the surfaces of Ag NWs, however, when the amount of Ag NW solution is further increased to 16 mL (~0.6 mmol) [Figure 5.9(D)]. Changing the amount/concnetration of $Cu(NO_3)_2$ couldn't result in well-coated $Ag@Cu_2O$ nanowires [(Figure 5.9(E,F)]. The above results demonstrate that well-defined $Ag@Cu_2O$ core-shell hetero-nanowires can be only achieved under certain conditions.

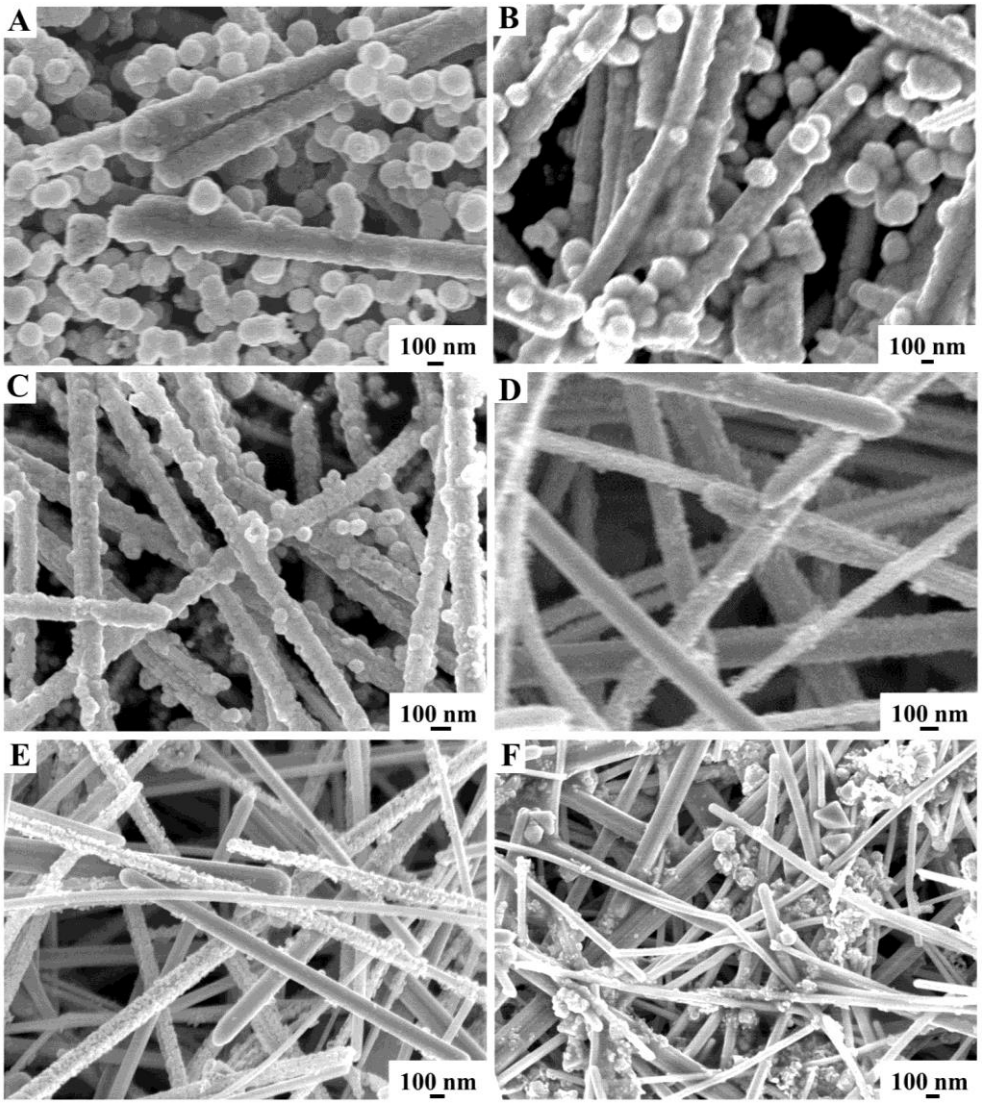

Figure 5.9 SEM images of the products prepared in the presence of different amounts of Ag solution (A-D) and different concentration of Cu^{2+} (E and F): (A) 1, (B) 4, (C) 8, (D) 16 mL, (E) 0.1 M, and (F) 0.2 M.

In order to demonstrate the applicability of our simple method, core-shell Ag@Cu_2O nanoparticles (NPs) [Figure 5.10(A, D-F)] were prepared under similar conditions by using Ag NPs [Figure 5.10(B, G-I)] as seeds. Pure Cu_2O NPs [Figure 5.10(C, J-L)] were also prepared in the absence of Ag for comparison. The resultant Ag@Cu_2O NPs and Cu_2O NPs were examined by XRD and SEM, respectively. The XRD results [Figure 5.10(A-C)] clearly reveal that all the diffraction peaks can be indexed to Ag (JCPDS 4-783) and Cu_2O (JCPDS 5-667), and no other impurity diffraction peaks were observed. The SEM images [Figure 5.10 (D-F)] show that large quantities of Ag@Cu_2O NPs in the range of 100 nm to 230 nm have been successfully fabricated. The pure Cu_2O nanospheres have an average diameter of 440 nm [Figure 5.10(J-L)]. These results demonstrate that the final morphology of the Ag@Cu_2O nanostructures greatly depends on the morphology of the Ag seeds.

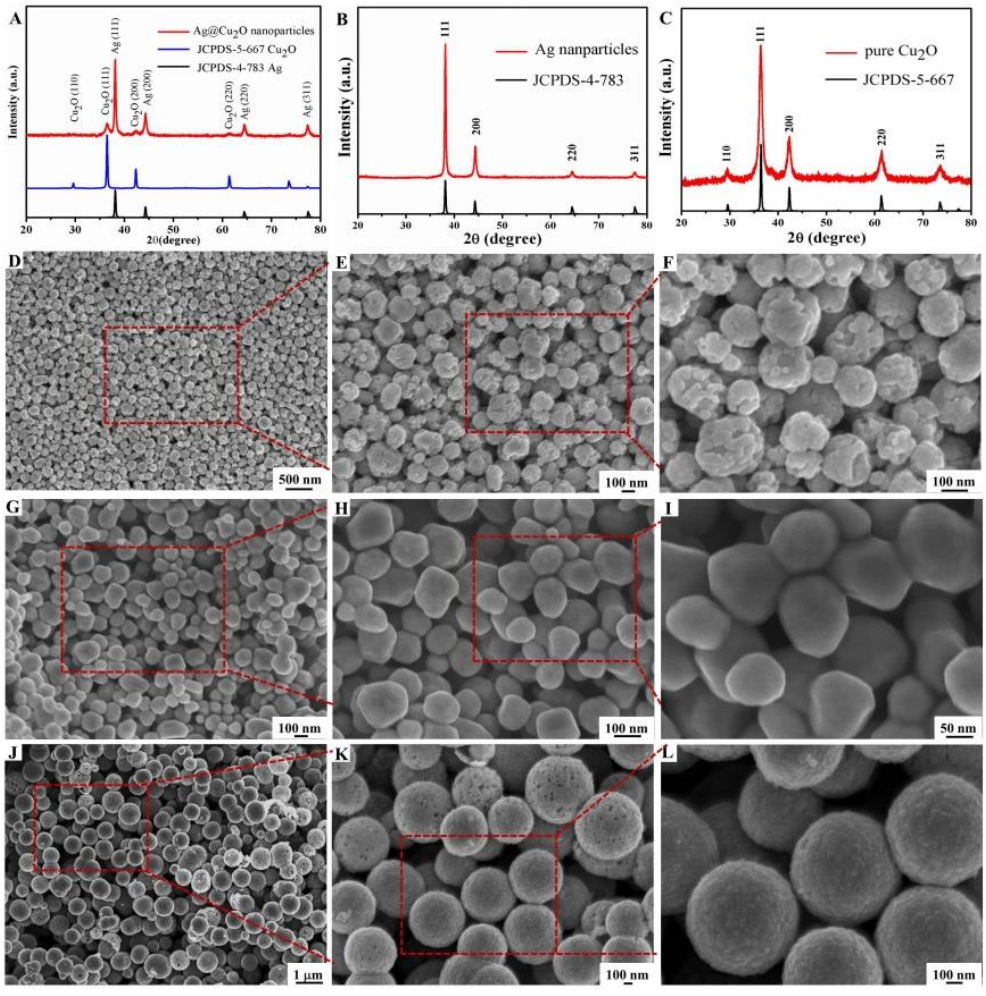

Figure 5.10 (A-C) XRD patterns, and (D-L) SEM images of as-prepared Ag@Cu_2O nanoparticles (A, D-F), Ag nanoparticles (B, G-I), and pure Cu_2O (C, J-L) (red dashed box identified the region each subsequent SEM image zooms in on the preceding image).

The resultant Ag@Cu_2O core-shell nanowires and nanoparticles are expected to show higher photocatalytic activity than pure Cu_2O NPs, due to the plasmonic enhancement of the Ag cores. The performance of the Ag@Cu_2O NWs, Ag@Cu_2O NPs, and pure Cu_2O nanospheres was evaluated by the photodegradation of MO under solar light irradiation. For comparison, the Ag NWs were also tested under identical experimental conditions. Figure 5.11(A-C) shows the absorption spectra of MO solutions after photocatalytic degradation for various durations over Ag@Cu_2O NWs, Ag@Cu_2O NPs, and pure Cu_2O nanospheres, respectively. Under solar light irradiation, the absorption peak at 464 nm diminishes gradually as the irradiation time increases. As shown in Figure 5.11(D), it can be clearly observed that in the absence of catalyst and in the presence of only Ag NWs under solar light irradiation, there is no evident photodegradation of MO. In contrast, the as-prepared Ag@Cu_2O NWs, Ag@Cu_2O NPs, and pure Cu_2O nanospheres all exhibit excellent photocatalytic performance. Under the solar light irradiation and in the presence of the photocatalyst (Ag@Cu_2O NWs or Ag@Cu_2O NPs or pure Cu_2O nanospheres), the significant MO degradation could involve in both a photocatalytic pathway and a photosensitization pathway, which is similar to the reported literatures.[306-308] Moreover, both the core-shell Ag@Cu_2O NWs and the Ag@Cu_2O NPs show higher photocatalytic activity than that of the pure Cu_2O nanospheres, while the Ag@Cu_2O core-shell NWs exhibit the highest performance, which can decolor 92% of MO within 140 min, while 83% and 71% of MO can be degraded over the Ag@Cu_2O NPs and pure Cu_2O nanospheres, respectively. In compared with previously reported Ag@Cu_2O nanoparticles and Cu_2O-Au composites, our nanostructures exhibit higher photoactivity in degradation of MO, e.g. 90% MO can be degraded by core-shell Ag@Cu_2O NWs within 2 h, but only ~75% MO was

degraded by the Ag@Cu_2O nanoparticles within the same time[11] and ~60% MO was degraded within 4 h by Cu_2O-Au composites.[163] The results clearly demonstrate that the hetero-growth of Cu_2O nanoshells on Ag NWs to build 1D core-shell heterostructures has been proven to be a useful and successful strategy for improving the photocatalytic properties of Cu_2O crystals.

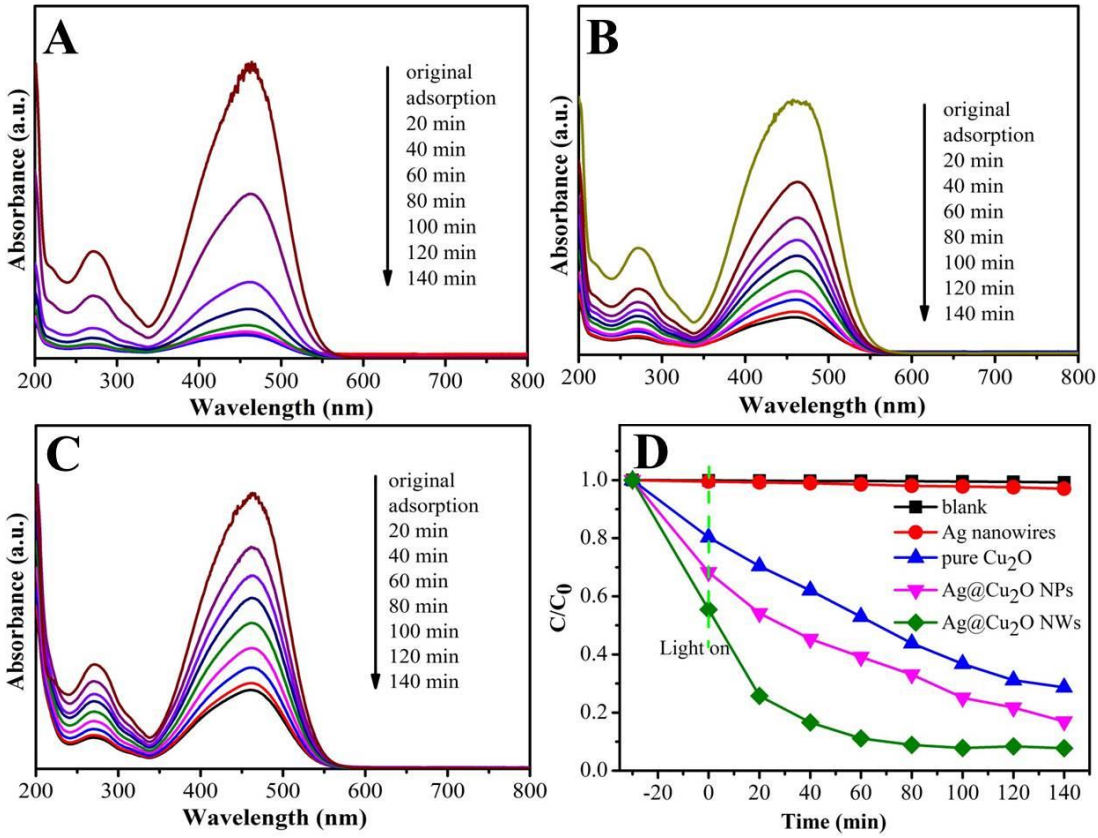

Figure 5.11 (A-C) Variation in the light absorption of the MO solution in the presence of the as-prepared photocatalysts under solar light irradiation for different irradiation times: (A) Ag@Cu_2O NWs, (B) Ag@Cu_2O NPs, and (C) pure Cu_2O nanospheres; (D) photocatalytic activity of MO oxidation under solar light irradiation.

In order to better understand the good performance of our core-shell Ag@Cu_2O NWs, their XRD, XPS, SEM and TEM characterizations have been conducted after photocatalytic test. The XRD pattern shows that the dominant peaks of Cu_2O (111) and

(200) become much weaker after photocatalysis test [Figure 5.12(A)]. In addition, there is no other peak detected except that of Ag nanowires. The binding energies measured by XPS show two peaks at 934.4 and 954.2 eV, which are respectively assigned to Cu 2p3/2 and Cu 2p1/2 of copper ions. Devolution of Cu 2p peaks into Cu^{2+} and Cu^{+} revealed two small peaks of Cu^{+} from Cu_2O at 932.6 and 952.3 eV, respectively [Figure 5.12(B)]. The peaks of Cu^{2+} stronger than that of Cu^{+} after photocatalytic test suggest a dense protection layer of CuO or $Cu(OH)_2$ on the surface of Cu_2O.

It should be noted that the morphology of photocatalysts changed after photocatalytic test. There are many sheet-like structures and uncovered Ag NWs formed due to the loss of Cu_2O nanoparticles [Figure 5.12(C)]. The TEM image in Figure 5.12(D) further confirms the loss of Cu_2O nanoparticles and the decrease of their density on the surface of Ag NWs. This result is similar to the previous reports,[287,309] and the morphology transformation could be explained as follows. Cu_2O nanoparticles are irradiated by solar light to produce electrons and holes. On the one hand, the photogenerated electrons quickly transferred to Ag NWs, which acting as electron sinks, not only reduce the recombination of photoinduced electrons and holes but also prolong the lifetime of photogenerated pairs. The photogenerated electrons accumulated in the conduction band of Cu_2O also transferred to O_2 molecules adsorbed on its surface, which facilitated their multiple-electron reduction reactions. The formed reactive species ($\cdot O_2^-$) can effectively bleach the dye. On the other hand, Cu_2O are oxidized into CuO by the accumulated holes in them, and the intermediate CuO can also generate electron-hole pairs under irradiation of solar light. As the photogenerated holes are captured by MO and the accumulated electrons can reduce CuO into Cu_2O, accompanied by the formation of sheet structure. [284,303]

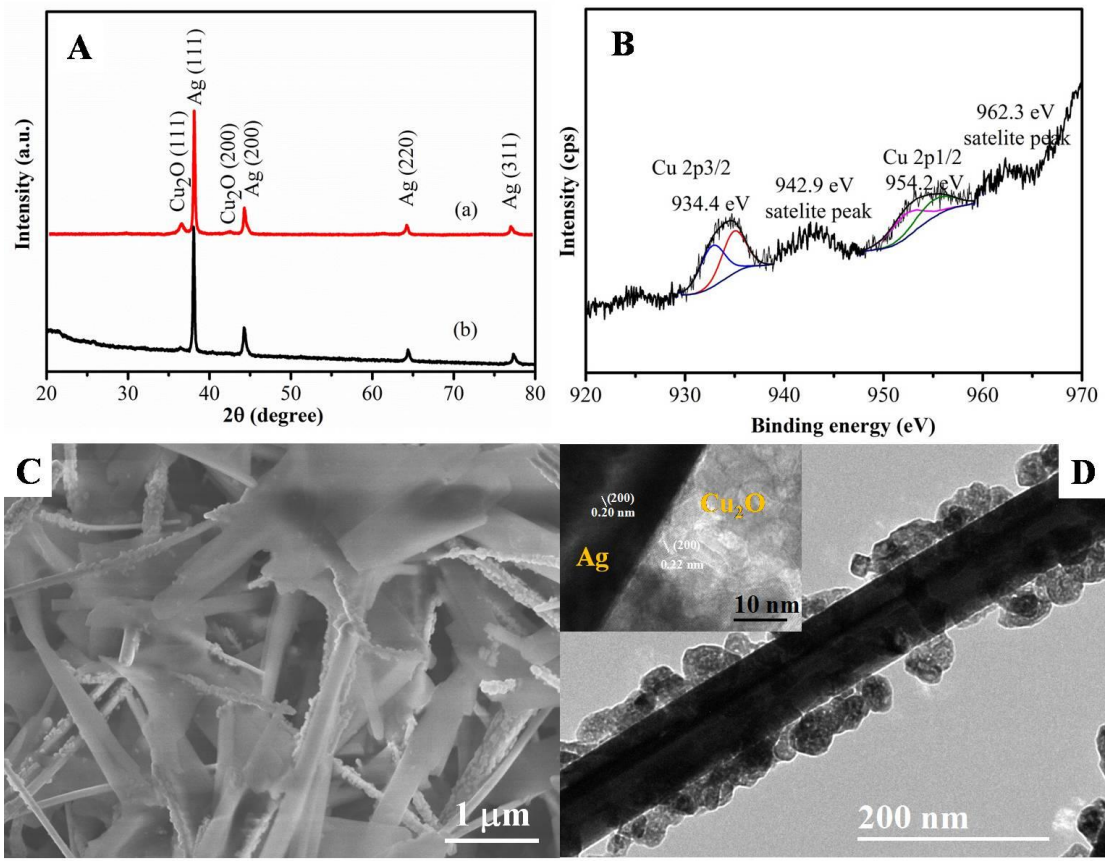

Figure 5.12 (A) XRD patterns of the sample before (a) and after (b) photocatalytic test; (B) XPS spectrum of Cu 2p, (C) SEM image and (D) TEM image of the sample after photocatalytic test.

It was reported that in the photodegradation of organic pollutants, reactive species such as $\cdot O_2^-$, h^+ and $\cdot OH$ played as bridge role of photocatalysts under the light irradiation,[310-313] and they could vary with the different photocatalysts.[314,315] To investigate the photocatalytic mechanism and to understand the better performance of 1D Ag@Cu_2O core-shell photocatalysts, the effect of scavengers on the degradation of MO was examined to clarify the contribution of different reactive species during photocatalysis study. P-benzoquinone (PBQ) is used as $\cdot O_2^-$ scavengers,[261,310-313,316,317] triethanolamine (TEOA) as h^+ scavengers,[261,314,315] and isopropanol (IPA) as $\cdot OH$ scavengers.[316,318] These scavengers were added into the MO solution together with the 1D Ag@Cu_2O core-shell hetero-nanowires before irradiation. As depicted in Figure 5.13, the complete

inhibition of degradation of MO in the presence of TEOA suggests that photogenerated holes are the major reactive species for the photocatalytic degradation of MO. The dramatic decrease in degradation of MO arising from removal of oxygen with N_2 bubbling demonstrates that molecular oxygen also played an important role in the photodegradation of MO over 1D Ag@Cu_2O core-shell hetero-nanowires. This is attributed to the electron trapping role of molecular oxygen, which could produce $\cdot O_2^-$ to inhibit the recombination of electron-hole pairs, and leave over holes to oxidize MO. The elimination of molecular oxygen would diminish the amount of holes and prevent the oxidation of MO due to the fast combination of electron-hole pairs. In order to confirm the roles of $\cdot O_2^-$ in the degradation of MO, PBQ is employed as the $\cdot O_2^-$ scavenger. The results show that the presence of PBQ significantly decreased the MO photodegradation efficiency from 92% to 45% within 140 min for 1D Ag@Cu_2O core-shell hetero-nanowires. In contrast, the addition of IPA had little effect on the MO degradation. The above results illustrate that both h^+ and $\cdot O_2^-$ are the main reactive species for 1D Ag@Cu_2O core-shell hetero-nanowires in the photocatalytic decolorization of MO under solar light irradiation, and the reactive $\cdot OH$ preferred to react with MO dye, due to the presence of N=N double bond and benzene ring in the azo-dye MO molecules, which are more reactive than hydroxyl group in IPA.[306,319]

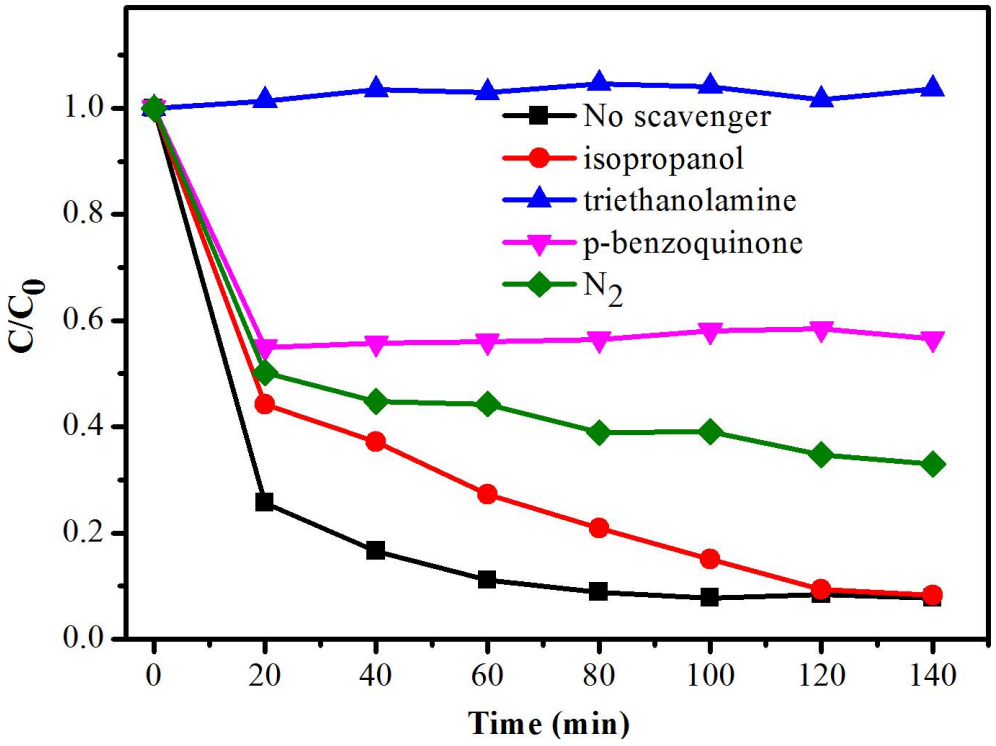

Figure 5.13 Photocatalytic degradation of MO over the 1D Ag@Cu_2O core-shell hetero-nanowires in the presence of scavengers.

The enhancement in photocatalytic activity of the 1D core-shell Ag@Cu_2O NWs may be ascribed to the synergistic effects of Ag NWs and surface Cu_2O. As evidenced by SEM and TEM images, there are clear interfaces between Ag NWs and Cu_2O nanoparticles, which can effectively suppress the recombination rate of electron-hole pairs.[15] More specifically, first, the direct coupling of Ag NWs and Cu_2O causes the Fermi level to equilibrate, which can lead to trapping of charges and increase carrier life.[11] The Ag NWs in the core-shell structures produce a Schottky barrier at the interface between the core and shell, which facilitates the capture and quick transfer of photoexcited electrons from the Cu_2O nanoshells to the Ag NWs under solar light irradiation [Figure 5.14].[15,284,320] The electrons accumulated in the Ag NWs are transferred to O_2 molecules to produce superoxide radical anions ($\bullet O_2^-$) through the multiple-electron reduction reactions to decompose organic pollutant.[43] Accumulation of the photoinduced holes in the valence band of the Cu_2O nanoshells leads to the

production of the hydroxyl radical (•OH) at the surface, which is responsible for the oxidation decomposition of the MO molecules.[284] Photo-excited electrons are effectively accumulated in the Ag NWs without recombining with holes, which could promote the effective separation of photogenerated electron-hole pairs. This leads to the significant enhancement of the photocatalytic activity of the Ag@Cu_2O core-shell structures. Second, the unique 1D Ag@Cu_2O core-shell nanostructures are expected to have excellent electron conductivity and mobility. The presence of metal nanowires can facilitate fast and long-distance electron transport, and the fast transfer of photo-induced electrons and holes over the Ag NWs and Cu_2O nanoshells suppresses the recombination of electron-hole pairs, which is favorable for highly efficient photocatalytic performance. Third, the core-shell Ag@Cu_2O nanowires have a large specific surface area for adsorbing dyes (45%, 32%, and 20% MO adsorption in the dark equilibration for Ag@Cu_2O NWs (10.3 m^2/g), Ag@Cu_2O NPs (8.8 m^2/g), and pure Cu_2O nanospheres, respectively, in our experiment), which can provide more active sites for the photodegradation of MO and thus promote diffusion of reactants and products during the reaction, accelerating the chemical reactions. Fourth, the high length-to-diameter ratio of the 1D metal-core@semiconductor-shell hetero-nanostructures may enhance the light absorption, trapping, and scattering through a local field enhancement effect of plasmonic Ag NWs,[321] and thus increase the quantity of photogenerated electrons and holes available to participate in the photocatalytic reactions, leading to an enhanced photocatalytic property of the Cu_2O.[320] It should be noted, however, that the photocatalytic mechanism over such 1D Ag@Cu_2O core-shell hetero-nanowires is still not completely understood, and a more detailed study is still underway.

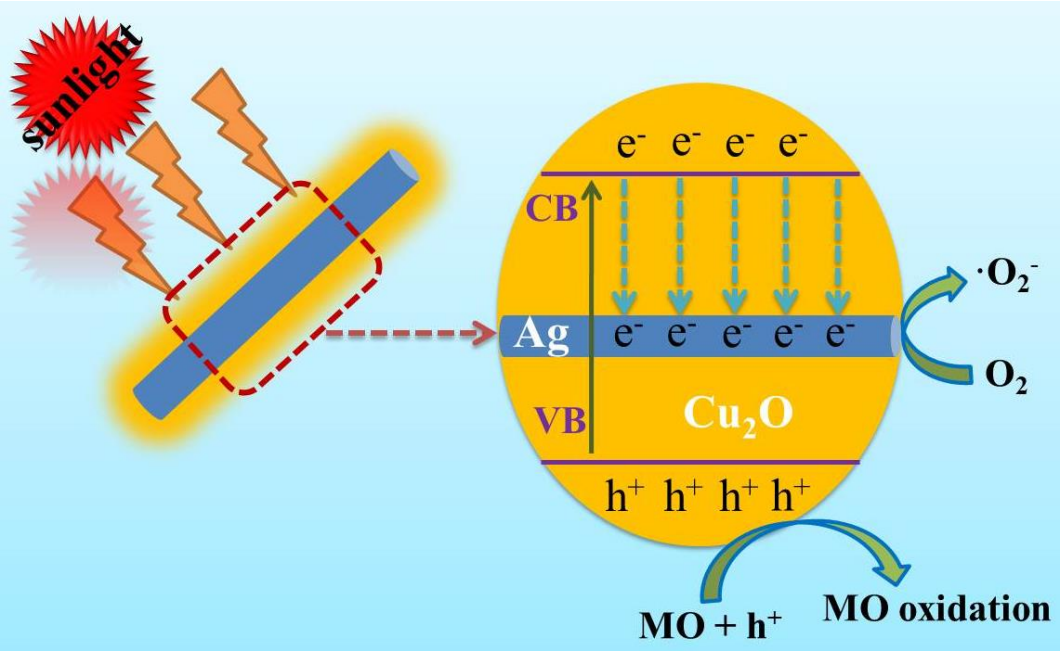

Figure 5.14 Schematic illustration of the transfer of photogenerated electron-hole pairs in the Ag@Cu_2O core-shell NWs under solar light irradiation.

5.4 Conclusion

In summary, 1D core-shell Ag@Cu_2O hetero-nanowires have been fabricated by a facile solution process at room temperature. The resulting unique heterostructures exhibit greater plasmonic enhancement of photocatalytic activity in MO oxidizing than Ag@Cu_2O nanoparticles and pure Cu_2O under solar light irradiation. Such rational design and fabrication of 1D metal-core@semiconductor-shell architectures may hold great potential in solar energy conversion, especially as an effective technique to improve photocatalytic activity.

Chapter 6 Facile synthesis of Ag@CdS Core-Shell hierarchical heteronanowires as highly efficient photocatalyst

6.1 Introduction

Recently, considerable interesting has been attracted on semiconductor-based photocatalysis because of its wide applications in renewable energy exploiting and developing as well as in environmental remediation and protection.[52,53,322-325] CdS is one such attractive visible-light-driven photocatalyst with a small band gap (2.4 eV), which make it an appealing candidate for application in hydrogen production and organic pollutant degradiation.[38,66,102,326-328] The inherent limitation of fast recombination rate of photoinduced electron-hole pairs, however, leads to reduced photocatalytic efficiency.[38,102] To enhance the lifetime of photogenerated carriers, modifications of CdS have been designed through combining it with novel plasmonic metals (e.g. Ag, Au, Pd, Pt).[7,27,35,38,102,178,180,182,329]

Compared with other noble metals, Ag is more attractive because of its high electrical and thermal conductivity, antibacterial characteristics, low cost, and nontoxicity. Ag nanostructures exhibit a wealth of optical and photoelectrochemical properties directly related to their geometry-dependent surface plasmon resonances, which makes 1D Ag nanostructures great potential candidates in the field of photocatalysis.[70,101,238] Furthermore, heterostructures of Ag nanowires (NWs) have also been widely reported in recent years, such as Ag-AgCl,[295] Ag-Ag_3PO_4,[42] Ag-TiO_2,[36] Ag-Cu_2O,[70] and Ag-ZnO [71]. In the case of the Ag-CdS hybrids, although there are a few reports on the degradation of organic pollutants, 1D architectures with hierarchical structures are rarely discussed. Such hierarchical nanostructures are able to interact with liquids and gases both at the surface and internally, and have attracted considerable attention for application in the field of photocatalysis.[327] Furthermore, the presence of metal Ag NWs in the hybrid makes it capable of transporting electrons more efficiently through those

Ag NWs during the process of irradiation, leading to a low recombination rate and thus to improved photocatalytic activity.

In this chapter, a simple oil bath approach was employed to synthesize 1D Ag@CdS core-shell NWs with hierarchical nanostructures. The morphology and structure of the as-prepared Ag@CdS core–shell NWs can be altered through tailoring the amounts of $Cd(NO_3)_2 \cdot 4H_2O$/thiourea. A systematic account of the research is presented, giving a detailed characterization of the morphology, crystal structure, phase constituents, and chemical composition. Moreover, the photocatalytic activity of the as-synthesized Ag@CdS core–shell NWs was evaluated by degradation of methyl orange (MO) and hydrogen production, and the 1D hierarchical Ag@CdS NWs showed better photocatalytic performance, which could result form their specific hierarchical nanostructures and proper constitution.

6.2 Experimental section

6.2.1 Experimental methods

Ag nanowires (Ag NWs) were fabricated according to our reported method.[71] In a typical synthesis, 10 mL 1,2-propanediol containing PVP40 was loaded into a 25-mL vial and heated under magnetic stirring in an oil bath at 135 ℃ for 1 h. NaCl was then quickly added, and the stirring was continued for another 5 min, followed by the addition of $AgNO_3$ solution. The mixed solution was then heated at 135 ℃ with magnetic stirring for 1 h, yielding the grey Ag NWs.

Core-shell Ag@CdS hierarchical hetero-nanowires were synthesized by a simple solution process. Typically, 1.2 mmol $Cd(NO_3)_2 \cdot 4H_2O$ and 0.6 mmol thiourea were added into 8 mL freshly prepared Ag NW solution to be dissolved under constant magnetic stirring for 30 min, and then 1 mL $NH_3 \cdot H_2O$ was added into the above reaction mixture with stirring for another 5 min. Next, the solution was stirred at 80 ℃ in oil bath for 1 h, and then the resultant samples were separated by centrifugation,

washed with Milli-Q water and absolute ethanol to remove impurities, and then dried at 60 ℃ (**A1**). Other samples (**A2**-**A17**) were also prepared under the identical conditions by varying the amounts of $Cd(NO_3)_2 \cdot 4H_2O$/thiourea. The detailed experimental parameters are listed in Table 6.1.

Pure CdS nanostructures were prepared using a similar procedure to that for Ag@CdS core-shell hetero-nanowires, except that 1,2-propanediol was added rather than the Ag NW solution.

Table 6.1 Experimental conditions for the synthesis of Ag@CdS core-shell hetero-nanowires.

Sample	Ag NWs (mL)	$Cd(NO_3)_2 \cdot 4H_2O$ (mmol)	Thiourea (mmol)	$NH_3 \cdot H_2O$ (mL)
A1	8	1.2	0.6	1
A2	8	1.2	0.6	---
A3	8	0.3	0.6	1
A4	8	0.6	0.6	1
A5	8	1.8	0.6	1
A6	8	2.4	0.6	1
A7	8	1.2	1.2	1
A8	8	1.2	2.4	1
A9	8	0.075	0.075	1
A10	8	0.15	0.15	1
A11	8	0.3	0.3	1
A12	8	0.15	0.075	1
A13	8	0.075	0.15	1
A14	8	0.3	0.15	1
A15	8	0.15	0.3	1
A16	8	0.6	0.3	1
A17	8	0.3	0.6	1

6.2.2 Characterization

The X-ray diffraction (XRD) measurements were performed on a GBC MMA X-ray diffractometer using Cu $K\alpha_1$ radiation (40 kV). The XRD patterns were recorded from 20 ° to 80 ° with a scanning rate of 4 °/min. Scanning electron microscope (SEM) images were collected using a field-emission scanning electron microscope (JSM-7500FA, JEOL) operated at an accelerating voltage of 5 kV. Transmission electron microscope (TEM) images and EDX spectra were collected on a field-emission transmission electron microscope (ARM-200F, JEOL), using an accelerating voltage of 200 kV. Ultraviolet/visible (UV/vis) absorption spectra were collected at room temperature on a UV-3600 (Shimadzu) spectrometer.

6.2.3 Photocatalytic testing

Photodegradation of MO over the as-synthesized Ag@CdS core-shell hybrids was evaluated under irradiation with a LSC-100 Solar Simulator (Newport). In an experiment, 20 mg photocatalyst was added into 50 mL of MO solution (10 mg/L) at room temperature. Prior to irradiation, the suspension was stirred in the dark to ensure the establishment of an adsorption-desorption equilibrium between the photocatalyst and the MO. Then, the solution was exposed to solar light irradiation under magnetic stirring. At each irradiation time interval, 2 mL of the suspension was collected and then centrifuged to remove the photocatalyst. The concentration of MO was analysed by a Shimadzu UV-3600 spectrophotometer, and the characteristic absorption of MO at 464 nm was used to evaluate its photocatalytic degradation. All of the measurements were carried out at room temperature.

The hydrogen evolution reaction over the as-synthesized Ag@CdS core-shell hybrids was performed in a glass gas-closed-circulation system with a top irradiation-type reaction vessel (LabSolar H_2). A 300-W Xenon lamp (Perfect, China) with a 420 nm cut-off filter ($\lambda \geq 420$ nm) was used as a visible-light source. The temperature of the reactant solution was maintained at 20℃ by a flow of cooling water during the test. In a

typical experiment, 30 mg photocatalyst was added into 50 mL of aqueous solution containing 0.25 M Na_2SO_3 and 0.35 M Na_2S as sacrificial reagents. Prior to the hydrogen evolution reaction, the system was evacuated by a pump and stirred for 30 min to remove the dissolved air in water. The amount of hydrogen gas was automatically analysed by an on-line gas chromatograph (GC-2014C).

6.3 Results and discussion

The phase compositions and purities of the as-prepared products were characterized by X-ray diffraction (XRD). Figure 6.1A shows a typical XRD pattern of the as-prepared sample. All of the diffraction peaks could be indexed to those of hexagonal wurtzite CdS (JCPDS No. 41-1049) and face-centred-cubic Ag (JCPDS card No. 04-0783). The lack of any characteristic peaks of impurities in the XRD pattern indicates the high purity of the products. The elemental compositions of the as-prepared samples were determined by energy dispersive X-ray (EDX) spectroscopy. As shown in Figure 6.1B, the EDX spectrum displays strong peaks due to exciting of the Ag, Cd, and S elements with weight percentages of 24.73 %, 56.16 %, and 19.11 %, respectively. Quantitative analysis confirmed that the atomic ratio of Ag:Cd:S is about 1 : 2.2 : 2.6, indicating a Ag/CdS composition. The Cu peak comes from the copper grid used to hold the sample for the TEM observations. These results confirmed the successful synthesis of the Ag@CdS hybrid.

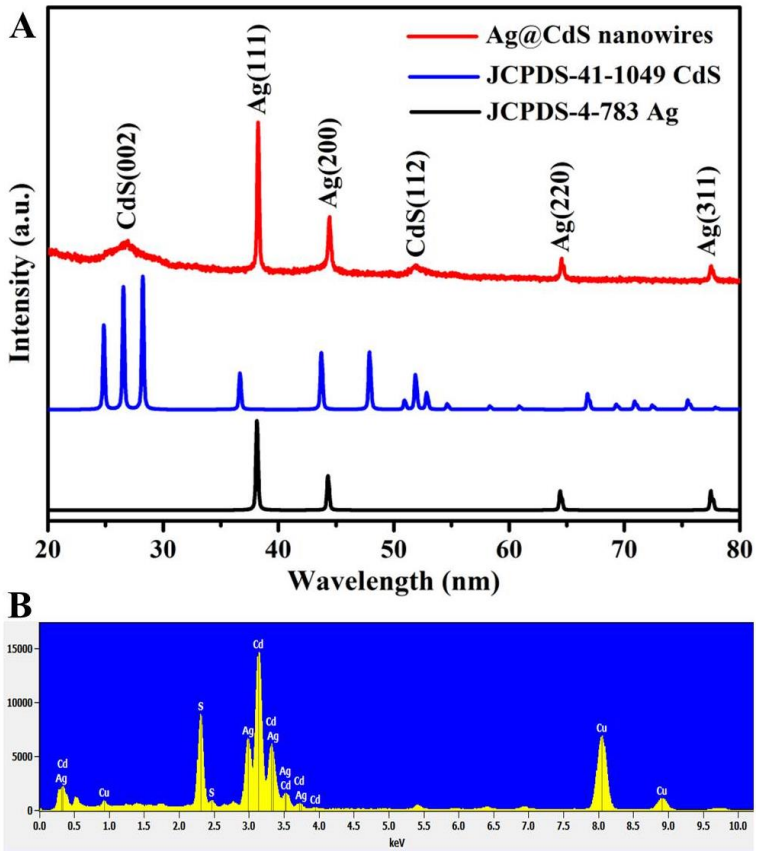

Figure 6.1 (A) XRD pattern and (B) EDX spectrum of the as-prepared Ag@CdS heterostructures (A1), for which the added amount of $Cd(NO_3)_2 \cdot 4H_2O$/thiourea was 1.2 mmol/0.6 mmol, respectively.

Characterizations by scanning electron microscopy (SEM) and transmission electron microscopy (TEM) provide insight into the morphology and detailed structure of the as-prepared Ag@CdS hybrid. A panoramic view of the as-prepared sample shows uniform hierarchical nanowire structures (Figure 6.2A). The enlarged SEM image in Figure 6.2B clearly reveals dense growth of many interleaved nanosheets and a few nanoparticles over the entire surface of the 1D nanowire to form a hierarchical nanostructure, with no visible individual or isolated CdS nanosheets or nanoparticles. Figure 6.2C clearly shows a TEM image of an individual Ag@CdS hierarchical nanostructure, in which sheet-like leaves surround the 1D nanowire to construct a hierarchical core-shell architecture. The hybrid shows strong contrast between the boundary and the centre of

the composite, in which the darker core is metallic Ag, and the brighter shell would be semiconducting CdS. The high-resolution TEM (HRTEM) image in Figure 6.2D shows lattice fringes with a spacing of 0.33 nm, which corresponds to the (002) planes of hexagonal wurtzite CdS. High-angle annular dark-field (HAADF) imaging was used to identify each chemical component. Due to the differences among Ag, S, and Cd in scattering electrons, the as-prepared Ag@CdS hybrid has different contrast in the HAADF image (Figure 6.2E), which is opposite to those observed in the bright field image, i.e. the bright segments indicate the presence of the heavier metal Ag, and the dark parts indicate the presence of CdS.

Furthermore, the distribution of elements in the Ag@CdS core–shell hetero-nanowires was studied with energy-dispersive X-ray (EDX) elemental mapping [Figure 6.2(F-H)]. The HAADF-TEM image in Figure 6.2E is the area where the elemental mapping was obtained. The blue, pink, and yellow colours represent the distributions of silver, sulfur, and cadmium, respectively. The presence of the three elements in the nanowires is in agreement with the proposed Ag@CdS composition. The spatial distribution of the colours verifies the core–shell structure, where the element Ag is located in the core, and the elements S and Cd of CdS are distributed on the outside as the shell.

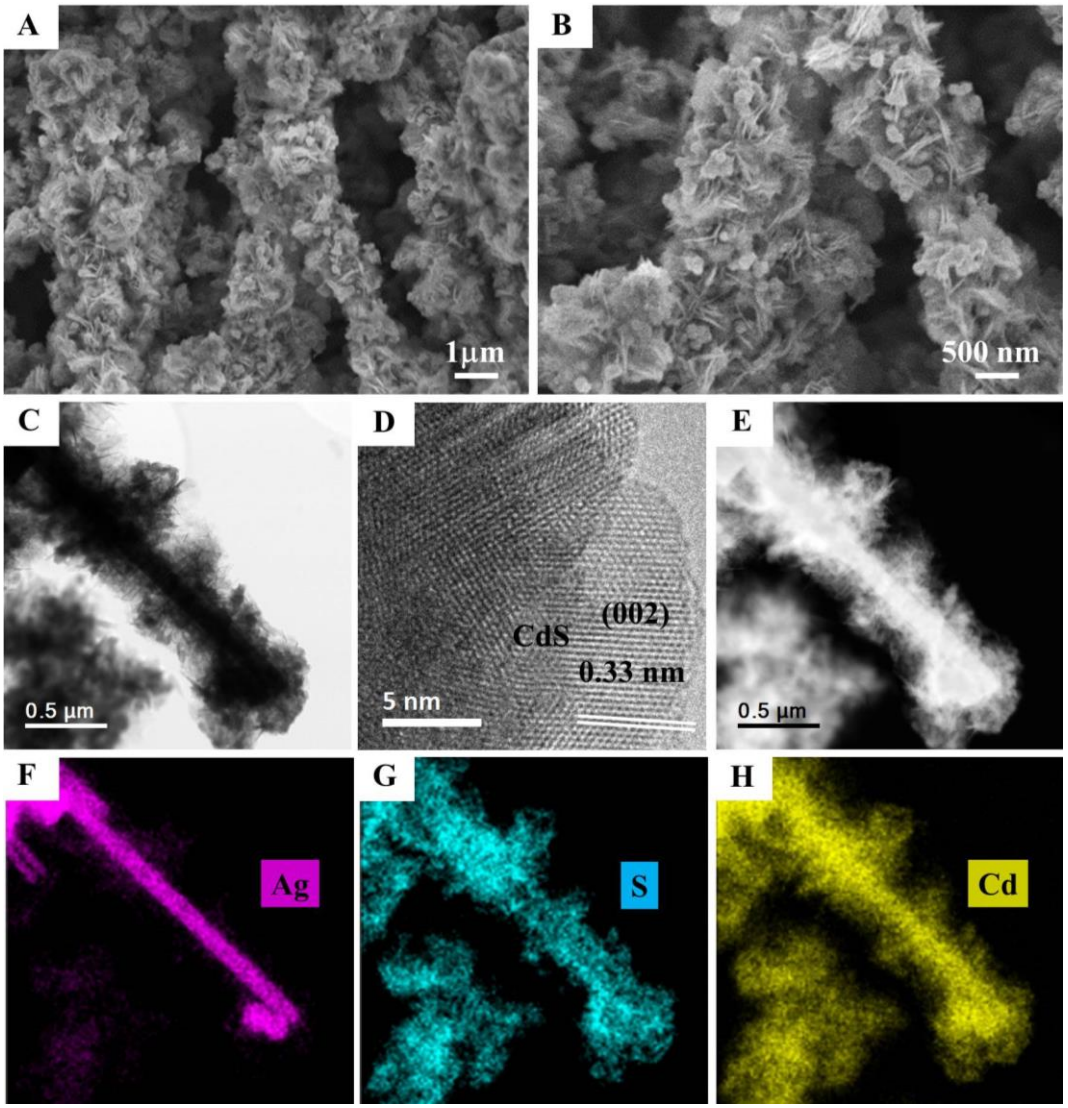

Figure 6.2 (A and B) SEM images of the as-prepared Ag@CdS heterostructures (A1) with the added amount of $Cd(NO_3)_2 \cdot 4H_2O$/thiourea 1.2 mmol/0.6 mmol; (C) TEM image, (D) HRTEM image, (E) HAADF STEM image, and (F-H) the corresponding EDX elemental mapping analysis of an individual Ag@CdS heterostructure.

Optical properties of the Ag@CdS heterostructures have been studied by analyzing UV-vis absorption spectra (see Figure 6.3). Remarkably, the surface plasmon resonance (SPR) absorption bands of the Ag NWs are significantly weakened and broadened, and there is a new characteristic absorption feature of CdS crystals with a weak band-gap absorption band at around 490 nm, which is similar to the reported absorption at 489 nm

of CdS NWs,[330] and 468-496 nm of CdS nanoparticles.[331] The spectral results observed herein could possibly reflect contributions to the synergistic effects between Ag NWs and CdS shells in Ag@CdS hybrids, and provide strong evidence that Ag NWs have essentially turned into Ag@CdS hybrid, with the product mainly composed of the CdS component,[332] as well as suggesting that the good contact between the Ag core and CdS shell might ensure effective charge transfer across the phase boundary and cause changes in the structure and shape of the product.[207,333] Their broad absorbance from the UV to the near-infrared window is crucial for the full use of sunlight.

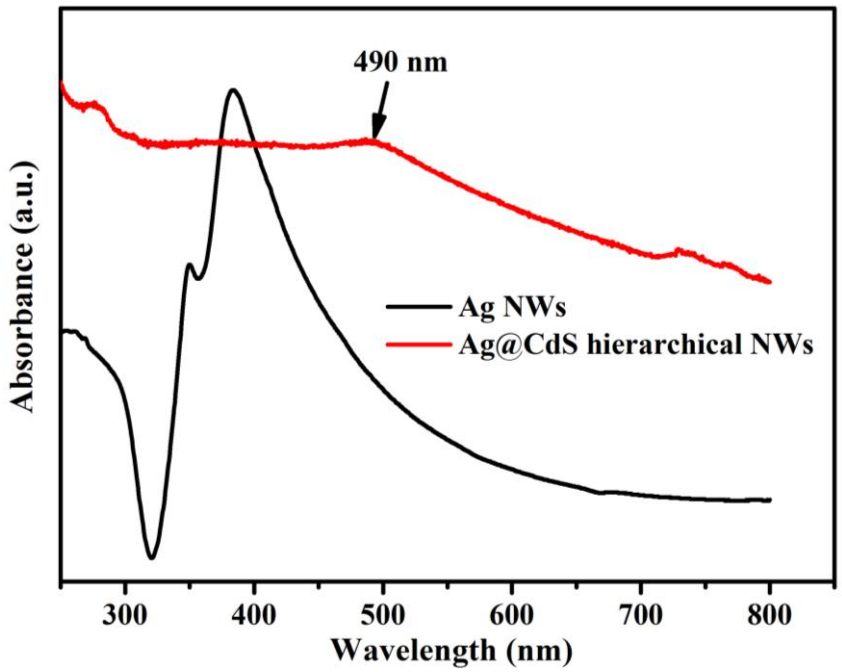

Figure 6.3 UV-Vis absorption spectra of Ag@CdS heterostructures (A1) with added amounts of $Cd(NO_3)_2 \cdot 4H_2O$/thiourea of 1.2 mmol/0.6 mmol.

In this work, the addition of ammonia, and the amounts of $Cd(NO_3)_2 \cdot 4H_2O$ and thiourea play significant roles in the construction of such 1D hierarchical nanostructures assembled from nanosheets and nanoparticles. As shown in Figure 6.4, it could not obtain these structures without adding ammonia into the reaction system. This result is reasonable, as thiourea does not easily decompose at low temperature. Thiourea can

decompose at the reaction temperature under basic conditions, such as when ammonia was introduced into the reaction solution.

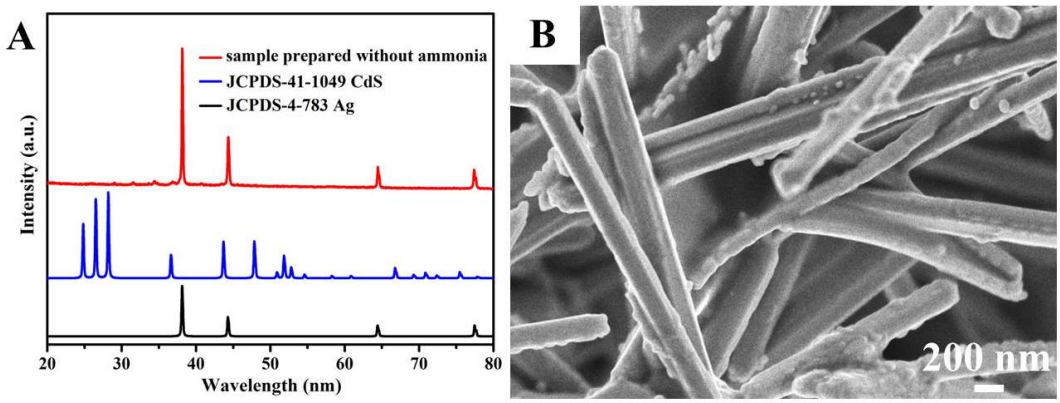

Figure 6.4 (A) XRD pattern and (B) SEM image of the product (A2) prepared without ammonia with added amounts of $Cd(NO_3)_2 \cdot 4H_2O$/thiourea of 1.2 mmol/0.6 mmol.

Controlled experiments have also shown that the amounts of $Cd(NO_3)_2 \cdot 4H_2O$ and thiourea are crucial to the formation of well-defined 1D hierarchical nanostructures assembled from nanosheets and nanoparticles. For instance, when the amount of $Cd(NO_3)_2 \cdot 4H_2O$ was decreased from 1.2 mmol to 0.3 mmol (Figure 6.5A) and 0.6 mmol (Figure 6.5B) while keeping the other experimental conditions unchanged, the morphology of the products significantly changed. As shown in Figure 6.5A and B, the Ag NWs are coated with many densely packed CdS nanoparticles. When the amount of $Cd(NO_3)_2 \cdot 4H_2O$ was further increased to 1.8 mmol (Figure 6.5C) and 2.4 mmol (Figure 6.5D), 1D hierarchical nanowires assembled from nanosheets and nanoparticles were obtained, which are similar to the product prepared in the presence of 1.2 mmol $Cd(NO_3)_2 \cdot 4H_2O$ (Figure 6.2A and B). Moreover, it was also found that the morphology of the 1D hierarchical nanowires was also sensitive to the amounts of thiourea. When the amount of thiourea was increased from 0.6 mmol to 1.2 mmol and 2.4 mmol, there were many nanoparticles and flower-like nanospheres constructed from interwoven nanosheets (Figure 6.5E and F). The above results directly indicate that the $Cd(NO_3)_2 \cdot 4H_2O$ and thiourea not only act as Cd and S sources but also as morphology

directors in the reaction process, and a higher ratio of $Cd(NO_3)_2 \cdot 4H_2O$/thiourea facilitates the formation of well-defined 1D hierarchical nanowires.

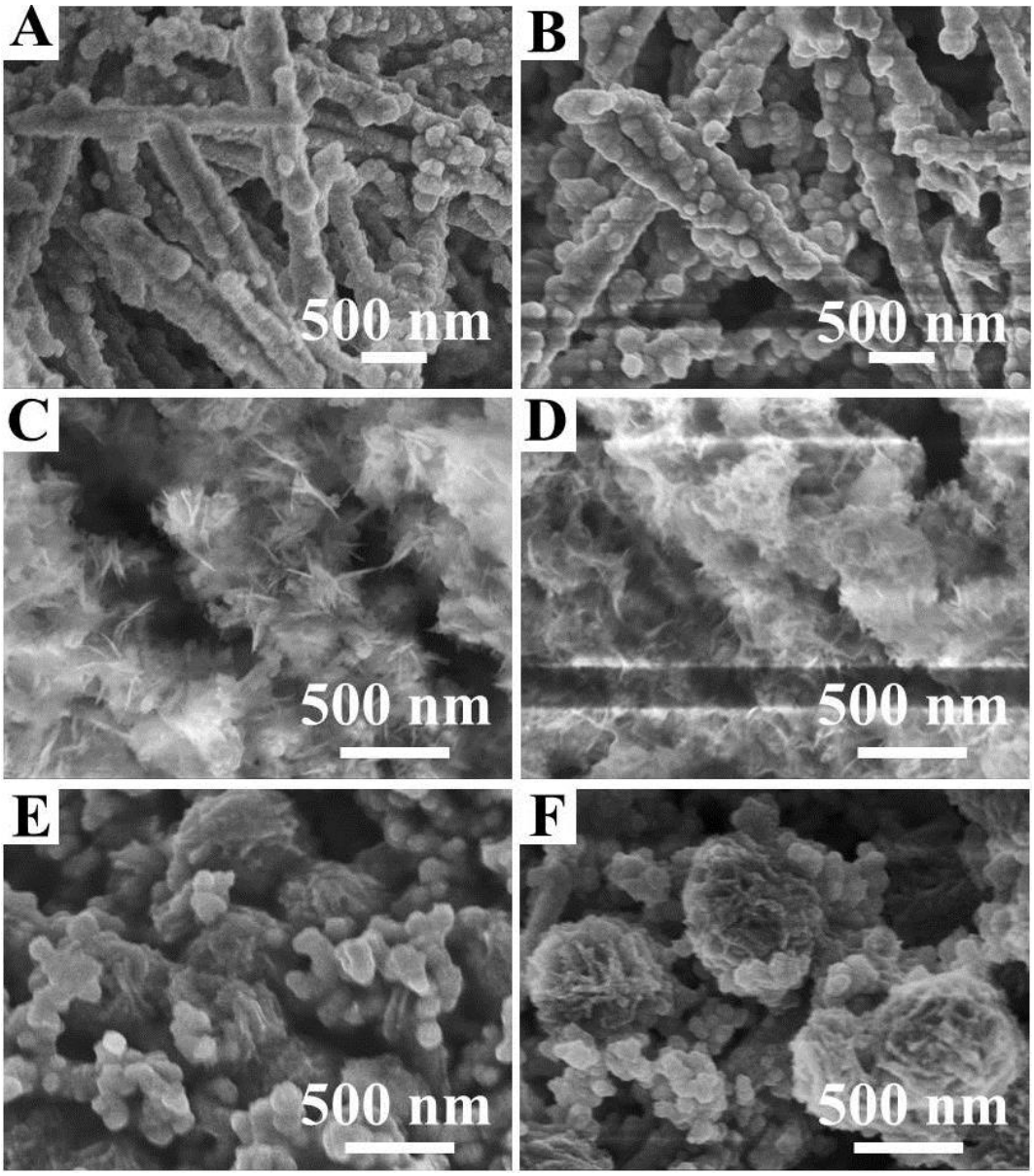

Figure 6.5 SEM images of the products prepared in the presence of different amount of $Cd(NO_3)_2 \cdot 4H_2O$/thiourea: (A) 0.3 mmol/0.6 mmol, (B) 0.6 mol/0.6 mmol, (C) 1.8 mmol/0.6 mmol, (D) 2.4 mmol/0.6 mmol, (E) 1.2 mmol/1.2 mmol, (F) 1.2 mmol/2.4 mmol.

Interestingly, no 1D hierarchical nanowires were obtained when the concentrations of reagents in the system were decreased. As shown in Figure 6.6(A-C), only 1D NWs with many nanoparticles on the surfaces were obtained when the ratio of $Cd(NO_3)_2 \cdot 4H_2O$/thiourea is 1:1, and the amounts of $Cd(NO_3)_2 \cdot 4H_2O$ were 0.075 mmol, 0.15 mmol, and 0.3 mmol, respectively. The TEM images in Figure 6.6(D-F) further provide evidence for the nature of the above representative product, in which 1D core-shell nanowires can be clearly observed with nanoparticles covering the surfaces of Ag NWs. It can also be seen that the shell thickness increased with increasing amounts of reagents in the system. Nevertheless, the morphologies could not be significantly changed by increasing the amounts of $Cd(NO_3)_2 \cdot 4H_2O$ and thiourea. For example, similar 1D nanowires with nanoparticles on the surface of Ag NWs were obtained, when the amount of $Cd(NO_3)_2 \cdot 4H_2O$ or thiourea was increased to 0.15 mmol, respectively (Figure 6.6G and H), while keeping the other experimental conditions the same as for the sample prepared in Figure 6.6A. The same phenomena could be observed when the amount of $Cd(NO_3)_2 \cdot 4H_2O$ or thiourea was increased to 0.3 mmol (Figure 6.6I and J, compared with Figure 6.6B) and 0.6 mmol (Figure 6.6K and L, compared with Figure 6.6C), respectively.

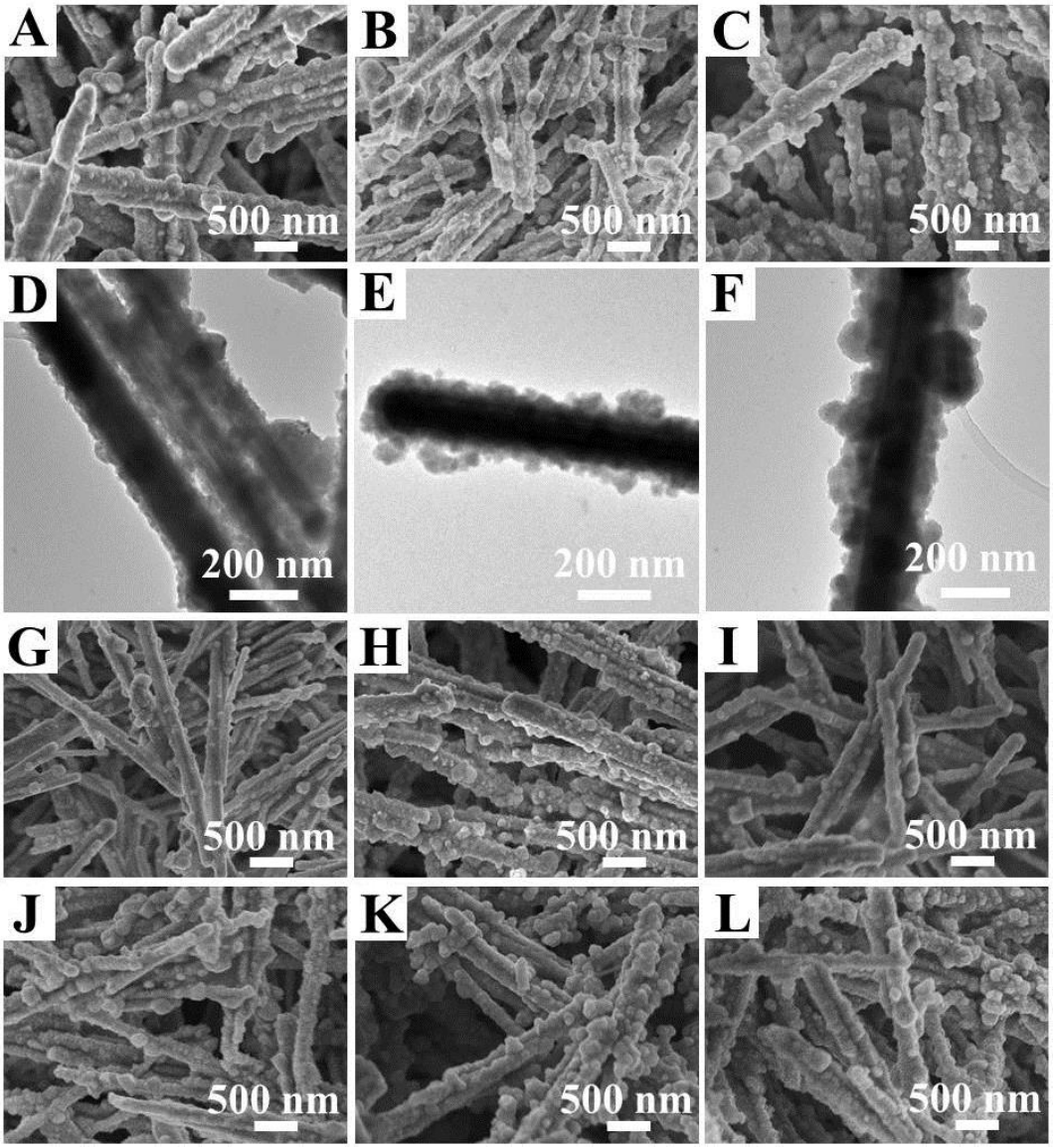

Figure 6.6 (A-C, G-L) SEM images and (D-F) TEM images of the product prepared in the presence of different amount of $Cd(NO_3)_2 \cdot 4H_2O$/thiourea: (A, D) 0.075 mmol/0.075 mmol, (B, E) 0.15 mmol/0.15 mmol, (C, F) 0.3 mmol/0.3 mmol, (G) 0.15 mmol/0.075 mmol, (H) 0.075 mmol/0.15 mmol, (I) 0.3 mmol/0.15 mmol, (J) 0.15 mmol/0.3 mmol, (K) 0.6 mmol/0.3 mmol, (L) 0.3 mmol/0.6 mmol.

All the above results indicate that the morphology of the 1D hierarchical nanowires was sensitive to the amounts of reagents, and in particular, larger amounts of

$Cd(NO_3)_2 \cdot 4H_2O$ with higher ratios of $Cd(NO_3)_2 \cdot 4H_2O$/thiourea were of special benefit to the formation of well-defined 1D hierarchical nanowires.

To determine the potential applications of the as-synthesized 1D Ag@CdS hierarchical nanowires in photocatalysis, the photodegradation of organic contaminants and hydrogen generation via water splitting over the 1D Ag@CdS hierarchical nanowires were evaluated. For comparison, the Ag NWs, Ag@CdS nanowires with various proportions and morphologies (A4, A9-A11), and pure CdS nanoflowers were also tested under identical experimental conditions. As shown in Figure 6.7A, it can be clearly seen that no obvious MO dye photodegradation was detected without any catalysts under solar light irradiation. All the as-prepared Ag@CdS nanostructures exhibit high photocatalytic performance, however, with sample A1 showing the highest photocatalytic performance, and it almost degrades 96% of MO dye within 240 min, while 85% of MO dye can be degraded over the pure CdS nanoflowers. In contrast, the Ag@CdS nanowire photocatalysts with various other proportions of reagents (A9-A11) show relatively low photocatalytic activities towards MO degradation, which may result from the high ratios of metallic Ag nanowires. Table 6.2 summarized the BET surface areas, the nominal and actual CdS loadings of the samples.

Table 6.2 BET surface areas, the nominal and actual CdS loadings of the samples

Sample	BET surface area ($m^2 g^{-1}$)	nominal CdS loading (wt%)	actual CdS loading (wt%)[a]
A1	23.71	73	73
A4	10.74	73	63
A9	11.13	25	17
A10	11.29	40	29
A11	6.05	57	48
Pure CdS	23.98		

Note: [a] Determined using ICP-OES analysis.

The above results clearly indicate that the core–shell constitutions have important impact on the photocatalytic activity of Ag@CdS. Furthermore, the Ag@CdS nanowires with the same noninal 1:2 ratio (A4, the actual CdS loading is 63 wt %) also show relatively low activity towards MO degradation, which may due to the lack of hierarchical structures. The specific surface area of the hierarchical heterostructures (A1) was determined to be 23.71 $m^2 g^{-1}$, which was larger than that of the particulate CdS-coated heterostructures (from 6.05 to 11.29 $m^2 g^{-1}$). Taking into account that the enhanced performance of 1D Ag@CdS hierarchical nanowires (A1) may be ascribed to their specific hierarchical nanostructure with large specific surface area and proper constitution, which could provide more active sites for MO photodegradation and thus facilitate diffusion of reactants and products during the reaction. Furthermore, the interfacial charge transfer in the hybrid may also account for the enanced photodegradation performance of MO.

In addition, Figure 6.7B shows the hydrogen evolution via water splitting of the samples based on aqueous solutions containing 0.25 M Na_2SO_3 and 0.35 M Na_2S sacrificial reagents under irradiation by visible light with $\lambda \geq 420$ nm. The 1D Ag@CdS hierarchical nanowires (A1) clearly show higher catalytic activity, since the initial rate of hydrogen generation is 73.5 μmol h^{-1} and 181.2 μmol of hydrogen is generated after 4 h, which is about 1.35 times higher than the performance of the pure CdS nanoflowers (17.6 μmol h^{-1}, 134.5 μmol H_2 after 4 h), while the other Ag@CdS samples with different proportions and morphologies (A4, A9-A11) exhibit relative low photocatalytic activities, with less than 100 μmol H_2 for the same irradiation time, which is in good agreement with the above photocatalytic activities towards MO degradation. Figure 6.7C provides a histogram of the MO degradation rates and hydrogen evolution, which highlights the 1D Ag@CdS hierarchical nanowires (A1) being the best for both reactions. On the basis of the above results, it can be concluded

that the construction of 1D Ag@CdS nanowires with hierarchical nanostructures has been proved to be an successful and feasible protocol to enhance the photocatalytic performances of CdS.

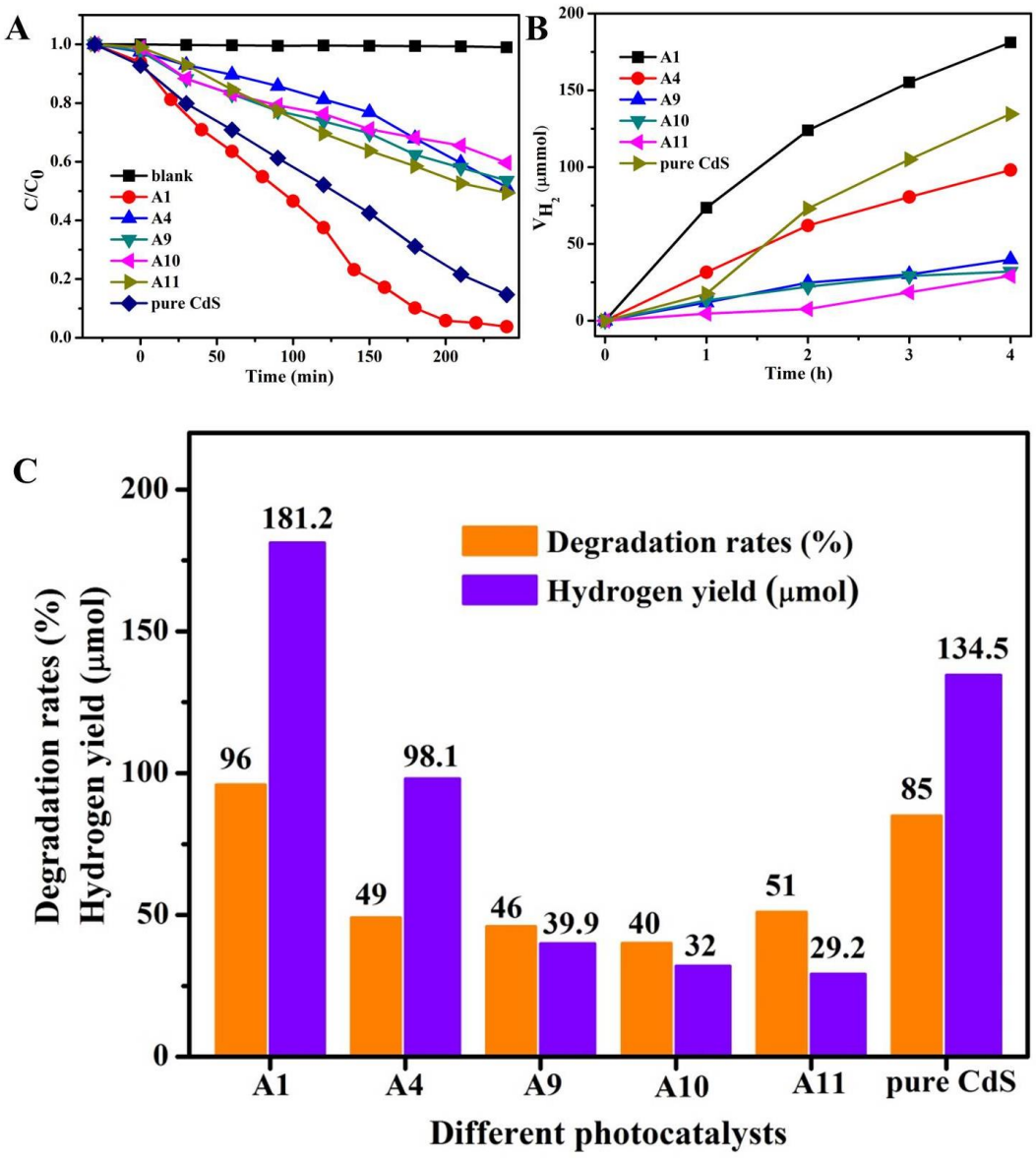

Figure 6.7 (A) Photocatalytic activities of 1D Ag@CdS hierarchical nanowires and other as-prepared photocatalysts towards MO dye degradation under irradiation by solar light. (B) Photocatalytic hydrogen evolution curves of 1D Ag@CdS hierarchical nanowires and other as-prepared photocatalysts under irradiation by visible light with $\lambda >$ 420 nm. (C) Degradation rates and hydrogen yield by various photocatalysts.

6.4 Conclusion

In summary, one-dimensional (1D) Ag@CdS core-shell heteronanowires with hierarchical nanostructures have been fabricated by a facile oil bath approach at low temperature, and they exhibit better photocatalytic activity towards methyl orange (MO) degradation and hydrogen generation compared to pure CdS nanoflowers. Such rational design and fabrication of 1D metal-core@semiconductor-shell hierarchical architectures may hold great potential for solar energy conversion, especially as an effective technique to improve photocatalytic performance.

Chapter 7 Ambient Synthesis of a Multifunctional 1D/2D Hierarchical Ag-Ag_2S Nanowire/Nanosheet Heterostructure with Diverse Applications

The contents of this chapter were published in CrystEngComm, 2016, 18, 930-937.[207]

7.1 Introduction

Semiconductor-noble metal-based hybrid nanostructures have promising potential in energy, environmental, and catalysis applications, due to their unique optical, electrical, catalytic properties arising from each component and their synergistic interactions.[29,210,334] Their great potential drives engineering nanofabrication and property of such semiconductor-metal hybrid nanomaterials with different architectures.[188,335,336] Being one of important semiconductor-noble metal hybrids, Ag-Ag_2S with different heterostructures, including nanotubes,[29] nanowires,[337] nanoprisms,[338,339] and nanoparticles,[340,341] have been widely exploited in the past several years. It was reported that Ag-Ag_2S nanohybrids showed excellent properties in resistive switches,[337,342-344] DNA hybridization probes,[339] bactericidal effects,[338,340,345] photodegradation of pollutants,[29,341] and water splitting.[342] From the fabrication perspective, most fabrications of Ag-Ag_2S hybrids suffered from the drawbacks of high temperature,[341] complicated processes,[342,345] and high energy consumption,[337] which seriously restrict their development and practical applications. It still remains a challenging but exciting topic to explore a facile strategy to prepare well-defined and unique multidimensional Ag-Ag_2S heterostructures, as well as to investigate their novel properties and potential applications.

Generally, the composition and structure of the hybrids play the pivotal role in determining their functions and applications.[346-349] Recent advances demonstrate that complex one-dimensional/two-dimensional (1D/2D) heterostructures composed of 1D nanowires and 2D nanosheets exhibit great potential in photocatalysis,[350] energy storage,[351] counter electrodes,[352] and photoelectrochemical cells,[353] owing to their

unique structural features, which allows it to transport charge carriers very well along the axial direction and has relatively large surface area. However, to the best of our knowledge, there are sparse reports on preparation of 1D/2D Ag-Ag_2S heterostructures and exploration of their fascinating properties. Herein, a new type of 1D/2D Ag-Ag_2S architecture has been fabricated by an extremely simple solution route under ambient conditions, and the as-synthesized Ag-Ag_2S hybrids exhibit favorable multifunctional properties for energy and environmental applications.

7.2 Experimental section

7.2.1 Experimental methods

Ag nanowires (Ag NWs) were prepared according to our previous report with a minor modification.[70] In a typical synthesis, 10 mL of 1,2-propanediol containing PVP40 was loaded into a 25 mL vial, and heated with magnetic stirring in an oil bath at 135 ℃ for 1 h. 1 mL of NaCl in 1,2-propanediol solution (1 mM) was then quickly added, and stirring for another 5 min. Finally, $AgNO_3$ (0.1 M solution in 1,2-propanediol) was added to the mixture. The mixture solution was then heated at 135 ℃ with magnetic stirring for 1 h, yielding the gray Ag NWs.

Ag nanoparticles (Ag NPs) were prepared by the similar procedure applied to Ag NWs, except without NaCl.

1D/2D Ag-Ag_2S hierarchical heterostructures were prepared from the above synthesized Ag nanowires and sulphur powder. 8 mL freshly prepared Ag NW solution was firstly added into 10 mL ethanol under constant magnetic stirring for 10 min. Then, 0.0048 g sulfur powder was added into the reaction mixture. The reaction mixture was stirred for 24 h, and then the resultant Ag-Ag_2S precipitate was separated by centrifugation, washed with de-ionized water and absolute ethanol several times to remove impurities, and then dried at 60 ℃.

Ag-Ag_2S heteronanoparticles were prepared using the similar approach to 1D/2D Ag-Ag_2S hierarchical heterostructures, except 8 mL of Ag NPs solution was added rather than Ag NWs solution.

Pure Ag_2S nanospheres were prepared from $AgNO_3$ and saturated Na_2S solution in ethanol in the presence of PVP. The reaction mixture was stirred for 24 h.

7.2.2 Characterization

The X-ray diffraction (XRD) measurements were performed on a GBC MMA X-ray diffractometer using Cu Kα1 radiation (40 kV). The XRD patterns were recorded from 20 ° to 80 ° with a scanning rate of 4 °/min. SEM images were collected using a field-emission scanning electron microscope (JSM-7500FA, JEOL) operated at an accelerating voltage of 5 kV. TEM images were collected on a field-emission transmission electron microscope (ARM-200F, JEOL), using an accelerating voltage of 200 kV. Ultraviolet/visible (UV/vis) absorption spectra were recorded at room temperature on a UV-3600 (Shimadzu) spectrometer.

7.2.3 SERS measurement

2 mg as-synthesized 1D/2D Ag-Ag_2S hierarchical heterostructures were added into 200 μL of MB solution with a concentration of 10^{-3}, 10^{-4}, 10^{-5}, and 10^{-6} M, respectively. The mixture was ultrasonically dispersed for 10 min and shaken for 12 h in the dark at room temperature. Then, the dispersion was dropped onto a glass slide for the SERS measurement. All SERS spectra were collected on a JY HR 800 Raman spectrometer under excitation of 632 nm with a power of 13.5 mW.

7.2.4 Battery performance measurements

The electrode slurry for lithium/sodium ion batteries was prepared by mixing 70 wt% active powder material, 15 wt% carbon black, and 15 wt% carboxymethyl cellulose

(CMC) binder. The slurry was pasted on copper foil, followed by drying in a vacuum oven overnight at 80 ℃, and then pressing at a pressure of 30 MPa to enhance the contact between the mixture and the copper foil. For the lithium ion battery test, lithium foil was employed as both reference and counter electrode. The electrolyte was 1 M LiPF6 in an ethylene carbonate (EC)–diethyl carbonate (DEC) solution (1:1 v/v). For the sodium ion battery test, sodium foil was cut by the doctor blade technique from bulk sodium stored in mineral oil, which then was employed as both reference and counter electrode. The electrolyte was 1 M $NaClO_4$ in an EC/DEC solution (1:1 v/v). The cells were assembled in an argon-filled glove box, and their electrochemical performance was tested with a Land Test System in the voltage range of 0-2.5 V with a current density of 30 mA g^{-1}.

7.2.5 Decoloration test

The application of as-synthesized 1D/2D Ag-Ag_2S hierarchical heterostructures for decoloration of organic dyes was evaluated in both a dark environment and under solar light irradiation. In the experiment, 50 mg of the heterostructures were added into 50 mL of MB solution (10^{-5} M) at room temperature. After ultrasonic dispersion, the suspension was stirred in the dark for 30 min to ensure the establishment of an adsorption-desorption equilibrium between the hybrid structures and the MB. Then, the solution was exposed to irradiation of a LSC-100 Solar Simulator (Newport) under magnetic stirring. At each irradiation time interval, 2 mL of the suspension was collected and then centrifuged to remove the photocatalysts. The concentration of MB was analyzed by a Shimadzu UV-3600 spectrophotometer, and the characteristic absorption of MB at 664 nm was used to evaluate the decoloration activity. All of the measurements were carried out at room temperature.

7.3 Results and discussion

A typical Ag-Ag_2S architecture is synthesized through the reaction of Ag nanowires (NWs) with sulfur powder in ethanol at room temperature. The X-ray diffraction (XRD) pattern of the as-prepared sample in Figure 7.1A indicates that the product is a hybrid consisting of monoclinic Ag_2S (JCPDS card No. 14-0072) and face-centered cubic Ag (JCPDS card No. 04-0783). The absence of impurity peaks in the XRD pattern suggests the high purity of the Ag-Ag_2S hybrid synthesized by this facile approach. The energy-dispersive X-ray (EDX) analysis result shown in Figure 7.1B indicates that the as-prepared hybrid is composed of Ag and S with an atomic ratio (i.e. Ag/S) higher than the stoichiometric ratio of 2:1 for Ag_2S, demonstrating the successful synthesis of the Ag-Ag_2S hybrid.

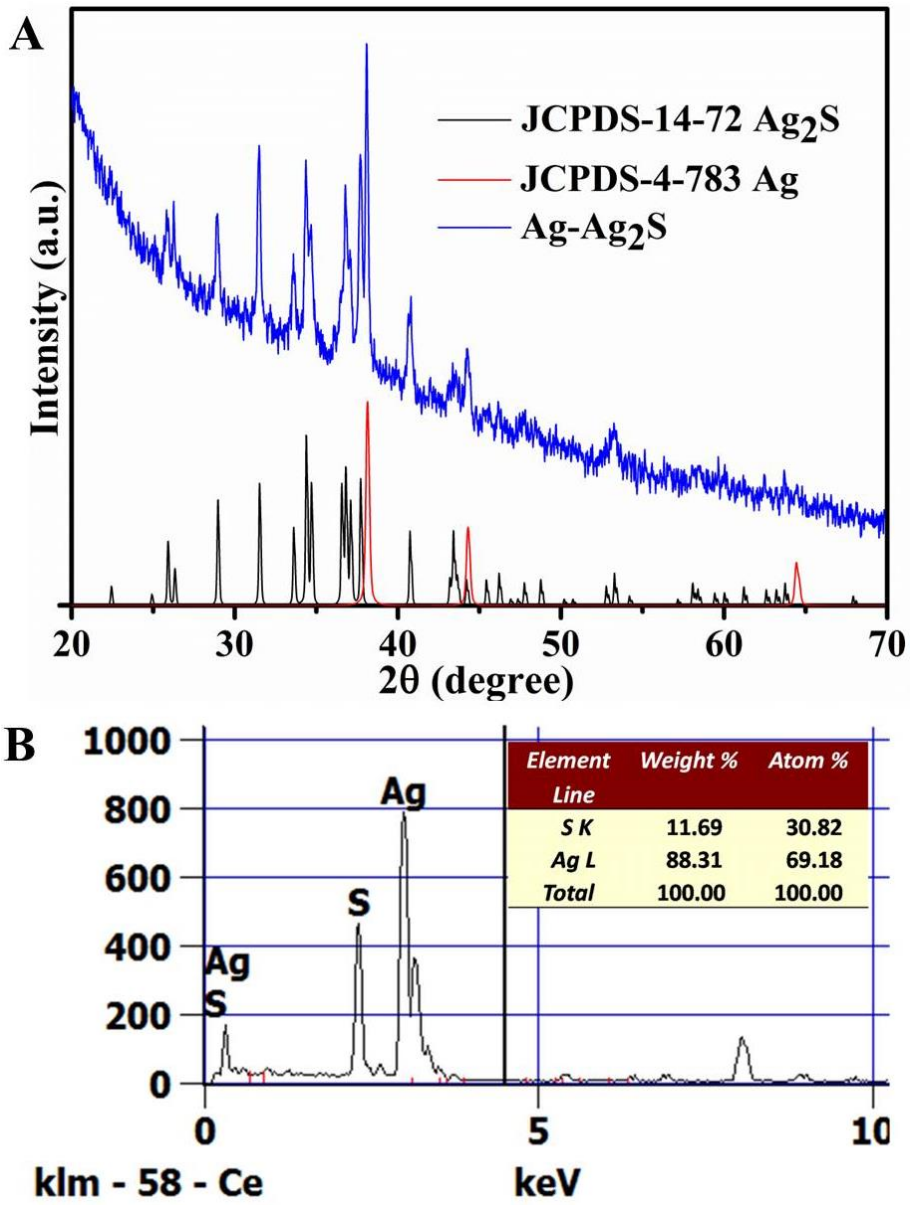

Figure 7.1 (A) XRD pattern and (B) EDX spectrum of the as-prepared Ag-Ag_2S heterostructures with the S/Ag ratio of 1:2.

Characterizations by scanning electron microscopy (SEM) and transmission electron microscopy (TEM) provide insight into the morphology and detailed structure of the as-prepared Ag-Ag_2S hybrid. A panoramic view of the as-prepared sample shows uniform nanowires ~100 nm in diameter and several micrometers in length (Figure 7.2A). The enlarged SEM image in Figure 7.2B reveals that many sheet-like nanostructures (~15 nm in thickness) have densely grown on the entire surface of the 1D nanowire to form a

1D/2D hierarchical nanostructure. Figure 7.2C clearly shows a TEM image of an individual 1D/2D Ag-Ag_2S hierarchical nanostructure, in which sheet-like leaves surround 1D nanowire in a three-dimensional (3D) manner. The hybrid has two kinds of segments with different contrasts, in which the darker segment is metallic Ag and the brighter segment should be semiconducting Ag_2S. The high-resolution TEM (HRTEM) image in Figure 7.2D shows a lattice fringe of 0.208 nm, which corresponds to the (200) planes of monoclinic Ag_2S. The selected area electron diffraction (SAED) pattern (Figure 7.2E) also reveals the presence of Ag_2S in the hybrid. High-angle annular dark-field (HAADF) imaging was used to identify each chemical component. Due to the differences between Ag and S in scattering electrons, the as-prepared Ag-Ag_2S hybrid has different contrasts in the HAADF image (Figure 7.2F), which is opposite to those observed in the bright field image, i.e. the bright segments indicate the presence of the heavier metal Ag, and the dark parts indicate the presence of Ag_2S. Elemental mapping of a single 1D/2D heterostructure obtained by HAADF-TEM reveals the homogeneous distribution of Ag and S elements in the hybrid (Figure 7.2G and 7.2H).

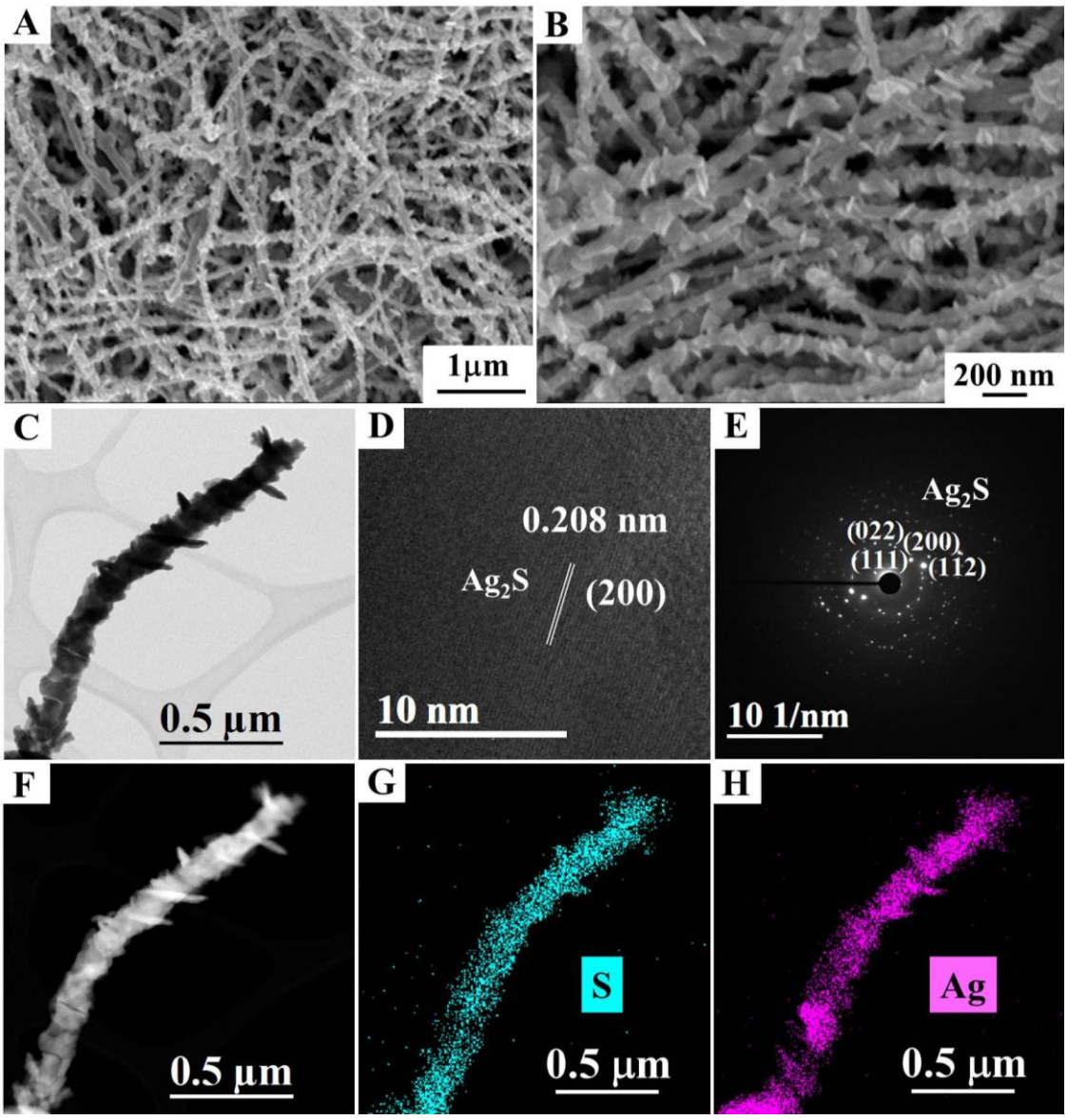

Figure 7.2 (A, B) SEM image of the as-prepared Ag-Ag_2S heterostructures with the S/Ag ratio of 1:2; (C) TEM image, (D) HRTEM image, (E) SAED pattern, (F) HAADF image, and (G, H) corresponding EDX elemental mapping analysis of an individual Ag-Ag_2S heterostructure.

The above results demonstrate the successful synthesis of 1D/2D Ag-Ag_2S hierarchical heterostructures. To understand the formation mechanism of such an interesting structure, time-dependent experiments are carried out and samples are collected at different time intervals. The morphological and structural evolution of the products

obtained with different reaction times were examined by SEM (Figure 7.3). Before the addition of S powder, the Ag NWs are very straight, and the surfaces are very smooth (Figure 7.3 A). After addition of S powder and reaction for 30 min, no significant difference was observed on the surfaces of the Ag NWs at this early stage (Figure 7.3B), although the reaction mixture changed from grey to yellow due to the formation of a thin Ag_2S layer on the surfaces of the NWs. As the reaction proceeded for 1.5 – 4 h, the surfaces of the nanowires became rougher, and a few spiny or scaly structures were formed, as shown in Figure 7.3(C-E). The epitaxial growth of the Ag_2S nanostructures could be due to the excessive crystallization of Ag_2S in some places on the surface of the nanowire. When the reaction time was lengthened to 6 – 8 h, more and more quasi-nanosheets were formed on the nanowires to form a mace-like structure, as shown in Figure 7.3(F-G). With further extended reaction time, the nanosheets adhering to the nanowires became larger and became joined to one another (Figure 7.3H). After reaction for 24 h, the final products were entirely composed of the 1D/2D hybrid heterostructures (Figure 7.3I).

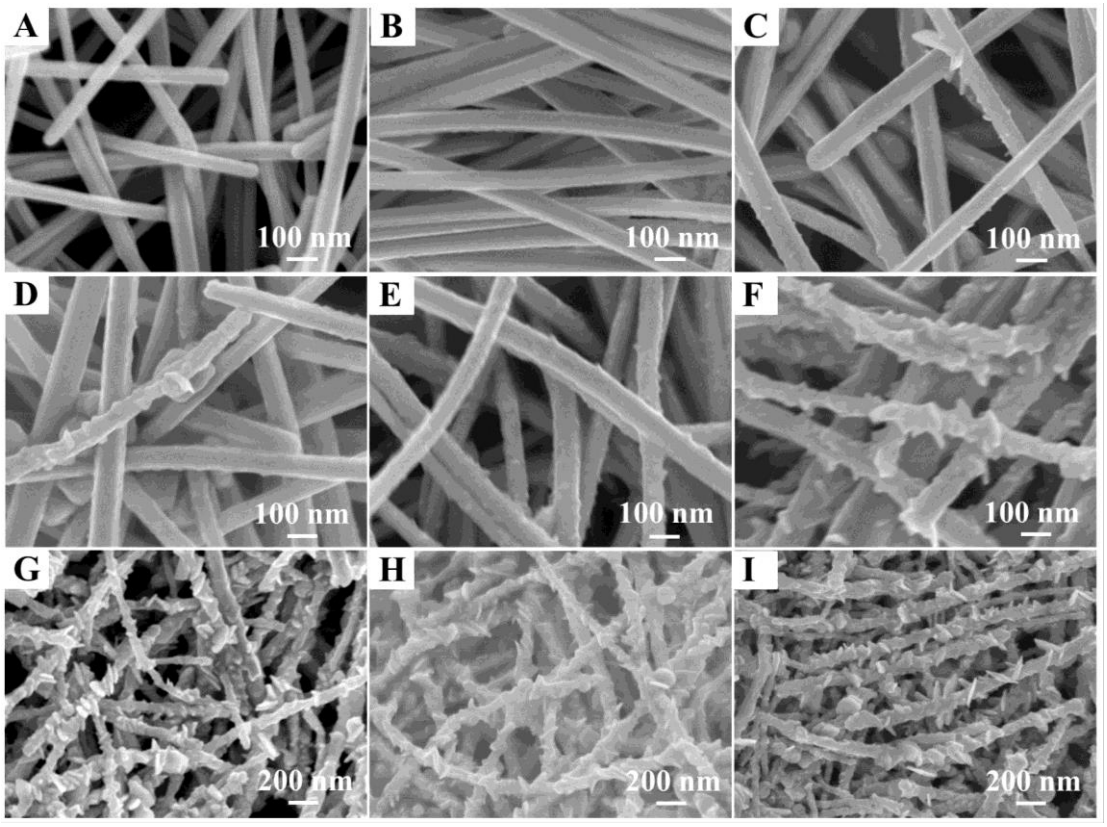

Figure 7.3 SEM images of the products obtained with the S/Ag ratio of 1:2 at different reaction times: (A) 0 min, (B) 30 min, (C) 1.5 h, (D) 2 h, (E) 4 h, (F) 6 h, (G) 8 h, (H) 12 h, and (I) 24 h.

These structures and morphologies were further analyzed by TEM and high-resolution TEM. As shown in Figure 7.4A, the TEM images confirm that for the products obtained within 30 min, a thin Ag_2S layer is coated on the surface of the Ag NWs to form a well-defined core-shell Ag-Ag_2S nanowire with a relatively smooth surface, due to the sulfuration of the Ag NWs. The corresponding HRTEM image (Figure 7.4B) clearly reveals that the resolved lattice fringes are 0.199 nm, corresponding to the *d*-spacing of the (-131) planes of monoclinic Ag_2S. With the growth of the Ag_2S shell, the surface of the hetero-nanowires became coarse [Figure 7.4(C-D)]. Further prolonging the reaction time to 6 h led to the formation of a mace-like structure with a few quasi-nanosheets on the nanowires [Figure 7.4(E-F)].

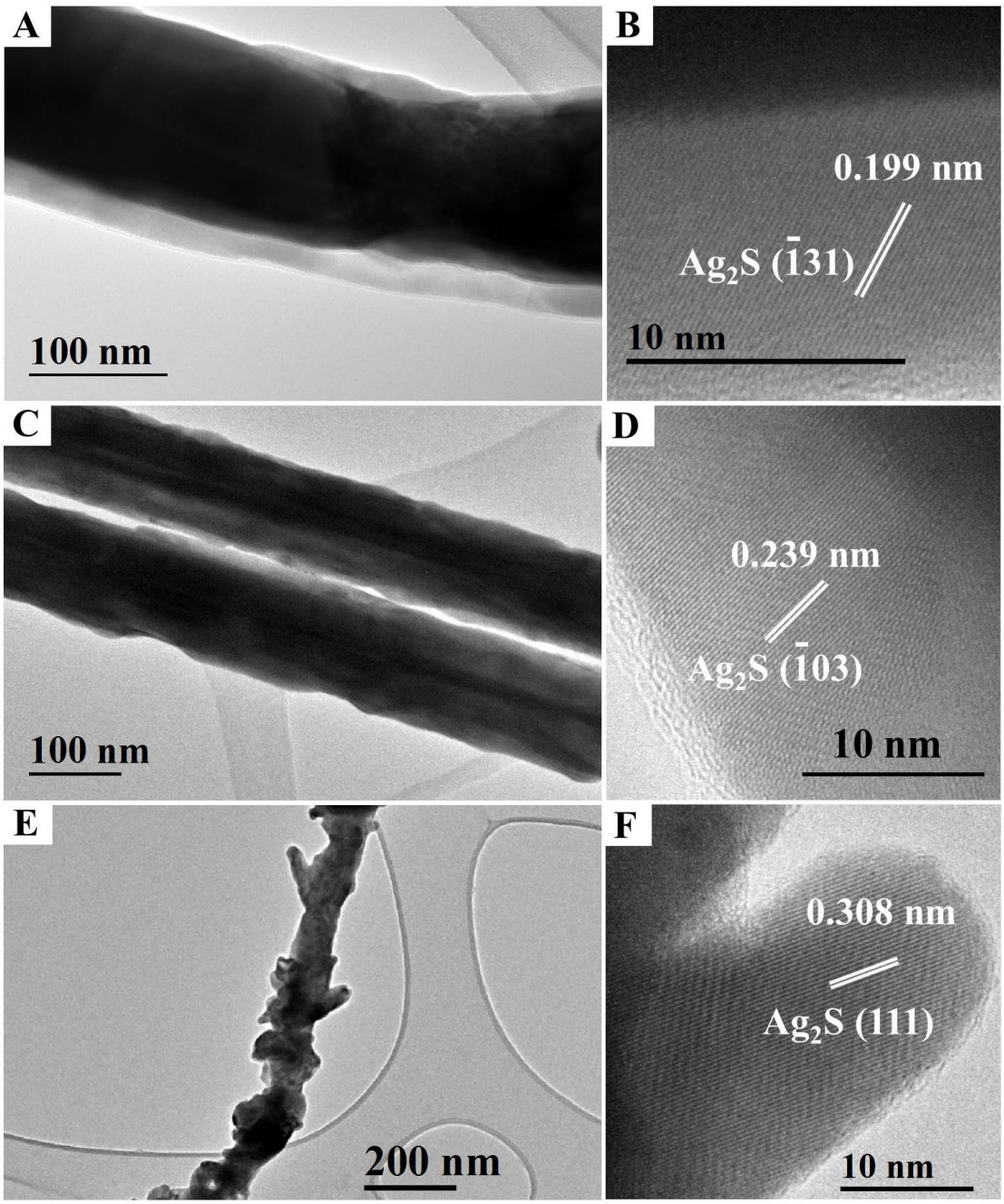

Figure 7.4 TEM images (A, C, and E) and corresponding HRTEM images (B, D, and F) of the products obtained at different reaction times: (A, B) 30 min, (C, D) 4 h, and (E, F) 6 h.

The crystalline structures and optical properties of above products were further studied and the results are shown in Figure 7.5. The XRD patterns (Figure 7.5A) clearly reveal that the intensity of the Ag_2S diffraction peaks are gradually increased with increasing

reaction time, demonstrating the gradually formation of the Ag-Ag_2S hybrid and the increase content of Ag_2S. It is well known that Ag NWs show intense surface plasmon resonance (SPR) absorption in the visible region, which is highly sensitive to their diameter and length-to-diameter ratio, as well as the optical and electronic properties of their surroundings.[70,236,238] The absorption spectra shown in Figure 7.5B were from ethanol-Ag and ethanol-Ag-Ag_2S dispersions collected at different reaction times, which were measured with a UV-3600 (Shimadzu) spectrometer in the UV-Vis-NIR region at room temperature. The scan speed is medium and the interval is 1 nm. The pure Ag NWs exhibit two absorbance peaks at 350 and 385 nm. The peak at 350 nm could be attributed to the longitudinal mode of the nanowires, which is similar to that of bulk Ag[238-240] or the out-of-plane quadrupole resonance of Ag NWs.[241-243] The peak at 385 nm is assigned to the transverse plasmon resonance of Ag NWs.[238-240] The optical response of the Ag NWs was observed to be markedly affected by the formation of Ag_2S.

Upon the formation of the Ag_2S shell (30 min), the longitudinal mode almost disappeared and the transverse plasmon resonance of the Ag cores observed at about 385 nm decreased with redshifted and significantly broadened, which could possibly contributed to the synergistic effects between Ag NWs and Ag_2S shell in Ag-Ag_2S hybrids: the higher refractive index of Ag_2S (1.9-2.5)[354-356] than that of ethanol ($\sim$1.359)[238,357] and its high relative dielectric constant (ε_r= 6),[358,359] as well as the confinement of free electrons within the Ag core.[124,238]

The peak width of SPR band increased slightly with increasing time (30 min-4 h), which implied that Ag nanowires are becoming more isolated with less and less electronic interactions between nearby unites. When the reaction time is 6 h, the spectra exhibited a new absorption band cantered around 495 nm and a very weak SPR peak. The new absorption is ascribed to the band gap of Ag_2S, which is similar to the reported absorption between 490-520 nm of rod-like Ag_2S nanocrystals,[360] 530 nm of Ag_2S

nanofibers,[344] 573 nm of Ag_2S nanotubes,[361] 443 nm of Ag_2S nanoparticle chains,[362] and 514-531 nm of the Ag_2S/Ag heterostructures.[345] The weak SPR observed herein indeed suggested that the good contact between the Ag_2S and Ag segments might ensure an effective charge transfer across the phase boundary, and the changes in the structure and shape of the product.

When the time was increased to 8 h, the SPR absorption bands of Ag NWs almost disappeared owing to its further sulfuration, and the characteristic absorption feature of Ag_2S moved to the longer wavelength region at around 515 nm. The observed red-shifts may reflect the grain/crystallite growth of the Ag_2S and enlargement of the Ag_2S domains in the heterostructures. Eventually, with more and more quasi-nanosheets formed on the nanowires (see Figure 7.3G and 7.3H), the characteristic absorption feature of Ag_2S moved to around 525 nm for the time at 12 h, providing strong evidence that essentially Ag NWs have turned into Ag-Ag_2S hybrid and the product mainly composed of Ag_2S component. The final dispersion was brownish black in appearance. The Ag-Ag_2S NWs obtained at 24 h exhibit similar absorption profile in comparison with the products obtained at 12 h, in which the characteristic absorption feature of Ag_2S remained at 525 nm and did not shift with increasing reaction time, due to the lack of obvious changes in the structures and shapes of final products (see Figure 7.3I). Their broad absorbance from the UV to the near-infrared window is crucial for the full use of sunlight.

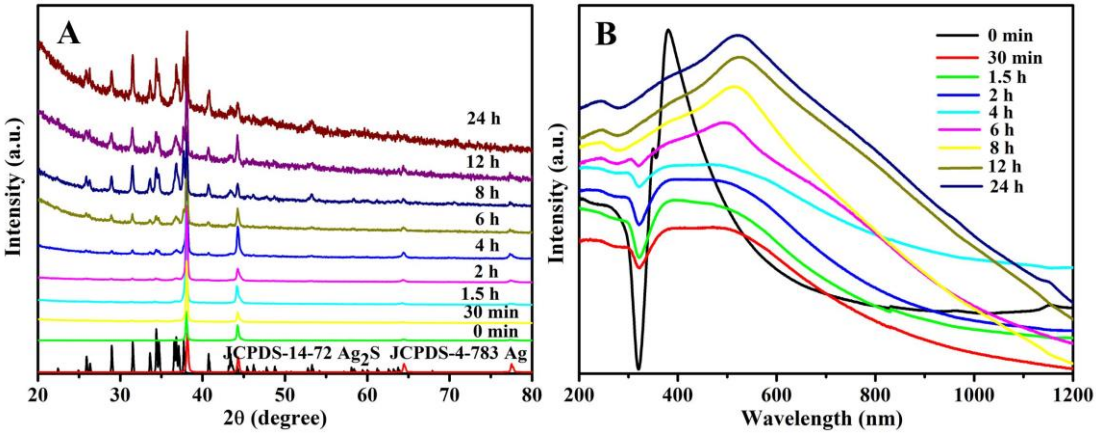

Figure 7.5 (A) XRD patterns and (B) UV-Vis-NIR absorption spectra of the products obtained with the S/Ag ratio of 1:2 at different reaction times.

It should be noted that the formation of 1D/2D Ag-Ag_2S hierarchical heterostructures is strongly dependent on the Ag/S ratio. Figure 7.6(A-D) present SEM images of Ag-Ag_2S heterostructures obtained from different ratios of Ag/S after reaction for 24 h. The surfaces of heterostructures become smoother and smoother with the S/Ag ratio decreasing from 0.4:1 (Figure 7.6A), through 0.33:1 (Figure 7.6B) and 0.22:1 (Figure 7.6C), to 0.2:1 (Figure 7.6D). For the heterostructures obtained from the ratio of 0.2:1, the morphology of the initial Ag NWs remains almost unchanged, except for the formation of a thin Ag_2S layer on the surface of the Ag NWs, as shown by the TEM and HRTEM images in Figure 7.6(E and F).

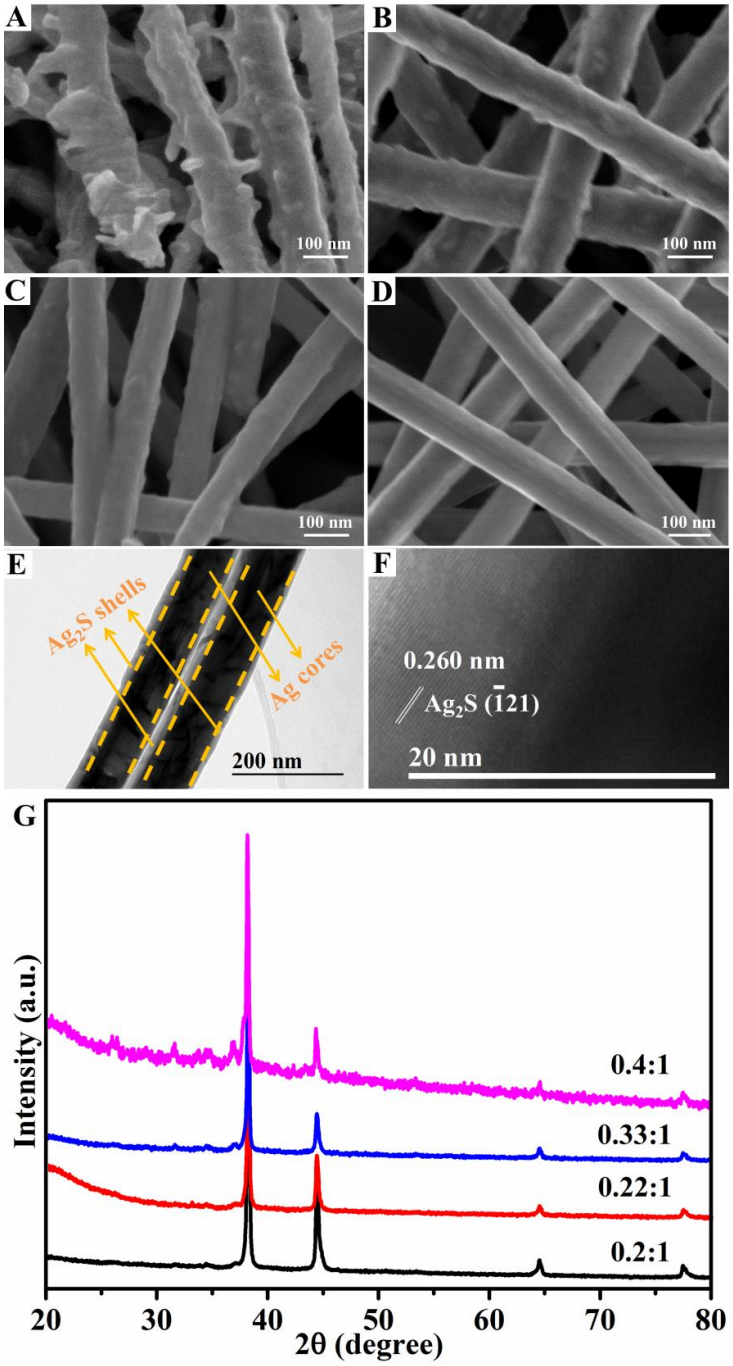

Figure 7.6 (A-D) SEM images of the products prepared with different molar ratios of sulfur powder to Ag nanowires: (A) 0.4:1, (B) 0.33:1, (C) 0.22:1, and (D) 0.2:1; (E) TEM image and (F) HRTEM image of the product prepared with an S to Ag ratio of 0.2:1; (G) XRD patterns of the products prepared with different molar ratios of sulfur powder to Ag nanowires.

Based on these results, the formation of the 1D/2D Ag-Ag_2S hierarchical heterostructures can be illustrated in Scheme 7.1A, in which the diffusion and Ostwald ripening processes dominate the evolution of heterostructure morphology. It is well known that the room temperature diffusion of metals through semiconductors to form metal-semiconductor pairs generally occurs on the nanometer scale when the band-gap energy of the semiconductor is lower than about 2.5 eV.[335,363,364] The band gap of bulk Ag_2S crystal is about 0.9 eV at room temperature, and 1.4-2.3 eV for its nanoscale analogues.[335,345] Therefore, the diffusion of Ag metal within the Ag-Ag_2S nanowires well satisfies the aforementioned diffusion criterion.

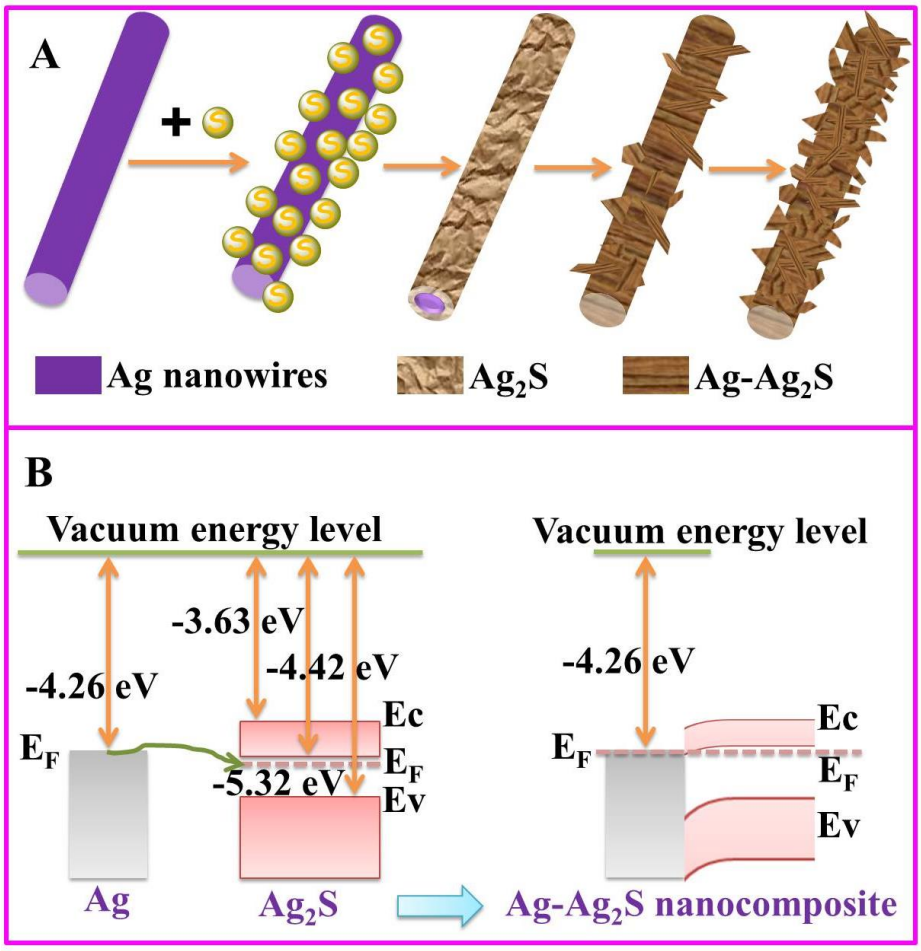

Scheme 7.1 (A) Schematic illustration of the synthesis of 1D/2D Ag-Ag_2S heterostructures and (B) Simplified band structures in Ag-Ag_2S system before and after contact.

Scheme 7.1B shows a simplified diagram of energy level of Ag-Ag_2S nanocomposites, and the work function of Ag, the dominant energy level, the bottom of the conduction band and the top of the valence band of Ag_2S, which are -4.26eV, -3.63 eV, -4.42 eV and -5.32eV, respectively, from the vacuum energy level.[335,345,365,366] In equilibrium, the Fermi levels of Ag and Ag_2S should be at the same level. According to the potential alignment, the electrons (majority carriers) can drift from the Fermi level of Ag to the Fermi level (E_F, which is approximately treated as the donor level) of the *n*-type Ag_2S semiconductor upon they are in contact, leaving some positive charge buildup on the metal contact interface,[345,367] which could facilitate the diffusion of Ag in Ag_2S and result in substitutional interstitial processes.[365,366] As a consequence, the Ag-Ag_2S interface causes the bending and upshift of energy bands.[367]

In the presence of S powder, which could serve as a strong oxidant, the surface reactive Ag atoms of the nanowires are oxidized to form a thin uniform Ag_2S layer at an early stage. The subsequent diffusion of Ag would continue, as well as its reaction with S at different sites, leading to the growth of convexity due to the increase in internal energy arising from the interfacial strain caused by the lattice mismatch between Ag and Ag_2S, and due to the large volume expansion during the sulfurization reaction, since the molar volumes of Ag and Ag_2S are 10.3 cm^3 mol^{-1} and 34.3 cm^3 mol^{-1}, respectively.[358] The initially formed Ag_2S convexity continues its growth and undergoes an Ostwald ripening process to turn into nanosheets. With the growth of Ag_2S, the diffusion of Ag atoms from the internal Ag core to the surface Ag_2S becomes slower and slower, leading to negligible difference in the 1D/2D hybrid heterostructures obtained after 24 h. The SEM images and XRD pattern of a sample reacted for 6 days are shown in Figure 7.7, which are similar to those obtained at 24 h. Compared to previously reported methods for the fabrication of 1D Ag-Ag_2S heterostructures, a major advantage of the present work is the use of stable sulfur powder rather than Na_2S to synthesize this new type of well-defined 1D/2D hybrid architecture under ambient conditions.[339,368] The sulfur powder could enable a mild sulfuration process with well-controlled kinetics.[364]

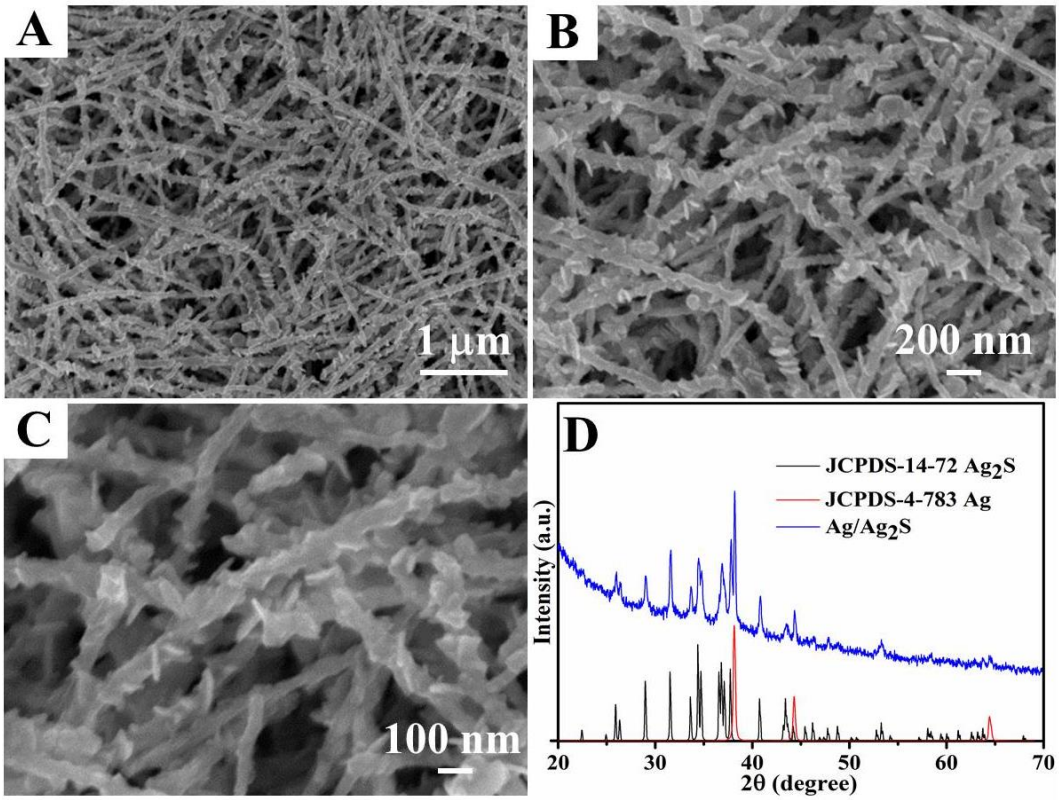

Figure 7.7 (A-C) SEM images and (D) XRD pattern of the Ag-Ag_2S heterostructures obtained after 6 days.

As a proof-of-concept application of this intriguing hybrid nanostructure, the obtained 1D/2D hierarchical Ag-Ag_2S heterostructures were used as multifunctional materials in rechargeable Li/Na-ion batteries, in decolouration of organic dyes, as well as in surface-enhanced Raman spectroscopy (SERS) detection. Figure 7.8A shows the cycling performance and coulombic efficiency of electrodes in Li-ion batteries fabricated from the 1D/2D hierarchical Ag-Ag_2S heterostructures. Their capacities drop in the first few cycles due to the formation of a solid electrolyte interphase (SEI) film, which is similar to what happens in other nanostructure based electrodes.[369,370] The first few cycles involve the formation of a stable SEI film resulting from the electrolyte decomposition, which degrades the capacity. The capacity slowly decreases to around 201 mAh g^{-1} after 25 cycles of charging and discharging, followed by a gradual increase to 302 mAh g^{-1}

after 200 cycles. The increasing trend in the capacity is similar to that in the reported literature, and the capacity is larger than that of pure Ag_2S nanoparticles.[371]

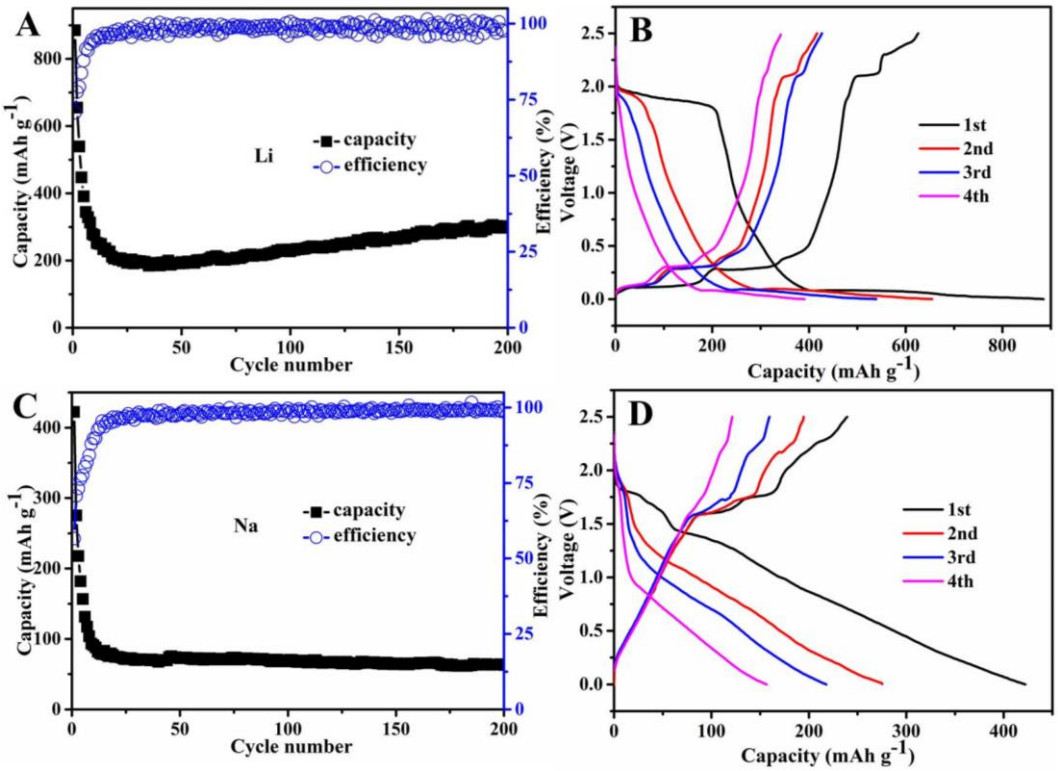

Figure 7.8 Cycling performance and Charge-discharge voltage profiles for the first 4 cycles of the 1D/2D hierarchical Ag-Ag_2S heterostructure electrode used as anode for the lithium battery (A and B) and the sodium battery (C and D) at a specific current of 30 mA g^{-1}.

From the charge-discharge curves in Figure 7.8B, the initial discharge and charge capacities are 885 and 626 mA h g^{-1}, respectively, corresponding to a coulombic efficiency of 71%, which is higher than that of the reported Ag_2S/C nanocomposite (~61%) and pure Ag_2S (~40%), and the charge capacity of the Ag-Ag_2S heterostructure electrode was also larger than for the other two.[371] Nevertheless, the coulombic efficiency increased to above 98% after 25 cycles, suggesting excellent retention capacity of the Ag-Ag_2S electrode with 1D/2D morphology. These electrochemical characteristics can be attributed to their composition and unique 1D/2D structure: (1)

the Ag in the hybrid possesses much better electrical conductivity than the pure Ag_2S and provides interconnected charge pathways so that the conductivity and mechanical strength of the whole heterostructure electrode are improved; (2) the 1D nanowires with good electronic conductivity and the 2D nanosheets effectively shorten the diffusion length of Li ions in the small primary subunits;[372] (3) the unique hierarchical 1D/2D structure could not only provide more sites or paths for lithium ion storage or transport, but also provides enough space to buffer the volume expansion during cycling and facilitate good contact with the conductive carbon black.[373]

In addition to the lithium ion battery, the 1D/2D hierarchical Ag-Ag_2S heterostructure electrode was also used as anode for the sodium ion battery for the first time. As shown in Figure 7.8C and Figure 7.8D, its capacity decreased dramatically from 422 to 91 mAh g^{-1} in the first 10 cycles, followed by a gradual decrease to 63 mAh g^{-1} after 200 cycles. The initial discharge and charge capacities are 422 and 239 mA h g^{-1}, respectively, corresponding to a coulombic efficiency of 57%, and the coulombic efficiency increased to above 98% after 30 cycles, which also suggesting excellent capacity retention of the Ag-Ag_2S electrode with 1D/2D morphology.

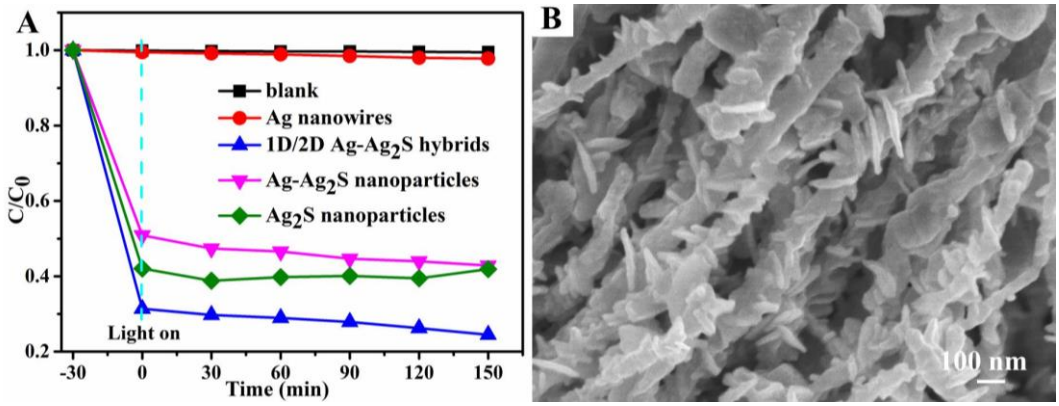

Figure 7.9 (A) Decoloration activity of the 1D/2D hierarchical Ag-Ag_2S compared with Ag-Ag_2S nanoparticles and pure Ag_2S nanoparticles and (B) SEM images of 1D/2D hierarchical Ag-Ag_2S.

Figure 7.9A shows the removal of methylene blue (MB) by the 1D/2D Ag-Ag_2S hierarchical heterostructure under both visible light illumination and in dark conditions. Approximately 76% of the dye is decolorized under solar light exposure of 150 min as compared to the 69% efficiency in dark conditions, demonstrating the weak photocatalytic effect of the 1D/2D Ag-Ag_2S hierarchical heterostructures (Figure 7.9B). It is also implied, however, that the adsorption process is quicker than the photodegradation process. Ag_2S works more as an adsorbent and less as a photosensitizer and electron donator in imparting the decoloration effects to the Ag NWs under solar light irradiation. The adsorption process transfers MB molecules to the photocatalyst surfaces, but the solar-light-driven photocatalysis process cannot radically eliminate the MB. It is well-known that both the surfaces properties (e.g. surface charge) and specific surface area contribute to the final adsorption property.[374] The zeta potential and the specific surface area of both Ag-Ag_2S hierarchical heterostructures and nanoparticles were tested. The average zeta potential of both 1D/2D hierarchical heterostructures and nanoparticles was measured to be -15 mV. The strong electrostatic interactions between positively charge MB molecules and negatively charged Ag-Ag_2S heterostructures lead to their excellent adsorption capacity. The better absorption of 1D/2D hierarchical heterostructures than core-shell nanoparticles is attributed to the larger specific surface area. The Brunauer–Emmett–Teller (BET) surface area of 1D/2D hierarchical heterostructures was determined to be 8.13 $m^2 g^{-1}$, which is larger than that of nanoparticle heterostructures (5.89 $m^2 g^{-1}$). The higher surface area could increase the number of active sites for adsorbing MB molecules effectively. In addition, the 1D/2D hierarchical heterostructures may provide a better anchoring surface in comparison with relatively smooth surface of core-shell nanoparticles. In summary, the advantages of these 1D/2D hierarchical heterostructures as an adsorbent are lager specific surface area, the unique morphology of 1D/2D hierarchical heterostructures, as well as stronger attraction between MB molecules and adsorbent surface. Compared with Ag-Ag_2S nanoparticles (Figure 7.10), pure Ag_2S nanoparticles (Figure 7.11), and Ag NWs, the

excellent decoloration of MB on the 1D/2D Ag-Ag_2S hierarchical heterostructures can be ascribed to their strong adsorption capability in the dark, due to the interfacial effect (the electrostatic interaction of the positively charged MB molecules with the negatively charged Ag-Ag_2S heterostructures) after introduction of Ag_2S nanosheets onto the surface of the Ag NWs, and the weak photodegradation of the adsorbed MB molecules through the heterostructures.

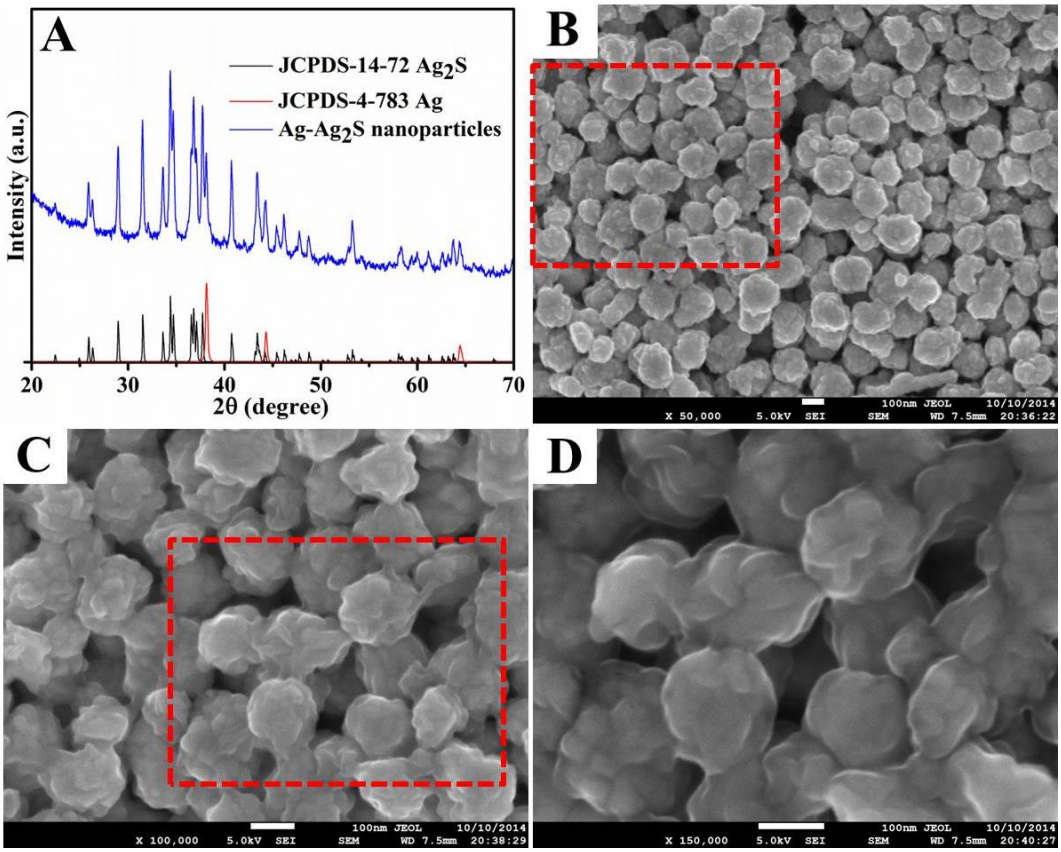

Figure 7.10 (A) XRD pattern and (B-D) SEM images of the Ag-Ag_2S nanoparticles (red dashed box identified the region each subsequent SEM image zooms in on the preceding image).

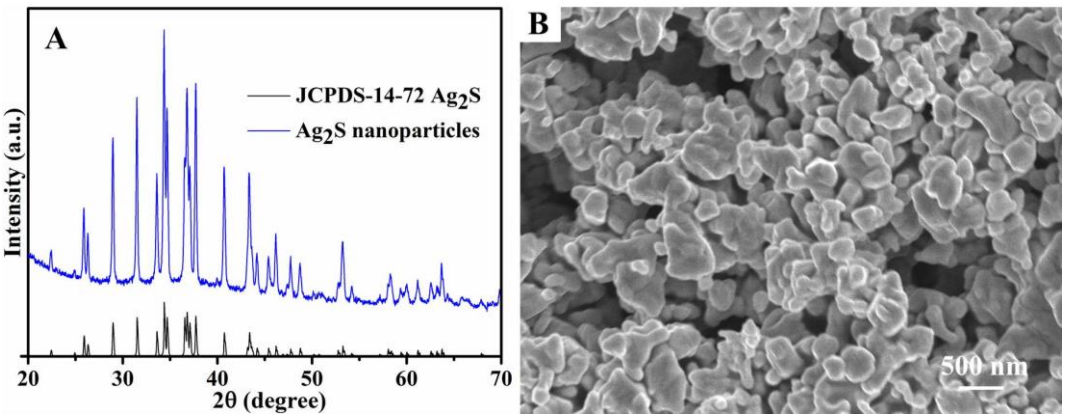

Figure 7.11 (A) XRD pattern and (B) SEM image of the pure Ag_2S nanoparticles.

Surface-enhanced Raman scattering (SERS) spectroscopy is a powerful tool for detection of traces of chemical and biological species. To study the SERS responses of our as-prepared 1D/2D hierarchical Ag-Ag_2S heterostructures, the commonly used organic dye methylene blue (MB) was selected as a target molecule. The original Raman spectrum of MB is dominated by ν(C–C) ring stretching at $\sim$1622 cm^{-1}, α(C–H) in-plane ring deformation at $\sim$ 1398 cm^{-1}, and δ(C–N–C) skeletal deformation at $\sim$449 cm^{-1}.[49,375] Figure 7.12 shows the Raman spectra of MB deposited on different glass slides coated with 1D/2D hierarchical Ag-Ag_2S nanowires, Ag-Ag_2S nanoparticles, and pure Ag_2S nanoparticles, in comparison with the spectrum of MB. It is obvious that most signals of the characteristic peaks were highly enhanced in the SERS spectra compared with that of MB solution (10^{-3} M). The characteristic peaks of MB are located almost in the same place or only slightly shifted, which indicates the adsorption of MB on the substrate surface. According to the peak at $\sim$1626 cm^{-1}, the signal enhanced by the 1D/2D hierarchical Ag-Ag_2S heterostructures and the Ag-Ag_2S nanoparticles is higher than that from the pure Ag_2S nanoparticles, which demonstrates the significant role of Ag in the hybrid structure in enhancement.

It is generally accepted that both electromagnetic enhancement and chemical enhancement could contribute to the overall surface enhancement.[376] The unique strong local plasmon resonance from the Ag metal in the hybrid structure generates more "hot spots" that can contribute to the SERS enhancement, compared to the pure Ag_2S nanoparticles.[69] The highest intensity in the case of the 1D/2D hierarchical Ag-Ag_2S heterostructures is probably due to the hierarchical and concave structures constructed from 1D nanowires and 2D nanosheets, which may boost their enhancement in comparison with spherical nanoparticles with smooth surfaces.[376,377] The enhancement of pure Ag_2S nanoparticles is relatively weaker, since the localized surface plasmon resonance (LSPR) of Ag_2S is usually located in the near-infrared/infrared region, and the SERS enhancement mainly results from the charge transfer resonance between the Ag_2S and MB molecules.[69,339,376,378,379]

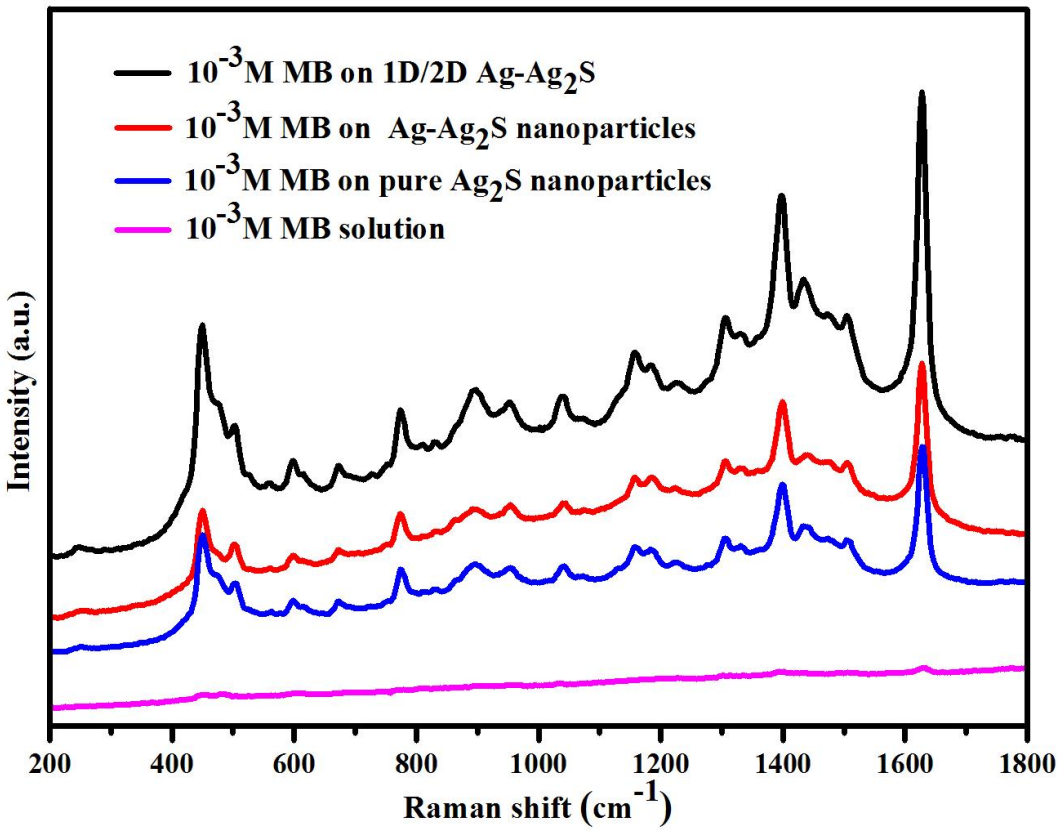

Figure 7.12 SERS spectra of the 1D/2D hierarchical Ag-Ag_2S compared with Ag-Ag2S nanoparticles and pure Ag_2S nanoparticles.

In order to demonstrate the application of as-fabricated 1D/2D hierarchical Ag-Ag_2S as a promising SERS-active substrate, the dependence of SERS signal on the concentration of adsorbed MB also was examined (Figure 7.13). The intensity of spectra increases with the increase of concentration from 10^{-6} M to 10^{-3} M. At low concentration (i.e.10^{-5}/10^{-6} M), the characteristic peaks of MB at ~1622 cm^{-1} , ~ 1398 cm^{-1} and ~ 449 cm^{-1} are faintly visible, and they become much more prominent and sharp at higher concentration (i.e. 10^{-4} ~ 10^{-3} M). This result is probably due to more dye molecules adsorbed on the substrate surface, which can create more surface active "hot spots" compared to the lower concentrations.[380-382]

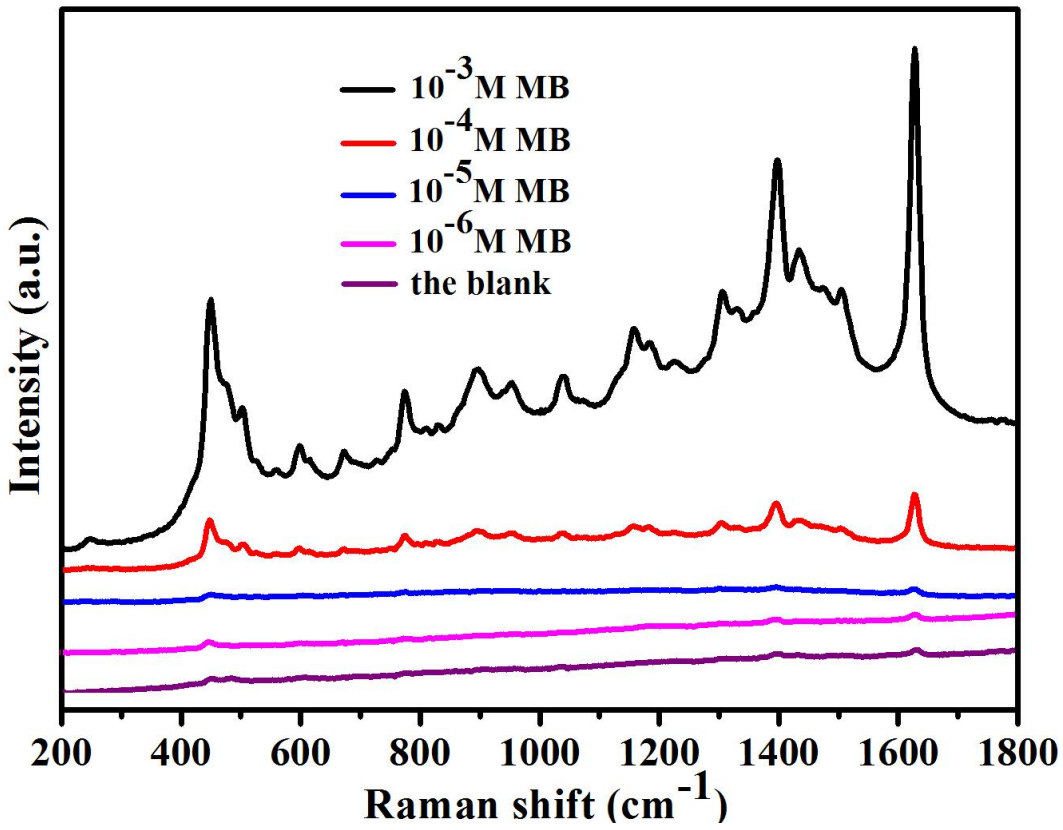

Figure 7.13 SERS spectra of MB solutions with different concentrations adsorbed on 1D/2D hierarchical Ag-Ag_2S hybrid heterostructures.

7.4 Conclusions

In summary, unique 1D/2D hierarchical Ag-Ag_2S heterostructures were successfully prepared at room temperature by an extremely simple solution method. The growth of Ag-Ag_2S hybrids is dominated by the diffusion and Ostwald ripening processes. The resultant 1D/2D hierarchical Ag-Ag_2S heterostructures exhibit good capacity when used as Li/Na ions battery anodes, high sensitivity for detection of organic dyes through SERS, and decoloration activity towards organic dyes. It was expected that this work could open up new avenues towards the facile and rational synthesis of multifunctional 1D/2D hierarchical architectures of semiconductor-noble metal hybrids for diverse applications.

Chapter 8 Conclusions and Outlook

8.1 General Conclusions

In this thesis, 1D Ag NW-based plasmonic metal/semiconductor hybrid nanostructures, including Ag@ZnO, Ag@Cu_2O, Ag@CdS, and Ag-Ag_2S with various morphologies and structures, have been fabricated by a facile wet-chemical method, and the influence of various reaction parameters has been systematicaly investigated. Their applications are mainly focused on photocatalysis, and the potential of Ag-Ag_2S hybrids in SERS detection and lithium/sodium ion batteries were also investigated. General conclusions can be drawn as follows:

During the synthesis of plasmonic Ag@ZnO core-shell hybrids, including hetero-nanowires and hetero-nanoparticles, it was found that the formation of Ag@ZnO core-shell hybrids is highly dependent on the amount of water and the concentration of $Zn(NO_3)_2$ $6H_2O$ in the reaction system. The resulting Ag@ZnO core-shell NWs with various morphologies and proportions and Ag@ZnO core–shell NPs exhibit greater plasmonic enhancement of photocatalytic activity in RhB oxidation than pure ZnO under solar light irradiation. The sample with fusiform ZnO on the surface of Ag NWs (A1) prepared with 0.6 M $Zn(NO_3)_2$ $6H_2O$ and 14.5 mL water showed the highest catalytic activity compared with Ag@ZnO NPs and pure ZnO prepared under the same conditions, as demonstrated by the 99% decoloration of RhB within 60 min with a rate constant (k) of 0.0641 min^{-1}, which is higher than that of core–shell NPs (0.0613 min^{-1}) and pure ZnO (0.0098 min^{-1}), respectively. In addition, this sample exhibited much higher stability than pure ZnO, with the photocatalytic efficiency reduced by about 10% and 25% after five cycles and eight cycles, respectively. The addition of scavengers indicates that $\cdot O_2^-$ is the major reactive species, and h^+ and $\cdot OH$ contribute greatly to the photocatalytic degradation of RhB. The enhanced photocatalytic performance of Ag@ZnO hybrids could be ascribed to the synergistic effects contributed by the surface ZnO and the Ag NW cores, the electron sink effect and SPR effect of the Ag NW cores, and the unique 1D core-shell structure for efficient mass transfer.

In the case of 1D plasmonic Ag@Cu_2O core-shell hetero-nanowires, the reaction time, the amount of Ag NWs, and the concentration of Cu^{2+} ions significantly influenced the formation of well-defined 1D Ag@Cu_2O core-shell hetero-nanowires. The resultant 1D Ag@Cu_2O NWs exhibited much higher photocatalytic activity towards degradation of methyl orange (MO) than Ag@Cu_2O core-shell nanoparticles or pure Cu_2O nanospheres under solar light irradiation. The 1D Ag@Cu_2O NWs could decolor 92% of the MO within 140 min, which is higher than for the MO degraded over the Ag@Cu_2O NPs (83 %) and pure Cu_2O nanospheres (71 %), respectively. The h^+ and O_2^- are the major reactive species, and molecular oxygen plays an important role in the photodegradation of MO over 1D Ag@Cu_2O core − shell hetero-nanowires. The enhancement in photocatalytic activity of the 1D core −shell Ag@Cu_2O NWs could be due to the formation of a Schottky barrier at the interface between the Ag NW core and the Cu_2O shell, the SPR effect of the Ag NW cores, the large specific surface area, the excellent electron conductivity and mobility, and the high length-to-diameter ratio of this unique 1D core-shell nanostructure.

Compared with 1D Ag@ZnO and Ag@Cu_2O heterostructures, the preparation of 1D Ag@CdS core-shell NWs with hierarchical nanostructures has to be performed at 80 ^oC rather than ambient temperature. The formation of hierarchical NWs assembled from nanosheets and nanoparticles on the surface is strongly influenced by the amount of $Cd(NO_3)_2 \cdot 4H_2O$/thiourea, and in particular, a greater amount of $Cd(NO_3)_2 \cdot 4H_2O$ with a higher ratio of $Cd(NO_3)_2 \cdot 4H_2O$/thiourea promotes the formation of well-defined 1D hierarchical nanowires. The as-synthesized 1D hierarchical Ag@CdS core-shell hetero-nanowires exhibited enhanced photocatalytic performance towards the degradation of aqueous solutions of methyl orange (MO) and towards hydrogen generation than pure CdS. They could degrade 96% of MO dye within 240 min and generated 181.2 μmol of hydrogen after 4 h, while pure CdS nanoflowers could only degrade 85% of the MO and produce 134.5 μmol H_2 under the same condictions. The enhanced performance could be attributed to the synergistic effects of the Ag NWs and surface CdS in the proper ratio, as well as the special hierarchical nanostructure, which could provide more active sites for the photocatalytic reaction.

Another new type of unique 1D/2D hierarchical Ag-Ag_2S heterostructures was fabricated by an extremely simple solution route at room temperature. The formation of well-defined 1D/2D hierarchical Ag-Ag_2S heterostructures is strongly dependent on the reaction time and the Ag/S ratio. The diffusion and Ostwald ripening processes dominate the evolution of the 1D/2D heterostructure morphology. The resultant 1D/2D Ag-Ag_2S hybrids exhibit favourable multifunctional properties for energy and environmental applications, such as good capacity when used as Li/Na ion battery anodes, high sensitivity towards the detection of methylene blue (MB) dye through SERS, and decoloration activity towards MB dye. For application in Li/Na batteries, the resultant 1D/2D Ag-Ag_2S hybrids deliver initial discharge and charge capacities of 885 and 626 mA h g^{-1} at a specific current of 30 mA g^{-1}, and show excellent cycling stability (302 mAh g^{-1} over 200 cycles) and higher rate capability compared with Ag_2S NPs based anode. The hybrids were also used as anode for the sodium ion battery for the first time, and delivered a capacity of 63 mAh g^{-1} after 200 cycles with the coulombic efficiency above 98%. For removal of methylene blue (MB), about 76% of the dye was decolorized under exposure to solar light for 150 min, which is higher than that of Ag-Ag_2S nanoparticles, pure Ag_2S nanoparticles, and Ag NWs. The excellent performance was ascribed to their strong adsorption capability in the dark, due to the interfacial effect (the electrostatic interaction of the positively charged MB molecules with the negatively charged Ag-Ag_2S heterostructures) after the introduction of Ag_2S nanosheets onto the surface of the Ag NWs and the weak photodegradation of the adsorbed MB molecules through the heterostructures. In the SERS detection, the detection limit of MB can be as low as 10^{-6} M, which could be due to the local plasmon resonance from the Ag metal in the hybrid structure, the hierarchical and concave structures constructed from 1D nanowires and 2D nanosheets.

8.2 Outlook

Based on this thesis work and the above understanding, there are still several challenges to be solved: Firstly, although the photocatalytic mechanisms have been discussed in the thesis, the detailed mechanism of plasmonic photocatalysis is very complicated and hard to systematize, because it involves a number of factors including constitution, morphology, size, bandgap, facet, defects, and surface area.

To better understand plasmonic photocatalysis, further studies should be carried out on various theoretical and experimental aspects in this area, especially the processes of charge generation, separation and transportation across the interface and the surface of the plasmonic photocatalysts, along with advanced characterization techniques (such as femtosecond/picosecond time-resolved transient absorption spectroscopy,[2,383] surface photovoltage technique,[384,385] EPR technique,[386] time-resolved microwave conductivity method,[387] stopped flow technique,[388] and photocurrent measurement[389] etc.). Secondly, use a probe molecule which is not visible-light sensitised to remove this complexity from the system. Thirdly, the construction of highly tunable and more complex hierarchical architectures, hollow structures, and porous structures with large surface area, improved light-harvesting capacity and high-energy conversion efficiency, based on 1D nanostructures assembled from 0D, 1D, and 2D building blocks is highly desirable. Fourthly, the exploration of a highly efficient new systems with good photostability is needed for practical applications, by methods such as introducing an insulator layer at the interface junction, in combination with other polar semiconductors with an internal electric field, plasmonic metals such as Au, Cu, Pt, and their alloys, and non-metal plasmonic nanomaterials with low prices and unique features to form a multicomponent system. Finally, their applications in other fields can be investigated, such as production of H_2 and O_2, CO_2 reduction, organic synthesis, solar cells, and various biomedical research applications.

REFERENCES

1. M. Rycenga, C.M. Cobley, J. Zeng, W. Li, C.H. Moran, Q. Zhang, D. Qin, Y. Xia, *Chem. Rev.*, 2011, 111, 3669-3712.

2. R. Jiang, B. Li, C. Fang, J. Wang, *Adv. Mater.*, 2014, 26, 5274-5309.

3. S. Linic, P. Christopher, D.B. Ingram, *Nat. Mater.*, 2011, 10, 911-921.

4. Q. Zhang, W. Li, C. Moran, J. Zeng, J. Chen, L.-P. Wen, Y. Xia, *J. Am. Chem. Soc.*, 2010, 132, 11372-11378.

5. Z.W. Seh, S. Liu, M. Low, S.-Y. Zhang, Z. Liu, A. Mlayah, M.-Y. Han, *Adv. Mater.*, 2012, 24, 2310-2314.

6. X.-F. Wu, H.-Y. Song, J.-M. Yoon, Y.-T. Yu, Y.-F. Chen, *Langmuir*, 2009, 25, 6438-6447.

7. P. Rai, R. Khan, S. Raj, S.M. Majhi, K.-K. Park, Y.-T. Yu, I.-H. Lee, P.K. Sekhar, *Nanoscale*, 2014, 6, 581-588.

8. L. Zhang, H. Jing, G. Boisvert, J.Z. He, H. Wang, *ACS Nano*, 2012, 6, 3514-3527.

9. L. Zhang, D.A. Blom, H. Wang, *Chem. Mater.*, 2011, 23, 4587-4598.

10. P. Ramasamy, D.-M. Seo, S.-H. Kim, J. Kim, *J. Mater. Chem.*, 2012, 22, 11651-11657.

11. J. Li, S.K. Cushing, J. Bright, F. Meng, T.R. Senty, P. Zheng, A.D. Bristow, N. Wu, *ACS Catal.*, 2013, 3, 47-51.

12. Y. Zhang, H. Ding, Y. Liu, S. Pan, Y. Luo, G. Li, *J. Mater. Chem.*, 2012, 22, 10779-10786.

13. C. Ren, B. Yang, M. Wu, J. Xu, Z. Fu, Y. lv, T. Guo, Y. Zhao, C. Zhu, *J. Hazard. Mater.*, 2010, 182, 123-129.

14. W. Zhao, Y. Guo, Y. Faiz, W.-T. Yuan, C. Sun, S.-M. Wang, Y.-H. Deng, Y. Zhuang, Y. Li, X.-M. Wang, H. He, S.-G. Yang, *Appl. Catal. B: Environ.*, 2015, 163, 288-297.

15. H. Wang, L. Zhang, Z. Chen, J. Hu, S. Li, Z. Wang, J. Liu, X. Wang, *Chem. Soc. Rev.*, 2014, 43, 5234-5244.

16. L. Jing, W. Zhou, G. Tian, H. Fu, *Chem. Soc. Rev.*, 2013, 42, 9509-9549.

17. N. Zhang, S. Liu, X. Fu, Y.-J. Xu, *J. Phys. Chem. C*, 2011, 115, 9136-9145.

18. Y. Zheng, L. Zheng, Y. Zhan, X. Lin, Q. Zheng, K. Wei, *Inorg. Chem.*, 2007, 46, 6980-6986.

19. C. Yu, K. Yang, Y. Xie, Q. Fan, J.C. Yu, Q. Shu, C. Wang, *Nanoscale*, 2013, 5, 2142-2151.

20. C. Mondal, J. Pal, M. Ganguly, A.K. Sinha, J. Jana, T. Pal, *New J. Chem.*, 2014, 38, 2999-3005.

21. M. Misra, P. Kapur, M.L. Singla, *Appl. Catal. B: Environ.*, 2014, 150–151, 605-611.

22. Z. Ai, L. Zhang, S. Lee, W. Ho, *J. Phys. Chem. C*, 2009, 113, 20896-20902.

23. C.-H. Kuo, Y.-C. Yang, S. Gwo, M.H. Huang, *J. Am. Chem. Soc.*, 2011, 133, 1052-1057.

24. Z. Wang, S. Zhao, S. Zhu, Y. Sun, M. Fang, *CrystEngComm*, 2011, 13, 2262-2267.

25. W. Zhang, X. Yang, Q. Zhu, K. Wang, J. Lu, M. Chen, Z. Yang, *Ind. Eng. Chem. Res.*, 2014, 53, 16316-16323.

26. B. Lu, A. Liu, H. Wu, Q. Shen, T. Zhao, J. Wang, *Langmuir*, 2016, 32, 3085-3094.

27. X. Ma, K. Zhao, H. Tang, Y. Chen, C. Lu, W. Liu, Y. Gao, H. Zhao, Z. Tang, *Small*, 2014, 10, 4664-4670.

28. S. Han, L. Hu, N. Gao, A.A. Al-Ghamdi, X. Fang, *Adv. Funct. Mater.*, 2014, 24, 3725-3733.

29. W. Yang, L. Zhang, Y. Hu, Y. Zhong, H.B. Wu, X.W. Lou, *Angew. Chem., Int. Ed.*, 2012, 51, 11501-11504.

30. L. Ma, S. Liang, X.-L. Liu, D.-J. Yang, L. Zhou, Q.-Q. Wang, *Adv. Funct. Mater.*, 2015, 25, 898-904.

31. G. Manna, R. Bose, N. Pradhan, *Angew. Chem., Int. Ed.*, 2014, 53, 6743-6746.

32. K.K. Haldar, G. Sinha, J. Lahtinen, A. Patra, *ACS Appl. Mater. Interfaces*, 2012, 4, 6266-6272.

33. H. Li, W. Lu, J. Tian, Y. Luo, A.M. Asiri, A.O. Al-Youbi, X. Sun, *Chem. Eur. J.*, 2012, 18, 8508-8514.

34. Y. Pan, S. Deng, L. Polavarapu, N. Gao, P. Yuan, C.H. Sow, Q.-H. Xu, *Langmuir*, 2012, 28, 12304-12310.

35. S. Liu, Y.-J. Xu, *Nanoscale*, 2013, 5, 9330-9339.

36. B. Cheng, Y. Le, J. Yu, *J. Hazard. Mater.*, 2010, 177, 971-977.

37. H.R. Liu, G.X. Shao, J.F. Zhao, Z.X. Zhang, Y. Zhang, J. Liang, X.G. Liu, H.S. Jia, B.S. Xu, *J. Phys. Chem. C*, 2012, 116, 16182-16190.

38. Y. Liu, M. Chi, H. Dong, H. Jia, B. Xu, Z. Zhang, *Appl. Surf. Sci.*, 2014, 313, 558-562.

39. L. Wu, S. Fang, L. Ge, C. Han, P. Qiu, Y. Xin, *J. Hazard. Mater.*, 2015, 300, 93-103.

40. Y. Bi, J. Ye, *Chem. Commun.*, 2009, 6551-6553.

41. H. Hu, Z. Jiao, G. Lu, J. Ye, Y. Bi, *RSC Adv.*, 2014, 4, 31795-31798.

42. Y. Bi, H. Hu, S. Ouyang, Z. Jiao, G. Lu, J. Ye, *J. Mater. Chem.*, 2012, 22, 14847-14850.

43. H. Hu, Z. Jiao, T. Wang, J. Ye, G. Lu, Y. Bi, *J. Mater. Chem. A*, 2013, 1, 10612-10616.

44. W. Song, X. Han, L. Chen, Y. Yang, B. Tang, W. Ji, W. Ruan, W. Xu, B. Zhao, Y. Ozaki, *J. Raman Spectrosc.*, 2010, 41, 907-913.

45. I.A. Ji, J.H. Bang, *Mater. Lett.*, 2013, 97, 158-161.

46. J. Yin, Y. Zang, C. Yue, Z. Wu, S. Wu, J. Li, Z. Wu, *J. Mater. Chem.*, 2012, 22, 7902-7909.

47. Y. Zang, J. Yin, X. He, C. Yue, Z. Wu, J. Li, J. Kang, *J. Mater. Chem. A*, 2014, 2, 7747-7753.

48. L. Yang, W. Ruan, X. Jiang, B. Zhao, W. Xu, J.R. Lombardi, *J. Phys. Chem. C*, 2009, 113, 117-120.

49. W. Jin, P. Xu, L. Xiong, Q. Jing, B. Zhang, K. Sun, X. Han, *RSC Adv.*, 2014, 4, 53543-53546.

50. Y. Wang, W. Song, W. Ruan, J. Yang, B. Zhao, J.R. Lombardi, *J. Phys. Chem. C*, 2009, 113, 8065-8069.

51. L. Chen, H.K. Seo, Z. Mao, Y.M. Jung, B. Zhao, *Anal. Methods*, 2011, 3, 1622-1627.

52. M.R. Hoffmann, S.T. Martin, W. Choi, D.W. Bahnemann, *Chem. Rev.*, 1995, 95, 69-96.

53. X. Chen, S. Shen, L. Guo, S.S. Mao, *Chem. Rev.*, 2010, 110, 6503-6570.

54. L. Yang, H. Zhou, T. Fan, D. Zhang, *Phys. Chem. Chem. Phys.*, 2014, 16, 6810-6826.

55. H. Kisch, *Angew. Chem., Int. Ed.*, 2013, 52, 812-847.

56. N. Serpone, A. Emeline, *J. Phys. Chem. Lett.*, 2012, 3, 673-677.
57. K. Hashimoto, H. Irie, A. Fujishima, *Jpn. J. Appl. Phys.*, 2005, 44, 8269.
58. J. Schneider, M. Matsuoka, M. Takeuchi, J. Zhang, Y. Horiuchi, M. Anpo, D.W. Bahnemann, *Chem. Rev.*, 2014, 114, 9919-9986.
59. M. Fujihira, Y. Satoh, T. Osa, *Nature*, 1981, 293, 206-208.
60. C. Tian, Q. Zhang, A. Wu, M. Jiang, Z. Liang, B. Jiang, H. Fu, *Chem. Commun.*, 2012, 48, 2858-2860.
61. Y. Wang, R. Shi, J. Lin, Y. Zhu, *Energy Environ. Sci.*, 2011, 4, 2922-2929.
62. J. Kondo, *Chem. Commun.*, 1998, 357-358.
63. W.-C. Huang, L.-M. Lyu, Y.-C. Yang, M.H. Huang, *J. Am. Chem. Soc.*, 2011, 134, 1261-1267.
64. Y. Li, Y. Hu, S. Peng, G. Lu, S. Li, *J. Phys. Chem. C*, 2009, 113, 9352-9358.
65. J.S. Jang, U.A. Joshi, J.S. Lee, *J. Phys. Chem. C*, 2007, 111, 13280-13287.
66. N. Bao, L. Shen, T. Takata, K. Domen, *Chem. Mater.*, 2007, 20, 110-117.
67. K. Nagasuna, T. Akita, M. Fujishima, H. Tada, *Langmuir*, 2011, 27, 7294-7300.
68. H. Jia, W. He, W.G. Wamer, X. Han, B. Zhang, S. Zhang, Z. Zheng, Y. Xiang, J.-J. Yin, *J. Phys. Chem. C*, 2014, 118, 21447-21456.
69. Q. Cao, R. Che, N. Chen, *Chem. Commun.*, 2014, 50, 4931-4933.
70. J. Xiong, Z. Li, J. Chen, S. Zhang, L. Wang, S. Dou, *ACS Appl. Mater. Interfaces*, 2014, 6, 15716-15725.
71. J. Xiong, Q. Sun, J. Chen, Z. Li, S. Dou, *CrystEngComm*, 2016, 18, 1713-1722.
72. J. Wang, D.N. Tafen, J.P. Lewis, Z. Hong, A. Manivannan, M. Zhi, M. Li, N. Wu, *J. Am. Chem. Soc.*, 2009, 131, 12290-12297.
73. M. Misra, P. Kapur, M.L. Singla, *Appl. Catal. B: Environ.*, 2014, 150, 605-611.
74. G. Liu, L. Wang, H.G. Yang, H.-M. Cheng, G.Q.M. Lu, *J. Mater. Chem.*, 2010, 20, 831-843.
75. J.-H. Sun, S.-Y. Dong, Y.-K. Wang, S.-P. Sun, *J. Hazard. Mater.*, 2009, 172, 1520-1526.
76. F. Xu, Y. Shen, L. Sun, H. Zeng, Y. Lu, *Nanoscale*, 2011, 3, 5020-5025.
77. H. Xu, W. Wang, W. Zhu, *J. Phys. Chem. B*, 2006, 110, 13829-13834.
78. Y. Zhang, B. Deng, T. Zhang, D. Gao, A.-W. Xu, *J. Phys. Chem. C*, 2010, 114, 5073-5079.

79. C. Li, J. Yuan, B. Han, W. Shangguan, *Int. J. Hydrogen Energy*, 2011, 36, 4271-4279.

80. S. In, A. Orlov, R. Berg, F. García, S. Pedrosa-Jimenez, M.S. Tikhov, D.S. Wright, R.M. Lambert, *J. Am. Chem. Soc.*, 2007, 129, 13790-13791.

81. R. Asahi, T. Morikawa, T. Ohwaki, K. Aoki, Y. Taga, *Science*, 2001, 293, 269-271.

82. E. Aazam, *J. Ind. Eng. Chem.*, 2014, 20, 4033-4038.

83. A. Kudo, M. Sekizawa, *Chem. Commun.*, 2000, 1371-1372.

84. D. Dvoranova, V. Brezova, M. Mazúr, M.A. Malati, *Appl. Catal. B: Environ.*, 2002, 37, 91-105.

85. K. Takanabe, K. Kamata, X. Wang, M. Antonietti, J. Kubota, K. Domen, *Phys. Chem. Chem. Phys.*, 2010, 12, 13020-13025.

86. S. Min, G. Lu, *J. Phys. Chem. C*, 2011, 115, 13938-13945.

87. W.J. Youngblood, S.-H.A. Lee, K. Maeda, T.E. Mallouk, *Acc. Chem. Res.*, 2009, 42, 1966-1973.

88. J. He, J. Wang, Y. Chen, J. Zhang, D. Duan, Y. Wang, Z. Yan, *Chem. Commun.*, 2014, 50, 7063-7066.

89. Z.W. Seh, S. Liu, M. Low, S.Y. Zhang, Z. Liu, A. Mlayah, M.Y. Han, *Adv. Mater.*, 2012, 24, 2310-2314.

90. J. Lu, P. Zhang, A. Li, F. Su, T. Wang, Y. Liu, J. Gong, *Chem. Commun.*, 2013, 49, 5817-5819.

91. H. Li, Y. Zhou, W. Tu, J. Ye, Z. Zou, *Adv. Funct. Mater.*, 2015, 25, 998-1013.

92. F. Zhang, Y. Ding, Y. Zhang, X. Zhang, Z.L. Wang, *ACS Nano*, 2012, 6, 9229-9236.

93. T. Liu, B. Li, Y. Hao, F. Han, L. Zhang, L. Hu, *Appl. Catal. B: Environ.*, 2015, 165, 378-388.

94. W. Yao, B. Zhang, C. Huang, C. Ma, X. Song, Q. Xu, *J. Mater. Chem.*, 2012, 22, 4050-4055.

95. Y. Wang, Q. Wang, X. Zhan, F. Wang, M. Safdar, J. He, *Nanoscale*, 2013, 5, 8326-8339.

96. J. Tian, Z. Zhao, A. Kumar, R.I. Boughton, H. Liu, *Chem. Soc. Rev.*, 2014, 43, 6920-6937.

97. C.-T. Dinh, H. Yen, F. Kleitz, T.-O. Do, *Angew. Chem., Int. Ed.*, 2014, 53, 6618-6623.

98. P. Wang, B. Huang, Y. Dai, M.-H. Whangbo, *Phys. Chem. Chem. Phys.*, 2012, 14, 9813-9825.

99. B. Weng, S. Liu, Z.-R. Tang, Y.-J. Xu, *RSC Adv.*, 2014, 4, 12685-12700.

100. L. Jiang, G. Zhou, J. Mi, Z. Wu, *Catal. Commun.*, 2012, 24, 48-51.

101. M. Long, W. Cai, *Nanoscale*, 2014, 6, 7730-7742.

102. H. Cui, Z. Gao, Z. Cui, S. Zhu, Z. Li, Y. Liang, X. Yang, *Curr. Nanosci.*, 2015, 11, 633-639.

103. C. Su, L. Liu, M. Zhang, Y. Zhang, C. Shao, *CrystEngComm*, 2012, 14, 3989-3999.

104. S. Lal, S. Link, N.J. Halas, *Nat. Photonics*, 2007, 1, 641-648.

105. W. Hou, S.B. Cronin, *Adv. Funct. Mater.*, 2013, 23, 1612-1619.

106. S.K. Ghosh, T. Pal, *Chem. Rev.*, 2007, 107, 4797-4862.

107. X. Zhou, G. Liu, J. Yu, W. Fan, *J. Mater. Chem.*, 2012, 22, 21337-21354.

108. A.W. Sanders, D.A. Routenberg, B.J. Wiley, Y. Xia, E.R. Dufresne, M.A. Reed, *Nano Lett.*, 2006, 6, 1822-1826.

109. T.K. Sau, A.L. Rogach, F. Jäckel, T.A. Klar, J. Feldmann, *Adv. Mater.*, 2010, 22, 1805-1825.

110. X. Kou, W. Ni, C.-K. Tsung, K. Chan, H.-Q. Lin, G.D. Stucky, J. Wang, *Small*, 2007, 3, 2103-2113.

111. P. Jain, X. Huang, I. El-Sayed, M. El-Sayed, *Plasmonics*, 2007, 2, 107-118.

112. K.L. Kelly, E. Coronado, L.L. Zhao, G.C. Schatz, *J. Phys. Chem. B*, 2003, 107, 668-677.

113. Y. Xia, Y. Xiong, B. Lim, S.E. Skrabalak, *Angew. Chem., Int. Ed.*, 2009, 48, 60-103.

114. C. Burda, X. Chen, R. Narayanan, M.A. El-Sayed, *Chem. Rev.*, 2005, 105, 1025-1102.

115. S.F. Chen, J.P. Li, K. Qian, W.P. Xu, Y. Lu, W.X. Huang, S.H. Yu, *Nano Res.*, 2010, 3, 244-255.

116. I. Unlu, J.W. Soares, D.M. Steeves, J.E. Whitten, *Langmuir*, 2015, 31, 8718-8725.

117. X. Wang, Y. Ying, J. Lei, P. Hu, X. Peng, *RSC Adv.*, 2014, 4, 42441-42444.

118. M. Miljevic, B. Geiseler, T. Bergfeldt, P. Bockstaller, L. Fruk, *Adv. Funct. Mater.*, 2014, 24, 907-915.

119. F. Xiao, F. Wang, X. Fu, Y. Zheng, *J. Mater. Chem.*, 2012, 22, 2868-2877.

120. S. Sun, W. Wang, S. Zeng, M. Shang, L. Zhang, *J. Hazard. Mater.*, 2010, 178, 427-433.

121. W. Hou, W.H. Hung, P. Pavaskar, A. Goeppert, M. Aykol, S.B. Cronin, *ACS Catal.*, 2011, 1, 929-936.

122. H.W. Choi, E.J. Kim, S.H. Hahn, *Chem. Eng. J.*, 2010, 161, 285-288.

123. W.-T. Chen, T.-T. Yang, Y.-J. Hsu, *Chem. Mater.*, 2008, 20, 7204-7206.

124. R.T. Tom, A.S. Nair, N. Singh, M. Aslam, C.L. Nagendra, R. Philip, K. Vijayamohanan, T. Pradeep, *Langmuir*, 2003, 19, 3439-3445.

125. C.-H. Kuo, T.-E. Hua, M.H. Huang, *J. Am. Chem. Soc.*, 2009, 131, 17871-17878.

126. L. Zhang, H. Wang, *ACS Nano*, 2011, 5, 3257-3267.

127. J. Jiang, L. Zhang, H. Li, W. He, J.J. Yin, *Nanoscale*, 2013, 5, 10573-10581.

128. R. Su, R. Tiruvalam, Q. He, N. Dimitratos, L. Kesavan, C. Hammond, J.A. Lopez-Sanchez, R. Bechstein, C.J. Kiely, G.J. Hutchings, *ACS Nano*, 2012, 6, 6284-6292.

129. C. Gu, C. Cheng, H. Huang, T. Wong, N. Wang, T.-Y. Zhang, *Cryst. Growth Des.*, 2009, 9, 3278-3285.

130. E. Grabowska, A. Zaleska, S. Sorgues, M. Kunst, A. Etcheberry, C. Colbeau-Justin, H. Remita, *J. Phys. Chem. C*, 2013, 117, 1955-1962.

131. A. Bumajdad, M. Madkour, *Phys. Chem. Chem. Phys.*, 2014, 16, 7146-7158.

132. S.-i. Naya, K. Kimura, H. Tada, *ACS Catal.*, 2013, 3, 10-13.

133. S.K. Cushing, J. Li, F. Meng, T.R. Senty, S. Suri, M. Zhi, M. Li, A.D. Bristow, N. Wu, *J. Am. Chem. Soc.*, 2012, 134, 15033-15041.

134. J. Yu, G. Dai, B. Huang, *J. Phys. Chem. C*, 2009, 113, 16394-16401.

135. C. Gomes Silva, R. Juárez, T. Marino, R. Molinari, H. García, *J. Am. Chem. Soc.*, 2011, 133, 595-602.

136. J. Tang, *ChemSusChem*, 2010, 3, 800-801.

137. Y. Tian, T. Tatsuma, *J. Am. Chem. Soc.*, 2005, 127, 7632-7637.

138. X. Zhou, C. Hu, X. Hu, T. Peng, J. Qu, *J. Phys. Chem. C*, 2010, 114, 2746-2750.

139. E. Kowalska, R. Abe, B. Ohtani, *Chem. Commun.*, 2009, 241-243.

140. E. Kowalska, O.O.P. Mahaney, R. Abe, B. Ohtani, *Phys. Chem. Chem. Phys.*, 2010, 12, 2344-2355.

141. A. Primo, A. Corma, H. Garcia, *Phys. Chem. Chem. Phys.*, 2011, 13, 886-910.

142. Y. Tian, T. Tatsuma, *Chem. Commun.*, 2004, 1810-1811.

143. A. Primo, T. Marino, A. Corma, R. Molinari, H. Garcá, *J. Am. Chem. Soc.*, 2011, 133, 6930-6933.

144. S. Pany, B. Naik, S. Martha, K. Parida, *ACS Appl. Mater. Interfaces*, 2014, 6, 839-846.

145. P. Thiyagarajan, H.-J. Ahn, J.-S. Lee, J.-C. Yoon, J.-H. Jang, *Small*, 2013, 9, 2341-2347.

146. M. Gratzel, *Nature*, 2001, 414, 338-344.

147. W.J. Youngblood, S.-H.A. Lee, Y. Kobayashi, E.A. Hernandez-Pagan, P.G. Hoertz, T.A. Moore, A.L. Moore, D. Gust, T.E. Mallouk, *J. Am. Chem. Soc.*, 2009, 131, 926-927.

148. W. Tu, Y. Zhou, H. Li, P. Li, Z. Zou, *Nanoscale*, 2015, 7, 14232-14236.

149. D.B. Ingram, P. Christopher, J.L. Bauer, S. Linic, *ACS Catal.*, 2011, 1, 1441-1447.

150. Y. Lu, H. Yu, S. Chen, X. Quan, H. Zhao, *Environ. Sci. Technol.*, 2012, 46, 1724-1730.

151. H. Duan, Y. Xuan, *Physica E*, 2011, 43, 1475-1480.

152. T. Torimoto, H. Horibe, T. Kameyama, K.-i. Okazaki, S. Ikeda, M. Matsumura, A. Ishikawa, H. Ishihara, *J. Phys. Chem. Lett.*, 2011, 2, 2057-2062.

153. H. Zhu, X. Ke, X. Yang, S. Sarina, H. Liu, *Angew. Chem., Int. Ed.*, 2010, 49, 9657-9661.

154. Z. Liu, W. Hou, P. Pavaskar, M. Aykol, S.B. Cronin, *Nano Lett.*, 2011, 11, 1111-1116.

155. Y.-C. Pu, G. Wang, K.-D. Chang, Y. Ling, Y.-K. Lin, B.C. Fitzmorris, C.-M. Liu, X. Lu, Y. Tong, J.Z. Zhang, Y.-J. Hsu, Y. Li, *Nano Lett.*, 2013, 13, 3817-3823.

156. H. Zhang, A.O. Govorov, *J. Phys. Chem. C*, 2014, 118, 7606-7614.

157. C.K. Ngaw, Q. Xu, T.T.Y. Tan, P. Hu, S. Cao, J.S.C. Loo, *Chem. Eng. J.*, 2014, 257, 112-121.

158. J.-J. Chen, J.C.S. Wu, P.C. Wu, D.P. Tsai, *J. Phys. Chem. C*, 2011, 115, 210-216.

159. W. Xie, Y. Li, W. Sun, J. Huang, H. Xie, X. Zhao, *J. Photochem. Photobiol. A: Chem.*, 2010, 216, 149-155.

160. D.D. Evanoff, G. Chumanov, *ChemPhysChem*, 2005, 6, 1221-1231.

161. D. Tsukamoto, Y. Shiraishi, Y. Sugano, S. Ichikawa, S. Tanaka, T. Hirai, *J. Am. Chem. Soc.*, 2012, 134, 6309-6315.

162. Q. Wang, B. Geng, S. Wang, *Environ. Sci. Technol.*, 2009, 43, 8968-8973.

163. Q. Hua, F. Shi, K. Chen, S. Chang, Y. Ma, Z. Jiang, G. Pan, W. Huang, *Nano Res.*, 2011, 4, 948-962.

164. T. Kou, C. Jin, C. Zhang, J. Sun, Z. Zhang, *RSC Adv.*, 2012, 2, 12636-12643.

165. H. Zhu, M. Du, D. Yu, Y. Wang, L. Wang, M. Zou, M. Zhang, Y. Fu, *J. Mater. Chem. A*, 2013, 1, 919-929.

166. D. Jiang, W. Wang, S. Sun, L. Zhang, Y. Zheng, *ACS Catal.*, 2015, 5, 613-621.

167. Y. Zhang, N. Zhang, Z.-R. Tang, Y.-J. Xu, *ACS Sustainable Chem. Eng.*, 2013, 1, 1258-1266.

168. N. Zhang, Y.-J. Xu, *Chem. Mater.*, 2013, 25, 1979-1988.

169. N. Zhang, X. Fu, Y.-J. Xu, *J. Mater. Chem.*, 2011, 21, 8152-8158.

170. A. Nakajima, T. Kobayashi, T. Isobe, S. Matsushita, *Mater. Lett.*, 2011, 65, 3051-3054.

171. S.-i. Naya, T. Nikawa, K. Kimura, H. Tada, *ACS Catal.*, 2013, 3, 903-907.

172. K. Qian, B.C. Sweeny, A.C. Johnston-Peck, W. Niu, J.O. Graham, J.S. DuChene, J. Qiu, Y.-C. Wang, M.H. Engelhard, D. Su, E.A. Stach, W.D. Wei, *J. Am. Chem. Soc.*, 2014, 136, 9842-9845.

173. Z. Zheng, B. Huang, X. Qin, X. Zhang, Y. Dai, M.-H. Whangbo, *J. Mater. Chem.*, 2011, 21, 9079-9087.

174. L. Kong, W. Chen, D. Ma, Y. Yang, S. Liu, S. Huang, *J. Mater. Chem.*, 2012, 22, 719-724.

175. A. Tanaka, K. Hashimoto, H. Kominami, *J. Am. Chem. Soc.*, 2012, 134, 14526-14533.

176. B. Li, T. Gu, T. Ming, J. Wang, P. Wang, J. Wang, J.C. Yu, *ACS Nano*, 2014, 8, 8152-8162.

177. T.-T. Yang, W.-T. Chen, Y.-J. Hsu, K.-H. Wei, T.-Y. Lin, T.-W. Lin, *J. Phys. Chem. C*, 2010, 114, 11414-11420.

178. I. Majeed, M.A. Nadeem, M. Al-Oufi, M.A. Nadeem, G.I.N. Waterhouse, A. Badshah, J.B. Metson, H. Idriss, *Appl. Catal. B: Environ.*, 2016, 182, 266-276.

179. R. Singh, B. Pal, *J. Mol. Catal. A: Chem.*, 2013, 378, 246-254.

180. X. Song, W. Yao, B. Zhang, Y. Wu, *Int. J. Photoenergy*, 2012, 2012, 5.

181. J. Li, S.K. Cushing, P. Zheng, T. Senty, F. Meng, A.D. Bristow, A. Manivannan, N. Wu, *J. Am. Chem. Soc.*, 2014, 136, 8438-8449.

182. N. Kumar, V.K. Komarala, V. Dutta, *Chem. Eng. J.*, 2014, 236, 66-74.

183. M.J. Berr, P. Wagner, S. Fischbach, A. Vaneski, J. Schneider, A.S. Susha, A.L. Rogach, F. Jäckel, J. Feldmann, *Appl. Phys. Lett.*, 2012, 100, 223903.

184. K. Wu, Z. Chen, H. Lv, H. Zhu, C.L. Hill, T. Lian, *J. Am. Chem. Soc.*, 2014, 136, 7708-7716.

185. N.E. Fard, R. Fazaeli, R. Ghiasi, *Chem. Eng. Technol.*, 2016, 39, 149-157.

186. R. Costi, A.E. Saunders, E. Elmalem, A. Salant, U. Banin, *Nano Lett.*, 2008, 8, 637-641.

187. J.U. Bang, S.J. Lee, J.S. Jang, W. Choi, H. Song, *J. Phys. Chem. Lett.*, 2012, 3, 3781-3785.

188. W.-T. Chen, Y.-K. Lin, T.-T. Yang, Y.-C. Pu, Y.-J. Hsu, *Chem. Commun.*, 2013, 49, 8486-8488.

189. J. Zhang, Y. Wang, J. Zhang, Z. Lin, F. Huang, J. Yu, *ACS Appl. Mater. Interfaces*, 2013, 5, 1031-1037.

190. W.-T. Chen, Y.-J. Hsu, *Langmuir*, 2010, 26, 5918-5925.

191. Y. Kim, K.Y. Park, D.M. Jang, Y.M. Song, H.S. Kim, Y.J. Cho, Y. Myung, J. Park, *J. Phys. Chem. C*, 2010, 114, 22141-22146.

192. Y. Wang, W. Yang, L. Zhang, Y. Hu, X.W. Lou, *Nanoscale*, 2013, 5, 10864-10867.

193. M.-A. Einarsrud, T. Grande, *Chem. Soc. Rev.*, 2014, 43, 2187-2199.

194. Z. Zhang, L. Zhang, M.N. Hedhili, H. Zhang, P. Wang, *Nano Lett.*, 2013, 13, 14-20.

195. A. Pearson, H. Zheng, K. Kalantar-zadeh, S.K. Bhargava, V. Bansal, *Langmuir*, 2012, 28, 14470-14475.

196. F. Xiao, *J. Phys. Chem. C*, 2012, 116, 16487-16498.

197. H. Eom, J.-Y. Jung, Y. Shin, S. Kim, J.-H. Choi, E. Lee, J.-H. Jeong, I. Park, *Nanoscale*, 2014, 6, 226-234.

198. Q. Dong, H. Yu, Z. Jiao, G. Lu, Y. Bi, *RSC Adv.*, 2014, 4, 59114-59117.

199. J. Lan, X. Zhou, G. Liu, J. Yu, J. Zhang, L. Zhi, G. Nie, *Nanoscale*, 2011, 3, 5161-5167.

200. F.J. Boerio, *Thin Solid Films*, 1989, 181, 423-433.

201. D.-K. Lim, K.-S. Jeon, H.M. Kim, J.-M. Nam, Y.D. Suh, *Nat. Mater.*, 2010, 9, 60-67.

202. S. Schlücker, *Angew. Chem., Int. Ed.*, 2014, 53, 4756-4795.

203. X. Wang, W. Shi, G. She, L. Mu, *Phys. Chem. Chem. Phys.*, 2012, 14, 5891-5901.

204. Z. Sun, C. Wang, J. Yang, B. Zhao, J.R. Lombardi, *J. Phys. Chem. C*, 2008, 112, 6093-6098.

205. W. Song, Y. Wang, B. Zhao, *J. Phys. Chem. C*, 2007, 111, 12786-12791.

206. L. Yang, X. Jiang, W. Ruan, J. Yang, B. Zhao, W. Xu, J.R. Lombardi, *J. Phys. Chem. C*, 2009, 113, 16226-16231.

207. J. Xiong, C. Han, W. Li, Q. Sun, J. Chen, S. Chou, Z. Li, S. Dou, *CrystEngComm*, 2016, 18, 930-937.

208. J. Ran, J. Zhang, J. Yu, M. Jaroniec, S.Z. Qiao, *Chem. Soc. Rev.*, 2014, 43, 7787-7812.

209. J. Xiong, C. Han, Z. Li, S. Dou, *Sci. Bull.*, 2015, 60, 2083-2090.

210. S.T. Kochuveedu, Y.H. Jang, D.H. Kim, *Chem. Soc. Rev.*, 2013, 42, 8467-8493.

211. D. Lin, H. Wu, R. Zhang, W. Pan, *Chem. Mater.*, 2009, 21, 3479-3484.

212. A. McLaren, T. Valdes-Solis, G. Li, S.C. Tsang, *J. Am. Chem. Soc.*, 2009, 131, 12540-12541.

213. Y. Lai, M. Meng, Y. Yu, X. Wang, T. Ding, *Appl. Catal. B: Environ.*, 2011, 105, 335-345.

214. Y. Bai, H. Yu, Z. Li, R. Amal, G.Q.M. Lu, L. Wang, *Adv. Mater.*, 2012, 24, 5850-5856.

215. W.-j. Sun, J. Li, G. Mele, Z.-q. Zhang, F.-x. Zhang, *J. Mol. Catal. A: Chem.*, 2013, 366, 84-91.

216. Q. Deng, X. Duan, D.H.L. Ng, H. Tang, Y. Yang, M. Kong, Z. Wu, W. Cai, G. Wang, *ACS Appl. Mater. Interfaces*, 2012, 4, 6030-6037.

217. Y. Wei, J. Kong, L. Yang, L. Ke, H.R. Tan, H. Liu, Y. Huang, X.W. Sun, X. Lu, H. Du, *J. Mater. Chem. A*, 2013, 1, 5045-5052.

218. X. Liu, M.-H. Liu, Y.-C. Luo, C.-Y. Mou, S.D. Lin, H. Cheng, J.-M. Chen, J.-F. Lee, T.-S. Lin, *J. Am. Chem. Soc.*, 2012, 134, 10251-10258.

219. F. Liao, Y. Huang, J. Ge, W. Zheng, K. Tedsree, P. Collier, X. Hong, S.C. Tsang, *Angew. Chem., Int. Ed.*, 2011, 50, 2162-2165.

220. Z. Cheng, X. Zhan, F. Wang, Q. Wang, K. Xu, Q. Liu, C. Jiang, Z. Wang, J. He, *RSC Adv.*, 2015, 5, 81723-81727.

221. X. Zhan, Y. Bao, F. Wang, Q. Wang, Z. Cheng, Z. Wang, K. Xu, Z. Fang, J. He, *Appl. Phys. Lett.*, 2015, 106, 123904.

222. M. Macias-Montero, R.J. Peláez, V.J. Rico, Z. Saghi, P. Midgley, C.N. Afonso, A.R. González-Elipe, A. Borras, *ACS Appl. Mater. Interfaces*, 2015, 7, 2331-2339.

223. M. Ahmad, S. Yingying, A. Nisar, H. Sun, W. Shen, M. Wei, J. Zhu, *J. Mater. Chem.*, 2011, 21, 7723-7729.

224. M.N. Tahir, F. Natalio, M.A. Cambaz, M. Panthofer, R. Branscheid, U. Kolb, W. Tremel, *Nanoscale*, 2013, 5, 9944-9949.

225. Y. Chen, D. Zeng, K. Zhang, A. Lu, L. Wang, D.-L. Peng, *Nanoscale*, 2014, 6, 874-881.

226. M. Wu, W.-J. Chen, Y.-H. Shen, F.-Z. Huang, C.-H. Li, S.-K. Li, *ACS Appl. Mater. Interfaces*, 2014, 6, 15052-15060.

227. S. Kuriakose, V. Choudhary, B. Satpati, S. Mohapatra, *Phys. Chem. Chem. Phys.*, 2014, 16, 17560-17568.

228. Y. Jin, J. Xi, Z. Zhang, J. Xiao, F. Xiao, L. Qian, S. Wang, *Nanoscale*, 2015, 7, 5510-5515.

229. Z. Cheng, M. Yu, G. Yang, L. Kang, *CrystEngComm*, 2015, 17, 1765-1768.

230. E. Mosquera, C. Rojas-Michea, M. Morel, F. Gracia, V. Fuenzalida, R.A. Zárate, *Appl. Surf. Sci.*, 2015, 347, 561-568.

231. T. Jiang, X. Qin, Y. Sun, M. Yu, *RSC Adv.*, 2015, 5, 65595-65599.

232. V.P. Dinesh, P. Biji, A. Ashok, S.K. Dhara, M. Kamruddin, A.K. Tyagi, B. Raj, *RSC Adv.*, 2014, 4, 58930-58940.

233. M.E. Aguirre, H.B. Rodríguez, E. San Román, A. Feldhoff, M.A. Grela, *J. Phys. Chem. C*, 2011, 115, 24967-24974.

234. S. Wang, Y. Yu, Y. Zuo, C. Li, J. Yang, C. Lu, *Nanoscale*, 2012, 4, 5895-5901.

235. A. Callegari, D. Tonti, M. Chergui, *Nano Lett.*, 2003, 3, 1565-1568.

236. R. Jin, Y. Cao, C.A. Mirkin, K.L. Kelly, G.C. Schatz, J.G. Zheng, *Science*, 2001, 294, 1901-1903.

237. P. Mulvaney, *Langmuir*, 1996, 12, 788-800.

238. P. Ramasamy, D.-M. Seo, S.-H. Kim, J. Kim, *J. Mater. Chem.*, 2012, 22, 11651-11657.

239. Y. Sun, B. Gates, B. Mayers, Y. Xia, *Nano Lett.*, 2002, 2, 165-168.

240. Z. Wang, J. Liu, X. Chen, J. Wan, Y. Qian, *Chem. Eur. J.*, 2005, 11, 160-163.

241. S. Chen, D.L. Carroll, *Nano Lett.*, 2002, 2, 1003-1007.

242. R. Jin, Y. Charles Cao, E. Hao, G.S. Metraux, G.C. Schatz, C.A. Mirkin, *Nature*, 2003, 425, 487-490.

243. Y. Gao, L. Song, P. Jiang, L.F. Liu, X.Q. Yan, Z.P. Zhou, D.F. Liu, J.X. Wang, H.J. Yuan, Z.X. Zhang, X.W. Zhao, X.Y. Dou, W.Y. Zhou, G. Wang, S.S. Xie, H.Y. Chen, J.Q. Li, *J. Cryst. Growth*, 2005, 276, 606-612.

244. F. Li, Y. Yuan, J. Luo, Q. Qin, J. Wu, Z. Li, X. Huang, *Appl. Surf. Sci.*, 2010, 256, 6076-6082.

245. L. Yongchun, L. Yanhong, W. Dejun, W. Lingling, X. Tengfeng, J. Tengfei, *J. Phys. D: Appl. Phys.*, 2011, 44, 315502.

246. X. Wang, X. Kong, Y. Yu, H. Zhang, *J. Phys. Chem. C*, 2007, 111, 3836-3841.

247. K.K. Haldar, T. Sen, A. Patra, *J. Phys. Chem. C*, 2008, 112, 11650-11656.

248. Z. Wu, C. Xu, Y. Wu, H. Yu, Y. Tao, H. Wan, F. Gao, *CrystEngComm*, 2013, 15, 5994-6002.

249. D.-M. Tang, G. Liu, F. Li, J. Tan, C. Liu, G.Q. Lu, H.-M. Cheng, *J. Phys. Chem. C*, 2009, 113, 11035-11040.

250. V. Vamathevan, R. Amal, D. Beydoun, G. Low, S. McEvoy, *J. Photochem. Photobiol. A: Chem.*, 2002, 148, 233-245.

251. H. Li, Y. Sun, B. Cai, S. Gan, D. Han, L. Niu, T. Wu, *Appl. Catal. B: Environ.*, 2015, 170–171, 206-214.

252. X. Li, S. Fang, L. Ge, C. Han, P. Qiu, W. Liu, *Appl. Catal. B: Environ.*, 2015, 176–177, 62-69.

253. T. Sun, J. Qiu, C. Liang, *J. Phys. Chem. C*, 2008, 112, 715-721.

254. Q. Wan, T.H. Wang, J.C. Zhao, *Appl. Phys. Lett.*, 2005, 87, 083105.

255. H. Zeng, W. Cai, P. Liu, X. Xu, H. Zhou, C. Klingshirn, H. Kalt, *ACS Nano*, 2008, 2, 1661-1670.

256. N. Kislov, J. Lahiri, H. Verma, D.Y. Goswami, E. Stefanakos, M. Batzill, *Langmuir*, 2009, 25, 3310-3315.

257. H. Fu, T. Xu, S. Zhu, Y. Zhu, *Environ. Sci. Technol.*, 2008, 42, 8064-8069.

258. C. Yu, G. Li, S. Kumar, K. Yang, R. Jin, *Adv. Mater.*, 2014, 26, 892-898.

259. Q. Yuan, L. Chen, M. Xiong, J. He, S.-L. Luo, C.-T. Au, S.-F. Yin, *Chem. Eng. J.*, 2014, 255, 394-402.

260. Y. He, L. Zhang, B. Teng, M. Fan, *Environ. Sci. Technol.*, 2015, 49, 649-656.

261. X. Ding, K. Zhao, L. Zhang, *Environ. Sci. Technol.*, 2014, 48, 5823-5831.

262. L. Chen, R. Huang, S.-F. Yin, S.-L. Luo, C.-T. Au, *Chem. Eng. J.*, 2012, 193–194, 123-130.

263. J. Yu, J. Xiong, B. Cheng, S. Liu, *Appl. Catal. B: Environ.*, 2005, 60, 211-221.

264. R. Georgekutty, M.K. Seery, S.C. Pillai, *J. Phys. Chem. C*, 2008, 112, 13563-13570.

265. Z. Xiong, L.L. Zhang, J. Ma, X.S. Zhao, *Chem. Commun.*, 2010, 46, 6099-6101.

266. J. Ryu, W. Choi, *Environ. Sci. Technol.*, 2004, 38, 2928-2933.

267. K. Shankar, J.I. Basham, N.K. Allam, O.K. Varghese, G.K. Mor, X. Feng, M. Paulose, J.A. Seabold, K.-S. Choi, C.A. Grimes, *J. Phys. Chem. C*, 2009, 113, 6327-6359.

268. A.B.F. Martinson, J.E. McGarrah, M.O.K. Parpia, J.T. Hupp, *Phys. Chem. Chem. Phys.*, 2006, 8, 4655-4659.

269. Y. Ohsaki, N. Masaki, T. Kitamura, Y. Wada, T. Okamoto, T. Sekino, K. Niihara, S. Yanagida, *Phys. Chem. Chem. Phys.*, 2005, 7, 4157-4163.

270. T. Tachikawa, S. Tojo, M. Fujitsuka, T. Sekino, T. Majima, *J. Phys. Chem. B*, 2006, 110, 14055-14059.

271. Z.-R. Tang, F. Li, Y. Zhang, X. Fu, Y.-J. Xu, *J. Phys. Chem. C*, 2011, 115, 7880-7886.

272. N. Wu, J. Wang, D.N. Tafen, H. Wang, J.-G. Zheng, J.P. Lewis, X. Liu, S.S. Leonard, A. Manivannan, *J. Am. Chem. Soc.*, 2010, 132, 6679-6685.

273. Z. Liu, X. Zhang, S. Nishimoto, T. Murakami, A. Fujishima, *Environ. Sci. Technol.*, 2008, 42, 8547-8551.

274. J.R. Jennings, A. Ghicov, L.M. Peter, P. Schmuki, A.B. Walker, *J. Am. Chem. Soc.*, 2008, 130, 13364-13372.

275. T. Tachikawa, T. Majima, *J. Am. Chem. Soc.*, 2009, 131, 8485-8495.

276. Z.-R. Tang, X. Yin, Y. Zhang, Y.-J. Xu, *RSC Adv.*, 2013, 3, 5956-5965.
277. X. Bai, L. Wang, R. Zong, Y. Zhu, *J. Phys. Chem. C*, 2013, 117, 9952-9961.
278. Z. Li, L. Cheng, Q. Sun, Z. Zhu, M.J. Riley, M. Aljada, Z. Cheng, X. Wang, G.R. Hanson, S. Qiao, S.C. Smith, G.Q. Lu, *Angew. Chem., Int. Ed.*, 2010, 49, 2777-2781.
279. Z. Li, Ö. Kurtulus, N. Fu, Z. Wang, A. Kornowski, U. Pietsch, A. Mews, *Adv. Funct. Mater.*, 2009, 19, 3650-3661.
280. Z. Li, A.J. Du, Q. Sun, M. Aljada, L.N. Cheng, M.J. Riley, Z.H. Zhu, Z.X. Cheng, X.L. Wang, J. Hall, E. Krausz, S.Z. Qiao, S.C. Smith, G.Q. Lu, *Chem. Commun.*, 2011, 47, 11894-11896.
281. Z. Li, X. Ma, Q. Sun, Z. Wang, J. Liu, Z. Zhu, S.Z. Qiao, S.C. Smith, G. Lu, A. Mews, *Eur. J. Inorg. Chem.*, 2010, 2010, 4325-4331.
282. A. Kudo, Y. Miseki, *Chem. Soc. Rev.*, 2009, 38, 253-278.
283. G. Liu, L. Wang, H.G. Yang, H.-M. Cheng, G.Q. Lu, *J. Mater. Chem.*, 2010, 20, 831-843.
284. B. Cheng, Y. Le, J. Yu, *J. Hazard. Mater.*, 2010, 177, 971-977.
285. T. Hirakawa, P.V. Kamat, *J. Am. Chem. Soc.*, 2005, 127, 3928-3934.
286. Y. Zhao, W. Wang, Y. Li, Y. Zhang, Z. Yan, Z. Huo, *Nanoscale*, 2014, 6, 195-198.
287. Z. Zheng, B. Huang, Z. Wang, M. Guo, X. Qin, X. Zhang, P. Wang, Y. Dai, *J. Phys. Chem. C*, 2009, 113, 14448-14453.
288. M. Wang, L. Sun, Z. Lin, J. Cai, K. Xie, C. Lin, *Energy Environ. Sci.*, 2013, 6, 1211-1220.
289. W.-Y. Cheng, T.-H. Yu, K.-J. Chao, S.-Y. Lu, *ChemCatChem*, 2014, 6, 293-300.
290. Y. Wang, K. Yu, H. Yin, C. Song, Z. Zhang, S. Li, H. Shi, Q. Zhang, B. Zhao, Y. Zhang, Z. Zhu, *J. Phys. D: Appl. Phys.*, 2013, 46, 175303.
291. Z. Ai, L. Zhang, S. Lee, W. Ho, *J. Phys. Chem. C*, 2009, 113, 20896-20902.
292. C.-H. Kuo, Y.-C. Yang, S. Gwo, M.H. Huang, *J. Am. Chem. Soc.*, 2010, 133, 1052-1057.
293. W. Fan, S. Jewell, Y. She, M.K.H. Leung, *Phys. Chem. Chem. Phys.*, 2014, 16, 676-680.
294. C. Su, L. Liu, M. Zhang, Y. Zhang, C. Shao, *CrystEngComm*, 2012, 14, 3989-3999.

295. Y. Bi, J. Ye, *Chem. Commun.*, 2009, 6551-6553.
296. B. Wiley, Y. Sun, Y. Xia, *Acc. Chem. Res.*, 2007, 40, 1067-1076.
297. L. Zhang, D.A. Blom, H. Wang, *Chem. Mater.*, 2011, 23, 4587-4598.
298. R. Ji, W. Sun, Y. Chu, *RSC Adv.*, 2014, 4, 6055-6059.
299. W.-T. Wu, Y. Wang, L. Shi, W. Pang, Q. Zhu, G. Xu, F. Lu, *J. Phys. Chem. B*, 2006, 110, 14702-14708.
300. M. Yin, C.-K. Wu, Y. Lou, C. Burda, J.T. Koberstein, Y. Zhu, S. O'Brien, *J. Am. Chem. Soc.*, 2005, 127, 9506-9511.
301. Z. Zhang, P. Wang, *J. Mater. Chem.*, 2012, 22, 2456-2464.
302. L. Wei, C. Shifu, *J. Electrochem. Soc.*, 2010, 157, H1029-H1035.
303. D. Tahir, S. Tougaard, *J. Phys.: Condens. Matter*, 2012, 24, 175002.
304. Y.-C. Yang, H.-J. Wang, J. Whang, J.-S. Huang, L.-M. Lyu, P.-H. Lin, S. Gwo, M.H. Huang, *Nanoscale*, 2014, 6, 4316-4324.
305. R. Bardhan, N.K. Grady, T. Ali, N.J. Halas, *ACS Nano*, 2010, 4, 6169-6179.
306. Y. Lei, G. Wang, S. Song, W. Fan, M. Pang, J. Tang, H. Zhang, *Dalton Trans.*, 2010, 39, 3273-3278.
307. X. Zhang, Z. Ai, F. Jia, L. Zhang, *J. Phys. Chem. C*, 2008, 112, 747-753.
308. Y. Wang, K. Deng, L. Zhang, *J. Phys. Chem. C*, 2011, 115, 14300-14308.
309. L. Pan, J.-J. Zou, T. Zhang, S. Wang, Z. Li, L. Wang, X. Zhang, *J. Phys. Chem. C*, 2014, 16335–16343.
310. J. Cao, B. Luo, H. Lin, B. Xu, S. Chen, *J. Hazard. Mater.*, 2012, 217-218, 107-115.
311. M. Yin, Z. Li, J. Kou, Z. Zou, *Environ. Sci. Technol.*, 2009, 43, 8361-8366.
312. J. Cao, X. Li, H. Lin, S. Chen, X. Fu, *J. Hazard. Mater.*, 2012, 239–240, 316-324.
313. H. Lin, H. Ye, S. Chen, Y. Chen, *RSC Adv.*, 2014, 4, 10968-10974.
314. L. Chen, R. Huang, S.-F. Yin, S.-L. Luo, C.-T. Au, *Chem. Eng. J.*, 2012, 193-194, 123-130.
315. Q. Yuan, L. Chen, M. Xiong, J. He, S.-L. Luo, C.-T. Au, S.-F. Yin, *Chem. Eng. J.*, 2014, 255, 394-402.
316. J. Zhou, G. Tian, Y. Chen, Y. Shi, C. Tian, K. Pan, H. Fu, *Sci. Rep.*, 2014, 4, 4027.

317. H. Katsumata, T. Sakai, T. Suzuki, S. Kaneco, *Ind. Eng. Chem. Res.*, 2014, 53, 8018-8025.

318. E. Chelnokov, V. Cuba, D. Simeone, J.M. Guigner, U. Schmidhammer, M. Mostafavi, S. Le Caër, *J. Phys. Chem. C*, 2014, 118, 7865-7873.

319. Z. Wei, L. Xiaolin, Y. Zhi, T. Xuehui, M. Yujie, L. Ming, H. Nantao, W. Hao, Z. Yafei, *Nanotechnology*, 2016, 27, 265703.

320. Y. Pan, S. Deng, L. Polavarapu, N. Gao, P. Yuan, C.H. Sow, Q.-H. Xu, *Langmuir*, 2012, 28, 12304-12310.

321. Y. Qu, R. Cheng, Q. Su, X. Duan, *J. Am. Chem. Soc.*, 2011, 133, 16730-16733.

322. X. Hu, G. Li, J.C. Yu, *Langmuir*, 2009, 26, 3031-3039.

323. X. Wang, K. Maeda, A. Thomas, K. Takanabe, G. Xin, J.M. Carlsson, K. Domen, M. Antonietti, *Nat. Mater.*, 2009, 8, 76-80.

324. Z. Zou, J. Ye, K. Sayama, H. Arakawa, *Nature*, 2001, 414, 625-627.

325. X. Li, J. Yu, M. Jaroniec, *Chem. Soc. Rev.*, 2016, 45, 2603-2636.

326. Q. Li, B. Guo, J. Yu, J. Ran, B. Zhang, H. Yan, J.R. Gong, *J. Am. Chem. Soc.*, 2011, 133, 10878-10884.

327. C. Wei, C. Cheng, J. Zhao, S. Zheng, M. Hao, H. Pang, *Dalton Trans.*, 2014, 43, 5687-5693.

328. Z. Yu, B. Yin, F. Qu, X. Wu, *Chem. Eng. J.*, 2014, 258, 203-209.

329. N. Zhang, S. Liu, X. Fu, Y.-J. Xu, *J. Mater. Chem.*, 2012, 22, 5042-5052.

330. İ. Şişman, *InTech*, 2011, 41-58

331. S. Mlowe, D.J. Lewis, M.A. Malik, J. Raftery, E.B. Mubofu, P. O'Brien, N. Revaprasadu, *New J. Chem.*, 2014, 38, 6073-6080.

332. C.-H. Kuo, T.-E. Hua, M.H. Huang, *J. Am. Chem. Soc.*, 2009, 131, 17871-17878.

333. H. Duan, Y. Xuan, *Sol. Energ. Mat. Sol. C.*, 2014, 121, 8-13.

334. X. Huang, Z. Zeng, S. Bao, M. Wang, X. Qi, Z. Fan, H. Zhang, *Nat. Commun.*, 2013, 4, 1444.

335. X. Hong, Z. Yin, Z. Fan, Y.-Y. Tay, J. Chen, Y. Du, C. Xue, H. Chen, H. Zhang, *Small*, 2014, 10, 479-482.

336. Z. Fan, X. Zhang, J. Yang, X.-J. Wu, Z. Liu, W. Huang, H. Zhang, *J. Am. Chem. Soc.*, 2015, 137, 10910-10913.

337. G.R. Bourret, R.B. Lennox, *Nanoscale*, 2011, 3, 1838-1844.

338. S. Xiong, B. Xi, K. Zhang, Y. Chen, J. Jiang, J. Hu, H.C. Zeng, *Sci. Rep.*, 2013, 3, 2177.

339. B. Liu, Z. Ma, *Small*, 2011, 7, 1587-1592.

340. X. Ma, Y. Zhao, X. Jiang, W. Liu, S. Liu, Z. Tang, *ChemPhysChem*, 2012, 13, 2531-2535.

341. F. Jiang, Q. Tian, M. Tang, Z. Chen, J. Yang, J. Hu, *CrystEngComm*, 2011, 13, 7189-7193.

342. Y. Li, X. Ye, Y. Ma, L. Qi, *Small*, 2015, 11, 1183-1188.

343. C. Liang, K. Terabe, T. Hasegawa, M. Aono, *Nanotechnology*, 2007, 18, 485202.

344. H. Wang, L. Qi, *Adv. Funct. Mater.*, 2008, 18, 1249-1256.

345. M. Pang, J. Hu, H.C. Zeng, *J. Am. Chem. Soc.*, 2010, 132, 10771-10785.

346. J. Hu, A. Liu, H. Jin, D. Ma, D. Yin, P. Ling, S. Wang, Z. Lin, J. Wang, *J. Am. Chem. Soc.*, 2015, 137, 11004-11010.

347. C. Yuan, H.B. Wu, Y. Xie, X.W. Lou, *Angew. Chem., Int. Ed.*, 2014, 53, 1488-1504.

348. C. Lan, J. Gong, Y. Jiang, *J. Alloys Compd.*, 2013, 575, 24-28.

349. C. Lan, J. Gong, Y. Jiang, Q. Ding, *CrystEngComm*, 2012, 14, 8063-8067.

350. W. Zhou, Z. Yin, Y. Du, X. Huang, Z. Zeng, Z. Fan, H. Liu, J. Wang, H. Zhang, *Small*, 2013, 9, 140-147.

351. J. Liu, J. Jiang, C. Cheng, H. Li, J. Zhang, H. Gong, H.J. Fan, *Adv. Mater.*, 2011, 23, 2076-2081.

352. X.Q. Chen, Z. Li, Y. Bai, Q. Sun, L.Z. Wang, S.X. Dou, *Chem. Eur. J.*, 2015, 21, 1055-1063.

353. B. Xu, P. He, H. Liu, P. Wang, G. Zhou, X. Wang, *Angew. Chem., Int. Ed.*, 2014, 53, 2339-2343.

354. D. Okoli, G. Okeke, A. Ekpunobi, *Pac. J. Sci. Tech.*, 2010, 11, 411-415.

355. Y.-T. Long, C. Jing, Localized Surface Plasmon Resonance Based Nanobiosensors, Springer, Berlin Heidelberg, 2014.

356. J. Zhu, Y. Shen, A. Xie, L. Zhu, *J. Mater. Chem.*, 2009, 19, 8871-8875.

357. T. Hirakawa, P.V. Kamat, *J. Am. Chem. Soc.*, 2005, 127, 3928-3934.

358. J. Zeng, J. Tao, D. Su, Y. Zhu, D. Qin, Y. Xia, *Nano Lett.*, 2011, 11, 3010-3015.

359. S. Chang, Q. Li, X. Xiao, K.Y. Wong, T. Chen, *Energy Environ. Sci.*, 2012, 5, 9444-9448.

360. Y. Zhao, D. Zhang, W. Shi, F. Wang, *Mater. Lett.*, 2007, 61, 3232-3234.

361. X. Fu, H. Zou, L. Zhou, *J. Nanosci. Nanotechnol.*, 2010, 10, 5851-5856.

362. D. Li, H.-Z. Xie, J.-K. Liu, C.-J. Duan, *J. Exp. Nanosci.*, 2011, 6, 209-216.

363. T. Mokari, A. Aharoni, I. Popov, U. Banin, *Angew. Chem., Int. Ed.*, 2006, 45, 8001-8005.

364. L. Xu, Z. Yin, S.-W. Cao, Z. Fan, X. Zhang, H. Zhang, C. Xue, *Chem. Eur. J.*, 2014, 20, 2742-2745.

365. J. Yang, J.Y. Ying, *Angew. Chem., Int. Ed.*, 2011, 50, 4637-4643.

366. J. Yang, J.Y. Ying, *J. Am. Chem. Soc.*, 2010, 132, 2114-2115.

367. Y. Li, L. Li, Y. Gong, S. Bai, H. Ju, C. Wang, Q. Xu, J. Zhu, J. Jiang, Y. Xiong, *Nano Res.*, 2015, 8, 3621-3629.

368. D. Seo, C.I. Yoo, J. Jung, H. Song, *J. Am. Chem. Soc.*, 2008, 130, 2940-2941.

369. C. Han, Z. Li, W.-j. Li, S.-l. Chou, S.-x. Dou, *J. Mater. Chem. A*, 2014, 2, 11683-11690.

370. S. Zhang, W. Li, B. Tan, S. Chou, Z. Li, S. Dou, *J. Mater. Chem. A*, 2015, 3, 4793-4798.

371. Y. Hwa, C.-M. Park, H.-J. Sohn, *J. Electroanal. Chem.*, 2012, 667, 24-29.

372. X. Xu, B. Dong, S. Ding, C. Xiao, D. Yu, *J. Mater. Chem. A*, 2014, 2, 13069-13074.

373. S. Chen, Y. Xin, Y. Zhou, F. Zhang, Y. Ma, H. Zhou, L. Qi, *J. Mater. Chem. A*, 2014, 2, 15582-15589.

374. L. Chen, T. Ji, L. Brisbin, J. Zhu, *ACS Appl. Mater. Interfaces*, 2015, 7, 12230-12237.

375. W. Liu, P. Miao, L. Xiong, Y. Du, X. Han, P. Xu, *Phys. Chem. Chem. Phys.*, 2014, 16, 22867-22873.

376. Q. Kuang, S. Yang, *CrystEngComm*, 2014, 16, 4940-4944.

377. C. Qiu, L. Zhang, H. Wang, C. Jiang, *J. Phys. Chem. Lett.*, 2012, 3, 651-657.

378. J.R. Lombardi, R.L. Birke, *J. Phys. Chem. C*, 2008, 112, 5605-5617.

379. L. Jiang, P. Yin, T. You, H. Wang, X. Lang, L. Guo, S. Yang, *ChemPhysChem*, 2012, 13, 3932-3936.

380. S. Kundu, U. Nithiyanantham, *RSC Adv.*, 2013, 3, 25278-25290.

381. E. Nalbant Esenturk, A.R. Hight Walker, *J. Raman Spectrosc.*, 2009, 40, 86-91.

382. M. Sackmann, A. Materny, *J. Raman Spectrosc.*, 2006, 37, 305-310.

383. A. Comin, K. Korobchevskaya, C. George, A. Diaspro, L. Manna, *Nano Lett.*, 2012, 12, 921-926.

384. J. Jiang, X. Zhang, P. Sun, L. Zhang, *J. Phys. Chem. C*, 2011, 115, 20555-20564.

385. T. Jiang, T. Xie, Y. Zhang, L. Chen, L. Peng, H. Li, D. Wang, *Phys. Chem. Chem. Phys.*, 2010, 12, 15476-15481.

386. O.I. Micic, Y. Zhang, K.R. Cromack, A.D. Trifunac, M.C. Thurnauer, *J. Phys. Chem.*, 1993, 97, 7277-7283.

387. C.A. Emilio, M.I. Litter, M. Kunst, M. Bouchard, C. Colbeau-Justin, *Langmuir*, 2006, 22, 3606-3613.

388. H.H. Mohamed, C.B. Mendive, R. Dillert, D.W. Bahnemann, *J. Phys. Chem. A*, 2011, 115, 2139-2147.

389. S. Sardar, P. Kar, H. Remita, B. Liu, P. Lemmens, S. Kumar Pal, S. Ghosh, *Sci. Rep.*, 2015, 5, 17313.

APPENDIX A: LIST OF PUBLICATIONS

1. Jinyan Xiong, Zhen Li*, Jun Chen, Shanqing Zhang, Lianzhou Wang, Shixue Dou, "Facile synthesis of highly efficient one-dimensional plasmonic photocatalysts through Ag@Cu_2O core-shell heteronanowires", ***ACS Appl. Mater. Interfaces***, **2014**, 6, 15716-15725; **Citations: 33**; **Impact Factor: 7.145**.

2. Jinyan Xiong, Qiao Sun, Jun Chen, Zhen Li*, Shixue Dou, "Ambient controlled synthesis of advanced core-shell plasmonic Ag@ZnO photocatalysts", ***CrystEngComm***, **2016**, 18, 1713-1722; **Impact Factor: 3.849**. (**Inside Front Cover**)

3. Jinyan Xiong, Chao Han, Weijie Li, Qiao Sun, Jun Chen, Shulei Chou, Zhen Li*, Shixue Dou, "Ambient synthesis of a multifunctional 1D/2D hierarchical Ag-Ag_2S nanowire/nanosheet heterostructure with diverse applications", ***CrystEngComm***, **2016**, 18, 930-937; **Impact Factor: 3.849**.

4. Jinyan Xiong, Chao Han, Zhen Li*, Shixue Dou, "Effects of nanostructure on clean energy: big solutions gained from small features", ***Sci. Bull.***, **2015**, 60, 2083-2090; **Impact Factor: 1.789**.

5. Jinyan Xiong, Xulei Du, Zhen Li*, Qiao Sun, Huagui Yang, Jun Chen, Shixue Dou, "Facile synthesis of Ag@CdS Core-Shell hierarchical heteronanowires as highly efficient photocatalyst", for submission to ***CrystEngComm***, **2016**.

APPENDIX B: CONFERENCES ATTENDED

1. 5th Australia-China Conference on Science, Technology and Education In conjunction with 5th Australia-China Symposium for Materials Science, 21-23 July 2014, Wollongong, Australia.
2. Nanotech France 2016 and Joint Conferences (EGF 2016, NanoMetrology France 2016 and NanoMatEn 2016) and Exhibition, Oral Presentation: “Facile Synthesis of Highly Efficient One-Dimensional Plasmonic”, 1-3 June 2016, Paris, France.

APPENDIX C: AWARDS RECEIVED

1. Faculty Scholarship & International Postgraduate Tuition Award Faculty, UOW, 2013-2016
2. 2015 ISEM Postgraduate Student Merit Award, UOW
3. AIIM HDR Student Conference and International Travel Grants.